

Sheffield Hallam University

Molecular dynamics simulations of calamitic and discotic liquid crystals

DE LUCA, Marc Dominic

Available from the Sheffield Hallam University Research Archive (SHURA) at:

<http://shura.shu.ac.uk/3187/>

A Sheffield Hallam University thesis

This thesis is protected by copyright which belongs to the author.

The content must not be changed in any way or sold commercially in any format or medium without the formal permission of the author.

When referring to this work, full bibliographic details including the author, title, awarding institution and date of the thesis must be given.

Please visit <http://shura.shu.ac.uk/3187/> and <http://shura.shu.ac.uk/information.html> for further details about copyright and re-use permissions.

CITY CAMPUS POND STREET
SHEFFIELD S1 1WB

101 531 909 2



BEN
376721

Sheffield Hallam University

REFERENCE ONLY

ProQuest Number: 10694426

All rights reserved

INFORMATION TO ALL USERS

The quality of this reproduction is dependent upon the quality of the copy submitted.

In the unlikely event that the author did not send a complete manuscript and there are missing pages, these will be noted. Also, if material had to be removed, a note will indicate the deletion.



ProQuest 10694426

Published by ProQuest LLC (2017). Copyright of the Dissertation is held by the Author.

All rights reserved.

This work is protected against unauthorized copying under Title 17, United States Code
Microform Edition © ProQuest LLC.

ProQuest LLC.
789 East Eisenhower Parkway
P.O. Box 1346
Ann Arbor, MI 48106 – 1346

MOLECULAR DYNAMICS SIMULATIONS OF CALAMITIC AND DISCOTIC LIQUID CRYSTALS

Marc Dominic De Luca BSc(Hons)

A thesis submitted in partial fulfilment
of the requirements of
Sheffield Hallam University
for the degree of Doctor of Philosophy

June 1997

Department of Applied Physics, Sheffield Hallam University
in collaboration with the
Defence Research Agency, Malvern.



MOLECULAR DYNAMICS SIMULATIONS OF CALAMITIC AND DISCOTIC LIQUID CRYSTALS

ABSTRACT

Significant progress has been made in recent years in modelling liquid crystal phases using the Monte Carlo and molecular dynamics simulation techniques. We describe the technique of molecular dynamics in the microcanonical ensemble that we have used in simulations of liquid crystal systems. A review and discussion of some of the important simulations that have been performed to date on non-spherical hard particle models, soft anisotropic single site models, and realistic atom-atom based models is presented.

We report the results of molecular dynamics simulation studies of a system of particles interacting via an anisotropic potential proposed by Luckhurst and Romano, scaled by part of the well depth formulation employed by Gay and Berne. The resultant hybrid Gay-Berne Luckhurst-Romano (HGBLR) potential has an approximately spherical hard core with anisotropic long range attractive interactions with a dependency on the intermolecular vector joining a pair of sites. The spherical hard core nature of individual HGBLR centres notwithstanding we have parameterised single-site HGBLR centres to represent both calamitic and discotic mesogens. Both systems are shown to exhibit a range of mesophases on cooling from the isotropic liquid to form a crystal, including uniaxial-nematic and columnar-like phases. Unlike previous hard particle studies these ordered phases obtain because of the presence of the long range attractive interactions. A comparison between the different structures formed with the two different parameterisations is presented including graphical representations of the simulation cell .

In order to more closely represent the short range anisotropic interactions of real mesogens, a 3-HGBLR-site model has been parameterised to represent the mesogen *para*-terphenyl. Details of the parameterisation are discussed. Two versions of this model, a twisted central site 3-HGBLR-site model obtained from a molecular mechanics minimum energy conformation of *para*-terphenyl, and an all coplanar 3-HGBLR-site model have been studied using the molecular dynamics technique. The resultant models are found to be biaxial unlike previous anisotropic single site studies utilising soft potentials. Both models appear to exhibit a variety of uniaxial and biaxial mesophases but inclusion of the twisted site appears to promote the formation of biaxial phases. A comparison of the two models is made.

CONTENTS

ACKNOWLEDGEMENTS	v
ADVANCED STUDIES	vi
PUBLICATIONS	vii
<u>CHAPTER I</u>	1
<u>INTRODUCTION</u>	
I.1 Introduction	1
I.2 Liquid Crystal Phases	4
I.2.1 Calamitic Phases	5
I.2.2 Discotic Phases	7
I.3 References	9
<u>CHAPTER II</u>	11
<u>THE HYBRID GAY-BERNE LUCKHURST-ROMANO</u>	
<u>POTENTIAL AND THE MOLECULAR DYNAMICS METHOD</u>	
II.1 Introduction	11
II.2 The Interaction Potential	12
II.2.1 Hard Particle Potentials	15
II.2.2 Soft Particle Potentials	16
II.2.3 Anisotropic Soft Pair Potentials and the Origin of the HGBLR Potential	17
II.3 Computational Techniques in Molecular Dynamics	30
II.3.1 Periodic Boundary Conditions and the Minimum Image Convention	31
II.3.2 Finite Size Effects	33
II.3.3 Simulation Box Geometry	34
II.3.4 Potential Truncation	35
II.3.5 Initial Conditions	36
II.3.6 Integrating the Equations of Motion	37
II.3.6.1 Translational Equations of Motion	39
II.3.6.2 Rotational Equations of Motion	40
II.3.6.2.1 Rotational Equations of Motion for Cylindrically Symmetric Molecules	40
II.3.6.2.2 Rotational Equations of Motion for Arbitrarily Shaped Molecules	43
II.3.7 Hard Particle Dynamics	46
II.4 Simulation Averages	47

II.4.1	Thermodynamic and Dynamic Averages	49
II.4.2	Distribution Functions and Order Parameters	51
II.5	References	55
Chapter III		60
<u>COMPUTER SIMULATION OF LIQUID CRYSTALS</u>		
III.1	Introduction	60
III.2	Anisotropic Repulsive Forces vs Anisotropic Attractive Dispersion Forces	62
III.3	Hard Particle Liquid Crystal Simulations	65
III.3.1	Hard Particle Models: Hard Ellipses	66
III.3.2	Hard Particle Models: Infinitely Thin Hard Platelets	69
III.3.3	Hard Particle Models: Spherocylinders	72
III.3.4	Hard Particle Models: Cut Spheres	81
III.3.5	Hard Particle Models: Ellipsoids of Revolution	84
III.3.6	Hard Particle Models: Spheroids	89
III.3.7	Hard Particle Models: Rigid and Semi-flexible Hard Sphere Chains	89
III.4	Single-Site Soft Potential Simulations	90
III.5	Lattice Models	111
III.6	Realistic Models	112
III.7	Summary	117
III.8	References	118
 <u>CHAPTER IV</u>		
<u>MOLECULAR DYNAMICS SIMULATIONS OF CALAMITIC AND DISCOTIC SINGLE-SITE HYBRID GAY-BERNE LUCKHURST-ROMANO POTENTIAL</u>		
IV.1	Introduction	124
IV.2	Parameterisation of a Single HGBLR Centre	125
IV.3	Discotic HGBLR Simulations	135
IV.3.1	Details of the Discotic Simulations	135
IV.3.2	Discotic Simulation Results	138
IV.3.2.1	Energy Fluctuations, Potential Energy and Rank Orientational Order Parameter	138
IV.3.2.2	Radial Distribution Function and Second Rank Orientational Correlation Coefficient	144
IV.3.2.3	Preliminary Identification of Phases	152
IV.3.2.4	Mean Square Particle Displacement and Diffusion Coefficients	153
IV.3.2.5	Graphical Representations of Discotic HGBLR Centres	158
IV.3.2.6	Discotic HGBLR Centres: Brief Summary	164
IV.4	Calamitic HGBLR Simulations	166

IV.4.1	Details of the Calamitic Simulations	166
IV.4.2	Calamitic Simulation Results	168
IV.4.2.1	Energy Fluctuations, Potential Energy and Rank Orientational Order Parameter	168
IV.4.2.2	Radial Distribution Function and Second Rank Orientational Correlation Coefficient	181
IV.4.2.3	Mean Square Particle Displacement and Diffusion Coefficients	186
IV.4.2.4	Preliminary Identification of Phases	193
IV.4.2.5	Graphical Representations of Calamitic HGBLR Centres	193
IV.4.2.6	Calamitic HGBLR Centres: Brief Summary	195
IV.5	Summary Comparison of Discotic and Calamitic HGBLR Centres	200
IV.5.1	Phase Transition Temperatures	200
IV.5.2	Anisotropic Diffusion Effects	200
IV.5.3	Structural Effects	201
IV.6	Concluding Remarks	
IV.7	References	203

CHAPTER V **204**

SIMULATION OF THE NEMATOGEN *PARA*-TERPHENYL USING A MULTI-HYBRID-GAY-BERNE LUCKHURST-ROMANO-SITE SITE POTENTIAL

V.1	Introduction	204
V.2	A 32-Lennard-Jones-Site Site Representation of an Energy Minimised Conformer of the Nematogen <i>Para</i> -Terphenyl	204
V.3	Choosing the Number of Sites and Type of Site Parameterisation of the Multi-HGBLR-Site Site Model of <i>Para</i> -Terphenyl	211
V.4	Parameterisation of a 3-HGBLR-Site Site Model of <i>Para</i> -Terphenyl	216
V.5	Calculating the Reduced Moment of Inertia Tensor	236
V.6	Preliminary Simulation of the 3-HGBLR-Site Site Representation of <i>Para</i> -Terphenyl	239
V.6.1	Implementation of a Cutoff	239
V.6.2	Choice of Time Step	240
V.6.3	Choice of Density	240
V.7	Details of <i>Para</i> -Terphenyl Simulations	241
V.8	<i>Para</i> -Terphenyl Simulation Results: Comparison of the Twisted Central Site and All Coplanar Site 3-HGBLR-Site Site Models	243
V.8.1	Potential Energy and the Second Rank Orientational Order Parameter	243

V.8.2	Radial Distribution Function and Second Rank Orientational Correlation Coefficient	253
V.8.3	Mean Square Particle Displacement	267
V.8.4	Graphical Representations	270
V.9	Conclusions	280
V.10	References	288
<u>CHAPTER VI</u>		290
<u>CONCLUSIONS AND FUTURE WORK</u>		
<u>APPENDIX A</u>		294
<u>SINGLE-SITE AND MULTI-SITE HGBLR DERIVATIONS</u>		
A.1	Single-Site HGBLR Derivation	295
A.2	Multi-Site HGBLR Derivation	300
<u>APPENDIX B</u>		310
<u>INVESTIGATION OF λ AND χ' PARAMETER SPACE</u>		
B.1	Coarse Grid Search	311
B.2	Fine Grid Search	315
<u>APPENDIX C</u>		317
<u>PUBLICATIONS</u>		

ACKNOWLEDGEMENTS

A big thank you to all those who've helped (or hindered), me on my way in completing this thesis, not least: Professor Chris Care; Dr., Maureen Neal; Dr., Damien McDonnel; Dr., Mike Griffiths; Dr., Martin Callaway, Caroline Johnson, Gail Hawley, Nicolas Gilhooly; Jason Marsh; Jacqueline De Luca; Thomas De Luca and not forgetting Sydney.

To all those down the Broadfield; thanks for the beers!

To all the simulants in the modelling lab; thanks for the advice (wish I had taken it!).

To the computer "techs" at the University; thanks for the assistance

Thank you!

MDD, Sheffield, June 1997

ADVANCED STUDIES

During the period of research the following courses and conferences were attended, in addition to ongoing seminars at Sheffield Hallam University and regular discussion meetings held locally at Sheffield University and presentations to the collaborating institution at Sheffield Hallam University and DRA Malvern.

November 1990

Amdahl VP1100/1200 Course, Manchester Computing Centre, UK.

December 1990

British Liquid Crystal Society Introductory Meeting, Leeds University, UK.

July 1991

Understanding Self-Assembly and Organisation in Liquid Crystals, University of Leeds, UK.

April 1991

CCP5 Meeting: Beyond the Pair Potential, Keele University, UK.

September 1991

Computer Simulation of Liquid Crystals A NATO Advanced Research Workshop, Il Ciocco, Barga, Italy.

June 1992

British Liquid Crystal Society Discotics Meeting, University of East Anglia, UK

June 1993

CCP5 Meeting, Sheffield Hallam University, UK.

PUBLICATIONS

The following papers have been accepted for publication in the stated peer reviewed journal in connection with the work presented in this thesis. They are collected together and presented as appendix C.

M. D. De Luca, M. P. Neal, and C. M. Care, 1994, Molecular dynamics simulations of discotic liquid crystals using a hybrid Gay-Berne Luckhurst-Romano potential, *Liquid Crystals*, **16**, 257-266.

M. D. De Luca, M. K. Griffiths, C. M. Care, and M. P. Neal, 1994, Computer modelling of discotic liquid crystals, *International Journal of Electronics*, **6**, 907-917.

M. P. Neal, M. D. De Luca and C. M. Care, 1995, Molecular dynamics simulations of calamitic and discotic liquid crystals using a hybrid Gay-Berne Luckhurst-Romano Potential, *Molecular Simulation*, **14**, 245-258.

CHAPTER I

INTRODUCTION

The term liquid crystal is commonly used to describe a number of different states of matter that lie intermediate between normal crystalline solids and isotropic liquids. The component molecules of such states of matter possess some degree of long range orientational and often additionally, partial translational order, but in all cases the substance remains fluid albeit quite viscous at times. In the macroscopic regime the long range order manifests itself in the anisotropic behaviour of the bulk properties of a liquid crystal sample. These bulk properties are exploited in the many technological applications of liquid crystals.

In order to appreciate the potential range of applications [1] of liquid crystals it is necessary to arrive at a comprehensive understanding of the thermodynamic processes driving the underlying ordering phenomena. Additionally, such an understanding is of importance in its own right. This may be achieved through computer simulation techniques - at least for idealised models of liquid crystals.

This thesis will concern us with the particular technique of molecular dynamics (MD). Presently the limitations in performance of computer technology allow us to gain insight into the formation of liquid crystal mesophases through simplified models of mesogens as a collection of site-site and single-site anisotropic potentials interacting in a pair-wise fashion. It is the aim of this study to investigate the properties of a system of particles interacting via an anisotropic pair potential which is characterised by orientational dependant terms with

respect to the particles themselves and with respect to the intermolecular vector separating them. Accordingly, we have taken a potential proposed by Luckhurst and Romano [2] and modified it by part of the well depth scaling term employed by Gay and Berne [3]: the hybrid Gay-Berne Luckhurst-Romano potential. This potential has the property of a spherical hard core for a given orientation of a pair of molecules, together with a long range anisotropic attractive region. As such it is possible to parameterise the potential to represent a rod-like mesogen favouring side-by-side alignment or as a disc-like mesogen favouring end-to-end alignment. Despite the spherical nature of the HGBLR hard core, the model is found to exhibit a range of mesophases. We present the results of molecular dynamics simulations in the microcanonical ensemble of systems of single-site HGBLR particles parameterised to represent both calamitic and discotic mesogens in chapter IV.

The spherical hard core of the HGBLR model is unrealistic as real mesogens must necessarily deviate from spherical symmetry. Thus in an attempt to more accurately model a real liquid crystal forming compound, we have rigidly joined three such sites with discotic parameterisation to represent the mesogen *para*-terphenyl. In chapter V we propose a tractable methodology for parameterising this new model based on comparison with a Lennard-Jones atom-atom representation of *para*-terphenyl. The resultant 3-HGBLR-site model is biaxial and this model too has been studied using molecular dynamics. We present results for two models: an all coplanar site model and a model with the central site twisted about the molecular long axis with respect to the coplanar end rings.

Since the first MD experiments of Alder and Wainwright [4], significant advances have been made in simulation technique. Chapter II provides an introduction to the general molecular dynamics technique followed by details of the Hybrid Gay-Berne Luckhurst-Romano potential. The origins of the potential are clearly presented together with a brief history of single site anisotropic potentials. Specific methods that we have employed in our simulations, for example the methods used in integrating the equations of motion, or in subsequent analysis of the data produced are explained later in this chapter.

Today, there is a vast amount of literature available on computer simulation of liquid crystals. Previous work can be divided broadly into four categories:

Hard Particle Models;

Soft Particle Models;

Lattice Models;

Realistic Models.

In chapter III we present a review of some of these models that have been studied pointing out some of the surprising results obtained from simple models. The different models each are seen to provide particular features to simulations which have helped our understanding, through comparison with either real experiments on liquid crystals, or, comparison with theory or indeed other simulations, of the formation of liquid crystal phases. Both single-site hard particle and single-site soft particle models have been used extensively due to their relative computational simplicity. However, it is clear that in order to simulate the subtleties of real mesogens realistic models will have to be used. Evidence is

presented that these realistic atom-atom and united atom models are just becoming computationally feasible with today's resources.

For the rest of this chapter we shall briefly mention, as an introduction, the structure of a few liquid crystal mesophases that have been reported in the simulation literature and are exhibited by real liquid crystal systems.

I.2 Liquid Crystal Mesophases

Liquid crystal mesophases represent a number of different states of matter which are characterised by the partial orientational and sometimes additionally translational ordering of their constituent molecules. Liquid crystalline materials were first observed in the late nineteenth century [5]. It is not intended to give a detailed discussion on liquid crystal mesophases in this introduction as many excellent publications and reviews exist to serve this purpose (see section I.3): a brief introduction describing the various types of mesophase will be provided instead.

Liquid crystals can be divided into two distinct groups differentiated by the way in which their respective liquid crystal phases are formed [6]. Lyotropic liquid crystals composed of amphiphilic organic molecules such as soaps and detergents form mesophases which incorporate water into their structure. The type of mesophase expressed is dependent on the relative concentration of amphiphile to solvent and to some extent on the relative temperature [7].

Thermotropic mesophases are temperature dependent states that do not require the action of a solvent in their formation [8,9]. It is models of this group of liquid crystals that we have investigated in this study. It is necessary for liquid crystal

molecules to deviate from spherical symmetry in order to exhibit orientationally ordered phases [10]. Thus many liquid crystal molecules have elongated rod-like or more recently discovered flattened disc-like shapes [11]. Thermotropic liquid crystals may exhibit many mesophases over a range of temperatures, a phenomenon known as polymorphism. Generally the phases described become more ordered as the temperature is lowered, although it is possible to experience re-entrant phenomena where some previously observed phase reappears again at lower temperature. Some of these phases have been previously classified based on symmetry considerations alone [12,13] leading to the now familiar nematic and smectic phases, although with the advent of discotic mesophases different phase symmetries have had to be considered [9,14].

I.2.1 Calamitic Mesophases

For our purposes here it is sufficient to describe just two types of calamitic mesophase, namely, the nematic and the smectic. In a uniaxial nematic liquid crystal long range orientational order exists between the principle symmetry axes of the constituent molecules: they tend to be aligned along a given direction labelled by a unit vector, the director, \hat{n} . The uniaxial nematic phases possess $D_{\infty h}$ symmetry in Schoenflies notation. Other symmetries exist, for example in a biaxial nematic orientational ordering of the remaining molecular semi-axes is present additionally leading to D_{2h} . The component molecules of a nematic phase show no translational order at long range and the phase remains quite fluid and exhibits structural features typical of a dense liquid. The nematic phase is the lowest class of liquid crystal in terms of symmetry breaking operations necessary to form it from an isotropic phase.

Nematic phases are formed from achiral molecules or racemic mixtures of optically active species. Nematic-like ordered phases formed by non-racemic mixtures of chiral molecules display a helical distribution of the components of \hat{n} such that:

$$n_x = \cos(q_0 z + \phi) \quad [1.5]$$

$$n_y = \sin(q_0 z + \phi) \quad [1.4]$$

$$n_z = 0 \quad [1.3]$$

where q_0 is a constant and ϕ is an arbitrary phase angle. Thus the sense of \hat{n} rotates in the plane perpendicular to n_z on moving along n_z . Such phases are called cholesterics after such behaviour was identified for pure cholesterol esters.

Smectic phases possess at least one degree of translational order in addition to the orientational order exhibited by nematic mesophases at long range. The translational order manifests itself as a layered structure. In the smectic-A phase for example, the constituent molecules are still aligned along the director, \hat{n} , but additionally these molecules are confined to a series of layers lying perpendicular to the director. The molecules remain translationally disordered within the layers which themselves slide easily over each other maintaining the fluidity of the phase. Because of this smectic phases are often described as two-dimensional liquids.

Other types of smectic exist. In the smectic-C phase the constituent molecules are tilted with respect to the layer planes. In this case both a nematic director and smectic layer direction can be identified. The tilt angle is often seen to vary with temperature and tilt angles of up to 45° between these directions have been

observed. Once again there is no translational ordering of molecules within the smectic-C layers. If component molecules of a smectic-C phase are optically active then the direction of tilt describes a precession in a helical fashion moving along the layer normal and a smectic-C* phase results.

Some more ordered smectic phases exist. The particles consisting a smectic-B phase do exhibit orientational order and are arranged in layers perpendicular to \hat{n} . Additionally though the molecules are distributed on a quasi-triangular lattice within the layers. The molecular positional order does not extend to great distances but the bond orientational order of the quasi-lattice is preserved over macroscopic distances. Such phases characterised by D_{6h} point group symmetry are called hexatic smectic-B and differ from crystal-B phases (see below) in which both the bond orientational order and positional order of the molecules is preserved at long range. Hexatic smectic-B phases consisting of tilted molecules exist and are denoted smectic-F and smectic-I depending on the direction of tilt.

Other smectic phases exist and are denoted S_B , S_E , S_G , S_H , S_I and S_K . However, these are in fact all crystals exhibiting long range positional order. Generally they have a 3-dimensional structure consisting of layers stacked upon each other in a similar fashion as graphite. The forces between the layers are weak leading to these crystalline phases resembling true smectics in some experiments.

I.2.1 Discotic Mesophases

Discotic mesophases here refer to those phases formed by disc-like mesogenic molecules. The discotic nematic phase has all the properties of the previously described calamitic nematic (see above): the principal symmetry axis, now the

molecular short axis of the disc-like particles, tend to align along a common direction \hat{n} .

Some disc-like mesogens form columnar phases whereby the discs assemble themselves in columns, often parallel to \hat{n} . The centres of the columns are usually arranged on a triangular lattice. Within the columns the discoid molecules are irregularly spaced, with positional correlations existing over short range only and diffusion occurs parallel to the column axis, leading these phases to have been termed one-dimensional liquids. Indeed an interesting potential application of columnar systems as molecular wires, with electrical conductivity occurring along the columns only is presently being investigated [15]. Sometimes the discoid molecules are tilted with respect to the columnar axis and this often leads to the columns themselves being distributed on a rectangular lattice.

I.3 References

- [1] See for example Bahadur, B., 1990, *Liquid Crystals, Applications and Uses, Volume 1*, editor (World Scientific Publishing Company, Singapore); Bahadur, B., 1984, *Molecular Crystals and Liquid Crystals*, **109**, 1-93; 1983, *Ibid*, **99**, 345-374; Scheuble, B., S., 1989, *Kontakte*, **1**, 34-48; Meier, G., Sackmann, E., and Grabmeier, J., G., 1975, *Applications of Liquid Crystals* (Springer-Verlag, Berlin, Germany).
- [2] Luckhurst, G. R., and Romano, S., 1980, *Proceedings of the Royal Society London A*, **373**, 111-130.
- [3] Gay, J. G., and Berne, B. J., 1981, *Journal of Chemical Physics*, **74**, 3316- 3319.

- [4] Alder, B. J., and Wainwright, T. E., 1957, *Journal of Chemical Physics*, **27**, 1208-1209; 1959, *Ibid*, **31**, 459-466.
- [5] Reinitzer, F., 1888, *Monatshefte fur Chemie*, **9**, 421; Lehmann, O., 1890, *Zeitschrift fur Kristallographie.*, **18**, 464.
- [6] Priestly, E. B., 1975, *Liquid Crystal Mesophases in Introduction to Liquid Crystals, 2nd edition*, edited by Priestly, E. B., Wojtowicz, P. J., and Ping Sheng, (Plenum Press, New York USA).
- [7] Laughlin, R. G., 1994, *The Aqueous Phase Behaviour of Surfactants* (Academic Press, London, UK); Friberg, S., 1976, *Lyotropic Liquid Crystals* (American Chemical Society, Washington D. C., USA).
- [8] Vertogen, G., and de Jeu, W. H., 1988, *Thermotropic Liquid Crystals, Fundamentals* (Springer-Verlag, Berlin, Germany).
- [9] Chandrasekhar, S., 1992, *Liquid Crystals, 2nd Edition* (Cambridge University Press, Cambridge, UK); de Gennes, P. G., and Prost, J., *The Physics of Liquid Crystals, 2nd Edition* (Clarendon Press, Oxford, UK).
- [10] Gray, G. W., 1979, *Liquid Crystals and Molecular Structure - Nematics and Cholesterics* in *The Molecular Physics of Liquid Crystals*, edited by Luckhurst, G. R., and Gray, G. W., (Academic Press, London, UK).
- [11] Chandrasekhar, S., Sadashiva, B., K., and Suresh, K., A., 1977, *Pramana*, **9**, 471; Billard, J., Dubois, J., C., Tinh, N., H., and Zann, A., 1978, *Nouveau Journal de Chemie*, **2**, 535; Chandrasekhar, S., 1983, *Philosophical Transactions of the Royal Society, London A*, **309**, 93-103; Chandrasekhar, S., and Ranganath, G. S., 1990, *Reports on Progress in Physics*, **53**, 57-84; 1993, *Liquid Crystals*, **14**, 3-14.
- [12] Friedel, G., 1922, *Annales de Physique*, **18**, 273.
- [13] Sackmann, H., and Demus, D., 1966, *Molecular Crystals and Liquid Crystals*, **2**, 81.

- [14] Gray, G. W., and Goodby, J. W., 1984, *Smectic Liquid Crystals* (Leonard Hill, Glasgow and London, UK)
- [15] Boden, N., Bushby, R. J., and Clements, J., 1993, *Journal of Chemical Physics*, **98**, 5920-5931.

CHAPTER II

THE HYBRID GAY-BERNE LUCKHURST-ROMANO POTENTIAL AND THE MOLECULAR DYNAMICS METHOD

II.1 Introduction

This chapter describes the technique of molecular dynamics (MD) that we have used in carrying out simulations of calamitic and discotic liquid crystals. An MD simulation involves solving Newton's classical equations of motion for a system of particles interacting through a prescribed potential function. At a given time, with knowledge of the positions and orientations of the particles with respect to each other we may calculate the forces acting on the particles using the potential of interaction. Newton's second law allows direct computation of the acceleration on individual particles. Knowing therefore, the positions and accelerations of individual particles, we may use Newton's equations of motion to estimate the positions of the all particles (i.e. the new configuration of the system) at a small time interval in the future. Repeating this process allows us to calculate the time evolution of the system. This is the essence of molecular dynamics.

We have developed an original potential of interaction to model both calamitic and discotic liquid crystal systems. This potential is a hybrid model formed by scaling the Luckhurst-Romano [1] potential by the energy well depth expression of the Gay-Berne [2] potential. Accordingly it is called the "hybrid Gay-Berne Luckhurst-Romano potential". In this chapter we shall begin with a discussion of the basic form of the potential that has been used in MD simulations, illustrating

its origins in earlier work. Next a brief description of the standard techniques of MD that we have incorporated into our programs is provided. The molecular dynamics code was written as an original piece of source code, incorporating some available routines in common use [3], together with wholly original code for analysis; for example, calculating directionally resolved order parameters. Such routines that are in standard use are not explained in detail, and references to the original work are provided where appropriate. However the different methods which we have used in solving the equations of motion are detailed, as are the analytical calculation of order parameters and directionally resolved structural features. These are the relevant tools which when combined with MD allow us to gain insight into the phase behaviour of our liquid crystal models.

II.2 The Interaction Potential

The microscopic configuration of the classical system at any given time is completely described by specifying a set of generalised coordinates \mathbf{q} and generalised momenta \mathbf{p} conjugate to \mathbf{q} such that for a system of N particles:

$$\mathbf{q} = \{\mathbf{q}_1, \mathbf{q}_2, \mathbf{q}_3, \dots, \mathbf{q}_N\}; \quad [\text{II.1}]$$

$$\mathbf{p} = \{\mathbf{p}_1, \mathbf{p}_2, \mathbf{p}_3, \dots, \mathbf{p}_N\}. \quad [\text{II.2}]$$

If we assume that the Born-Oppenheimer approximation [4] is valid for the description of the constituent particles, then the Hamiltonian of the system may be written as the sum of kinetic energy and potential energy, components K and V respectively as so [3];

$$H(\mathbf{q}, \mathbf{p}) = K(\mathbf{p}) + V(\mathbf{q}). \quad [\text{II.3}]$$

Note that in equation [II.3] the kinetic energy appears only as a function of the momenta \mathbf{p} , and the potential energy appears only as a function of the particle positions \mathbf{q} . The sets \mathbf{p} and \mathbf{q} are sets of vectors, thus for a molecular system an element of \mathbf{q} , \mathbf{q}_i say, would consist of three coordinates describing the position vector of the centre of mass of the molecule, and three coordinates describing the orientation of a vector fixed in the molecule with respect to some axis system.

The total kinetic energy and total potential energy may be obtained from [II.4] and [II.5] respectively:

$$K = \sum_{i=1}^N \mathbf{p}_i^2 / 2m_i; \quad [\text{II.4}]$$

$$V = \sum_{i=1}^N v_1(\mathbf{q}_i) + \sum_{i=1}^N \sum_{j>i}^N v_2(\mathbf{q}_i, \mathbf{q}_j) + \sum_{i=1}^N \sum_{j>i}^N \sum_{k>j>i}^N v_3(\mathbf{q}_i, \mathbf{q}_j, \mathbf{q}_k) + \dots, \quad [\text{II.5}]$$

where m_i is the mass of particle i . The terms v_2, v_3, \dots in [II.5] above represent contributions to the potential energy from pairwise, three body, and higher interactions respectively. The term v_1 is a single particle interaction term which represents the effect of an external field on the system. The notation on the summation signs is arranged so that account is taken of distinct combinations of i , j and k only, avoiding zero contributions from particle self interactions. In the simulations which we have carried out and are reported herein there are no external effects (such as external fields, or container walls due to implementation of periodic boundary conditions), and so $v_1=0$. The second term is called the pair potential and dominates the remaining terms. It describes the interaction energy between a pair of particles each specified by the generalised configurational coordinates \mathbf{q}_i and \mathbf{q}_j . Higher order terms become less significant and can be

non-additive, [5] although the term v_3 is likely to have a reasonable contribution to V for densities typical of liquids. For example, estimates have shown that in the case of the lattice energy of argon an approximate 10% contribution comes from terms of higher order than v_2 [3]. It is thought that terms higher than v_3 are small compared to v_2 and v_3 .

As can be seen in equation [II.5] calculation of three body terms involves a triple sum over the particle indices i, j and k . Calculation of the potential energy of interaction and subsequent forces between particles is the most expensive part of an MD simulation. Thus despite the magnitude of the contribution from the v_3 term it is seldom included. Instead an effective pair potential is used such that equation [II.5] becomes;

$$V = \sum_{i=1}^N \sum_{j>i}^N v_2^{\text{eff}}(\mathbf{q}_i, \mathbf{q}_j) = \sum_{i=1}^N \sum_{j>i}^N V(\mathbf{q}_i, \mathbf{q}_j), \quad \text{[II.6]}$$

where v_2^{eff} is an effective pair potential that takes into account average non-additive higher body effects in [II.5]. This is the form the potential energy will take in all the simulations reported here. It should be noted though that some workers [e.g. 6] assert that the assumptions implicit in the effective pair potential may be an important source of error in computer simulations. The error may be more severe in the simulation of liquid crystals which can have many condensed phases. However we are restricted in our choice here not only because of the expense involved in their computation, but by the lack of quantitative experimental data on the effects of higher body interactions.

II.2.1 Hard Particle Potentials

Historically some of the first experiments looking at the behaviour of the individual particles of a liquid were performed using identical coins placed on a table and pushed together or aggregates of marbles or ball bearings which were shaken up and down in some container of sorts [see for example 7]. Such experiments provided remarkably good models of the structure of dense liquids at low temperatures. Similarly when liquid behaviour was first investigated in 2- [8] and 3-dimensions [9] using an electronic computer, hard discs and hard spheres were chosen to represent the constituent particles of the liquid. The hard sphere potential has the following discontinuous properties;

$$V_{\text{HS}} = \begin{cases} \infty & (r < \sigma) \\ 0 & (\sigma \leq r) \end{cases} \quad [\text{II.7}]$$

The form of equation [II.7] is shown in figure II.1, clearly two hard spheres approaching each other experience no interaction until a critical distance $r=\sigma$ is reached. For separations less than σ the pair potential energy between the two hard spheres becomes infinite. This is the unphysical case when the two hard spheres are actually overlapping and clearly should not be allowed. For this reason the dynamics of hard spheres (at liquid or gas densities) is characterised by relatively long periods of free flight interspersed with elastic collisions when any pair of particles becomes separated by the hard sphere radius distance of closest approach $r=\sigma$. The hard sphere potential, although quite unrealistic is of great importance as a reference system whose behaviour is well known, from which perturbation theories may be developed.

More complicated anisometric hard particle potentials such as platelets, ellipsoids, spherocylinders and cut spheres have been used in the simulation of liquid crystals and these will be discussed in chapter III. Not all shapes of hard particle can be easily used in a computer simulation. The problem of hard particle interactions reduces to one of being able to determine whether, at any given time, two particles are in contact. This involves evaluation of a so called contact function. The contact function expression has been elucidated for only a few geometric shapes, where it takes a relatively simple form.

II.2.2 Soft Particle Potentials

The second class of so called soft interaction pair potentials does not contain discontinuities that characterise the hard particle potentials. Rather, these decay asymptotically to zero as the interparticle separation is increased. The soft sphere potential has the form;

$$V_{ss}(r) = \varepsilon(\sigma / r)^{\nu}. \quad [\text{II.8}]$$

The parameter ν governs the rate of decay of the soft sphere potential. Two examples of [II.8] with repulsion parameters $\nu=6$ and $\nu=12$ are shown in figure II.2. The repulsion parameter ν can take any real positive value. However for these rather idealised soft sphere potentials ν is often chosen to be a positive integer [3]. Figure II.2 clearly shows that the larger the (positive) value of ν , the more severe the repulsive interaction up to the limit of the hard sphere case where $\nu = \infty$.

None of the pair potentials considered so far have any attractive component. In an attempt to explain why real gases did not obey the ideal gas law, van der

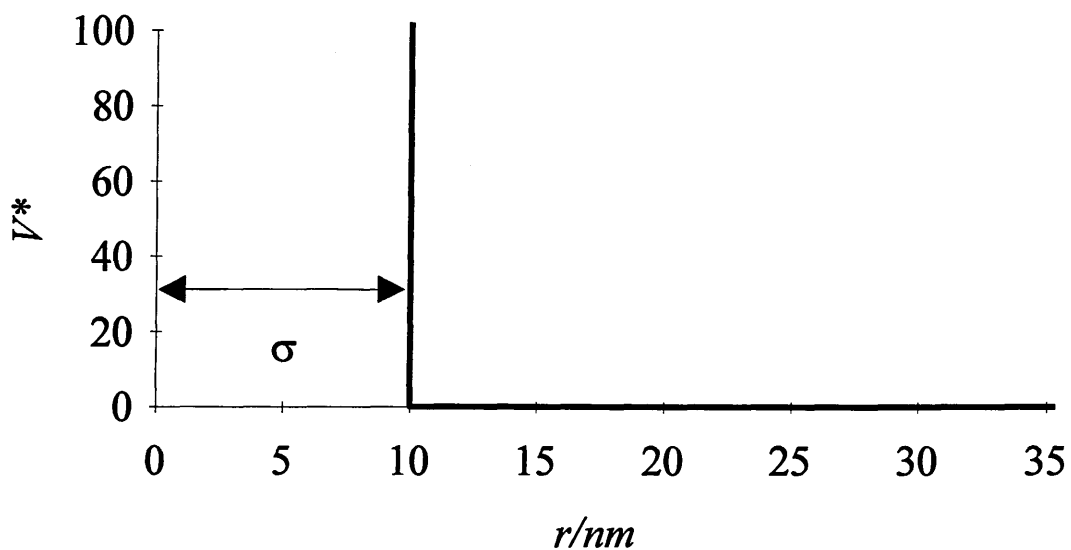


Figure II.1

The hard sphere potential $V^* = V_{HS}$ of equation [II.7]. σ is the hard sphere radius.

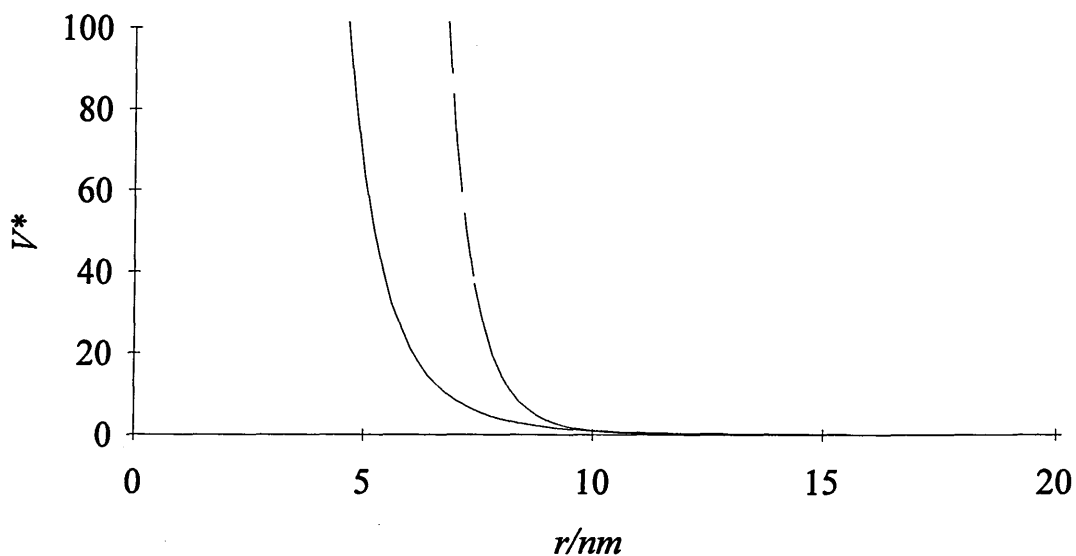


Figure II.2

The soft sphere potential $V^* = V_{SS}$, equation [II.8]. Solid line corresponds to repulsion parameter $\nu = 6$, dashed line corresponds to repulsion parameter $\nu = 12$, $\sigma = 10nm$

Waals first considered the idea of attractive intermolecular forces [10] by adding an attractive term to the pressure of the equation of state of an ideal gas. In 1903 Mie proposed a phenomenological pair potential with an attractive component of the form;

$$V_{\text{Mie}} = -A/r^n + B/r^m, \quad [\text{II.9}]$$

where n and m are attractive and repulsive parameters respectively.

In reality, in the case of neutral atoms at large separation the dominant attractive term in the interatomic potential comes from dipole-induced dipole interactions which vary as r^{-6} [11]. Higher order induced multipole interactions exist, but they are small in comparison to the leading dipole-induced dipole interactions. These dispersive interactions are always attractive [12], since a change in the electronic charge distributions of one atom, simply causes an appropriate change in the induced multipole of another atom. For molecular systems, there may well be additional contributions from permanent-permanent, permanent-induced, etc., electric multipole interactions

At short separations the atoms experience a repulsive interaction. As they approach closely their electronic charge distributions begin to overlap causing a strong repulsion between the similarly charged atomic nuclei, because of a reduction in the electrostatic screening effects normally present at larger distances. Further their electron clouds begin to distort in order to satisfy the requirements of the Pauli exclusion principle, this distortion manifests itself as a strong repulsion between the two atoms. Calculation of the form of the repulsive interaction is difficult. For example, it is not pairwise additive as the dispersion

forces (approximately) are. The influence of a third atom in the vicinity of a close pair modifies the interaction between the pair [13]. Fortunately, because it is so rapidly varying, it is not necessary to specify the precise form of the short range repulsion. Thus this short range component of the interatomic potential is often described as r^{-n} , with n in the range $9 \leq n \leq 15$ [11]. Choosing $n = 12$ [14] and appropriate values of the constants A and B ($A = 4\epsilon\sigma^{12}$ and $B = 4\epsilon\sigma^6$), and keeping $m = 6$ leads to a particular form of the Mie potential;

$$V_{\text{LJ}}(r) = 4\epsilon \left[\left(\frac{\sigma}{r} \right)^{12} - \left(\frac{\sigma}{r} \right)^6 \right]. \quad [\text{II.10}]$$

Equation [II.10] is the Lennard-Jones 12-6 potential, which has been used extensively in "realistic" computer simulations of monatomic fluids such as liquid argon [see for example 3]. Figure II.3 illustrates the form of [II.10] which clearly, qualitatively, has the form we require for describing the pair potential energy between two isolated atoms.

Adopting a convention that an attractive force is indicated by a negative sign the force acting between two atoms moving in the potential [II.10] may be obtained by the gradient of the potential with respect to pair separation;

$$F(r) = -\nabla_r V(r), \quad [\text{II.11}]$$

and is illustrated in figure II.4. The force curve of figure II.4, has qualitatively the same form as the potential energy curve illustrated in figure II.3.

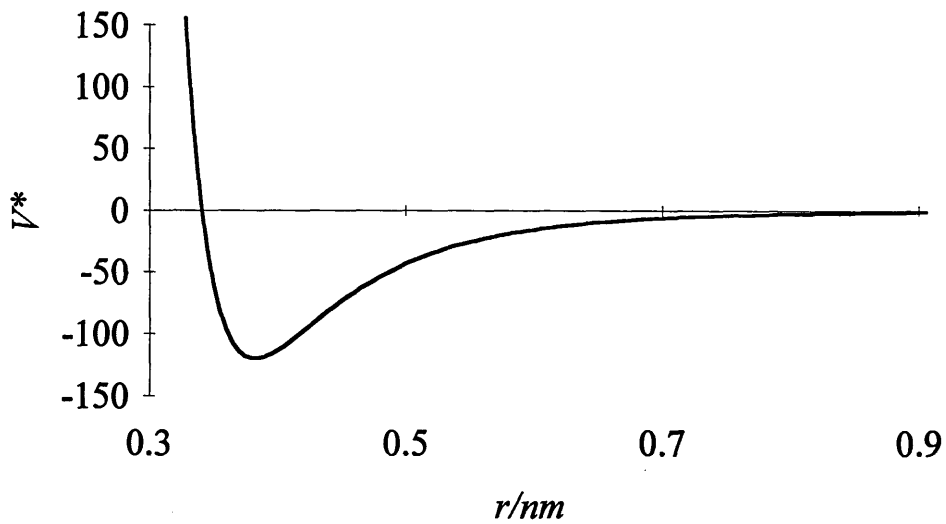


Figure II.3

The Lennard-Jones 12-6 potential, equation [II.10], parameterised as for argon with $\sigma = 0.341\text{nm}$ and $\epsilon = 119.8k_B\text{K}$ [3]. The potential is expressed in terms of reduced units. The k_B is the Boltzmann constant.

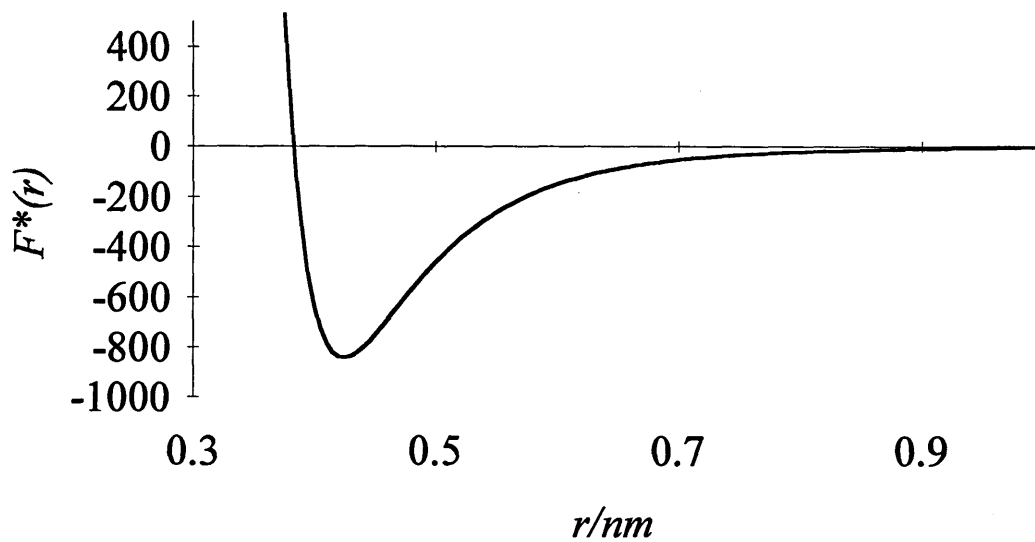


Figure II.4

The behaviour of the force between two atoms interacting via the Lennard-Jones 12-6 potential parameterised for argon (see figure II.3).

II.2.3 Anisotropic Soft Pair Potentials and the Origin of the HGBLR Potential

The potentials just described possess spherical symmetry, and are therefore not suitable for the simulation of liquid crystals. In order to arrive at a model suitable for describing (microscopically or phenomenologically) liquid crystals we necessarily must include an anisotropic component in the intermolecular pair potential. Based upon calculations of the second virial coefficient of cylindrical molecules, Corner [15] proposed a general form of potential for such molecules as;

$$V_{\text{Corner}} = \varepsilon(\Omega) f\left(\frac{r}{\sigma(\Omega)}\right). \quad [\text{II.12}]$$

The potential [II.12] depends on the relative orientations of the two molecules which is introduced through the parameter Ω . For fixed Ω however [II.12] remains spherically symmetric. As with the Lennard-Jones potential when written in the form of [II.10], ε is a function that scales the energy well depth and f is a function depending on molecular separation r , but now both ε and f depend additionally on the relative orientation of the particles.

Several potentials having the analytical form of [II.12] have been used in computer simulations of liquid crystals. By envisaging molecules represented as the rigid union of a set of ellipsoids, Berne and Pechukas [16] developed a soft non-spherical potential based on the Gaussian overlap model. The overlap integral of two Gaussian ellipsoids may be represented as;

$$I_{\text{BP}}(\hat{\mathbf{u}}_1, \hat{\mathbf{u}}_2, \mathbf{r}) = \varepsilon_0 \varepsilon_1(\hat{\mathbf{u}}_1, \hat{\mathbf{u}}_2) \exp\left[-r^2 / \sigma^2(\hat{\mathbf{u}}_1, \hat{\mathbf{u}}_2, \hat{\mathbf{r}})\right]. \quad [\text{II.13}]$$

The unit vectors $\hat{\mathbf{u}}_i$ represent the orientation of the principle symmetry axis of each ellipsoid of revolution, and \mathbf{r} is vector joining their centres. By analogy with equation [II.12] we see that $\varepsilon_1(\hat{\mathbf{u}}_1, \hat{\mathbf{u}}_2)$ and $\sigma(\hat{\mathbf{u}}_1, \hat{\mathbf{u}}_2, \hat{\mathbf{r}})$ represent strength and range parameters respectively with f taking an exponential form. The unit vectors $\hat{\mathbf{u}}_i$ represent the orientation of the principle symmetry axis of each ellipsoid of revolution. For constant orientation of $\hat{\mathbf{u}}_i$ [II.13] generates a series of ellipsoidal equipotentials in \mathbf{r} . Berne and Pechukas obtained expressions for the strength and range parameters:

$$\varepsilon_0 \varepsilon_1(\hat{\mathbf{u}}_1, \hat{\mathbf{u}}_2) = \varepsilon_0 \left[1 - \chi^2 (\hat{\mathbf{u}}_1 \cdot \hat{\mathbf{u}}_2)^2 \right]^{-\frac{1}{2}}; \quad [\text{II.14}]$$

$$\sigma(\hat{\mathbf{u}}_1, \hat{\mathbf{u}}_2, \hat{\mathbf{r}}) = \sigma_0 \left(1 - \frac{1}{2} \chi \left\{ \frac{(\hat{\mathbf{r}} \cdot \hat{\mathbf{u}}_1 + \hat{\mathbf{r}} \cdot \hat{\mathbf{u}}_2)^2}{1 + \chi(\hat{\mathbf{u}}_1 \cdot \hat{\mathbf{u}}_2)} + \frac{(\hat{\mathbf{r}} \cdot \hat{\mathbf{u}}_1 - \hat{\mathbf{r}} \cdot \hat{\mathbf{u}}_2)^2}{1 - \chi(\hat{\mathbf{u}}_1 \cdot \hat{\mathbf{u}}_2)} \right\} \right)^{-\frac{1}{2}}. \quad [\text{II.15}]$$

The terms ε_0 and σ_0 are strength and range constants and χ represents the anisotropy of the ellipsoids;

$$\chi = (\sigma_{\parallel}^2 - \sigma_{\perp}^2) / (\sigma_{\parallel}^2 + \sigma_{\perp}^2), \quad [\text{II.16}]$$

where σ_{\parallel} and σ_{\perp} are the major and minor axes of the ellipsoidal Gaussians. Equations [II.14] and [II.15] give an expression for the extent of overlap between two ellipsoidal Gaussians with respect to their relative orientations. In fact, as Berne and Pechukas state [16], the overlap model gives an expression for the orientational dependence of molecular interactions, but it does not accurately reproduce the distance dependence. In order to achieve this, the authors suggest that the strength and range parameters of the Gaussian overlap model are used as the strength and range parameters of a simple atomic potential. For example

incorporation into the Lennard-Jones 12-6 potential, leading to the overlap potential of Berne and Pechukas;

$$V_{\text{BP}}(\hat{\mathbf{u}}_1, \hat{\mathbf{u}}_2, \mathbf{r}) = 4\varepsilon_1(\hat{\mathbf{u}}_1, \hat{\mathbf{u}}_2) \left\{ \left(\frac{\sigma(\hat{\mathbf{u}}_1, \hat{\mathbf{u}}_2, \hat{\mathbf{r}})}{r} \right)^{12} - \left(\frac{\sigma(\hat{\mathbf{u}}_1, \hat{\mathbf{u}}_2, \hat{\mathbf{r}})}{r} \right)^6 \right\}. \quad [\text{II.17}]$$

Equation [II.17] represents the interaction between two molecules represented as ellipsoids of revolution [16]. One graphical way of illustrating the behaviour of [II.17], is to plot the distance dependence of the potential energy for a few select orientations. Common configurations include parallel end-end and side-side, X and T [17]. The distance dependence of the Berne-Pechukas potential for these four basic configurations is shown in figure [II.5].

Equation [II.17] has certain characteristics that make it particularly amenable to computer simulation studies [18]. It is a relatively simple function dependent on only three parameters, allowing for relative ease of calculation of the potential energy. Further the function is readily differentiable facilitating analytical computation of the forces and torques of a system of Berne-Pechukas particles. Variation of the parameter χ (equation II.16) allows a range of molecular eccentricities, from very long prolate to flat oblate to be studied.

The Berne-Pechukas potential (equation [II.17]) was first used in computer simulations investigating the stability of the nematic phase and co-operative re-orientation effects. For more details see chapter III.

As can be seen in figure [II.5], the well depths of parallel configurations of Berne-Pechukas particles have equal magnitude. For prolate systems we would expect the side-side configurations of molecules to be favoured over end-end configurations. This is suggested by considering the potential energy curves exhibited by a linear array of Lennard-Jones centres [2] having an axial ratio of 3:1.

Subsequently, modifications of the Berne-Pechukas potential have been suggested [2, 18, 19] There are two principle changes. The first involves scaling the existing strength parameter with an additional function dependent on the intermolecular separation vector \mathbf{r} ;

$$\varepsilon(\hat{\mathbf{u}}_1, \hat{\mathbf{u}}_2, \hat{\mathbf{r}}) = \varepsilon_0 \varepsilon_1^\nu(\hat{\mathbf{u}}_1, \hat{\mathbf{u}}_2) \varepsilon_2^\mu(\hat{\mathbf{u}}_1, \hat{\mathbf{u}}_2, \hat{\mathbf{r}}). \quad [\text{II.18}]$$

The scaling function $\varepsilon_2(\hat{\mathbf{u}}_1, \hat{\mathbf{u}}_2, \hat{\mathbf{r}})$ has the form of $\sigma(\hat{\mathbf{u}}_1, \hat{\mathbf{u}}_2, \hat{\mathbf{r}}) / \sigma_0$; the exponents ν and μ are treated as adjustable parameters that influence the relative well depths of different configurations (see for example Luckhurst and Simmonds, ref. [21]).

Secondly (as can be seen in figure [II.5]), the Berne-Pechukas potential has the unrealistic feature that the well width is larger for end-end configurations, with respect to side-side configurations. This property is not exhibited by a four site linear Lennard-Jones array [2]. Gay and Berne suggested a shifted form of the range parameter for use within the Lennard-Jones function, yielding the Gay-Berne potential;

$$V_{\text{GB}}(\hat{\mathbf{u}}_1, \hat{\mathbf{u}}_2, \mathbf{r}) =$$

$$4\varepsilon_0\varepsilon_1^{\nu}(\hat{\mathbf{u}}_1, \hat{\mathbf{u}}_2)\varepsilon_2^{\mu}(\hat{\mathbf{u}}_1, \hat{\mathbf{u}}_2, \hat{\mathbf{r}})\left\{\left(\frac{\sigma_0}{r - \sigma(\hat{\mathbf{u}}_1, \hat{\mathbf{u}}_2, \hat{\mathbf{r}}) + \sigma_0}\right)^{12} - \left(\frac{\sigma_0}{r - \sigma(\hat{\mathbf{u}}_1, \hat{\mathbf{u}}_2, \hat{\mathbf{r}}) + \sigma_0}\right)^6\right\}. \quad [\text{II.19}]$$

This is illustrated in figure II.6. As can be seen in figure II.6, sliding the Gay-Berne potential minimum position, rather than a simple scaling with intermolecular distance, removes the dilatory effect on the well depth width. Thus the well depth widths for both end-end and side-side configurations of Gay-Berne particles are now equal.

The Gay-Berne particles have been shown to provide a rich degree of polymorphism. They have been used successfully in simulations of calamitic and discotic liquid crystals by a number of workers, notably Luckhurst and co-workers [21], and Rull and co-workers [22]. These simulations are discussed more fully in chapter III.

The Luckhurst-Romano potential is the sum of a simple anisotropic and a scalar pair potential, having the following form;

$$V_{\text{LR}} = V_0 + V_A, \quad [\text{II.20}]$$

where V_0 is the Lennard-Jones 12-6 potential and;

$$V_A = -4\varepsilon\lambda\left\{\left(\frac{\sigma}{r}\right)^{12} + \left(\frac{\sigma}{r}\right)^6\right\}P_2(\cos(\beta_{ij})), \quad [\text{II.21}]$$

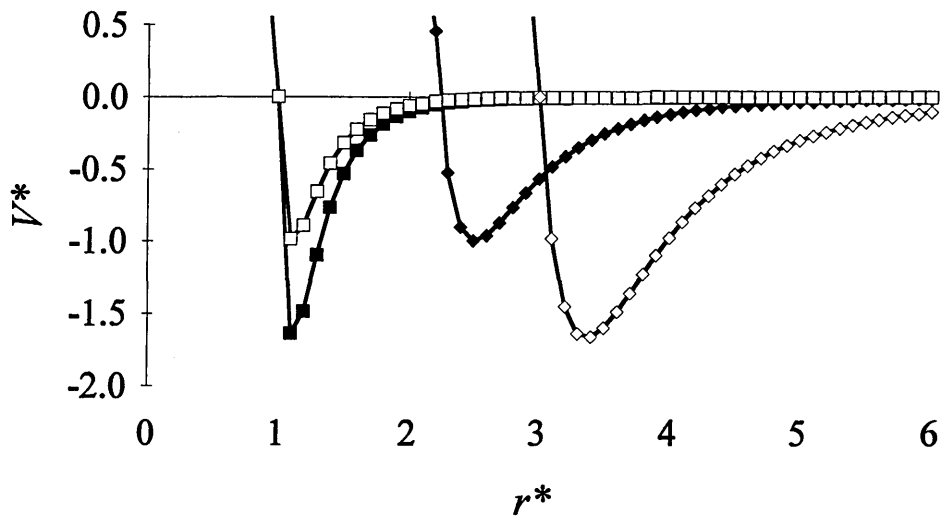


Figure II.5

Distance dependence of the Berne-Pechukas potential, equation II.17 parameterised with $\sigma_0 = 1$, $\varepsilon_0 = 1$ and $\sigma_{\parallel} / \sigma_{\perp} = 3$. The different symbols correspond to the configurations: closed squares, side-side; open squares, X-configuration; closed diamonds, T-configuration; open diamonds, end-end.

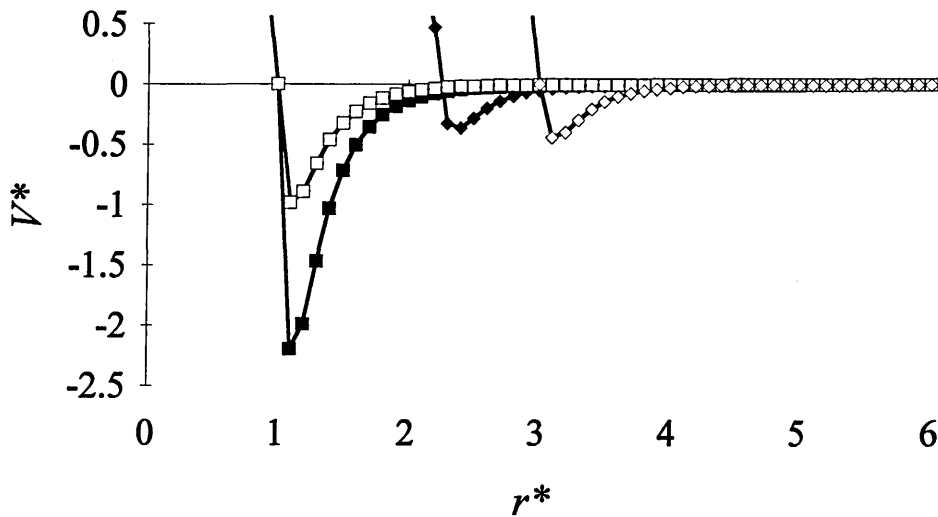


Figure II.6

Distance dependence of the Gay-Berne potential, equation II.19 parameterised with $\sigma_0 = 1$, $\varepsilon_0 = 1$, $\sigma_s / \sigma_e = 3$ and $\varepsilon_s / \varepsilon_e = 5$ with $\nu = 1$ and $\mu = 2$. For a key to the configurations see figure II.5.

where β_{ij} is the angle between the principle symmetry axes of two rod-like particles, and P_2 is the second Legendre polynomial. The anisotropic term is simple and has the same form as that used in the Maier-Saupe mean field theory of nematics [23, 24]. In an earlier form, this potential was used in a simulation of rod-like particles confined to the sites of a lattice [25], More recently the V_A has been used in simulations where the particles were not restricted to a lattice [26]. Although lattice models cannot hope, truly to closely represent a fluid phase, because of the obvious restriction of no translational motion, it is sometimes convenient to turn one's attention to a small part of an altogether wider problem. In the case of lattice models, detailed studies of the effects of particle reorientation could be made. The Luckhurst-Romano potential was successfully used in an off lattice simulation of simple cylindrically symmetric particles [26] and more recently in an Monte Carlo simulation of a siloxane cyclic polymer system [27]. Again these are discussed more fully in chapter III.

For the simulations reported herein, we have used a modified form of the Luckhurst-Romano potential, formed by scaling it with part of the anisotropic well depth expression of Gay and Berne. The result is a fairly simple anisotropic pair potential, the hybrid Gay-Berne Luckhurst-Romano potential (HGBLR) which has the following form;

$$V_{\text{HGBLR}}(\hat{\mathbf{u}}_1, \hat{\mathbf{u}}_2, \mathbf{r}) = \epsilon_2(\hat{\mathbf{u}}_1, \hat{\mathbf{u}}_2, \hat{\mathbf{r}}) \{V_0(r) + V_A(\hat{\mathbf{u}}_1, \hat{\mathbf{u}}_2, r)\}. \quad [\text{II.22}]$$

Where:

$$V_0(r) = 4\epsilon \left\{ \left(\frac{\sigma}{r} \right)^{12} - \left(\frac{\sigma}{r} \right)^6 \right\}; \quad [\text{II.23}]$$

$$V_A(\hat{\mathbf{u}}_1, \hat{\mathbf{u}}_2, r) = -4\varepsilon\lambda \left\{ \left(\frac{\sigma}{r} \right)^{12} + \left(\frac{\sigma}{r} \right)^6 \right\} P_2(\hat{\mathbf{u}}_1 \cdot \hat{\mathbf{u}}_2); \quad [\text{II.24}]$$

$$\varepsilon_2(\hat{\mathbf{u}}_1, \hat{\mathbf{u}}_2, \hat{\mathbf{r}}) = 1 - \frac{\chi'}{2} \left\{ \frac{(\hat{\mathbf{r}} \cdot \hat{\mathbf{u}}_1 + \hat{\mathbf{r}} \cdot \hat{\mathbf{u}}_2)^2}{1 + \chi'(\hat{\mathbf{u}}_1 \cdot \hat{\mathbf{u}}_2)} + \frac{(\hat{\mathbf{r}} \cdot \hat{\mathbf{u}}_1 - \hat{\mathbf{r}} \cdot \hat{\mathbf{u}}_2)^2}{1 - \chi'(\hat{\mathbf{u}}_1 \cdot \hat{\mathbf{u}}_2)} \right\}; \quad [\text{II.25}]$$

and;

$$\chi' = \{1 - \varepsilon_e / \varepsilon_s\} / \{1 + \varepsilon_e / \varepsilon_s\}. \quad [\text{II.26}]$$

The HGBLR potential has a number of characteristics which may make it extremely useful in the task of simulating mesogens.

The inclusion of the part well depth scaling function of the Gay-Berne potential introduces a dependence on the intermolecular vector. Thus the HGBLR potential, in contrast to the Luckhurst-Romano potential correctly distinguishes between the parallel configurations, for example end-end and side-side.

The HGBLR potential has the advantage over the Gay-Berne potential of computational simplicity and therefore speed. In a comparative test with the Gay-Berne potential, the HGBLR potential was found to be an order of magnitude faster on a scalar processor [28]. This provides some motivation for developing the HGBLR potential as later several HGBLR sites would be joined together to provide more realistic models of mesogens.

The HGBLR potential with a disc-like and rod-like parameterisation is presented in two-dimensions in figures IV.2 and IV.3 respectively. Inspection of these

figures reveals that the potential has a spherical hard core surrounded by an anisotropic attractive region. This is unrealistic for liquid-crystal forming molecules, which must necessarily deviate from spherical symmetry. Therefore in the simulation of single HGBLR centres, any observed liquid crystal phases would be due solely to the attractive anisotropic component in the potential, as we know that hard spheres do not form a liquid crystal phase. Later simulations, involving multiple HGBLR centres will provide a non-spherical hard core through the geometrical disposition of their centres.

The anisotropy parameter χ' which represents the relative ratio of the side-side to end-end interactions can take a range of values, including negative values, enabling the anisotropic attractive part of individual HGBLR centres to be representative of disc-like or rod-like mesogens equally well.

The HGBLR potential has formed the basis of the MD simulations reported in chapters IV and V. As preliminary work, systems of individual HGBLR centres have been simulated, with calamitic and discotic parameterisations. This work is presented in chapter IV. Subsequently HGBLR sites have been rigidly joined to form multisite models of calamitic mesogens; the results of MD simulations of these models are presented in chapter V.

The remainder of this chapter will be concerned with carrying out the MD simulations and extracting useful information from them.

II.3 Computational Techniques in Molecular Dynamics

With a knowledge of the forces and torques acting on a system of particles, we may apply the rules of classical mechanics to compute the classical trajectories of the individual particles. In this way we may calculate the time evolution of such a system of particles: these are the basic principles of molecular dynamics.

In what follows we shall talk generally about molecules. In the case of atoms there may be no need to consider their orientations due to symmetry effects, and the situation is simplified.

We shall consider a system of particles which interact through a continuous potential. The special techniques which apply to MD of particles which interact through a discontinuous potential will be mentioned briefly at the end of this section.

We do not consider the continuous classical trajectories of the particles in an MD simulation. Instead we have a complete description of the particle positions and momenta in a series of chronologically ordered system configurations. Typically the time interval δt is chosen so that a particle will not travel further than half its own diameter in this time interval [3]. Further restrictions may be imposed on the choice of δt through the method chosen to solve the equations of motion of the particles [29].

This is not the case in a Monte Carlo [30, 31] (MC) simulation, where configurations are generated randomly; the probability of a configuration occurring depends only on the previous configuration, and not on the past history of the system. MD has a distinct advantage over MC in this respect as we may

use the former to study the dynamical or time evolution of a system of interest. This is important in the study of liquid crystals. If the molecules can be shown to possess self-particle diffusion and yet also possess a degree of orientational order then these provide strong evidence for the existence of a liquid crystal mesophase, as opposed to a plastic crystal, genuine crystal or an ordered glass phase. The choice of molecular dynamics over MC techniques allows us to collect data on particle self-diffusion.

II.3.1 Periodic Boundary Conditions and the Minimum Image

Convention

In our MD simulations we wish to examine a liquid crystal in bulk. A standard method of removing surface effects is the use of periodic boundary conditions (PBCs). The central simulation box and contents are effectively completely surrounded by an infinite number of replicas in all coordinate directions. This has the effect of producing an infinite number of particles from the given finite number contained in the central simulation box. When considering particle pairs, A and B say, with the minimum image convention we only consider a finite number (typically only one) of the replicas of particle B when computing the interactions between A and the Bs. These replicas of B are those that have the shortest interparticle separations between A and replicas of B. Because the interparticle potential is relatively short ranged with respect to the large distances out to the majority of the replicas of B, there are only significant contributions to the potential energy of the system from short range interactions: the closest replicas of B

Of course it is not possible to store an infinite number of particle coordinates. In practice therefore, when using the minimum image convention on just one

particle replica B, PBCs are implemented using the following technique. Whenever a particle travels through one of the simulation box "walls" it reappears entering the simulation box through the opposite "wall".

There are several problems which are introduced with the implementation of PBCs. For molecular systems a particle leaving a face of the central simulation box, to reappear at the opposite face will generally have a different orientation with respect to a given molecule. The change in orientation causes a jump discontinuity in the potential energy of the system. In the microcanonical ensemble, used exclusively in these studies, this can lead to energy conservation problems such as energy pumping. The effect is however, generally absorbed by the allowed fluctuations in the total energy of the system.

If external effects are to be included in the simulation they must have the same periodicity as the simulation box [3]. An example of an external effect might be the imposition of an electric or magnetic ordering field on a liquid crystal. In all of the studies reported here, we do not consider external effects.

Interparticle correlations may only be calculated up to a maximum of half the box length when PBCs are applied. This is necessary to avoid spurious contributions to distribution functions from particles interacting with themselves or with multiple replicas of particle B.

More recently a different approach towards boundary conditions has been attempted. Radial boundary conditions have been used in the simulation of nematic droplets [32]. However the technique has not been fully extended to deal with bulk liquid crystals.

II.3.2 Finite Size Effects

In the microcanonical ensemble the density of a simulation dictates the length of the side of the simulation box for a given number of particles N . For example for a cubic simulation box the length of a side of the cube L , is given by;

$$L = (\sigma / N)^{1/3}. \quad [\text{II.27}]$$

It is crucial that L is longer than the distance at which the interparticle potential is significant. For the intermolecular potentials considered in this work, which decay as r^{-6} this is not a problem for the number of particles 108, 256 and 500 that we have considered. However in the simulation of other systems, for example of electrostatic charge-charge interactions and dipole-dipole interactions which decay as r^{-1} and r^{-3} respectively, special techniques (see [3] and references therein) are required for small numbers of particles as the potential may still be significant over the range of the box.

Ideally we would wish to simulate a macroscopic number of particles. Unfortunately this is infeasible, and so in practice PBCs are employed together with the minimum image convention on typically 10^2 to 10^4 particles. It is important to ask whether the simulation of a relatively small number of particles in PBCs is a good representation of the macroscopic system it is supposed to correspond to? For example the use of PBCs with cubic simulation cell of length L implies that the maximum correlation distance that may be investigated is $L/2$. Such a simulation will be insensitive to fluctuations with wavelength longer than L . This may have severe consequences, especially near phase transitions where long ranged fluctuations often characterise a transition: some observed transitions tend to exhibit properties typical of higher order transitions [3]. Thus the nematic

to isotropic transition which is described as weakly first order (i.e. a first order phase transition with a small latent heat [33]) may in fact be observed as an essentially continuous transition [34].

II.3.3 Simulation Box Geometry

If periodic boundary conditions are to be applied, the geometry of the simulation box must be space filling, so that the box can be effectively repeated in all directions. Several space filling simulation boxes have been used in the past, a regular cube, cuboids, the rhombic dodecahedron and the truncated octahedron [3]. The cubic simulation box is most frequently chosen, no doubt because of its geometrical simplicity. In all the simulations reported herein we have used the cubic simulation box. PBCs are easy to code in the cubic simulation box.

The cuboid simulation box geometry has been used extensively by Frenkel and co-workers (see for example [35]). It is useful in simulations of ordered liquid crystals such as parallel spherocylinders. Parallel spherocylinders may be packed into a cuboid with relative ease if their principle molecular symmetry axes are aligned with the irregular side of the cuboid.

However the geometry of the simulation box may impose a degree of order or preferred orientation with observed liquid crystal or solid phases. For example when the formation of smectic phases has been observed in simulation boxes of cubic symmetry, the director of the system is found to align parallel to the box diagonal [17]. It is thought that this is the orientation that the system must take in order to fit in an integer number of smectic layers commensurate with the images created by the periodic boundary conditions. For this reason it may be preferable to use a simulation box geometry possessing a higher degree of symmetry when

simulating liquid crystals, such as the rhombic dodecahedron. Or, perhaps, performing MD at constant pressure [36] which enables changes in the box size and shape. To our knowledge a comprehensive comparison of simulation box geometries on the influence of the orientation of a liquid crystal phase with respect to the simulation box edges has not been performed.

II.3.4 Potential Truncation

The most time consuming part of an MD simulation is in the calculation of the pairwise potential and its derivatives. Since the largest contribution to the potential energy of a system comes from particles closest to the one of immediate concern, interactions from particles further than a prescribed cutoff distance may be considered negligible. Thus it is common practice to disregard interactions between particles separated by more than the cutoff distance. This procedure necessarily introduces a discontinuity into the potential function at the cutoff distance which can lead to stability problems [3]. Thus often an additional small linear term is added to the potential so that it goes smoothly to zero at the cutoff; the so called cut and shifted potential.

Long range corrections can be applied to cut and shifted potentials, by assuming that the particles outside the cutoff are approximately uniformly distributed as in an ideal gas: such that the radial distribution function $g(r) \approx 1$. The minimum length of the cutoff must be such that the approximation $g(r) \approx 1$ is valid, and an upper limit is imposed if PBCs and the minimum image convention are in use as the cutoff cannot be greater than some fraction of L : $\frac{1}{2}L$ for a cubic simulation box.

Obviously the implementation of a cutoff excludes information contributed to the system from the long ranged part of the potential. This information can be recovered however. For the systems here studied it would be sufficient to show that $g(r) \approx 1$ at $\frac{1}{2}L$ to apply long range corrections to recover thermodynamic information contributed from the long range part of the potential. However, as no critical comparison with real substances was made with the results of these simulations it was not necessary to apply long range corrections.

II.3.5 Initial Conditions

Our MD simulations are started from a face centred cubic lattice [3]. The molecular symmetry vectors are either all aligned along a given direction, or the directions of alignment are distributed such that the system $\langle P_2 \rangle = 0$. This is not a necessity and other lattices or random distributions may be used. The problem here is that at typical liquid densities assigning random coordinates within the confines of the box will inevitably lead to significant particle overlaps. If not identified this will cause computational difficulties, or in the case of hard particles, physical impossibilities where one hard particle is positioned so as to penetrate another. The simulations carried out in this work all have their origins on an α -fcc lattice. This has either been constructed at the density of interest, or at some other density from which the system has been either expanded or compressed to the density of interest through a simple scaling of the centre of mass coordinates followed by a period of equilibration.

The particles are assigned random translational velocities, acting on their centres of mass, chosen from a Gaussian distribution centred at the appropriate reduced temperature. Similarly the angular velocities of molecules about their centres of mass are chosen based on the appropriate temperature. The net linear momentum

of the complete system remains constant throughout the simulation (it is impossible to detect whether the simulation box is at rest or in uniform translational motion). Thus it is common practice to set this quantity to zero. Because of the box geometry, the net angular momentum of the whole system is not conserved however. Of course for linear molecules it is important that the components of angular velocity are chosen perpendicular to the principle molecular symmetry axis.

For molecules it is further necessary to specify their initial orientation. Sometimes an ordered configuration is chosen, in other instances the system may be initiated from a disordered state. Either way in every case reported herein the system is started at a high enough temperature and appropriate density that the initial lattice melts rapidly, and the orientations of the molecules become randomly distributed, resulting in an isotropic liquid phase. This is checked by monitoring a translational order parameter, which measures the persistence of the lattice, and the orientational pair correlation function $\langle G_2 \rangle$, and nematic order parameter $\langle P_2 \rangle$ (see section II.6.2).

II.3.6 Integrating the Equations of Motion

In this section we shall restrict our discussion to particles that move with continuous trajectories.

Generally after computing the potential energy and hence the total force on the centre of mass, and total torque about the centre of mass of each particle, it is a relatively simple matter to compute the motion of each particle. Chasles' theorem states that, "Any general displacement of a rigid body can be represented by a translation plus a rotation" [37]. If we choose the origin of the body as the centre

of mass, then the motion of the body may be described as a single translation of the centre of mass, and a single rotation about the centre of mass. It is appropriate for us to identify with this natural separation and thus the evaluations of these two quantities are handled separately. Indeed, with multisite models, forces and torques acting on individual sites are accumulated for each molecule to yield the overall force on the centre of mass and torque about the centre of mass of the whole molecule; directly applying Chasles' theorem.

For continuous potentials the particle trajectories are in principle exactly solvable within the limitations of the finite arithmetic used. However this is not actually the case for atomic or molecular liquids. With the exception of harmonic and weakly anharmonic systems, two initially close classical trajectories will eventually diverge exponentially from one another [38]. The equations of motion of our systems of particles contain a Lyapunov instability [39]. This manifests itself in a deviation of the particle trajectory from the classically exact trajectory after a finite length of time. However this should not necessarily be considered a problem. The primary requirement of an MD algorithm is stability [40]. Algorithms which allow the use of a large time step provide a more efficient sampling of phase space for a given amount of processing time. With the microcanonical ensemble it is far more important that the particle trajectories in phase space stay on the relevant constant energy hypersurface otherwise the microcanonical ensemble will not be sampled correctly, leading to erroneous ensemble averages [3]. This aspect is of greater importance than the accuracy with which the algorithm reproduces the correct classical trajectory. More surprisingly the existence of the Lyapunov instability promotes an efficient sampling of phase space reducing the chances of simulating a non-ergodic system (see section II.6).

II.3.6.1 Translational Equations of Motion

Firstly we shall start with the equation of motion of a particle itself. Consider the centre of mass acceleration of a particle. In Cartesian coordinates, using Newton's second law, the force on the centre of mass of a particle may be written;

$$m\ddot{\mathbf{r}} = \mathbf{f}. \quad [\text{II.28}]$$

If the particle moves in a potential which is independent of velocity and time then the Hamiltonian of a system of such particles is equal to the total energy [3]. Equation [II.28] may then be recast as two first order differential equations:

$$\dot{\mathbf{r}} = \mathbf{p} / m; \quad [\text{II.29}]$$

$$\dot{\mathbf{p}} = -\nabla_{\mathbf{r}}\mathcal{V} = \mathbf{f}. \quad [\text{II.30}]$$

In order to solve equation [II.28] or equations [II.29] and [II.30], we make use of finite difference methods frequently used in the solution of ordinary differential equations. Two distinct schemes are in common use, the n-order predictor-corrector schemes of the type of Gear [41] and the many forms of the Verlet algorithm [42]. We have used the half step leap-frog version of the Verlet algorithm [3 and references therein], which is briefly detailed below.

In this scheme an estimate for the particle velocities at the next half time step is made with [II.31] below, which is used to solve [II.32], advancing the particles a full time step. The particle velocities, in order to calculate the kinetic energy, are obtained from [II.33]:

$$\mathbf{v}(t + \frac{1}{2}\delta t) = \mathbf{v}(t - \frac{1}{2}\delta t) + \delta t \mathbf{a}; \quad [\text{II.31}]$$

$$\mathbf{r}(t + \delta t) = \mathbf{r}(t) + \delta t \mathbf{v}(t + \frac{1}{2}\delta t); \quad [\text{II.32}]$$

$$\mathbf{v}(t) = \frac{1}{2}(\mathbf{v}(t + \frac{1}{2}\delta t) + \mathbf{v}(t - \frac{1}{2}\delta t)). \quad [\text{II.33}]$$

In the above equations, \mathbf{a} , \mathbf{v} , and \mathbf{r} are acceleration, velocity and position vectors respectively and δt is the length of one time step.

II.3.6.2 Rotational Equations of Motion

Although a general technique for solving the rotational motion of an arbitrary shaped molecule would suffice for all MD simulations, there are some simplifications that may be adopted when dealing with cylindrically symmetric molecules. Consequently we have used two techniques in our simulations reported herein.

II.3.6.2.1 Rotational Equations of Motion for Cylindrically Symmetric Molecules

Because of symmetry considerations, rotation of a cylindrically symmetric molecule about the principle symmetry axis is undetectable. Consequently we may use a constraint method based on the leap-frog Verlet algorithm [42] to solve the rotational equations of motion [17, 43-45]. The method we have used is outlined below.

The torque on a molecule perpendicular to the symmetry axis $\hat{\mathbf{u}}$ may be written;

$$\boldsymbol{\tau} = \hat{\mathbf{u}} \times \mathbf{g} = \hat{\mathbf{u}} \times \mathbf{g}^{\perp}, \quad [\text{II.34}]$$

where if necessary \mathbf{g}^{\perp} , the perpendicular force component may be obtained from;

$$\mathbf{g}^\perp = \mathbf{g} - (\mathbf{g} \cdot \hat{\mathbf{u}})\hat{\mathbf{u}}. \quad [\text{II.35}]$$

The rotational equation of motion of the molecular symmetry axis may be written in terms of the second time derivative of a unit vector $\hat{\mathbf{u}}$ as so;

$$\ddot{\hat{\mathbf{u}}} = \frac{\mathbf{g}^\perp}{I} + \lambda \mathbf{u}. \quad [\text{II.36}]$$

Equation [II.36] may be thought of as an expression for the acceleration of the vector $\hat{\mathbf{u}}$. I stands for the moment of inertia of the molecule and λ is a Lagrange multiplier which constrains the symmetry vector to remain a unit vector; hence no hat on \mathbf{u} in the second term of [II.36]. Actually there is no reason for the symmetry vector to be a unit vector, this is chosen merely for convenience. However whatever length is chosen for the symmetry vector, this length must remain constant. To solve [II.36] we need an expression for λ at time t . Consider a first order estimate for a half time step advance of the vector $\hat{\mathbf{u}}$ [46];

$$\hat{\mathbf{u}}(t) = \hat{\mathbf{u}}(t - \frac{1}{2}\delta t) + \frac{1}{2}\delta t \left[\frac{\mathbf{g}^\perp(t)}{I} + \lambda(t)\mathbf{u}(t) \right]. \quad [\text{II.37}]$$

An expression for λ is obtained by taking the scalar product of each side with $\hat{\mathbf{u}}$ and using the facts that $\mathbf{g}^\perp \cdot \hat{\mathbf{u}} = 0$, $\hat{\mathbf{u}} \cdot \hat{\mathbf{u}} = 1$ and $\hat{\mathbf{u}} \cdot \dot{\hat{\mathbf{u}}} = 0$ (this last condition is due to the constraint any change in $\hat{\mathbf{u}}$ must be perpendicular to \mathbf{g} , thus $\hat{\mathbf{u}}$ and $\dot{\hat{\mathbf{u}}}$ are orthogonal), giving;

$$\lambda(t) = \frac{-2\dot{\hat{\mathbf{u}}}(t - \frac{1}{2}\delta t) \cdot \mathbf{u}(t)}{\delta t}. \quad [\text{II.38}]$$

Note that the hat has been removed from $\hat{\mathbf{u}}(t)$ again in both [II.37] and [II.38]; it is lambda that constrains \mathbf{u} to be a unit vector. Substitution of λ into [II.36] leads to an expression for $\ddot{\mathbf{u}}$;

$$\delta t \ddot{\mathbf{u}}(t) = \frac{\delta t \mathbf{g}^\perp(t)}{I} - 2 \left[\dot{\mathbf{u}}(t - \frac{1}{2} \delta t) \cdot \hat{\mathbf{u}}(t) \right] \hat{\mathbf{u}}. \quad [\text{II.39}]$$

Two half step Taylor series expansions may then be combined to obtain an expression advancing $\hat{\mathbf{u}}$ a full time step:

$$\dot{\mathbf{u}}(t + \frac{1}{2} \delta t) = \dot{\mathbf{u}}(t) + \frac{1}{2} \delta t \ddot{\mathbf{u}}(t) + \frac{1}{6} \delta t^2 \dddot{\mathbf{u}}(t) + \dots; \quad [\text{II.40}]$$

$$\dot{\mathbf{u}}(t - \frac{1}{2} \delta t) = \dot{\mathbf{u}}(t) - \frac{1}{2} \delta t \ddot{\mathbf{u}}(t) + \frac{1}{6} \delta t^2 \dddot{\mathbf{u}}(t) - \dots, \quad [\text{II.41}]$$

which are combined, truncating after the third order derivative to give;

$$\dot{\mathbf{u}}(t + \frac{1}{2} \delta t) = \dot{\mathbf{u}}(t - \frac{1}{2} \delta t) + \delta t \ddot{\mathbf{u}}(t), \quad [\text{II.42}]$$

from which the new direction of $\hat{\mathbf{u}}$ may be calculated using [II.43];

$$\hat{\mathbf{u}}(t + \delta t) = \hat{\mathbf{u}}(t) + \delta t \dot{\mathbf{u}}(t + \frac{1}{2} \delta t). \quad [\text{II.43}]$$

Finally the angular velocity necessary to compute the rotational kinetic energy may be calculated from;

$$\boldsymbol{\omega}(t) = \frac{1}{2 \delta t} \left(\hat{\mathbf{u}}(t - \frac{1}{2} \delta t) + \hat{\mathbf{u}}(t + \frac{1}{2} \delta t) \right). \quad [\text{II.44}]$$

II.3.6.2.2 Rotational Equations of Motion for Arbitrarily Shaped Molecules

In later simulations where the molecules do not possess cylindrical symmetry, we have used the method of quaternions [47]. A quaternion is a set of four parameters [II.45] (three of which are independent), satisfying the constraint [II.46]:

$$\mathbf{q} = \{q_0, q_1, q_2, q_3\}; \quad [\text{II.45}]$$

$$q_0^2 + q_1^2 + q_2^2 + q_3^2 = 1. \quad [\text{II.46}]$$

The orientation of a vector fixed in the molecule $\hat{\mathbf{u}}^b$ is related to its corresponding space fixed coordinates $\hat{\mathbf{u}}^s$ through rotation matrix \mathbf{R} :

$$\hat{\mathbf{u}}^b = \mathbf{R}(\mathbf{q})\hat{\mathbf{u}}^s; \quad [\text{II.47}]$$

$$\mathbf{R} = \begin{pmatrix} q_0^2 + q_1^2 - q_2^2 - q_3^2 & 2(q_1q_2 + q_0q_3) & 2(q_1q_3 - q_0q_2) \\ 2(q_1q_2 - q_0q_3) & q_0^2 - q_1^2 + q_2^2 - q_3^2 & 2(q_2q_3 + q_0q_1) \\ 2(q_1q_3 + q_0q_2) & 2(q_2q_3 - q_0q_1) & q_0^2 - q_1^2 - q_2^2 + q_3^2 \end{pmatrix}. \quad [\text{II.48}]$$

After Fincham [40] the method of quaternions that we have used is briefly described below. Quaternion parameters are assigned to each molecule based on the Euler angle convention of Goldstein [37], thus [3];

$$\begin{aligned} q_0 &= \cos\frac{1}{2}\theta \cos\frac{1}{2}(\phi + \psi); \\ q_1 &= \sin\frac{1}{2}\theta \cos\frac{1}{2}(\phi - \psi); \\ q_2 &= \sin\frac{1}{2}\theta \sin\frac{1}{2}(\phi - \psi); \\ q_3 &= \cos\frac{1}{2}\theta \sin\frac{1}{2}(\phi + \psi). \end{aligned} \quad [\text{II.49}]$$

The quaternion parameters satisfy the following equations of motion [3];

$$\begin{pmatrix} \dot{q}_0 \\ \dot{q}_1 \\ \dot{q}_2 \\ \dot{q}_3 \end{pmatrix} = \frac{1}{2} \begin{pmatrix} q_0 & -q_1 & -q_2 & -q_3 \\ q_1 & q_0 & -q_3 & q_2 \\ q_2 & q_3 & q_0 & -q_1 \\ q_3 & -q_2 & q_1 & q_0 \end{pmatrix} \begin{pmatrix} 0 \\ \omega_x^b \\ \omega_y^b \\ \omega_z^b \end{pmatrix}. \quad [\text{II.50}]$$

In matrix notation the form of [II.50], with the time at which these quantities are known stated explicitly, may be written;

$$\dot{\mathbf{Q}}(t) = \frac{1}{2} \mathbf{Q}(t) [0, \omega^b(t)]^T. \quad [\text{II.51}]$$

The motion of the vector $\hat{\mathbf{u}}$ is dictated by the torque on the molecule calculated in the force loop. An estimate for the on-step angular momentum is made through a first order expansion over half a time step;

$$\mathbf{j}^s(t) = \mathbf{j}^s(t - \frac{1}{2}\delta t) + \frac{1}{2}\delta t \tau^s(t). \quad [\text{II.52}]$$

Rotating this to the body-fixed system, by analogy with equation [II.47] allows calculation of the body-fixed angular velocity through equation [II.54];

$$\mathbf{j}^b(t) = \mathbf{R}(\mathbf{q}(t)) \mathbf{j}^s(t); \quad [\text{II.53}]$$

$$\omega^b(t) = \mathbf{I}^{-1} \mathbf{j}^b(t), \quad [\text{II.54}]$$

where \mathbf{I} is the body fixed diagonal moment of inertia tensor and is constant;

$$\mathbf{I} = \begin{bmatrix} I_{xx} & 0 & 0 \\ 0 & I_{yy} & 0 \\ 0 & 0 & I_{zz} \end{bmatrix}. \quad [\text{II.55}]$$

I_{xx}, I_{yy} and I_{zz} are the principle moments of inertia. Thus [II.54] simplifies to a set of three equations, each describing the angular velocity of the molecule in the three orthogonal coordinate directions;

$$\omega_{\alpha}^b(t) = I_{\alpha\alpha} j_{\alpha}^b(t); \quad \alpha = x, y, z. \quad [\text{II.56}]$$

We have arrived at values for the components of body-fixed angular velocity at the on-step, i.e. at time t and may evaluate the kinetic energy of rotation for each molecule thus;

$$K_{\text{rot}} = \frac{1}{2} (I_{xx} \omega_x^2 + I_{yy} \omega_y^2 + I_{zz} \omega_z^2). \quad [\text{II.57}]$$

To advance the equations of motion a first order estimate for $\mathbf{Q}(t + \frac{1}{2}\delta t)$ is made with [II.58];

$$\mathbf{Q}(t + \frac{1}{2}\delta t) = \mathbf{Q}(t) + \frac{1}{2}\delta t \dot{\mathbf{Q}}(t). \quad [\text{II.58}]$$

The rotation matrix $\mathbf{R}(\mathbf{q}(t + \delta t))$ may then be reassembled according to [II.48] using the updated values. Application of [II.47] regains the necessary space-fixed vectors as;

$$\hat{\mathbf{u}}^s = \mathbf{R}^T(\mathbf{q}(t + \delta t)) \hat{\mathbf{u}}^b. \quad [\text{II.59}]$$

In the computer algorithm of this scheme the quaternions are renormalised after their updated values are calculated, i.e. after [II.50]. In the face of the machine finite arithmetic this guarantees that the constraint [II.46] is preserved.

II.3.7 Hard Particle Dynamics

Particles interacting with discontinuous so called hard particle pair potentials move with straight line trajectories between impulsive collisions. The above algorithms cannot therefore be used for the solution of hard particle dynamics. Instead a new approach is adopted.

Consider a simulation in progress. The next colliding pair of particles and the time of collision are identified. This typically involves solving a quadratic equation in time [48]: the next collision can be identified by the use of the contact condition or contact function. The simulation is then "fast forwarded" to this point. At the collision the dynamics of the colliding pair are computed using the laws of conservation of (in general), translational kinetic, rotational kinetic and potential energy and conservation of (in general), linear and angular momentum. For some systems one or more of the components of energy or momentum may be absent. For example "smooth" hard spheres possess no potential energy, no rotational kinetic energy and no angular momentum, particles interacting via the square well potential may possess potential energy, but again do not possess rotational kinetic energy or angular momentum.

Just after a collision has occurred the system is in a new configuration and thermodynamic and dynamical observables of interest and correlation functions

of interest are collected for later averaging before repeating the cycle, looking firstly to locate the next collision.

For non-spherical systems evaluation of the contact function in order to locate the next collision can be very complex. Only simple anisometric hard particle potentials such as hard ellipsoids, cut spheres, rigid and flexible chains of hard spheres and spherocylinders have been simulated using molecular dynamics (see chapter III). One solution suggested for complicated contact functions is to use a step by step approach to solve the equations of motion as for continuous potentials [49]. The problem here though is that a collision may take place in between time steps putting a large restriction on the choice of δt . A method of handling collisions that occur between time steps has been devised [50] to handle this problem. For these reasons Monte Carlo simulation of anisometric hard particles is much easier. After an attempted move the contact function for the moved particle and its neighbours (within a known maximum displacement) may be relatively easily evaluated. If an overlap is found to exist, the configuration is simply rejected. There is no requirement to locate the next collision.

II.4 Simulation Averages

Now we shall turn our attention to the output of a simulation and to statistical mechanics required to convert this very detailed information into macroscopic "experimentally observable" properties. As the system evolves in time it follows a continuous trajectory in multidimensional phase space. We assume that the potential energy of the system contains no explicitly time dependant terms and is described completely by the configuration of the system. If $\Gamma(t)$ is a point on this trajectory, then the average of an observable A_{obs} sampled over a series discrete intervals, $\tau = 1 \rightarrow \tau_{\text{obs}}$, may be obtained from;

$$A_{\text{obs}} = \langle A(\Gamma(\tau)) \rangle = \frac{1}{\tau_{\text{obs}}} \sum_{\tau=1}^{\tau_{\text{obs}}} A(\Gamma(\tau)). \quad [\text{II.61}]$$

In an MD simulation where successive configurations are time ordered, the angle brackets $\langle \dots \rangle$ refer to a time average in addition to an average over all the particles of the system. Thus if we ensure that τ_{obs} is sufficiently large we should be able to arrive at a reasonable approximation for A_{obs} .

In a truly ergodic system the phase space trajectory visits all the accessible points in phase space before returning to an already visited point. Generally a proof of ergodicity does not exist [38]. Fortunately the Lyapunov instability introduces a degree of chaos into our simulations which can only help prevent the system becoming trapped in a non-ergodic region of phase space.

The observable A_{obs} can take many forms. In the next two sections we shall look at the thermodynamic and dynamic observables which we compute in the simulations, together with the order parameters and distribution functions which are invaluable in identifying and distinguishing liquid crystalline phases.

II.4.1 Thermodynamic and Dynamic Averages

In this section we shall describe some of the thermodynamic averages that we can obtain from our simulations in the microcanonical ensemble. The total energy of the system is simply the Hamiltonian H which we may now write as the sum of the averaged kinetic and potential terms;

$$E = \langle H \rangle = \langle K \rangle + \langle V \rangle. \quad [\text{II.62}]$$

The notation $\langle \dots \rangle$ represents an ensemble average, i.e. an average over all particles and all configurations. The potential energy for a given configuration is directly obtained from the pair potential. The total kinetic energy is the sum of the translational and rotational kinetic energies. In terms of the particle momenta for a system of N particles we may write;

$$\langle K \rangle = \frac{1}{2} \left\langle \sum_{i=1}^N |\mathbf{p}_i|^2 / m_i \right\rangle = \frac{3}{2} N k_B \langle T \rangle. \quad [\text{II.63}]$$

Equation [II.63] is a statement of the equipartition principle. In simulations of molecular systems, the kinetic energy of translation and rotation are evaluated separately in order to check they are apportioned correctly according to the theory: $\frac{1}{2} k_B T$ per degree of freedom. Equation [II.63] clearly allows us to calculate the average thermodynamic temperature also;

$$\langle T \rangle = 2 \langle K \rangle / 3 N k_B = \frac{1}{3 N k_B} \sum_{i=1}^N |\mathbf{p}_i|^2 / m_i. \quad [\text{II.64}]$$

Molecular dynamics allows the calculation of dynamical information about the system of interest. When studying liquid crystals it is important to be able to characterise the phase as still being fluid. The degree of fluidity of a phase may be established by calculating the particle self diffusion coefficient. This is related to the mean square displacement of particles from their starting positions at some given time via the Einstein relation valid at long time [51]. Taken as an average over the whole system this may be written;

$$\langle |\mathbf{r}(t) - \mathbf{r}(0)|^2 \rangle = 6Dt + C. \quad [\text{II.65}]$$

The diffusion coefficient can be obtained from the gradient of a plot of [II.65] at long times. Of course in the evaluation of [II.65] it is a prerequisite that the effects of the periodic boundary conditions have been removed. For this reason the true particle trajectories are stored from a simulation. However, assuming the particles do not travel more than half the box length in an interval between stored time steps $M\delta t$, (M is a positive integer), it is possible to recover the proper particle trajectories from those that have been subject to PBCs [3]. Further the particle mean square displacement is resolved into its components parallel and perpendicular to the instantaneous nematic director $\hat{\mathbf{n}}(t)$:

$$\begin{aligned} \langle |\mathbf{r}_{\parallel}(t) - \mathbf{r}_{\parallel}(0)|^2 \rangle &= \langle |(\mathbf{r}(t) - \mathbf{r}(0)) \cdot \hat{\mathbf{n}}(t)|^2 \rangle; \\ \langle |\mathbf{r}_{\perp}(t) - \mathbf{r}_{\perp}(0)|^2 \rangle &= \langle |(\mathbf{r}(t) - \mathbf{r}(0)) \times \hat{\mathbf{n}}(t)|^2 \rangle. \end{aligned} \quad [\text{II.66}]$$

These two components enable us to acquire valuable information about anisotropic diffusion present in the system. Anisotropic diffusion is a property of

all liquid crystal systems and information about the components of particle self diffusion as described above can assist greatly in identifying a phase.

II.4.2 Distribution Functions and Order Parameters

Distribution functions are vital in identifying the type of phase present in a simulation. For liquid crystals there are several spatial and orientational distribution functions which when considered collectively may uniquely characterise a phase.

One of the most fundamental distribution functions is the pair distribution function $g_2(\mathbf{r}_i, \mathbf{r}_j)$. For isotropic homogeneous systems this function depends only on the interparticle separation $\mathbf{r}_{ij} = |\mathbf{r}_j - \mathbf{r}_i|$, and is referred to as the radial distribution function, denoted $g(r)$ [11]. A definition convenient for use in computer simulations is given by Allen and Tildesley [3];

$$g(r) = \frac{Vol}{N^2} \left\langle \sum_{i=1}^N \sum_{j>i}^N \delta(\mathbf{r} - \mathbf{r}_{ij}) \right\rangle, \quad [\text{II.67}]$$

where Vol is the volume of the system.

The radial distribution function represents the probability of finding a particle a given distance away from a specified particle with respect to that same probability in an ideal gas. Thus, in a hypothetical pure solid at absolute zero for example, a plot of $g(r)$ would consist of a series of infinitely tall vertical lines (representing the δ functions of [II.67]), corresponding to the location of the lattice sites, in all directions with respect to a given site. In reality, however these delta functions would be broadened due to thermal excitation, into sharply

peaked Gaussians about a mean corresponding to the lattice site location [33]. The peaks in a liquid are even more diffuse and overlap because of the continuous relatively large scale motion of the particles with respect to one another. However structure should still be present in $g(r)$ at short range representing the shells of nearest neighbours surrounding each particle. At long range this order diminishes and the radial distribution function converges to the ideal gas value of 1. This will not of course occur for the solid since the periodicity of the lattice sites will manifest itself as a continuously oscillating $g(r)$ even at long range.

The distribution function $g(r)$ is related to experimental structure characterisation techniques such as X-ray diffraction and neutron scattering. [12]. Like the mean square particle displacement, the $g(r)$ can yield valuable anisotropic information about a phase when resolved into components parallel and perpendicular to the instantaneous system director $\hat{\mathbf{n}}(t)$:

$$g_{\parallel}(\eta) = \frac{(Vol)^{\frac{2}{3}}}{N^2} \left\langle \sum_{i=1}^N \sum_{j>i}^N \delta(\mathbf{r}(t) \cdot \hat{\mathbf{n}}(t) - \mathbf{r}_{ij}(t) \cdot \hat{\mathbf{n}}(t)) \right\rangle;$$

$$g_{\perp}(r_{\perp}) = \frac{(Vol)^{\frac{2}{3}}}{N^2} \left\langle \sum_{i=1}^N \sum_{j>i}^N \delta(\mathbf{r}(t) \times \hat{\mathbf{n}}(t) - \mathbf{r}_{ij}(t) \times \hat{\mathbf{n}}(t)) \right\rangle. \quad [\text{II.68}]$$

The components of $g(r)$ are important in distinguishing between an orientationally ordered phase such as the nematic phase, and a higher additionally translationally ordered phase, for example a smectic-A phase is characterised by the existence a one dimensional density wave parallel to the director. The function $g_{\parallel}(\eta)$ is particularly sensitive to this density wave. Additionally any evidence of structure in $g_{\perp}(r_{\perp})$ may indicate the onset of two-dimensional

translational order, such as in a columnar liquid crystal, or it may indicate that the system has indeed formed a genuine crystal.

A quantitative measure of angular correlations is provided by the second rank orientational correlation coefficient $G_2(r)$ [33, 52];

$$G_2(r) = \left\langle P_2(\mathbf{u}_i \cdot \mathbf{u}_j(r)) \right\rangle, \quad [\text{II.69}]$$

where P_2 is the second Legendre polynomial. $G_2(r)$ shows very short ranged order in the isotropic phase of a molecular fluid, quickly decaying to zero after a few molecular separations. In an orientationally ordered phase though, $G_2(r)$ decays to a limiting value equal to the square of the second rank orientational order parameter $\langle P_2 \rangle^2$ (see below) [33, 52].

The calculation of an order parameter is essential in quantitatively classifying and identifying phases and phase transitions in many materials [53]. The order parameter may take many different forms. For example the magnetisation in a ferromagnetic material or the electric polarisation in a Ferroelectric [53]. The lowest category of liquid crystal, in terms of degree of symmetry breaking from the isotropic phase is the uniaxial nematic. In the nematic phase molecules tend to align themselves with a preferred direction; the nematic director $\hat{\mathbf{n}}$ and the phase has point symmetry group $D_{\infty h}$. Thus in our simulations it is convenient to identify with a single molecule potential matrix property \mathbf{A} , say, defined as [52];

$$\mathbf{A} = \hat{\mathbf{u}}_z \otimes \hat{\mathbf{u}}_z, \quad [\text{II.70}]$$

where $\hat{\mathbf{u}}_z$ is a unit vector parallel to the molecular symmetry axis, i.e. $\hat{\mathbf{u}}_z^b = (0,0,1)$, and thus;

$$\mathbf{A}^b = \begin{bmatrix} 0 & 0 & 0 \\ 0 & 0 & 0 \\ 0 & 0 & 1 \end{bmatrix}. \quad [\text{II.71}]$$

In space-fixed coordinates the average components of \mathbf{A} are given by;

$$\langle A_{\alpha\beta}^s \rangle = \frac{1}{N} \sum_{i=1}^N \left\{ \sum_{\alpha'} \sum_{\beta'} (R_i)_{\alpha\alpha'} (A_i^b)_{\alpha'\beta'} (R_i^T)_{\beta\beta'} \right\}, \quad [\text{II.72}]$$

where α, β and α', β' range over the space-fixed (non primed) and body fixed (primed) Cartesian indices x, y and z , and the R_i are the components of the rotation matrix that rotates \mathbf{A}^b into the space-fixed frame. The right hand side of [II.72] is non-zero only when $\alpha' = \beta' = z$, thus [II.72] reduces to;

$$\langle A_{\alpha\beta}^s \rangle = \langle R_{\alpha z} R_{\beta z} \rangle = Q_{\alpha\beta} + \frac{1}{3} \delta_{\alpha\beta}. \quad [\text{II.73}]$$

Equation [II.73] defines the components of the ordering matrix, the so called \mathbf{Q} tensor [33], δ is the Kronecker δ . The rotation matrix that diagonalises \mathbf{Q} leads to a symmetric and traceless tensor that defines the director frame. \mathbf{Q} has three real eigenvalues denoted λ_+ , λ_0 and λ_- . Normally the largest eigenvalue, λ_+ is taken to be the value of $\langle P_2 \rangle$. The corresponding eigenvector yields the direction of the system director $\hat{\mathbf{n}}$ in the laboratory fixed frame. The remaining eigenvalues are small and of opposite sign and correspond to the degree of

biaxiality present in the phase. This particular method only allows $1 \geq \langle P_2 \rangle > 0$, because the largest positive value, λ_+ is always chosen as the eigenvalue to represent the magnitude of the order parameter. The order parameter $\langle P_2 \rangle$ can take values $0 > \langle P_2 \rangle \geq -0.5$ however, which correspond to the principle symmetry axes of the particles tending to lie orthogonal to the system director on average. Thus some workers have chosen to call $\langle P_2 \rangle$ the eigenvalue most different from the other two. There are some problems associated with this method applied to disordered phases. When the eigenvalues are small and approximately equal, a consistent choice of the eigenvalue corresponding to $\langle P_2 \rangle$ is difficult to make [54]. However, with small values of $\langle P_2 \rangle$, indicating that a system is not orientationally ordered, the director of the phase has no meaning, and it is therefore not appropriate to identify the corresponding eigenvalue.

In later simulations involving multisite HGBLR models we have found it useful to monitor the orientational ordering of three mutually perpendicular axes fixed in the molecule. This facilitates the identification of a phase where the principle molecular symmetry axes are found to be lying in a plane orthogonal to the director thereby eliminating the problem of consistently choosing a positive eigenvalue in assigning the director. More details are to be found in chapter V.

II.5 References

- [1] Luckhurst, G. R., and Romano, S., 1980, *Proceedings of the Royal Society London A*, **373**, 111-130.
- [2] Gay, J. G., and Berne, B. J., 1981, *Journal of Chemical Physics*, **74**, 3316- 3319.
- [3] Allen, M. P., and Tildesley, D .J., 1987, *Computer Simulation of Liquids* (Oxford, UK: Clarendon Press).
- [4] Atkins P. W., 1983, *Molecular Quantum Mechanics, 2nd edition* (Oxford University Press, Oxford, UK).

- [5] Monson, P. A., Rigby, M., and Steele, W. A., 1983, *Molecular Physics*, **49**, 893-898.
- [6] Wheatley, R. J., and Price, S. L., 1990, *Molecular Physics*, **71**, 1381-1404.
- [7] Waldram, J. R., 1985, *The Theory of Thermodynamics* (Cambridge University Press Cambridge, UK).
- [8] Metropolis, N., Rosenbluth, A. W., Rosenbluth, M. N., Teller, A. H., and Teller, E., 1953, *Journal of Chemical Physics*, **21**, 1087-1092.
- [9] Rosenbluth, M. N., and Rosenbluth, A. W., 1954, *Journal of Chemical Physics*, **22**, 881-884.
- [10] Israelachvili, J., 1991, *Intermolecular and Surfaces Forces, 2nd edition* (Academic Press, London, UK).
- [11] Hansen, J. P., and McDonald, I. R., 1986, *Theory of Simple Liquids, 2nd edition* (Academic Press, London, UK).
- [12] Trevena, H. D., 1975, *The Liquid Phase* (Wykeham Publications, London, UK).
- [13] Stone, A. J., 1979. *Intermolecular Forces in The Molecular Physics of Liquid Crystals*, edited by Luckhurst, G. R., and Gray, G. W., (Academic Press, London, UK).
- [14] Lennard-Jones, J. E., and Devonshire, A. F., 1937, *Proceedings of the Royal Society*, **A163**, 53-70.
- [15] Corner, J., 1948, *Proceedings of the Royal Society*, **A192**, 275-292.
- [16] Berne, B. J., and Pechukas, P., 1972, *Journal of Chemical Physics*, **56**, 4213-4216.
- [17] Luckhurst, G. R., Stephens, R. A., and Phippen, R. W., 1990, *Liquid Crystals*, **8**, 451-464.
- [18] Kushick, J., and Berne B. J., 1976, *Journal of Chemical Physics*, **64**, 1362-1367.
- [19] Walmsley, S. H., 1977, *Chemical Physics Letters*, **49**, 320-322.
- [20] Tsykalo, A. L., and Bagmet, A. D., 1978, *Molecular Crystals and Liquid Crystals*, **46**, 111-119.
- [21] Adams, D. J., Luckhurst, G. R., and Phippen, R. W., 1987, *Molecular Physics*, **61**, 1575-1580; Luckhurst, G. R., Stephens, R. A., and Phippen, R. W., 1990, *Liquid Crystals*, **8**, 451-464; Luckhurst, G. R., and Simmonds, P. S. J., 1993, *Molecular Physics*, **80**, 233-252; Emerson, A. P. J., Luckhurst, G. R., and Whatling, S. G., 1994, *Molecular Physics*, **82**, 113-124; Hashim, R., Luckhurst, G. R., and

- Romano, S., *Journal of the Chemical Society Faraday Transactions*, **91**, 2141-2148.
- [22] de Miguel, E., Rull, L. F., Chalam, M. K., and Gubbins, K. E., 1990, *Molecular Physics*, **71**, 1223-1231; de Miguel, E., Rull, L. F., and Gubbins, K. E., 1991, *Physica A*, **177**, 174-181; de Miguel, E., Rull, L. F., Chalam, M. K., Gubbins, K. E., and Van Swol, F., 1991, *Molecular Physics*, **72**, 593-605; de Miguel, E., Rull, L. F., Chalam, M. K., and Gubbins, K. E., 1991, *Molecular Physics*, **74**, 405-424; Chalam, M. K., Gubbins, K. E., de Miguel, E., and Rull, L. F., 1991, *Molecular Simulation*, **7**, 357-385; de Miguel, E., Rull, L. F., and Gubbins, K. E., 1992, *Physical Review*, **A45**, 3813-3822;
- [23] Maier, Von, W., and Saupe, A., 1958, *Zeitschrift für Naturforschung*, **13a**, 564-566; 1959, *Ibid.*, **14a**, 882-889; 1960, *Ibid.*, **15a**, 287-292.
- [24] Luckhurst, G. R., and Zannoni, C., 1977, *Nature*, **267**, 412-414.
- [25] Lasher, G., 1972 *Physical Review*, **A5**, 1350-1356.
- [26] Luckhurst, G. R., and Romano, S., 1980, *Proceedings of the Royal Society London A*, **373**, 111-130.
- [27] Everitt, D. R. R., Care, C. M., and Wood, R. M., 1987, *Molecular Crystals and Liquid Crystals*, **153**, 55-62.
- [28] De Luca, M. D., Neal, M. P., and Care, C. M., 1994, *Liquid Crystals*, **16**, 257-266; Neal, M. P., De Luca, M. D., and Care, C. M., 1995, *Molecular Simulation*, **14**, 245-258.
- [29] Hockney, R. W., and Eastwood, J. W., 1988, *Computer Simulations Using Particles* (Hilger, Bristol, UK).
- [30] Metropolis, N., and Ulam, S., 1949, *Journal of the American Statistical Association*, **44**, 335-341.
- [31] Binder, K., and Heerman, D. W., 1988, *Monte Carlo Simulation in Statistical Physics: An Introduction, Part 1* (Springer-Verlag, Berlin, Germany).
- [32] Chiccoli, C., Pasini, P., Semeria, F., and Zannoni, C., 1990, *Physics Letters A*, **150**, 311-314; Chiccoli, C., Pasini, P., Semeria, F., and Zannoni, C., 1992, *Molecular Crystals and Liquid Crystals*, **212**, 197-204.
- [33] Zannoni, C., 1979, *Distribution Functions and Order Parameters in The Molecular Physics of Liquid Crystals*, edited by Luckhurst, G. R., and Gray, G. W., (Academic Press, London, UK).

- [34] Luckhurst, G. R., and Simpson, P., 1982, *Molecular Physics*, **47**, 251-265.
- [35] Stroobants, A., Lekkerkerker, H. N. W., and Frenkel, D., 1986, *Physical Review Letters*, **57**, 1452-1455.
- [36] Anderson, H. C., 1980, *Journal of Chemical Physics*, **72**, 2384-2393.
- [37] Goldstein, H., 1980, *Classical Mechanics, 2nd edition* (Addison-Wesley, Reading, MA, USA).
- [38] Ladd, J. A. C., 1990, *Molecular Dynamics in Computer Modelling of Fluids Polymers and Solids*, edited by Catlow C. R. A., Parker, S. C., and Allen, M. P., (Kluwer Academic Publishers, Dordrecht, The Netherlands).
- [39] Hoover, W. G., 1986, *Molecular Dynamics, Lecture notes in physics*, (Springer Verlag, New York, USA).
- [40] Fincham, D., 1993, *Molecular Simulation*, **10**, 165-178.
- [41] Gear, C. W., 1971, *Numerical Initial Value Problems in Ordinary Differential Equations* (Prentice-Hall, Englewood Cliffs, NJ, USA).
- [42] Verlet, L., 1967, *Physical Review*, **159**, 98-103.
- [43] Singer, K., Taylor, A., and Singer, J. V. L., 1977, *Molecular Physics*, **33**, 1757-1795.
- [44] Fincham, D., 1983, *Computation of Condensed Phases* **5**, **10**, 43-45.
- [45] Fincham, D., 1993, *Molecular Simulation* **11**, 79-89.
- [46] Fincham, D., 1984, *Computation of Condensed Phases* **5**, **12**, 47-48.
- [47] Evans, D. J., 1977, *Molecular Physics* **34**, 317-325.
- [48] Alder, B. J., and Wainwright, T. E., 1959, *Journal of Chemical Physics*, **31**, 459-466.
- [49] Rebertous, D. W., and Sando, K. M., 1977, *Journal of Chemical Physics*, **67**, 2585-2590.
- [50] Stratt, R. M., Holmgren, S. L., and Chandler, D., 1981, *Molecular Physics*, **42**, 1233-1243.
- [51] Tildesley, D. J., 1984, in *Molecular Liquids, Dynamics and Interactions*, edited by Barnes, A. J., Orville-Thomas, W. J., and Yarwood, J., (NATO ASI Reidel, New York, USA).
- [52] Zannoni, C., 1991 *An Introduction to the Molecular Dynamics Method and to Orientational Dynamics in Liquid Crystals in Molecular Dynamics of Liquid Crystals*, edited by Luckhurst, G. R., (NATO ASI, Reidel, New York, USA).

- [53] Yeomans, J. M., 1992, *Statistical Mechanics of Phase Transitions* (Clarendon Press, Oxford, UK).
- [54] Hashim, R., Luckhurst, G. R., Prata, F., and Romano, S., 1993, *Liquid Crystals*, **15**, 283-309.

CHAPTER III

COMPUTER SIMULATION OF LIQUID CRYSTALS

III.1 Introduction

The first statistical mechanical computer simulations of model liquids were performed in the early 1950s on the MANIAC computer at Los Alamos, New Mexico, USA. This was the pioneering work of Metropolis *et al* [1] which established a version of the standard Monte Carlo method for solving many dimensional integrals [2]. The time saving technique used importance sampling and allowed for a simulation of 2-dimensional hard spheres [1], with Rosenbluth and Rosenbluth [3] continuing the work to look at hard spheres in three dimensions. Later in that decade, the molecular dynamics technique of Alder and Wainwright [4] was used to simulate hard spheres. Evaluation, discussion and comparison of the two simulation methodologies began immediately [see for example 5; 6]. Many rudimentary techniques introduced in this period are still in use today and some of these have been described in chapter II.

Both Metropolis Monte Carlo (MC) and molecular dynamics (MD) provided physicists and chemists with powerful tools with which to probe the liquid state at the microscopic level. These were a great asset because unlike the harmonic theory of solids, and the ideal gas law, there is no effective reference starting point in a general theory of fluids. Hard and soft sphere fluids were studied extensively [6]; nevertheless, at least fifteen years elapsed before the first attempts by Veillard-Baron [7] at simulating non-spherical hard convex bodies.

In this chapter we shall discuss some of the important simulations that have been performed to date employing the anisotropic potentials necessary to describe liquid crystalline phases. Early simulators were plagued initially by (a), mathematical problems, e.g. trying to find an effective way to compute the contact function of two hard bodies, and (b), by practical problems, e.g. low speed and small memory of early computers. Progress in both these areas has been made over the last four decades and in this chapter we shall detail some of the simulations of liquid crystals performed to date. These simulations can be roughly divided into four main categories:

- hard particle models;
- continuous potential models;
- lattice models;
- realistic atom-atom potential models.

For our purposes here we shall divide the following sections broadly according to the classification above. The order above does not represent any prejudice on the importance of these models. Most simulations, however have been performed on hard particle models, so we shall begin with these. A review of single site soft particle models follows. Although there are no other published works relating to the hybrid Gay-Berne Luckhurst-Romano (HGBLR) potential with the exception of those subsequently reported herein [8], this section is particularly important as it most closely relates to the HGBLR potential. We mention lattice models only briefly. As the computational power of modern computers rapidly increases, simulations of realistic models of liquid crystals are perhaps just becoming attainable. We present a review of the realistic simulations performed to date.

As will be seen, each of the above have their particular uses, either in providing insight into real liquid crystal mechanisms, or providing a test of theoretical approaches. Before we begin examining the results of computer simulations we shall begin with a brief discussion of two contrasting theories ascribing the formation of orientationally ordered phases to (a), geometric effects and (b), long range anisotropic dispersion forces respectively. Comparison of theories, with computer experiments and with experiments on real liquid crystals have enabled us to gain valuable insight into the formation of liquid crystal phases.

III.2 Anisotropic Repulsive Forces vs Anisotropic Attractive

Dispersion Forces.

At the time of the first simulations of liquid crystals the nature of the isotropic-nematic phase transition had, on the one hand, been hypothesised to be strongly dependant on geometric effects as first described by Onsager [9]. In attempting to describe the formation of lyotropic liquid crystal phases in suspensions of anisometric particles, Onsager had developed a theory which attributed the formation of the nematic phase of a system of long hard rods to excluded volume effects alone. Onsager calculated the first two virial coefficients for a system of long rods which he considered to be made up of many groups of rods, each group with a specific orientation. By minimising the available free energy of the system, Onsager arrived at a distribution function describing the orientations of the molecular long axes. He further showed that if the system was compressed to a sufficiently high density a transition to an orientationally ordered phase occurs. Isihara [10], applied the Onsager theory to rigid molecules of different shapes, including ellipsoidal and cylindrical molecules. Zwanzig [11] extended Onsager's rod work to include higher order terms in the virial expansion of the equation of state of a system of rectangular parallelepipeds length l , and square

base of side d . In the limit that $l \rightarrow \infty$, and $d \rightarrow 0$, and with the constraint $l^2 d = \text{constant}$, Zwanzig computed, exactly, the first seven virial coefficients for a small number of specific orientations of the parallelepipeds (Onsager theory was originally based on a continuous distribution of the orientations of the rods considered there). Zwanzig's analysis showed that at every order of the virial expansion considered, the system exhibited a van der Waals loop, associated with an order-disorder phase transition, at an appropriate density. A comparison with the Onsager work showed differences in the properties of the isotropic phase, but calculations truncated at the second virial coefficient were within 10% to 20% of those evaluated by Zwanzig (however, it should be noted that the third virial coefficient for an isotropic system of long thin rods is negligible [9]). This suggested that merely a second virial coefficient treatment may be sufficient to yield some valuable approximations when more complicated systems of rods are considered, e.g. the effects of external fields or the effects of allowing attractive forces to act between the rods [11].

At the same time, and on the other hand, Maier and Saupe [12] had demonstrated within the mean field approximation the existence of an orientational order-disorder transition in a system of cylindrically symmetric rigid molecules, dependent only on long range anisotropic attractive components of the pair potential. Maier and Saupe solved their system within the molecular field approximation. In these so called mean field theories the equilibrium configurational partition function is reduced to a product of single particle partition functions, one for each molecule each of which necessarily only depends on the coordinates of the molecule. This is the case for an ideal gas where the molecules of the gas may be considered to act independently of each other. The interaction of a molecule within the mean field is represented by a

pseudo-potential which is an effective one particle potential. There are many ways of arriving at a description of the pseudo-potential, and Luckhurst has listed some of these and also presents a derivation based on a hierarchy of molecular distribution functions [13].

In the Maier-Saupe theory the effective singlet orientational potential is;

$$V_{\text{MS}}(\cos\theta) = \langle v_2 \rangle \langle P_2 \rangle P_2(\cos\theta), \quad [\text{III.1}]$$

contributions from spatial coordinates are scalar functions and need not be considered.

In equation [III.1], θ is the angle between the director and the molecular symmetry axis of the molecule, $P_2(\cos\theta)$ is the second Legendre polynomial, v_2 , is an unknown that represents averaged anisotropic interaction parameters [14], and $\langle \dots \rangle$ represents an ensemble average (see section II.4). The behaviour of the order parameter $\langle P_2 \rangle$ for the classic Maier Saupe theory may be obtained by solving a single self consistent equation. Above a certain reduced temperature, $k_B T / v_2 = 0.222$, the value $\langle P_2 \rangle = 0$ is found corresponding to an orientationally disordered phase. However in the range $0.195 \leq k_B T / v_2 \leq 0.222$ two non-zero solutions are consistently obtained for $\langle P_2 \rangle$ both indicative of a nematic mesophase. The solutions that correspond to stable thermodynamic equilibrium phases may be identified by computing the excess orientational free energy [13], the other solutions corresponding to metastable phases. Below $k_B T / v_2 = 0.195$ only a single positive solution for $\langle P_2 \rangle$ is found; that of the low temperature nematic.

Thus we seem to have two conflicting theories about the nature of the nematic-isotropic transition, (a), that it is effected by excluded volume effects alone, or, (b), that it is the long range anisotropic dispersion forces that are responsible. In the light of these findings, computer simulations have been performed using many theoretical potential models to test the various aspects of these two viewpoints. It is to be noted, of course, in real systems, that it is a combination of the above effects (a) and (b) that is likely to determine whether a given molecule may form stable liquid crystalline phases.

III.3 Hard Particle Liquid Crystal Simulations

There have probably been more simulations performed on hard particle models of liquid crystals than any other type of model. The results of these have been of significance in trying to differentiate between the roles played by short-range excluded volume effects, and long-range attractive interactions in the formation of liquid crystals, as exemplified by hard-particle and the Maier-Saupe theories respectively.

It had been known for many years, that the structure of simple liquids could be explained by considering short range repulsive interactions alone [15]. The reasoning here is that most of the liquid part of a phase diagram of an atomic fluid say, is confined to the high density region. The high density region is defined as where $(\rho^*)^{1/3} \leq r_0$, ($\rho^* = \rho\sigma_0^3$, σ_0 is the Lennard-Jones range parameter such that $V_{LJ}(r = \sigma_0) = 0$), r_0 being the location of the minimum in the pair potential. For a small displacement about the minimum of the pair potential it is the repulsive component of the pair potential that is most rapidly varying. In comparison the fluctuations in energy due to contributions from the attractive component of the pair potential will be small. There are some exceptions to this,

a notable one is liquid water. The hydrogen bonding that occurs between water molecules is a rapidly varying attractive interaction [15].

Thus as we have seen, the hard sphere model is a good representation of simple atomic fluids. We may be able to use this as a starting point for models of liquid crystals. Early simulations on simple hard core fluids indicated solid-liquid coexistence at densities $\rho \geq \frac{2}{3}\rho_c$, where ρ_c is the density of regular close packing. There is the possibility therefore, that liquid-liquid coexistence between orientationally disordered and ordered phases obtains for suitably anisometric hard particles. Thus simulations of liquid crystals with somewhat idealised anisometric hard particle models have been attempted. Some of the results turned out to be rather surprising as we shall see below.

Hard core models fall into specific categories and it will be convenient to split the following subsections according to these models. We shall begin with not the simplest model, but rather the one that was used in the first attempts at simulating liquid crystals; hard ellipses moving on to infinitely thin hard platelets and subsequently full three-dimensional models.

III.3.1 Hard Particle Models: Hard Ellipses

The first attempted simulation of a liquid crystal with translational freedom can be ascribed to Vieillard-Baron [7]. Vieillard-Baron appreciated the limitations of the Zwanzig model. The fact that in the limit of $l \rightarrow \infty$ and $d \rightarrow 0$, the volume of each parallelepiped is zero, led him to describe the system as artificial. Further in the Zwanzig model the density at which the orientation-disorientation transition occurs was found to be strongly dependant on the point at which the terms considered in the virial series expansion were truncated. In this vein, Vieillard-

Baron proposed a model for a more realistic liquid crystal, which consisted of a system of hard ellipses, and used canonical MC to study the system. In order to evaluate whether two ellipses were in a condition of overlap, Vieillard-Baron introduced the contact function $\Psi_{\text{ellipses}}(\mathbf{r}, \hat{\mathbf{u}}_1, \hat{\mathbf{u}}_2)$ which was dependent on the orientation of the major axes $\hat{\mathbf{u}}_1$ and $\hat{\mathbf{u}}_2$ of a pair ellipses and the vector describing their separation \mathbf{r} : $\Psi_{\text{ellipses}} = 0$ when the ellipses are tangential and takes a non-zero value at other times. Evaluation of the contact function Ψ provides a decision criterion when updating attempted MC moves, and enables the pressure of the hard particle system to be computed. Further, Vieillard-Baron showed that a comparison with the contact function of hard discs leads to an inequality which simplifies the calculation of the pressure within the system. The evaluation of the contact function of hard particle models often presents great difficulty, and it is for this reason that only geometrically simple hard particle models are considered in simulations.

In a study of $N = 170$ ellipses with axial ratio minor/major axes $a/b = 1/6$, Vieillard-Baron observed two first-order phase transitions. If a close-packed system of ellipses is expanded from the close-packed area (the equivalent parameter is the density in three-dimensions), A_0 , then it undergoes a melting transition at $A_m / A_0 > 1$ (A_m being the area occupied by the system at the melting transition), which Vieillard-Baron described as an increasing function of increasing axial ratio a/b . Initially the ellipses are oriented in a particular direction on the close-packed lattice. At the melting transition it is the centres of mass of the ellipses that first become translationally uncorrelated in the $a/b = 1/6$ system, the ellipses maintaining their orientations. This is identified as the nematic phase, characterised by the directional order parameter M ;

$$M = \frac{1}{N^2} \left\langle \sum_{i=1}^N \sum_{j>i}^N \cos(2\theta_i - 2\theta_j) \right\rangle, \quad [\text{III.2}]$$

where θ is the angle between the major axis of an ellipse with a given fixed direction (chosen by Vieillard-Baron as the original direction of the ellipses' symmetry axes at the beginning of the simulation). M is a positive rotationally invariant quantity. Clearly for all ellipses pointing along the same direction $M = 1$; for a random orientation of the ellipses major symmetry axes $M \sim 1/N$. The directional order parameter is an example of a simple order parameter that may be used to quantify the degree of orientational order in the liquid crystal phase. The directional order parameter does not however give any information about the director orientation of the system.

In the absence of any precise information Vieillard-Baron speculated that the melting transition of the system of ellipses occurred at area $A_m / A_0 < 1.15$. This compares to the hard disc melting transition at area $A_m / A_0 < 1.266$. The difference between these two transition densities may be due to the effective single degree of translational freedom available to the ellipses in the dense nematic phase that contributes to the entropy of the phase, compared to the two-dimensional translational disorder of the hard disc system at the melting transition.

At a specific area of $A / A_0 = 1.40$, Vieillard-Baron observed $M = 0.7 \pm 0.1$. For larger ratios the directional order parameter decays smoothly. A disorientation transition is indicated at $A_d / A_0 = 1.775 \pm 0.025$, with a corresponding entropy change $0.05 \leq \Delta S / Nk_B \leq 0.12$, which as pointed out by Vieillard-Baron is much smaller than the entropy change associated with the

melting transition of hard discs; $\Delta S / Nk_B = 0.36$ [4]. Again the disorientation transition only effects the one degree of orientational freedom, and as such the nematic and isotropic branches of the isotherms are close and exhibit a large coexistence region.

Hard ellipses have been studied again more recently [16]. Constant-pressure MC simulations have been performed on a system of hard ellipses with aspect ratios $k = 2, 4$ and 6 . Both latter systems exhibit three phases, isotropic, nematic and solid. No nematic phase is indicated for ellipses of aspect ratio $k = 2$. Interestingly, while the isotropic-nematic phase transition appears first order for the $k = 4$ ellipse system, it appears to be continuous for the more eccentric $k = 6$. It should be noted however that in most cases only a system of approximately $N = 200$ ellipses is simulated and so the order of phase transition observed may suffer from small system size effects.

III.3.2 Hard Particle Models: Infinitely Thin Hard Platelets

Frenkel and Eppenga [17] examined, in detail, a system of thin discs in what was the first numerical determination of a thermodynamic isotropic-nematic transition in a system with full three-dimensional translational and orientational motion. Infinitely thin hard discs were chosen because, having zero volume they cannot freeze. However, the excluded volume of two non-parallel discs is non-zero, and so orientational ordering can occur and in fact the system is guaranteed to exhibit a nematic phase at a sufficiently high density. The infinitely thin hard disc model does offer further significant advantages [17]. As with the hard sphere model there is only one independent thermodynamic parameter that describes the system; the scaled density $\rho^* = \rho\sigma^3$, σ is the diameter of the hard discs. Thus the hard platelet fluid could be made to act as a reference system for discotic

mesogens, in a similar way that the hard sphere fluid has been valuable as a reference system for atomic fluids. Moreover, the authors point out that the hard disc system provides for a direct comparison with Onsager theory. For a system of hard discs, unlike rods, virial coefficients higher than the second are non-negligible. Thus a study of the hard discs system enables one to assess the severity of truncating the virial series at the second virial coefficient in Onsager theory.

Virial coefficients up to the fifth were calculated via diagrammatic techniques and via constant pressure MC simulation for comparison. The fifth virial coefficient is found to be negative, indicating that five particle platelet interactions actually decrease the pressure in the platelet fluid.

The Onsager theory has yielded a numerical solution which predicts a strong first order phase transition at a reduced pressure $P = 22.89$. The change in density at the transition is of the order 26% with $\rho_{\text{isotropic}} = 5.334$ and $\rho_{\text{nematic}} = 6.846$ [18]. At the transition the nematic order parameter defined as;

$$S = \frac{1}{N} \sum_{i=1}^N P_2(\mathbf{u}_i \cdot \mathbf{n}), \quad [\text{III.3}]$$

(where the symbols have their meanings as defined in chapter II), changes discontinuously from zero in the isotropic phase to $S = 0.784$.

The results of the simulations indicated a small change in the system density suggestive of a weakly first order phase transition at $P = 14.25$; much lower than that predicted by Onsager theory. The location of the phase transition was

computed by comparing the excess chemical potential obtained from the particle insertion method [19] and that obtained from the relation $\partial\mu/\partial P = 1/\rho^*$. Similarly the estimated change in density - which was found to be strongly system size dependent, for example with a system of $N = 50$ particles it is non-existent - occurs at a much lower density and the density change itself is lower; $\rho_{\text{isotropic}} = 3.78$ and $\rho_{\text{nematic}} = 4.07$ for $N = 400$ particles, a jump of $\Delta\rho^*/\rho^* \approx 8\%$. Furthermore, at the transition the order parameter S of equation [III.3] changes to $S \approx 0.37$ at the isotropic-nematic transition; again much lower than that predicted by Onsager theory.

Thus we see that Onsager theory overestimates the pressure, density and change in density at the isotropic-nematic transition in a system of infinitely thin hard platelets. As discussed above, this is due to the neglect of Onsager theory to consider virial coefficients higher than B_2 . Consequently Onsager theory is not capable of predicting the location of the isotropic-nematic transition for this system. This indicates the severity of truncating the virial series early, retaining just a few coefficients for systems which do not have vanishing higher order coefficients. System size effects are manifest in these simulations, with the change in density at the transition disappearing for $N = 50$. The effects of system size was also apparent in the fluctuations of the order parameter S close to the transition [17].

III.3.3 Hard Particle Models: Spherocylinders

Of course, systems of two-dimensional ellipses and platelets are rather idealised. Thus Vieillard-Baron turned his attention to a three-dimensional system of spherocylinders [20]. These are right cylinders of length l , diameter d capped at each end with a hemisphere. Spherocylinders were chosen for their geometrical simplicity. Detailed information about the form of a nematogenic intermolecular potential was not available. Vieillard-Baron thought that the spherocylinder provided a realistic model for mesogens so long as the molecules were not too long so that the effects of molecular flexibility could be ignored. He had previously worked out a scheme for computing the overlap function of a pair of spherocylinders [7], so the functional form of $\Psi_{\text{spherocylinders}}$ was already known. Further, even if realistic nematogens do not possess cylindrical symmetry [13] the well ordered nematic phase does possess symmetry $D_{\infty h}$, which may be obtained from assemblies of particles themselves possessing symmetry D_{2h} .

Vieillard-Baron used the MC technique described by Wood and Parker [21], attributed to Metropolis *et al* [1] in a simulation of 244 spherocylinders of length to breadth ratio $L/D = 2$ and 616 spherocylinders of $L/D = 3$. Introduced into this simulation was the calculation of the \mathbf{Q} orientation tensor (see section II.4.2), attributed to de Gennes for the calculation of orientational order parameters. The orientational order parameter may be re-expressed in terms of the \mathbf{Q} tensor as;

$$M = 3\langle \text{Tr}(\mathbf{Q}^2) \rangle, \quad \text{[III.4]}$$

where the trace Tr of \mathbf{Q}^2 is defined;

$$\text{Tr}(\mathbf{Q}^2) = \sum_{\alpha=1}^3 \sum_{\beta=1}^3 Q_{\alpha\beta} Q_{\beta\alpha}, \quad \text{[III.5]}$$

and a component of \mathbf{Q} is;

$$Q_{\alpha\beta} = \frac{1}{N} \sum_{i=1}^N \frac{3u_{i\alpha}u_{i\beta} - \delta_{\alpha\beta}}{2}. \quad [\text{III.6}]$$

In equations [III.5] and [III.6] above, $u_{i\alpha}$ is the α component of the i th molecule's principle symmetry vector described by $\hat{\mathbf{u}}_i$, α and β take the range $1 \leq \alpha, \beta \leq 3$. Diagonalisation of the \mathbf{Q} tensor leads to the order parameter $\langle P_2 \rangle$. Vieillard-Baron consistently chose the highest eigenvalue of the diagonalised \mathbf{Q} tensor to represent $\langle P_2 \rangle$, the second rank orientational order parameter with the corresponding eigenvector being the orientation of the system director $\hat{\mathbf{n}}$. More recently different choices for the eigenvalue of \mathbf{Q} that correspond to the second rank orientational order parameter have been discussed, see section II.4.2 for these and a description of the behaviour of $\langle P_2 \rangle$.

Vieillard-Baron describes experiencing "great numerical difficulties", which required the generation of a large number of configurations to melt and then equilibrate the systems at high packing fraction $\eta = 0.55$, where the packing fraction is given by $\eta = \rho v_1$: where v_1 is the volume of one spherocylinder, and ρ is the number density. Note η is a function of L/D . Thus the packing fraction was reduced to $\eta = 0.54$, and additionally another system was studied at $\eta = 0.50$. None of these systems was found to exhibit a nematic-isotropic phase transition. Comparisons of the isotropic spherocylinders were made with both the Scaled Particle Theory (SPT), and Onsager theory. At high densities up to $\eta = 0.54$ the spherocylinder system is always disordered in contradiction to the predictions of the SPT. However at lower densities away from the possible existence of a nematic phase, Vieillard-Baron concluded that SPT was rather

good at predicting the appropriate value of the pressure for the spherocylinder system.

In order to try and simulate a nematic phase Vieillard-Baron finally tried a system of 2392 spherocylinders with $L/D = 6$ and $\eta = 0.54$, but this proved to be far too time consuming and the calculation had to be abandoned. Vieillard-Baron decided that, despite the apparent simplicity of the spherocylinder model, it would hardly be useful as a reference system for the study of the nematic phase. This was not the case though as we shall see shortly. In fact Vieillard-Baron should only have observed liquid crystalline phase formation for the spherocylinders of length to breadth ratio 6. Veerman and Frenkel have shown that only an isotropic and normal crystal phase can exist for freely rotating spherocylinders with $L/D \leq 3$ [22]

The work of Vieillard-Baron proved inconclusive. This may well have been due to a lack of resources and given more time the isotropic-nematic phase transition of a system of spherocylinders may have been located. However, it was almost a decade before comprehensive simulations were performed on hard convex body fluids namely infinitely thin platelets [17].

Puzzled by the formation of translationally ordered phases in colloidal solutions of rigid rod-like particles, e.g. the tobacco mosaic virus, Frenkel and co-workers set out to investigate the phase behaviour of hard spherocylinders after Vieillard-Baron. Successful simulations of spherocylinders had been performed by 1986 [23]. Initially simulations were performed on a system of hard parallel spherocylinders, i.e. the spherocylinders are constrained to lie with their long axes perfectly aligned along a given director $\hat{\mathbf{n}}(z)$, say. Thus even at low

densities the resulting phase is a nematic gas or liquid. Although rather artificial, the system could be used to model the behaviour of nematic particles that are aligned in a magnetic field for example. Simulations of non-spherical potentials constrained to lie in a particular direction do have further practical advantages. It is not necessary to locate the director for example. The time dependence of $\hat{\mathbf{n}}$ disappears, such that time dependent functions resolved with respect to $\hat{\mathbf{n}}$ do not suffer from inaccuracies due to fluctuations in $\hat{\mathbf{n}}(t)$.

To obtain the equation of state constant-pressure and constant-stress MC simulations were carried out in the fluid and solid phases respectively, on system sizes of between 90 to 1080 particles of varying length to width ratios: $L/D = 0.25, 0.5, 1, 2, 3$ and 5 [24]. The latter constant-stress simulations allowing a change in all sample box dimensions to accommodate the crystal in a minimum equilibrium state. This circumvents spurious contributions to the free energy that may arise from residual stresses formed in a crystal forced to adopt a specific unit cell due to a fixed simulation box geometry. In order to locate phase transitions precisely the absolute (Helmholtz) free energy of the solid was calculated with reference to the appropriate Einstein crystal [25]. The absolute free energy of the isotropic liquid can be computed with respect to the dilute gas phase. It is not possible however, to construct a reversible thermodynamic path connecting the nematic phase with a reference phase of known free energy without crossing a phase transition. A solution has been proposed however [26]. If a strong enough magnetic field is applied to a nematic fluid, it is possible to expand the fluid to the low density limit (in this case a nematic gas) without it undergoing an orientational order-disorder phase transition. Knowledge of the free energy of the applied magnetic field allows the absolute free energy of the nematic fluid to be computed with respect to the low density gas limit.

Subsequent knowledge of the solid-fluid coexistence points enables determination of the melting points of the range of parallel spherocylinders. However, simulation results indicated a discontinuity in the equation of state at a density lower than the computed melting density for all but the $L/D = 0.25$ systems. Thus in order to investigate this behaviour further Stroobants *et al* [23] looked at the components of the radial distribution function; the transverse component, $g_{\perp}(x,y)$ and the longitudinal component, $g_{\parallel}(z)$ along the director. The results indicated smectic ordering with $g_{\perp}(x,y)$ being liquid like while $g_{\parallel}(z)$ exhibited a strong periodic density wave. Further demonstrations of the smectic ordering was offered through "snapshots" of the systems at different densities.

For sufficiently long parallel spherocylinders with $L/D > 3$ an additional phase was observed at densities in-between the smectic and crystalline phases. For this phase the $g_{\perp}(x,y)$ describe translational order within a plane perpendicular to the director, whereas the $g_{\parallel}(z)$ support translational disorder along the director. Information afforded by radial distribution functions does not however provide any knowledge of the fluidity of the system: an amorphous disordered solid would present a liquid like $g(r)$, but the phase is characterised as possessing an infinite viscosity. Liquid crystal phases by definition must possess molecular centre of mass diffusion. So, it is important to provide a check for this. As MC calculations cannot offer any direct dynamical information on the spherocylinder system, Stroobants *et al* [24] further performed MD simulations. Examination of the components of diffusion D_{\parallel} and D_{\perp} both showed liquid like behaviour in the smectic region indicative of fluidity and the phase was consequently identified as a columnar phase. The different mesophases observed for parallel spherocylinders are indicated schematically in figure III.1.

Thus Stroobants *et al* had found a smectic phase for parallel spherocylinders with $L/D \geq 0.5$. The authors looked for evidence of bond orientational order, and finding none, identified the phase as smectic A. It is important to note that these simulations of hard parallel spherocylinders provide unequivocal evidence that mesophases other than the nematic phase, in this case smectic and columnar phases, can be formed solely by anisometric hard particles. On the other hand however, using an extension of the Maier-Saupe theory of nematics [12], McMillan has proposed a smectic A phase formed from long ranged attractive interactions in the mean field approximation [27].

In addition this was the first instance of the absence of a change in density at the transition. Observation of strong pretransitional fluctuations identified the transition as being continuous.

Later, Frenkel *et al* looked at freely rotating spherocylinders with aspect ratio $L/D = 5$ which provided a rich polymorphism. Eventually the phase diagram for hard spherocylinders in the range $0 \leq L/D \leq \infty$ was established through simulation of freely rotating spherocylinders of $L/D = 0, 1, 3$ and 5 ; ($L/D = 0$ is the hard sphere case [28]) [16]. Veerman and Frenkel performed free energy calculations in order to distinguish the thermodynamically stable phase from several coexisting mechanically stable phases at different densities. It is possible to create a mechanically stable smectic phase with spherocylinders of $L/D = 3$. This phase is however, found subsequently to be thermodynamically unstable with respect to the isotropic liquid and the solid. Thus no mesophases are observed for freely rotating spherocylinders with $L/D \leq 3$. Although the spherocylinders studied here prevent an exact calculation of the aspect ratio above which a stable smectic phase exists, it is thought to be just above $L/D = 3$

[16]. Thus there is an isotropic-smectic-solid triple point for $L/D \approx 3$ at a certain density. Veerman and Frenkel further predict a second triple point, where a nematic phase stabilises at a slightly higher aspect ratio. This information allows a rough sketch of a tentative phase diagram in the range $0 \leq L/D \leq 6$. This is shown in figure III.2.

An important observation made on this system of hard spherocylinders is that of increasing collective orientational fluctuations on approach to the nematic phase from the isotropic phase. These fluctuations may be observed in the decay of certain particle correlation functions. Specifically Veerman and Frenkel [16] looked at the single particle correlation function of equation [III.7], the collective particle correlation function of [III.8] and the static orientational correlation factor given by [III.9]:

$$C_2^s = \langle P_2(\hat{\mathbf{u}}(0) \cdot \hat{\mathbf{u}}(t)) \rangle; \quad \text{[III.7]}$$

$$C_2^c = \sum_{i=1}^N \sum_{j>i}^N \langle P_2(\hat{\mathbf{u}}_i(0) \cdot \hat{\mathbf{u}}_j(t)) \rangle; \quad \text{[III.8]}$$

$$g_2 = \sum_{i=1}^N \sum_{j>i}^N \langle P_2(\hat{\mathbf{u}}_i \cdot \hat{\mathbf{u}}_j) \rangle. \quad \text{[III.9]}$$

In order to study dynamical processes, of course, MD simulations must be performed. This work highlights the advantage of combining appropriate ensemble MC calculations to arrive at a desired state point, then continuing the simulation employing MD to extract the desired dynamic data.

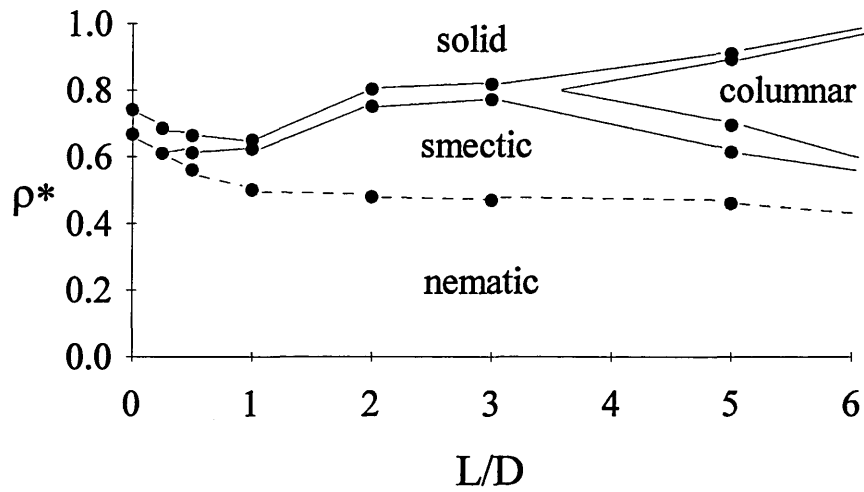


Figure III.1

Schematic phase diagram of parallel hard spherocylinders shown in the range $0 \leq L/D \leq 6$. Phase regions are as indicated. Approximate coexistence regions are bounded by straight lines. The dotted line indicates the nematic-smectic boundary.

After [24]

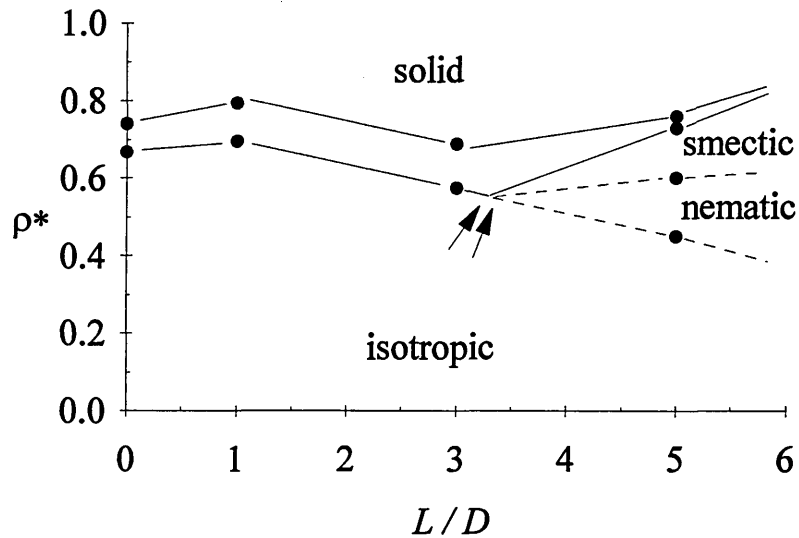


Figure III.2

Schematic phase diagram of the freely rotating hard spherocylinder system shown between $0 \leq L/D < 6$. The reduced density $\rho^* = \rho / \rho_{cp}$ is the density relative to the density of close packing. Phase regions are as indicated. The approximate locations of the predicted [V+F 90] isotropic-smectic-solid triple point and isotropic-nematic-smectic triple point are arrowed. The isotropic liquid-solid and smectic-solid coexistence region is that region enclosed by the continuous black lines. These data are taken from the following papers: (a) $L/D = 0$, [28]; (b) $L/D = 1, 3, 5$, [16].

III.3.4 Hard Particle Models: Cut Spheres

Another hard convex body for which the contact function can be evaluated relatively straight forwardly [29] is the cut sphere. Cut spheres are hard spheres that have had two slices removed above and below the equator, parallel to the equatorial plane and at an equal distance normal to it. Once again this model may be specified by the ratio of two parameters: the diameter of the sphere D and the distance between the cut planes L ($L < D$ necessarily). With the aspect ratio $L/D = 1$, the cut sphere model reverts to the hard sphere model. Thus once again there exists a reference system which can be used as a check on simulation conditions and provides known results for the hard sphere solid-isotropic liquid phase transition; useful for commencing a phase diagram of a model system.

Frenkel and co-workers have studied the behaviour of the cut sphere model. Initially cut spheres with $L/D = 0.1$ were simulated in the canonical MC ensemble [29]. On compression at reduced density $\rho^* = 0.35$ ($\rho^* = \rho / \rho_{cp}$ where ρ_{cp} is the density of regular close packing), the system spontaneously forms a discotic nematic phase with orientational order parameter $S = 0.73 \pm 0.02$.

Later nematic phases, were prepared pre-aligned along the edge of the simulation box. This fixes the director, and it is then no longer necessary to diagonalise the Q tensor. Upon further compression increased local ordering is noticed until at approximately $\rho^* = 0.45$ the system appears to form a columnar phase. The columns are arranged on a regular hexagonal array. Investigation of the longitudinal distribution function shows that the cut spheres themselves are disordered within the columns. Columnar phases formed in this way exhibited appreciable disorder. Thus well ordered and defect free columnar phases were prepared by expanding a regular crystalline phase. It is found, therefore, that cut-

spheres with $L/D = 0.1$ can form four distinct phases; isotropic, nematic, columnar and crystal.

Thereafter, more comprehensive simulations enabled a more precise location of the isotropic-nematic transition: in the nematic branch $\rho^*_{N-I} = 0.335 \pm 0.005$, and in the isotropic branch $\rho^*_{I-N} = 0.330 \pm 0.005$ [30]. As noted by the authors the density change at the transition is quite small, $\sim 1\%$.

Frenkel and Veerman studied cut discs of different axial ratios than described above [30]. The results were found to be quite surprising. For cut spheres with $L/D = 0.2$ no stable nematic phase is observed. Instead at densities above $\rho^* \approx 0.55$ compression of the isotropic phase leads to the appearance of a novel phase. Termed "cubatic" by the authors this phase is characterised by small stacks of discs forming short columns. The columns themselves appear to be disordered. The authors investigated higher order orientational correlation functions $g_l(r)$, where;

$$g_l(r) = \langle P_l(\hat{\mathbf{u}}(0) \cdot \hat{\mathbf{u}}(r)) \rangle. \quad [\text{III.10}]$$

In equation [III.10] P_l is the l^{th} Legendre polynomial. These order parameters give a quantitative measure of different types of ordering which may be present. The orientational correlation function $g_2(r)$, is sensitive to nematic ordering as has already been described in chapter II. The higher order orientational correlation functions $g_4(r)$ and $g_6(r)$ are sensitive to cubic orientational order. It is an investigation of these higher order orientational correlation functions that reveals the nature of the cubatic phase. Whereas $g_2(r)$ and $g_6(r)$ are found to

decay rapidly within one molecular diameter, by contrast with increasing density $g_4(r)$ and $g_8(r)$ decay progressively more slowly.

A snapshot of a typical configuration shown in the original publication helps to clarify the situation [30]. The cut spheres appear to be stacked in short columns as suggested earlier. It is clear though that these short stacks have cubic orientational symmetry with respect to neighbouring columns. This is the origin of the $g_4(r)$ and $g_8(r)$ behaviours.

There is the possibility that the apparent cubic orientational order of the short stacks of discs in the cubatic phase originates somehow in the cubic periodic boundary conditions of the simulation box. This possibility is correctly eliminated by the authors in their observations of the higher order orientational correlation functions. Any such periodic effects will manifest themselves as a significantly non zero value in $g_l(r)$ with $l \geq 4$ at a distance $r > L/2$ where L is the box length. The absence of any such behaviour in $g_6(r)$ provides the necessary evidence.

As the density is increased further the short stacks increase in length until at approximately $\rho^* \approx 0.60$ they become of order L . At this point it is observed that the columns tend to align themselves along the simulation box and a true columnar phase is formed.

Cut spheres with a more extreme axial ratio $L/D = 0.3$, yielded yet more surprises [30]. In this case it is found that the cubatic phase is absent in favour of the thermodynamically stable solid phase.

Thus we find that cut spheres of various aspect ratios exhibit a rich and varied phase diagram.

III.3.5 Hard Particle Models: Ellipsoids of Revolution

To investigate how far a molecule must deviate from sphericity before orientational ordering will stabilise in the liquid phase before freezing occurs, Frenkel and co-workers [26, 31] examined a system of hard ellipsoids of axial ratio $3 \geq x \geq 1/3$, using the contact function devised earlier by Vieillard-Baron [7]. At about the same time Perram *et al* were also investigating ellipsoids of axial ratio $x = 2, 3, 3.5$ [32] using a previously developed contact function [33]. If an ellipse is rotated about its principal symmetry axis, a say, the resultant shape mapped out in three-dimensions is the hard ellipsoid. These are characterised by their axial ratio $x \equiv (a/b)$: a is the length of the principal symmetry axis and b is the length of the two mutually perpendicular axes themselves being perpendicular to a . Both prolate $x \rightarrow \infty$ and oblate $x \rightarrow 0$ ellipsoids are possible. Once again with $x = 1$ the hard sphere reference model is obtained. In the study [26] specific axial ratios of $x = 3, 2.75, 2, 1.25, 0.8, 0.5, 1/2.75$ and $1/3$ were investigated.

It is found that for the more spherical ellipsoids, $1.25 \geq x \geq 0.8$ a rotationally disordered plastic solid phase exists. The molecules are centred on lattice sites but their molecular orientation does not align along any preferred direction. At more extreme axial ratios an orientationally ordered crystal phase is observed. These solid phases are formed directly from the isotropic liquid

At sufficient axial ratios $2.75 \leq x \leq 1/2.75$ the ellipsoids form an orientational ordered fluid at sufficiently high density (although see below). The nematic fluid is seen to form spontaneously on compressing the isotropic liquid.

Figure III.3 is a schematic of the phase diagram of hard ellipsoids. There are several things to note about this figure. Firstly it appears remarkably symmetrical under the oblate \leftrightarrow prolate transformation. This can be understood at lower densities because the second virial coefficients are equal under such a transformation. However, higher order terms are not and so this symmetry is not expected to persist at higher densities, indeed why such symmetry should persist at all at high density is unclear [34] although it could be a fortuitous result when higher oblate ellipsoid virial coefficients are taken into account.

Closer examination of figure III.3 reveals that the nematic phase of oblate ellipsoids is stable at lower densities than that of prolate ellipsoids of inverse axial ratio. However, theoretical calculations at axial ratios, $x = \infty$ or $x = 0$ that do not distinguish between the two extremes predict equal low coexistence densities at the freezing transition, thus the symmetry of the phase diagram is seen to reappear [35]. Still this symmetry cannot be exact because in the limit that the oblate ellipsoids become infinitely thin the higher order virial coefficients do not vanish as they do in the case of infinitely long ellipsoidal needles.

Subsequently, additional ellipsoids of more extreme axial ratio, $x = 10, 5, 1/5$ and $1/10$, have been studied together with a re-examination of the $x = 3$ and $x = 1/3$ systems [36]. It is found that the oblate ellipsoids are more aligned than the respective prolate ellipsoids at a given density.

Zarragoicoechea *et al* [37, 38] have investigated the behaviour of hard ellipsoids of axial ratio $a/b = 3$ with the addition of a permanent dipole moment $0 \leq \mu^* \leq 3.5$ orientated along the principal symmetry axis. With a zero value dipole moment this work allows comparison with previous simulations performed

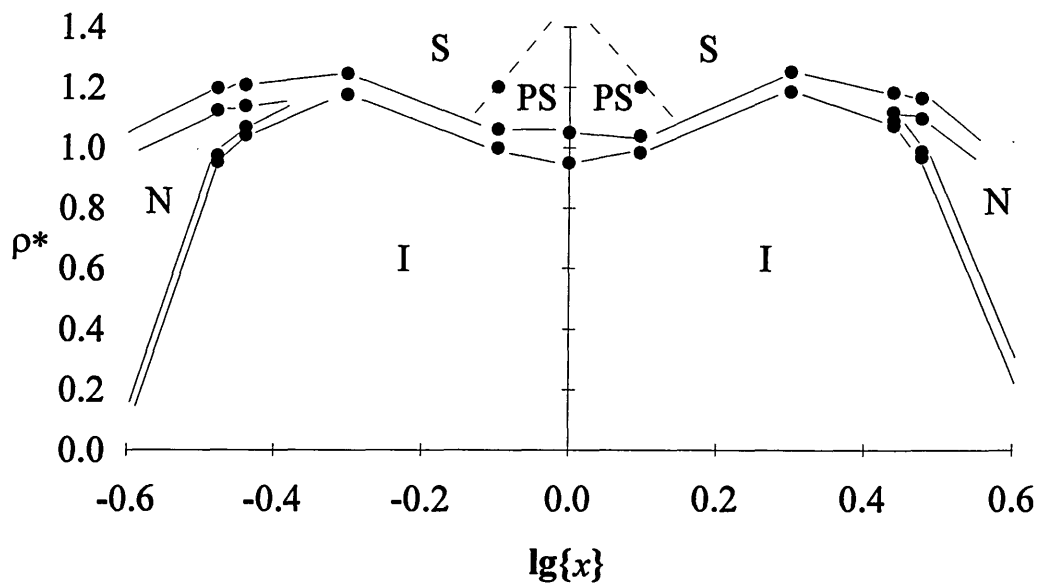


Figure III.3

Approximate schematic phase diagram of the hard ellipsoid-of-revolution system. The axial ratio is plotted as $\log_{10}\{x\}$ written above as $\lg\{x\}$ to show the approximate symmetry between oblate and prolate ellipsoids. Coexistence regions are shown bounded by solid straight lines. The indicated phases are as follows: I, isotropic liquid; N, nematic liquid crystal; S, solid phase; PS, orientationally disordered plastic solid phase. These data are taken from the following papers: (a) $\log_{10}\{x\} = 0$ (i.e. $x = 1$), [28]; (b) the remaining points [26].

at the same axial ratio [26]. Presently simulations with $N = 108$ and $N = 256$ [38] have shown significant system size dependence. The original simulations considered $N = 90$ and $N = 108$ (with $a/b = 3$) particles and no system size effects were observed. In both sets of simulations identical results within the statistical error are obtained and appear to indicate the presence of a stable nematic phase at $\rho^* \approx 0.36$ (here $\rho^* = Nb^3/V$). However, latterly by increasing the number of particles within the simulation box to $N = 256$, the pressure of the system is found to increase by approximately 30% and the eigenvalues of the \mathbf{Q} tensor take on values of an isotropic phase. Further if an aligned simulation is prepared with $\rho^* < 0.36$ and $N = 256$ it is found to systematically evolve towards the isotropic phase with sufficient attempted particles moves. Of course away from the previously proposed region of nematic stability this is to be expected. However close to $\rho^* \approx 0.36$ this should not be the case.

Zarragoicochea *et al* suggest that this effect is due to a system size dependence [38] as they found no difference between simulations performed using different simulation box geometries. However there is a further difference between the two sets of simulations in the choice of overlap criterion used. In their original study Frenkel and Mulder used the $\psi_{\text{ellipsoids}}$ overlap criterion previously proposed by Vieillard-Baron [7]. More recently Zarragoicochea *et al* have used an alternative criterion [38]. No exhaustive comparison between the overlap criteria has been performed. However the similarity of the results obtained for the $N = 108$ system tends to discount this possibility. It is of course still a possibility that the nematic phase of hard ellipsoids of axial ratio $a/b = 3$ exists in a very narrow density range close to the freezing transition that is imperceptible to the current simulation technique using a significant number of particles.

With a view to the above statements Mason and Allen [39] have repeated the work of Frenkel and Mulder [26] and additionally used MD to simulate the system of $a/b = 3$ hard ellipsoids. They too have seen spontaneous formation of the nematic phase.

The dynamics of hard ellipsoids on approach to the isotropic-nematic transition have been observed using (necessarily) molecular dynamics [40]. It is found that the collective reorientation decreases linearly to zero at the transition point. Similar effects are observed before the freezing transition of hard ellipsoids with $a/b = 2$ which do not form a nematic phase. More recently the dynamics of the isotropic phase of hard ellipsoids has been examined in greater detail [41].

Simulations with a finite dipole moment $\mu^* \neq 0$ proved to differ only slightly from those with $\mu^* = 0$. Specifically, no stable nematic phase is observed over the range of densities studied and the pressure remains comparable with that observed in the isotropic regime. With increasing dipole moment a tendency to increased anti-parallel short ranged order between nearest neighbour ellipsoids is observed contrary to that observed for dipolar hard spheres.

The comparisons of the work described above indicates the sensitivity of computer simulation methods to system size and box geometry effects particularly at phase transitions. These can often conceal the true nature of a phase transition. It is therefore important wherever possible to study the constraints imposed by such effects. However, with computationally demanding simulations sufficient resources are often unavailable for a detailed investigation.

III.3.6 Hard Particle Models: Spheroids

Spheroids form the more general class that ellipsoids belong to but generally they have non-equal axial ratios: $a \neq b \neq c$. These have been used in an attempt to simulate a biaxial liquid crystalline phase [36; 42]. In this study the three semi-axes were chosen such that $abc = 1$, $c/a = 10$ and b/a ranged between 1 and 10. For axial ratios close to the self conjugate value $b = \sqrt{ac}$ a stable biaxial phase is seen to form directly from the compression of the isotropic liquid. Away from these axial ratios either a discotic nematic or calamitic nematic, respectively, is identified. The biaxial phase is seen to form at densities at least one-and-a-half times higher than the nematic phase in uniaxial systems. The phase diagram is found to be approximately symmetrical under the transformation $\{a, b, c\} \leftrightarrow \{a^{-1}, b^{-1}, c^{-1}\}$ about $b = \sqrt{ac}$, though there are some systematic differences [42]. As has been observed in hard ellipsoid systems [26; 36] oblate uniaxial spheroids are found to be more aligned at slightly lower densities than the complementary prolate spheroids. Real liquid crystals are biaxial and so simulations of biaxial models represent an improvement over the usual axisymmetric hard particle models.

III.3.7 Hard Particle Models: Rigid and Semi-flexible Hard

Sphere Chains

Simulations of rigid fused [43] and tangential [44; 45] hard sphere models have been performed. Although the tangential hard spheres were not studied at sufficient elongations to form liquid crystal phases, fused spheres with a length to width ratio of 5.2 composed of eight equally spaced fused spheres were observed to spontaneously form a nematic phase at sufficient density. The introduction of flexibility into a seven sphere tangentially bonded molecule results in the formation of smectic, nematic and isotropic phase [46,47]. In an MD simulation

the hard spheres of a molecule were allowed to rattle within internal constraining square wells thus producing the required flexibility. Interestingly a preference for linear chains is seen in the nematic phase albeit within the narrow range of flexibility included in the model. In contrast no nematic phase but a metastable smectic phase which eventually converts to the isotropic liquid is observed for a similar five tangential rattling sphere model [48]. This model clearly demonstrates how molecular flexibility may be incorporated into hard sphere models. It will most likely prove to be of great use in simulating the flexible alkyl chains common to liquid crystal molecules.

An alternative approach due to Nicklas *et al* makes use of the so called rigid-flexible-rigid (rfr) model of liquid crystal dimers [49]. A model is constructed which consists of two rigid spherocylinders connected by a flexible alkyl chain. The spherocylinders are each formed from a rigid linear array of ten methylene type united atom sites. These are joined by 4, 5, 6 or 7 similar sites separated by the same inter-site spacing but having flexible bond angles and torsion angles. The model interacts via a MM2 [50] type force field which only considers repulsive interactions. Extensive MD simulations reveal a striking odd-even dependence of the stability of smectic and nematic liquid crystal phases and of the nematic order parameter on the number of methylene groups in the flexible linkage in qualitative agreement with observations on real rfr dimers.

III.4 Single-Site Soft Potential Simulations

Soft potentials vary smoothly with distance. They may be simply repulsive such as the soft sphere potential (see figure II.2), or they may have additional attractive components as in the Lennard-Jones 12-6 potential (see figure II.3) for example. The origins of soft potentials have already been outlined in chapter II and so in

this section we will concentrate on the simulations that have been performed to date.

Single site soft potentials used in liquid crystal simulation must necessarily have an orientational dependent term and as such are all types of Corner potential [51]. Anisotropic soft potentials based on the Lennard-Jones 12-6 potential are used [36].

A continuous potential may be formed from the scalar Lennard-Jones plus a suitable anisotropic component. Luckhurst and Romano have investigated the behaviour of a system interacting via the potential;

$$V_{LR} = V_0 + V_A. \quad [\text{III.11}]$$

A Lennard-Jones 12-6 form is chosen for V_0 . Assuming the particles are rigid and cylindrically symmetric the anisotropic potential V_A , describing the interaction of these particles, may be expanded in a series of spherical harmonics. It should be noted that real mesogens do not possess such cylindrical symmetry however, this may not be a serious approximation. From a molecular cluster viewpoint, clusters of molecules are less anisometric than individual molecules. If the clusters are preserved at the transition then the shorter range anisotropic forces of individual molecules may not be so important in nematic phase formation. Truncating this expansion at the second-rank terms yields;

$$V_a = u_2(r_{12})P_2(\cos\beta_{12}). \quad [\text{III.12}]$$

In [III.12] P_2 is once again the second Legendre polynomial and β_{12} is the angle between the symmetry axes of two particles. In essentially an extension of a previous simulation [52] that was confined to a lattice and considered only nearest neighbour interactions the scaling term $u_2(r_{12})$ is chosen to take one of two forms;

$$u'_2(r_{12}) = -4\lambda\varepsilon_0\left(\frac{\sigma_0}{r_{12}}\right)^6; \quad \text{[III.13]}$$

$$u''_2(r_{12}) = -4\lambda\varepsilon_0\left(\left(\frac{\sigma_0}{r_{12}}\right)^{12} - \left(\frac{\sigma_0}{r_{12}}\right)^6\right). \quad \text{[III.14]}$$

In the expressions [III.13] and [III.14] σ_0 and ε_0 are the Lennard-Jones strength and range parameters and r_{12} is the particle separation. The parameter λ is used to control the anisotropy and was given the value $\lambda = 0.15$ selected after preliminary simulations: smaller values of λ were not found to exhibit a liquid crystal phase above the melting point and additionally larger values of λ gave orientationally ordered phases that were found to be stable right up to the boiling point. Results using the pair potentials of [III.13] and [III.14] were found to be qualitatively similar and to be in reasonable accord with the nematogen 4,4'-dimethoxyazoxybenzene.

In the first simulation of a single-site soft potential with substantial anisotropy Kushick and Berne [53] used the Gaussian overlap model proposed by Berne and Pechukas [54] (see chapter II) in a simulation of 144 ellipses of axial ratios 2-to-1 and 3-to-1. At the start of the simulation the principle axes of the ellipses are orientated by the action of a magnetic field. Thereafter the field is switched off

and the system is allowed to relax. An order parameter given by equation [III.15] is monitored to see if the induced orientational order is destroyed at various densities. In two dimensions;

$$\zeta_{2\text{-dimensions}} = \frac{1}{N} \sum_{i=1}^N \left((\hat{\mathbf{u}}_i \cdot \hat{\mathbf{n}})^2 - \frac{1}{2} \right). \quad [\text{III.15}]$$

In expression [III.15] the $\hat{\mathbf{u}}_i$ and $\hat{\mathbf{n}}$ represent the directions of the principle axis of each ellipse and the direction of the director respectively. It is to be noted that the average is taken over all the particles of the last configuration only. This necessarily leaves the results susceptible to the inherent fluctuations in the degree of alignment of the particles of an orientationally ordered phase. This effect would be further enhanced close to phase transitions. Nevertheless the results for the ellipses indicated a persistence of orientational ordering in a system at $\rho/\rho_0 = 0.75$ with $\zeta = 0.83$. With knowledge of the solid-nematic transition observed by Vieillard-Baron [7] occurring at $\rho/\rho_0 = 0.87$ for hard ellipses of axial ratio 6-to-1, together with the observed melting density of hard discs (axial ratio 1) known to be $\rho/\rho_0 = 0.79$ the authors assumed, quite reasonably, that they had achieved stable rotational ordering below the density at which the solid is expected to form. By contrast an orientationally ordered state was observed for ellipses with axial ratio 2-to-1 at $\rho/\rho_0 = 0.90$ but this was not sustained at a density of $\rho/\rho_0 = 0.80$. The higher density is thought to correspond to an ordered solid phase.

The authors further report that they had also observed stable nematic ordering with soft ellipsoids in three-dimensions with the parameters $a = 3.5$, $\rho/\rho_0 = 0.71$

and $\zeta = 0.85$ using an appropriate expression for ζ valid in three-dimensions that is in fact;

$$\zeta = \frac{1}{N} \sum_{i=1}^N P_2(\hat{\mathbf{u}}_i \cdot \hat{\mathbf{n}}). \quad [\text{III.16}]$$

These were important results because they demonstrated the usefulness of the Gaussian overlap model in simulating orientationally ordered phases. However, these were preliminary experiments. Only a small number of particles were simulated at any time. Problems were encountered whereby the system would enter a long-lived metastable state or configurational phase-space bottleneck from which it was difficult to escape.

Tsykalo and Bagmet [55] studied the nematic phase of the Berne-Pechukas potential and of two modifications of the potential; a WCA [56] type split of the potential and a version of the potential scaled by a function dependent on the orientation of the particles with respect to the intermolecular vector. Thus;

$$\Phi_{\text{scaled BP}} = \frac{\Phi_{\text{BP}}}{\sigma^2(\hat{\mathbf{u}}_1, \hat{\mathbf{u}}_2, \hat{\mathbf{r}})}, \quad [\text{III.17}].$$

where $\sigma(\hat{\mathbf{u}}_1, \hat{\mathbf{u}}_2, \hat{\mathbf{r}})$ is the range function of the Berne-Pechukas potential (see equation [II.15]). A potential of the form of [III.17] does indeed introduce the necessary intermolecular vector dependency but the well depth anisotropy is necessarily controlled by the shape anisotropy parameter χ . Ideally a parameter independent of χ which may be adjusted to vary the well depth anisotropy is preferred. These systems were studied over a range of shape anisotropy in the

side-to-side end-to-end interaction ratio; $3.5 \geq \sigma_s / \sigma_e \geq 2.0$ at a variety of packing fractions; $0.50 \leq \eta \leq 0.55$, for only 1000 time steps after equilibrium. At sufficiently high packing fraction and shape anisotropy each system was found to possess residual nematic order after equilibration. The simulation results reported here cannot be considered accurate as only residual order is observed in systems that have been allowed to relax. Given sufficient length of run the residual order may eventually make way for a more stable thermodynamic phase with a different or perhaps even negligible degree of orientational ordering. Spontaneous order is not observed in this work, the importance of the work of Tsykalo and Bagmet therefore, lies in demonstrating the possibility of simulating anisotropic liquid crystalline phases using continuous potentials. Furthermore, although not elaborated on by the authors, the idea of including a well depth scaling term based on the relative orientation of the particles with respect to the intermolecular vector is introduced; an idea later expanded upon by Gay and Berne [57].

A nematic-isotropic transition was reported for a system of Berne-Pechukas centres [58] although in these studies again only a small number of particles were simulated with ensemble averages being collected only over the final 1000 simulation time steps after equilibrium had been attained. More recently the importance of large particle systems and long simulation runs over which the ensemble averaging is performed has been recognised. The results reported in the above publication are in qualitative agreement with experimental results and the tacit discrepancies reported therein are probably due to the aforementioned factors of system size and ensemble averaging.

In fact more recently it has been found that the nematic phase of the Berne-Pechukas potential is not thermodynamically stable. After extensive simulations it returns to the isotropic liquid phase [59].

Subsequently, several unrealistic features in the Berne-Pechukas potential were identified and in an attempt to correct for these undesirable features a cut and shifted rather than a simply scaled potential was employed by Gay and Berne [57]. The details of this Gay-Berne potential can be found in chapter II (see section II.2.3) where we have described the origins of the hybrid Gay-Berne Luckhurst-Romano potential which we have used in simulations of single-site calamitic and discotic liquid crystals and in a more ambitious multisite study of a calamitic mesogen; a discussion of some of the simulations to date using the Gay-Berne potential will suffice here.

The first successful simulation of a Gay-Berne fluid may be attributed to Adams *et al* [59]. Simulations were performed using the original parameterisation of Gay and Berne [57]; thus $\nu = 1$, $\mu = 2$, $\sigma_s / \sigma_e = 3$ and $\varepsilon_s / \varepsilon_e = 5$. These values are chosen to fit the Gay-Berne potential to a linear array of 4-Lennard-Jones centres each separated by $2\sigma_0 / 3$. In these preliminary simulations an isotropic to nematic transition is identified and the approximate transition temperature located, the nematic phase becoming stable at $T^* < 1.7$ for $\rho^* = 0.32$, ($\rho^* = \rho\sigma_0^3 / m$, σ_0 is the Lennard-Jones range parameter, m is the mass of the particle).

Luckhurst *et al* undertook more extensive simulations using a slightly differently parameterised version of the Gay-Berne. In particular the exponents ν and μ were exchanged so that the values $\nu = 2$ and $\mu = 1$ were employed. This change

does not effect the relative well depth minima for the side-by-side and end-to-end configurations, but it does help to stabilise the side-by-side configuration with respect to the X and T configurations. Thus it is thought that this parameterisation would be more likely to induce liquid crystal formation. The range and strength parameters, χ and χ' respectively, retain their previous values: thus $\sigma_s / \sigma_e = 3$ and $\varepsilon_s / \varepsilon_e = 5$. MD simulations performed with the above parameterisation demonstrate that the Gay-Berne model mesogen exhibits a diverse range of mesophases. In systems of $N = 256$ particles Luckhurst *et al* [60] identify nematic, smectic A, smectic B and a crystal phase in addition to the isotropic liquid in simulations performed at a density $\rho^* = 0.30$, with the aid of distribution functions and computer graphics.

Visualisation of the shape of the Gay-Berne potential obtained by plotting the contour corresponding to $U_{GB}(\hat{\mathbf{u}}_1, \hat{\mathbf{u}}_2, \mathbf{r}) = 0$ [60] shows that it is ellipsoidal in shape. It is therefore perhaps surprising that the Gay-Berne potential forms smectic liquid crystal phases because of the scaling arguments introduced by Frenkel [29]. However the argument proposed by Frenkel refers to hard particles only. It is therefore the long ranged anisotropic part of the Gay-Berne potential that is responsible for the formation of the observed more highly ordered mesophases. It should be noted that there is an internal well depth minimum in the Gay-Berne particle. This was also recognised by Gay and Berne [57]. However this is unlikely to cause problems in simulations of Gay-Berne particles since it is separated from the external potential minimum by an infinite potential barrier.

Extensive simulations of the Gay-Berne fluid have been performed by de Miguel and co-workers [61-67]. In particular the phase diagram of the Gay-Berne fluid

parameterised according to the original prescription of Gay and Berne [57] has been sketched out. With this parameterisation isotropic, nematic, smectic-B and a transition to a tilted smectic-B phase in addition to the crystalline phase are identified [64]. A smectic-A phase is not observed, although a density wave indicative of smectic-A layer structure was observed but found not to be stationary throughout the simulation. After sufficiently long runs the phase was in fact identified as smectic-B. Interestingly no smectic phase is observed along compression of an isotherm at $T^* = 1.25$. This is thought to be due to the system becoming trapped in a metastable region of phase space preventing the onset of one-dimensional spatial order, as subsequent simulations along isochores [65] show that the smectic-B phase is stable at higher temperatures. Along isotherms $T^* \leq 0.80$ the isotropic phase is seen to evolve directly into the smectic-B on compression of the system.

The observation of a tilted smectic-B phase [64] may be an artefact of compressing the system. In previous simulations of smectic-A and B phases the system director was always found to be aligned along the cubic simulation box diagonal [60]. It has been argued by Luckhurst *et al* that a diagonal orientation of the director allows the constraint that smectic layers must be commensurate with system periodic images to be more easily satisfied. It is quite possible therefore that once the director has been pinned in a certain direction say in a smectic-B phase further compression of the system may result in the observed tilted smectic-B phase, the director being unable to rotate in order to contain the correct number of layers composed of molecules normal to the layer surfaces commensurate with the system periodic images. However the observed tilt transition does appear to be weakly first order and has been observed in experimental systems [64].

In addition de Miguel *et al* have performed simulations on a WCA [56] split of the Gay-Berne potential [64]. The results indicated that the long range anisotropic attractive part of the potential does stabilise the onset on orientational order. For example along the isotherm $T^* = 0.95$ the isotropic-nematic transition is identified at the following reduced densities: full Gay-Berne potential, $\rho^* = 0.315$; WCA Gay-Berne, $\rho^* = 0.335$. However with the WCA Gay-Berne potential no smectic phases are observed indicating that the long range anisotropic attractive forces are vital to the formation of the smectic phase.

The same conclusions are reached in a study of the Gay-Berne mesogen parameterised to represent a real nematogen [68]. A methodology for projecting out the biaxiality of typical mesogens by performing Boltzmann weighted averages of the form;

$$V_{av}(\hat{\mathbf{u}}_1, \hat{\mathbf{u}}_2, \mathbf{r}) = \frac{\int_0^{2\pi} \int_0^{2\pi} V_{LJ} \exp(-V_{LJ} / k_B T) d\alpha_1 d\alpha_2}{\int_0^{2\pi} \int_0^{2\pi} \exp(-V_{LJ} / k_B T) d\alpha_1 d\alpha_2}, \quad [\text{III.18}]$$

where the V_{LJ} are provided by the sum of Lennard-Jones site-site terms and the α_i are rotation angles about the molecular long axes of a pair of molecules in an energy minimised conformation is presented. Parameters are then chosen to fit the ellipsoidal Gay-Berne potential to the Lennard-Jones site-site representation. Note the temperature dependency of [III.18]. Appropriately the known isotropic-nematic transition temperature for the real mesogen may be used. However in the case of *para*-terphenyl a number of Lennard-Jones site-site configurations have large Boltzmann contributions at the virtual nematic-isotropic transition

temperature. This leads to a complicated form for the potential energy surface $V_{av}(\hat{\mathbf{u}}_1, \hat{\mathbf{u}}_2, \mathbf{r})$ not in keeping with the smooth energy contours of the Gay-Berne potential. Consequently a higher temperature is used in the averaging process and this is not thought to significantly alter the qualitative appearance of the potential energy surface. This procedure will however decrease the predominant attractive features of the Lennard-Jones site-site representation.

To represent the nematogen *para*-terphenyl the following parameters are selected for the Gay-Berne model: $\nu = 0.74$, $\mu = 0.8$, $\sigma_e / \sigma_s = 4.4$, and $\epsilon_s / \epsilon_e = 39.6$. These values differ from those of the original Gay-Berne potential [57] but the most significant departure is seen in the value of the well depth anisotropy. Using this parameter set, at appropriate densities isotropic, nematic and smectic phases are identified. The isotropic-nematic phase transition is found to lie close to the nematic and isotropic coexistence regions of hard ellipsoids of corresponding axial ratio. It is reasonable, therefore to infer that the nematic phase of Gay-Berne particles is dominated by excluded volume effects [68].

In contrast an investigation into the phases observed with respect to the well depth anisotropy showed that below what appears to be a critical value of $\epsilon_s / \epsilon_e = 5$ smectic phases are not formed with this shape anisotropy. Such an observation substantiates the role of attractive forces in stabilising the formation of smectic phases.

Because of the small system sizes studied [60; 64] it is difficult to decide whether the observed smectic-B phase is in fact a crystal-B phase, characterised by the persistence of three-dimensional positional and bond orientational order at long range, or a hexatic-B phase which is characterised by long ranged bond

orientational order but only short ranged positional ordering. However the diffusion coefficients observed in the smectic phase of de Miguel *et al* [64] indicated a fluid rather than a crystal phase.

More recently Hashim *et al* [69] have performed constant pressure simulations of an originally parameterised Gay-Berne potential in order to investigate the nature of the smectic-B phase in greater detail. In these simulations results analogous to those of constant volume simulations are found. The smectic-B layer normal is found to orient itself along the simulation box diagonal. When it is artificially rotated to be aligned parallel to the simulation box edge it remains there. Smectic-B phases aligned along both of these directions were found to be equivalent. In particular the smectic-B layers are found to have a rippled structure with interdigitation of molecules from one smectic layer into the next as has been observed previously. It is suggested [69] that the tilted smectic-B phase observed by de Miguel *et al* [64] is in fact part of the rippled structure which was unobservable due to the small system size ($N = 256$ compared with $N = 500$ in this latest study). On the question of the type of smectic-B phase, positional correlations between particles in the same smectic layers were found to be weak. Thus the Gay-Berne smectic-B phase is identified as an hexatic-B phase rather than a crystal-B phase, at least with this parameterisation.

Because experiments on mesogens are generally performed under conditions of constant pressure such simulations are amenable to direct comparison with experiment. Indeed Hashim *et al* find reasonable agreement between their simulations and the mesogen 4,4'-dimethoxyazoxybenzene and some other mesogens where a direct comparison was unavailable.

Simulations of a Gay-Berne discogen have been attempted [70]. Using the parameterisation $\sigma_s / \sigma_e = 0.345$, $\varepsilon_s / \varepsilon_e = 1/5$ and $\nu = 2$ and $\mu = 1$. The well depth ratio was selected having been originally reduced from a value $\varepsilon_s / \varepsilon_e = 1/9$ which was assumed to be responsible for the observed formation of cavities within the simulation box. It is quite possible however that the cavities are formed when the system enters a liquid-vapour coexistence region at the given density and temperature. It is therefore also possible that simulations of the Gay-Berne discogen at higher densities would not have yielded such cavities, although the simulation density in this study was chosen to be around the nematic-isotropic transition density for the same shape hard ellipsoids [34], with which comparisons of the Gay-Berne discogen were subsequently made [70]. The Gay-Berne discogen is found to exhibit isotropic, discotic nematic, and two types of columnar phase depending on the density. At $\rho^* = 3.0$ the columnar phase exhibits rectangular symmetry which is suggested to be due to the interdigitated nature of the columns. This view is supported by the fact that at a lower density of $\rho^* = 2.5$ the column arrays are observed to possess the expected hexagonal symmetry.

System size effects on the behaviour of the Gay-Berne fluid have been investigated [65; 71]. In a comparative study of $N = 256$, $N = 500$ and $N = 864$ Gay-Berne particles [65], no appreciable system size dependence was found away from the transition. However results indicated that the transition itself becomes more weakly first order with increasing N . Hysteresis effects were noticeable in this study [65]. For example it was found that the nematic phase could be expanded considerably past the transition point before disordering to the isotropic phase. Conversely, the isotropic phase could be compressed only slightly past the transition to the nematic phase. A reduction in hysteresis effects

at the transition are seen with increasing N . Once again a region of phase space entrapment may have been located. Compression of the nematic phase along the isotherm $T^* = 1.8$ failed to yield any smectic phase, yet simulation along an isochore $\rho^* = 0.38$ does exhibit a stable smectic-B phase at $T^* = 1.8$

A detailed study of the Gay-Berne fluid with the strength parameters $\nu = 3$ and $\mu = 1$ has been undertaken using system sizes of $N = 512$ and $N = 1000$ particles [72]. Interestingly with these larger systems there was practically no hysteresis in contrast to that observed by Chalam *et al* [65]. Comparison of this model with previous Gay-Berne studies indicate that the properties of Gay-Berne particles with the same shape and energy anisotropies are markedly affected by a change in the change parameters ν and μ . Intensive studies, such as the work of Beradi *et al* [72] indicate the lengths of runs and rates of cooling and heating etc., required for even, what is considered to be relatively simple models, to yield accurate data in the vicinity of phase transitions.

As an interesting variation Chalam *et al* [65] have investigated the behaviour of the Gay-Berne fluid confined between two walls. At the wall fluid interface the potential takes the form;

$$V(z, \theta) = AV(z) \left(1 + \frac{B}{A} P_2(\cos\theta) \right), \quad [\text{III.19}]$$

where;

$$V(z) = \varepsilon_w \left(\left(\frac{\sigma_w}{z} \right)^9 - \left(\frac{\sigma_w}{z} \right)^3 \right); \quad [\text{III.20}]$$

$$\varepsilon_w = \left(\frac{10}{3}\right)^{1/2} \pi \varepsilon_0 \rho_s \sigma_0^3. \quad [\text{III.21}]$$

For positive values of the constants A and B the function [III.19] tends to align the particles normal to the wall: homeotropic alignment. The parameters σ_w and ε_w are the usual Lennard-Jones range and strength parameters but here they apply between the wall boundary and a given molecule. The strength parameter is a function of ρ_s which is the number density of molecules at the wall.

Choosing values of $A = B = 1$, the well depth for homeotropic wall alignment was found to be lower than that for side-by-side alignment of Gay-Berne particles. The system, studied via NVT-MD (constant number density, volume and temperature), was equilibrated by studying the constancy of order parameter and density profiles within the pore. It was found that the pore stabilised mesophase formation with respect to the bulk fluid. For example, compression along an isotherm $T^* = 0.65$ yielded isotropic, nematic and smectic phase in the centre of the pore away from the homeotropic alignment found at the walls. In comparison, compression along the same isotherm in the bulk fluid yields the smectic-B phase directly from the isotropic phase. Compression along higher isotherms did not yield any orientationally ordered phases within the pore.

More recently computer simulations have been performed on a chiral-type Gay-Berne model [73]. For reasons of computational simplicity the chiral potential takes the form of an additive term to the normal Gay-Berne model. Thus;

$$V_{\text{chiral GB}} = aV_a(\hat{\mathbf{u}}_1, \hat{\mathbf{u}}_2, \mathbf{r}) + cV_c(\hat{\mathbf{u}}_1, \hat{\mathbf{u}}_2, \mathbf{r}), \quad [\text{III.22}]$$

where $V_a(\hat{\mathbf{u}}_1, \hat{\mathbf{u}}_2, \mathbf{r})$ is the ordinary Gay-Berne model and the additional chiral term is given by;

$$V_c(\hat{\mathbf{u}}_1, \hat{\mathbf{u}}_2, \mathbf{r}) = 4\varepsilon(\hat{\mathbf{u}}_1, \hat{\mathbf{u}}_2, \hat{\mathbf{r}}) \left(\frac{\sigma_0}{r - \sigma(\hat{\mathbf{u}}_1, \hat{\mathbf{u}}_2, \hat{\mathbf{r}}) + \sigma_0} \right)^7 [(\hat{\mathbf{u}}_1 \times \hat{\mathbf{u}}_2) \cdot \hat{\mathbf{r}}](\hat{\mathbf{u}}_1 \cdot \hat{\mathbf{u}}_2). \quad [\text{III.23}]$$

Once again the dependency of the r^{-7} term is chosen to take the same form as the Gay-Berne potential for reasons of computational simplicity. Similar results are obtained for an r^{-11} dependency of $V_c(\hat{\mathbf{u}}_1, \hat{\mathbf{u}}_2, \mathbf{r})$ but it is known that an r^{-7} dependency arises from the multipole expansion of the interaction energy of two chiral molecules. Using the same parameters as Luckhurst *et al* [60] two types of simulation were performed: (a) variation of the chirality parameter along an isotherm $T^* = 1.5$ from $c = 0$ to $c = 2.0$, and (b) a second set of simulations performed by reducing the temperature along an isochiral $c = 0.8$ from $T^* = 3.0$ to $T^* = 0.25$.

The results from (a) indicate a change from the infinitely pitched nematic to a cholesteric phase somewhere in the range $0.6 \leq c \leq 0.7$. On further increasing the chirality parameter a second blue phase resembling BP II [74] occurs in the region $1.0 \leq c \leq 1.1$. With the second set of simulations (b) as the temperature is reduced ordering perpendicular to the director becomes manifest. It should be noted that through positional correlations occurring in $g(r^*)$ the phase is identified as a chiral smectic-A*.

In all chiral phases observed only half the pitch of the helix is formed within the simulation box and the helical axis is always formed parallel to one of the

simulation box faces. These effects are almost certainly due to constraints imposed by the periodic boundary conditions. In an analogous argument to that presented by Luckhurst *et al* [60] for achiral smectic phases, to be commensurate with its periodic images a repeatable part of the helix must occur within the simulation box. This condition is satisfied if;

$$L = n(p/2), \quad \text{[III.24]}$$

where n is an integer and p is the pitch of the helix. As observed by Memmer *et al* [73], this requirement creates a threshold value for the chirality parameter; as soon as the chirality parameter can produce a system that, to a good approximation satisfies [III.24], then a chiral phase may be formed. In order to alleviate these restraints larger systems (here $N = 256$) may be simulated allowing a larger value of n in [III.24]. Alternatively, as suggested for achiral smectic phases, constant pressure simulations may allow the chiral phase to adopt an unrestricted pitch. The use of a special type of twisted simulation cell has also been suggested [75].

Molecular dynamics simulations can provide detailed knowledge of individual particle dynamics which are not normally available from experiments. Indeed this is one of the advantages of MD over the Monte Carlo simulation technique. MD has been used to investigate the single particle translational and rotational dynamics of the Gay-Berne fluid [67]. Particle auto correlation functions take the form;

$$\phi_A(t) = \frac{\langle \mathbf{A}(t_0) \cdot \mathbf{A}(t_0 + t) \rangle}{\langle \mathbf{A}(t_0) \cdot \mathbf{A}(t_0) \rangle}, \quad \text{[III.25]}$$

where $\mathbf{A}(t)$ is a classical dynamical property of molecule i evaluated at time t . The self particle reorientational correlation functions are defined by;

$$\phi_l(t) = \langle P_l(\hat{\mathbf{u}}(t_0) \cdot \hat{\mathbf{u}}(t_0 + t)) \rangle. \quad [\text{III.26}]$$

In [III.26] P_l is a Legendre polynomial of order l and $\hat{\mathbf{u}}(t)$ is the usual unit vector representing the symmetry axis of molecule i . With a given correlation function the associated correlation time is defined by;

$$\tau_A = \int_0^{\infty} \phi_A(t) dt. \quad [\text{III.27}]$$

The main results indicated that the particles undergo diffusion along a cylindrical cage. Further, an increased velocity auto correlation function close to the isotropic-nematic transition is observed as a pre-transitional effect. Diffusion coefficients calculated from auto correlation functions and from the slope of plots of the molecular mean square displacements were found to be in excellent agreement.

In another study only accomplishable using MD, the dynamics of heat flow in nematic liquid crystals has been investigated using a modified version of the Gay-Berne potential; $\nu = 1$ and $\mu = 1$ [76] and in order to reduce to computational effort a WCA-type [56] both prolate and oblate Gay-Berne potentials [77]. The main results are that in the prolate nematic fluid the thermal conductivity along the director is approximately twice that observed perpendicular to the director. For the oblate fluid the reciprocal relationship is observed. These results are in accord with the observation that in the calamitic nematic phase diffusion is

greater along the director, and in the discotic nematic diffusion is observed greatest perpendicular to the director.

It is interesting to note that simulations of the 4 linear Lennard-Jones centres with which Gay and Berne originally parameterised their potential [57] do not exhibit any liquid crystalline phases [see 68]. It is thought that an increase in the axial ratio of linear Lennard-Jones site molecules may encourage liquid crystalline behaviour [68]. However, in order to keep the undulations manifest in the repulsive hard core of these systems to a minimum, this will only be possible with an increase in the number of sites, incurring a corresponding increase in simulation time. Indeed this is found to be the case when a linear model of 11 rigidly joined centres interacting with just the repulsive component of the Lennard-Jones potential is considered [78]. A site-site separation of $\sigma_0/2$ is employed making the model geometry similar to that of a prolate spherocylinder with axial ratio $L/D \approx 5$. Using fixed temperature and pressure MD techniques [78] which allow changes in box geometry as well as volume, a system of $N = 600$ particles is first equilibrated at low temperature which results in a curious herringbone-like orientation of the particles in layers. As the system is gradually heated it is seen to pass through slightly tilted-smectic, nematic and isotropic phases. The observations result from heating the system only. Allowing for the order present in the original configuration it is possible that the system may enter a metastable state from which it cannot escape given the available kinetic energy and length of simulation run using the MD technique. This may occur particularly on heating MD runs: previously orientationally ordered particles must attain sufficient orientational kinetic energy to break free of the potential well they find themselves in. It is likely therefore, that until the requisite energy is available the system will find itself trapped in a metastable

extension of corresponding branch of the equation of state. Such a situation is less likely, although not impossible, to arise in MC simulations. Because there is a finite chance of accepting a move which increases the overall energy of the system, it is possible that given sufficiently long runs a path from the metastable to a lower energy state may eventually be found. It is therefore vital that observations of different phases made by heating a model liquid crystal system are also confirmed by subsequently cooling said system from a well equilibrated isotropic state. In order to explore this possibility a little, the authors did perform one cooling simulation successfully reversing the smectic-nematic transition.

Very recently de Miguel *et al* have performed a series of MD simulations in an attempt to investigate the effect of varying the strength of the attractive interactions for a system of prolate Gay-Berne particles with $\chi = 3$ [85]. The main results indicate that smectic order is favoured at lower densities for high values of the molecular attractive interaction. As χ' is lowered the smectic phase is preempted by an increasingly stable nematic region at lower temperatures. Once again these results emphasise the importance of the role played by attractive forces in stabilising the smectic phase.

Recently two adaptations to generalise the Gay-Berne potential have been suggested. One considers an extension of the Gay-Berne in order to cope with biaxial molecules [80], while the second allows additionally for interactions between heterogeneous uniaxial or biaxial Gay-Berne particles [81]. This latter so called generalised Gay-Berne (GGB) potential has been used in an MD simulation of a bi-disperse liquid crystal mixture of Gay-Berne particles with axial ratios 3·5:1 and 3:1 in the microcanonical ensemble [82]. The results

indicate an extension of the nematic phase range due to the postponement of smectic ordering compared to the single component 3:1 Gay-Berne systems.

Bemrose *et al* [83] further studied the effect of concentration on the phase behaviour of the GGB potential necessarily involving the use of the isothermal-isobaric ensemble because the effective volume of a Gay-Berne particle becomes ambiguous at differing concentrations thus preventing the use of constant volume simulations providing a meaningful density for the Gay-Berne mixture.

Previously a simulation of a two component Gay-Berne mixture has been performed using MC based on Lorentz-Berthelot mixing rules [84]. However the use of this technique for the simulation of mixtures fails to correctly differentiate between all the T-configurations available in the system [82, 83].

These two modifications are of significant importance for the following reasons. Real mesogens are not uniaxial and therefore the inclusion of molecular biaxiality is an essential component in order to gain an accurate understanding of real mesophases. Indeed, in order to investigate the behaviour of biaxial single-site phases it is of course necessary to include a biaxial component in the intermolecular pair potential. Secondly, there is a great deal of interest in the study of mixtures of liquid crystal molecules. Mixtures of different liquid crystals and of liquid crystal forming molecules dissolved in non-liquid crystalline solvents have been shown to alter the range and stability of the nematic-isotropic transition. These effects are of particular technological importance in display technology for example.

It is clear that the Gay-Berne potential has been of great use in simulating liquid crystal phases and dynamical processes. It is anticipated that the above extensions and generalisations will encourage the continued use of the Gay-Berne potential to further our understanding of mesogenic systems.

III.5 Lattice Models

Some simulations of the orientational ordering in liquid crystals have been performed on particles whose centres of mass are restricted to lie on a lattice. These simulations, although missing an essential element that characterises liquid crystals, that is the fact that liquid crystal mesophases are fluid, have provided valuable insight into the effects of long ranged attractive dispersion forces in the formation of nematics. Because of their relative computational simplicity lattice models consisting of a large number of particles are possible, yielding detailed information about orientational phase transitions, which are directly comparable with theory [86]. Here though we shall just provide an introduction to lattice models. Lebwohl and Lasher [87, 88] performed MC simulations on a simple cubic lattice of rod-like particles interacting via the following orientational pair potential;

$$V_{ij_{L-L}} = -\varepsilon_{ij_{L-L}} P_2(\cos\beta_{ij}), \quad [\text{III.28}]$$

where β_{ij} is the angle between the principle symmetry axes of particles i and j , and $\varepsilon_{ij_{L-L}} > 0$ if the particles are nearest neighbours, otherwise $\varepsilon_{ij_{L-L}} = 0$. In a first investigation Lasher investigated this model whereby the particle symmetry axes had a distribution restricted to 12 directions distributed symmetrically over a sphere [87], the results indicating that a first order phase transition occurs for this system. A later investigation allowed the particle symmetry axes a full spherical

distribution [88]. In this latter work a first order phase transition was identified as well. However there were found to be significant differences between both lattice models. For example, the spontaneous order at the transition was found to be almost two-and-a-half times greater in the model with restricted orientational freedom. Additionally, the transition temperature of the non-restricted model was found to be higher than that of the original.

The Lebwohl-Lasher model has also been investigated by other workers [89, 90, 91]. In particular it has been used in an investigation of thin liquid crystal films [92] indicating a critical layer thickness below which no transition is observed.

Luckhurst [93] has examined the Lebwohl-Lasher model in detail using a cubic lattice of 20x20x20 particles, comparing the results with those simulations undertaken previously. A detailed study using a larger 30x30x30 has been performed concentrating in the region of the nematic-isotropic phase transition [94], accurately locating the transition temperature.

III.6 Realistic Models

Hard and soft potential models have been useful in furthering our understanding of the formation of liquid crystal phases. However, because of their relative simplicity they cannot hope to model the molecular subtleties of a real liquid crystal. These are known to be important in the formation and stabilisation of liquid crystal mesophases. Taking the hexa-*n*-alkoxybenzoates of triphenylene as an example, it is found that the presence of the alkyl chains are essential to the formation of a discotic-nematic phase, and the length of the alkyl chains is found to effect the transition temperature [95]. More recently it has been demonstrated

that if the benzoate groups are methylated, then the phase behaviour is found to be critically dependent on the position of methylation [96].

In performing simulations of realistic mesogens it is hoped that such molecular intricacies may be incorporated into a liquid crystal model. It would be very beneficial to be able to include such things as molecular shape and flexibility, electronic charge distribution responsible for electrostatic multipole interactions and molecular polarisability anisotropy: all considered to influence the formation of mesophases [36]. Such a model would prove to be extremely useful in molecular engineering applications, having the ability to predict appropriate phase properties before the molecule is even synthesised. Furthermore, a model from which the above features could be successfully decoupled could be used in a systematic investigation into their relative influence. Further realistic models provide a simultaneous simulation of both the molecular and phase structure [97].

Nevertheless, because of the inherent complexity of realistic models, say for example, site-site models based on the Lennard-Jones 12-6 potential, there have not been many simulations using these models performed to date. This is because of the immense amount of CPU time required to solve the models.

Presently this rather unfortunate situation notwithstanding there have been attempts at a preliminary survey in this area. A first foray by Picken *et al* [98] investigated the effects of including a point molecular charge distribution over the cyanobiphenyl group of 4-*n*-pentyl-4'-cyanobiphenyl (5CB). MD simulations of realistic 19-site united atom model with and without the partial charges, obtained from *ab initio* calculations were compared. Only $N = 64$ molecules of 5CB could be studied, however the authors believed that within the limited time

scale available they were able to qualitatively predict the influence of the resulting dipole moment.

The nematogen 5CB has been simulated more recently using the united atom approach and using a full atom-atom model explicitly including the hydrogen atoms [99]. Despite an incorrect prediction of the experimental torsion angle distribution of the phenyl rings, the results of the united atom model compared favourably with those where all atoms were considered explicitly. Analysis of the results of these 5CB simulations has been provided in part by the calculation and visualisation of two-dimensional distribution functions [100]. These so called cylindrical distribution functions may be appropriate for visualising pair distributions in the nematic phase, but they should be interpreted cautiously when used to investigate phases that do not possess cylindrical symmetry.

More notably Wilson and Allen have performed a simulation of the nematogen *trans*-4-(*trans*-4-*n*-pentylcyclohexyl)cyclohexylcarbonitrile (CCH5) using a 19-site combined atom model. The sites were located at the centres of mass of the carbon and nitrogen atoms obtained from the crystal structure data. Associated with each site is the following potential energy function;

$$E_{\text{total}} = \sum_{\text{bonds}} K_r (r - r_{eq})^2 + \sum_{\text{angles}} K_\theta (\theta - \theta_{eq})^2 + \sum_{\text{dihedrals}} \frac{V_n}{2} (1 + \cos(n\phi - \gamma)) + \sum_{i < j} \left(\frac{q_i q_j}{R_{ij}} + \frac{A_{ij}}{R_{ij}^{12}} - \frac{C_{ij}}{R_{ij}^6} \right). \quad [\text{III.29}]$$

In equation [III.29] the first three terms have force constants K_r , K_θ and V_n associated with bond stretching, bond bending and bond twisting respectively. Bond lengths are represented by r , bond bending angles by θ , and in the torsional

term ϕ represents the dihedral angle with the parameters n and γ being defined by the valency of the bonded atoms. Often due to the high frequency nature of bond vibrations, constraints removing velocity components in the direction of bonds are applied. A typical method is by use of the SHAKE algorithm [101]. The last term incorporates the non-bonded interactions between individual sites: A_{ij} and C_{ij} incorporate the Lennard-Jones constants ϵ_{0ij} and σ_{0ij} , (specifically $A_{ij} = 4\epsilon_{0ij}\sigma_{0ij}^{12}$ and $C_{ij} = 4\epsilon_{0ij}\sigma_{0ij}^6$) where in the case of interaction between two different species the Lorentz-Berthelot mixing rules (see chapter V) [5] may be used to calculate appropriate values of ϵ_{0ij} and σ_{0ij} , the q_i refer to partial charges on the specific (combined) atoms i and j . Expression [III.29] is typical of the type of force fields used to represent realistic mesogens.

Initial simulations showed that a system of 64 and 128 molecules exhibit a stable nematic phase [102]. However only three state points could be simulated with the given resources and so the results are somewhat tentative. Using a technique whereby each molecule was ascribed a spheroid constructed from principle components of the diagonalised moment of inertia tensor it was found that in the nematic phase the molecules were elongated in shape compared to those in the corresponding isotropic phase. Furthermore it was also possible to examine the CCH5 molecular conformation in the different phases simulated. Analysis of the dihedral angles in the alkyl chain of CCH5 found a preference for an all *trans* conformation in the nematic phase, thus stretching the molecule out along the principle symmetry axis [103].

A realistic study of the liquid crystal 4-ethoxybenzylidene-4'-*n*-butylaniline (EBBA) has also been carried out by Komolkin *et al* [97]. In this work the authors identified minimum energy conformations of EBBA using a similar atom-

atom potential as equation [III.29] but neglecting any electrostatic terms. These comprised 72 conformers to which an additional 120 higher energy conformers were added, resulting in a set of 192 possible molecular conformations. The simulation was performed on 60 EBBA molecules using Metropolis MC. Here a single MC step consisted of varying the molecular centres of gravity, the molecular orientation vectors (represented here as Euler angles), the box volume and the conformer of the molecule under consideration.

As with the work of Allen and Wilson co-operative effects between conformers of the nematic phase were identified. However it appears that only one state point was studied. This had an initial order parameter $\langle P_2 \rangle \sim 0.3$ which was found to settle at an equilibrated value of $\langle P_2 \rangle = 0.68$; certainly indicative of nematic-like orientational ordering. Evidence of molecular biaxial ordering was also sought but was not found. The simulation box edge was found not to change significantly from its initial value thus implying no change in the system density. This is hardly surprising because the system was started so close to the nematic phase anyway.

Because of the complexity of realistic models and the associated resources necessary to solve them, some workers have taken to simulating semi-realistic models. In these, certain structural elements of a mesogen may be represented as a single interaction site in the model, similar to the united-atom approach already in widespread use. For example Cross and Fung [104] have used this approach in a simulation of the mesogen 5CB. A pseudo potential which retains the important aspects of the structural anisotropy is substituted for the real atom-atom potential. Specifically the benzene rings of 5CB are treated as extended spherical atoms. Such a treatment is justified through the rapid rotation of the

two-fold biphenyl axis at temperatures typical of mesophase formation. The realistic models using the united atom approach has 19 individual sites. Use of the pseudo potential reduces this to only 9 sites, with a corresponding saving in computation effort: the pseudo potential model is found to be four times quicker than the realistic model. Even so in this study the system size was restricted to $N = 80$ molecules. Comparison between the two models validates the use of the pseudo potential approach for simulating realistic mesogens.

The use of realistic models allows for a detailed examination of the behaviour of the individual mesogen constituents, i.e. the rigid core, flexible spacer, alkyl chain etc. Indeed detailed studies of the conformation of 4-*n*-octyl-4'-cyanobiphenyl adsorbed on to graphite have been possible [105, 106]. It is found that there is a significant difference in the behaviour of adsorbed monolayers compared to the bulk liquid crystal phase. Models of liquid crystals adsorbed on to substrates could prove technologically very useful as many display devices rely on fixing the director orientation through surface treatments of the substrate. It is obvious though that only a detailed atomistic model will suffice in these cases.

III.7 Summary

We have seen that a variety of different models have been used in computer experiments of liquid crystal phases. Lattice simulations, although unrealistic, provide a valuable comparison with available lattice theories. However, perhaps it is the results of hard particle models that have led to the greatest surprises, for example, showing that smectic phases can be formed through excluded volume effects alone. Yet, on the other hand, it is the long range attractive forces of the soft single site models that are responsible for stabilising the smectic phase of the Gay-Berne fluid, for example. Single site hard and soft particle models have

provided a useful contrasting rôle in this respect. Extensions to multisite models may prove fruitful but it is clear, though, that in order to model accurately the subtleties of mesogenic molecules realistic models will have to be adopted. At present the simulation of a few realistic models is just possible. In the meantime continued development and extension of single site models appears to be a profitable alternative in furthering our understanding of liquid crystal phases.

III.8 References

- [1] Metropolis, N., Rosenbluth, A. W., Rosenbluth, M. N., Teller, A. H., and Teller, E., 1953, *Journal of Chemical Physics*, **21**, 1087-1092.
- [2] Metropolis, N., and Ulam, S., 1949, *Journal of the American Statistical Association*, **44**, 335-41.
- [3] Rosenbluth, M. N., and Rosenbluth, A. W., 1954, *Journal of Chemical Physics*, **22**, 881-884.
- [4] Alder, B. J., and Wainwright, T. E., 1957, *Journal of Chemical Physics*, **27**, 1208-1209; 1959, *Ibid*, **31**, 459-466.
- [5] Allen, M. P., and Tildesley, D.J., 1987, *Computer Simulation of Liquids* (Oxford, UK: Clarendon Press).
- [6] Ciccotti, G., Frenkel, D., and McDonald, I. R., 1987, *Simulations of Liquids and Solids* (Amsterdam: Elsevier Science Publishers B.V.).
- [7] Vieillard-Baron, J., 1972, *Journal of Chemical Physics*, **56**, 4729-4744.
- [8] De Luca, M. D., Neal, M. P., and Care, C. M., 1994, *Liquid Crystals*, **16**, 257-266; Neal, M.P., De Luca, M. D., and Care, C. M., 1995, *Molecular Simulation*, **14**, 245-258.
- [9] Onsager, L., 1949, *Annals of the New York Academy of Sciences*, **51**, 627-659.
- [10] Isihara, A., 1951, *Journal of Chemical Physics*, **19**, 1142-1147.
- [11] Zwanzig, R., 1963, *Journal of Chemical Physics*, **39**, 1714-1721.
- [12] Maier, Von, W., and Saupe, A., 1958, *Zeitschrift für Naturforschung*, **13a**, 564-566; 1959, *Ibid.*, **14a**, 882-889; 1960, *Ibid.*, **15a**, 287-292.
- [13] Luckhurst, G. R., 1979, *Molecular Field Theories of Nematics*, in *The Molecular Physics of Liquid Crystals*, edited by Luckhurst, G. R., and Gray, G. W., (Academic Press, London, UK).
- [14] Luckhurst, G. R., and Zannoni, C., 1977, *Nature*, **267**, 412-414.

- [15] Andersen, H. C., Chandler, D., and Weeks, J. D., 1976, *Advances in Chemical Physics*, **34** 105- 156.
- [16] Veerman, J. A. C., and Frenkel, D., 1990, *Physical Review A*, **41**, 3237-3244.
- [17] Frenkel, D., and Eppenga, R., 1982, *Physical Review Letters*, **49**, 1089-1092.
- [18] Kayser, R. F., and Raveché, 1978, *Physical Review A*, **17**, 2067-2071.
- [19] Widom, B., 1963, *Journal of Chemical Physics*, **39**, 2808-2812.
- [20] Vieillard-Baron, J., 1974, *Molecular Physics*, **28**, 809-818.
- [21] Wood, W. W., and Parker, F. R., 1957, *Journal of Chemical Physics*, **27**, 720-733.
- [22] Veerman, J. A. C., and Frenkel, D., 1989, *Physica A*, **156**, 599-612.
- [23] Stroobants, A., Lekkerkerker, H. N. W., and Frenkel, D., 1986, *Physical Review Letters*, **57**, 1452-1455.
- [24] Stroobants, A., Lekkerkerker, H. N. W., and Frenkel, D., 1987, *Physical Review*, **A36**, 2929-2944.
- [25] Frenkel, D., 1991, *Lecture Notes On: Free Energy Calculations in Computer Simulation in Materials Science*, edited by Meyer, M., and Pontikis, V., (Kluwer Academic Publishers, Netherlands).
- [26] Frenkel, D., and Mulder, B. M., 1985, *Molecular Physics*, **55**, 1171-1192; 1985, *Ibid*, **58**, 219.
- [27] McMillan, W. L., 1971, *Physical Review*, **A4**, 1239-1246.
- [28] Hoover, W. G., and Ree, F. H., 1968, *Journal of Chemical Physics*, **49**, 3609-3617.
- [29] Frenkel, D., 1989, *Liquid Crystals*, **5**, 929-940.
- [30] Veerman, J. A. C., and Frenkel, D., 1992, *Physical Review A*, **45**, 5632-5648.
- [31] Frenkel, D., Mulder, B. M., and McTaque, J. P., 1984, *Physical Review Letters*, **52**, 287-290; 1985, *Molecular Crystals and Liquid Crystals*, **123**, 119-128.
- [32] Perram, J. W., Wertheim, M. S., Lebowitz, J. L., and Williams, G. O., 1984, *Chemical Physics Letters*, **105**, 277-280.
- [33] Perram, J. W., and Wertheim, M. S., 1985, *Journal of Computational Physics*, **58**, 409-416.
- [34] Frenkel, D., 1987, *Molecular Physics*, **60**, 1-20; 1988, *Ibid*, **65**, 493.
- [35] Frenkel, D., 1985, *Molecular Physics*, **54**, 145-148.

- [36] Allen, M. P., and Wilson, M. R., 1989, *Journal of Computer-Aided Molecular Design*, **3**, 335-353.
- [37] Zarragoicoechea, G. J., Levesque, D., and Weis, J. J., 1991, *Molecular Physics*, **74**, 629-637.
- [38] Zarragoicoechea, G. J., Levesque, D., and Weis, J. J., 1992, *Molecular Physics*, **75**, 989-998.
- [39] Allen, M. P., 1983, *Philosophical Transactions of the Royal Society, London A*, **344**, 323-337.
- [40] Allen, M. P., and Frenkel, D., 1987, *Physical Review Letters*, **58**, 1748-1750.
- [41] Bereolos, P., Talbot, J., Allen, M. P., and Evans, G., T., 1993, *Journal of Chemical Physics*, **99**, 6087-6097.
- [42] Allen, M. P., 1990, *Liquid Crystals*, **8**, 499-511.
- [43] Whittle, M., and Masters, A. J., 1991, *Molecular Physics*, **72**, 247-265.
- [44] Archer, A. L., and Jackson, G., 1991, *Molecular Physics*, **73**, 881-896.
- [45] Amos, M. D., and Jackson, G., 1991, *Molecular Physics*, **74**, 191-210.
- [46] Wilson, M. R., and Allen, M. P., 1993, *Molecular Physics*, **80**, 277-295.
- [47] Wilson, M. R., 1994, *Molecular Physics*, **81**, 675-690.
- [48] Wilson, M. R., 1995, *Molecular Physics*, **85**, 193-205.
- [49] Nicklas, K., Bopp, P., and Brickmann, J., 1994, *Journal of Chemical Physics*, **101**, 3157-3171.
- [50] Alinger, N. L., 1977, *Journal of the American Chemical Society*, **99**, 8127-8134.
- [51] Corner, J., 1948, *Proceedings of the Royal Society, London*, **A192**, 275-292.
- [52] Luckhurst, G. R., and Romano, S., *Molecular Physics*, **40**, 129-139.
- [53] Kushick, J., and Berne B. J., 1976, *Journal of Chemical Physics*, **64**, 1362-1367.
- [54] Berne, B. J., and Pechukas, P., 1972, *Journal of Chemical Physics*, **56**, 4213-4216.
- [55] Tsykalo, A. L., and Bagmet, A. D., 1978, *Molecular Crystals and Liquid Crystals*, **46**, 111-119.
- [56] Weeks, J. D., Chandler, D., and Andersen, H. C., 1971, *Journal of Chemical Physics*, **54**, 5237-5247.
- [57] Gay, J. G., and Berne, B. J., 1981, *Journal of Chemical Physics*, **74**, 3316- 3319.

- [58] Decoster, D., Constant, E., and Constant, M., 1983, *Molecular Crystals and Liquid Crystals*, **97**, 263-276.
- [59] Adams, D. J., Luckhurst, G. R., and Phippen, R. W., 1987, *Molecular Physics*, **61**, 1575-1580.
- [60] Luckhurst, G. R., Stephens, R. A., and Phippen, R. W., 1990, *Liquid Crystals*, **8**, 451-464.
- [61] de Miguel, E., Rull, L. F., Chalam, M. K., and Gubbins, K. E., 1990, *Molecular Physics*, **71**, 1223-1231.
- [62] de Miguel, E., Rull, L. F., and Gubbins, K. E., 1991, *Physica A*, **177**, 174-181.
- [63] de Miguel, E., Rull, L. F., Chalam, M. K., Gubbins, K. E., and Van Swol, F., 1991, *Molecular Physics*, **72**, 593-605.
- [64] de Miguel, E., Rull, L. F., Chalam, M. K., and Gubbins, K. E., 1991, *Molecular Physics*, **74**, 405-424.
- [65] Chalam, M. K., Gubbins, K. E., de Miguel, E., and Rull, L. F., 1991, *Molecular Simulation*, **7**, 357-385.
- [67] de Miguel, E., Rull, L. F., and Gubbins, K. E., 1992, *Physical Review*, **A45**, 3813-3822.
- [68] Luckhurst, G. R., and Simmonds, P. S. J., 1993, *Molecular Physics*, **80**, 233-252.
- [69] Hashim, R., Luckhurst, G. R., and Romano, S., 1995, *Journal of the Chemistry Society Faraday Transactions*, **91**, 2141-2148.
- [70] Emerson, A. P. J., Luckhurst, G. R., and Whatling, S. G., 1994, *Molecular Physics*, **82**, 113-124.
- [71] de Miguel, E., 1993, *Physical Review E*, **47**, 3334-3342.
- [72] Berardi, R., Emerson, A. P. J., and Zannoni, C., 1993, *Journal of the Chemical Society Faraday Transactions*, **89**, 4069-4078.
- [73] Memmer, R., Kuball, H.-G., and Schönhofer, A., 1993, *Liquid Crystals*, **15**, 345-360.
- [74] de Gennes, P. G., and Prost, J., 1994, *The Physics of Liquid Crystals* (Clarendon Press, Oxford, UK).
- [75] Yoneya, M., and Berendsen, H. J. C., 1994, *Journal of the Physical Society of Japan*, **63**, 1025-1030.
- [76] Sarman, S., and Evans, D. J., 1993, *Journal of Chemical Physics*, **99**, 620-627.
- [77] Sarman, S., 1994, *Journal of Chemical Physics*, **101**, 480-489.

- [78] Paolini, G. V., Ciccotti, G., and Ferrario, M., 1993, *Molecular Physics*, **80**, 297-312.
- [79] Nosé, S., 1984, *Molecular Physics*, **52**, 255-268; Parrinello, M., and Rahman, A., 1981, *Journal of Applied Physics*, **52**, 7182-7190.
- [80] Berardi, R., Fava, C., and Zannoni, C., 1995, *Chemical Physics Letters*, **236**, 462-468.
- [81] Cleaver, D. J., Care, C. M., Allen, M. P., and Neal, M. P., 1995, *Physical Review E*, **54**, 559-567.
- [82] Bemrose, R. A., Care, C. M., Cleaver, D. J., and Neal, M. P., 1996, *Molecular Physics*, **90**, 625-635.
- [83] Bemrose, R. A., Care, C. M., Cleaver, D. J., and Neal, M. P., 1996, *Submitted to Molecular Crystals and Liquid Crystals*.
- [84] Lukac, R., and Vesely, F. J., 1995, *Molecular Crystals and Liquid Crystals*, **262**, 533-541.
- [85] de Miguel, E., Martin del Rio, E., Brown, J. T., and Allen, M. P., 1996, *Journal of Chemical Physics*, **105**, 4234-4249.
- [86] Allen, M. P., *Molecular Physics*, **68**, 181-189.
- [87] Lasher, G., 1972, *Physical Review*, **A5**, 1350-1354
- [88] Lebwohl, P. A., and Lasher, G., 1972, *Physical Review A*, **6**, 426-429; 1973, *Ibid*, **7**, 2222.
- [89] Jansen, H. J. F., Vertogen, G., and Ypma, J. G. J., 1977, *Molecular Crystals and Liquid Crystals*, **38**, 87-93.
- [90] Zannoni, C., and Guerra, M., 1981, *Molecular Physics*, **44**, 849-869.
- [91] Zhang, Z., Zuckermann, M. J., and Mouritsen, O. G., 1993, *Molecular Physics*, **80**, 1195-1221.
- [92] Cleaver, D. J., and Allen, M. P., 1993, *Molecular Physics*, **80**, 253-276.
- [93] Luckhurst, G. R., and Simpson, P., 1982, *Molecular Physics*, **47**, 251-265.
- [94] Fabbri, U., and Zannoni, C., 1986, *Molecular Physics*, **58**, 763-788.
- [95] Chandrasekhar, S., 1983, *Philisophical Transactions of The Royal Society, London*, **A309**, 93-103.
- [96] Phillips, T. C., Jones, J. C., and McDonnell, D. G., 1993, *Liquid Crystals*, **15**, 203-215
- [97] Komolkin, A. V., Molchanov, YU. V., and Yakutseni, P. P., 1989, *Liquid Crystals*, **6**, 39-45.
- [98] Picken, S. J., Van Gunsteren, W. F., Van Duijnen, P. Th., and De Jeu, W. H., 1989, *Liquid Crystals*, **6**, 357-371.

- [99] Komolkin, A. V., Laaksonen, A., and Maliniak, A., 1994, *Journal of Chemical Physics*, **101**, 4103-4116.
- [100] Komolkin, A. V., Maliniak, A., 1995, *Molecular Physics*, **84**, 1227-1238.
- [101] Ryckaert, J. P., Ciccotti, G., and Berendsen, H. J. C., 1977, *Journal of Computational Physics*, **23**, 327-341.
- [102] Wilson, M. A., and Allen, M. P., 1991, *Molecular Crystals and Liquid Crystals*, **198**, 465-477.
- [103] Wilson, M. A., and Allen, M. P., 1992, *Liquid Crystals*, **12**, 157-176.
- [104] Cross, C. W., and Fung, B. M., 1994, *Journal of Chemical Physics*, **101**, 6839-6848.
- [105] Cleaver, D. J., and Tildesley, D. J., 1994, *Molecular Physics*, **81**, 781-799.
- [106] Yoneya, M., and Iwakabe, Y., 1995, *Liquid Crystals*, **18**, 45-49.

CHAPTER IV

MOLECULAR DYNAMICS SIMULATIONS OF CALAMITIC AND DISCOTIC SINGLE-SITE HYBRID GAY-BERNE LUCKHURST- ROMANO POTENTIAL

IV.1 Introduction

The hybrid Gay-Berne Luckhurst-Romano (HGBLR) potential allows us to model both disc-like and rod-like interactions with comparative ease. The anisotropy in the attractive part of the HGBLR potential is determined by the anisotropy parameter χ' . By varying χ' , we have used molecular dynamics (MD) to simulate single HGBLR centres, parameterised to represent (a) disc-like and (b) rod-like interactions. The simulations were undertaken as a preliminary investigation of the properties of the HGBLR particles. Of particular interest was whether single-site HGBLR centres were capable of exhibiting mesogenic behaviour. Similar simulations were run on both systems in order to facilitate a ready comparison of disc-like and rod-like parameterised HGBLR centres. If single-site HGBLR particles are found to exhibit liquid crystalline behaviour, then the use of HGBLR centres in multisite models could prove very promising as models for simple liquid crystals.

It is found that despite the spherical hard core of the HGBLR centres, the anisotropic attractive region of the potential is sufficient to form a variety of mesophases. In this chapter therefore, we present details of the simulations of calamitic and discotic single-site HGBLR centres. Emphasis is placed upon structural features of the mesophases formed, rather than on extracting

thermodynamic information from the simulations. A brief summary of characteristics of the observed mesophases of each system is provided after a presentation of the simulation results. Finally we compare and contrast the calamitic and discotic systems highlighting their differences and similarities.

IV.2 Parameterisation of a single HGBLR centre

The HGBLR potential has a spherical hard core for a given fixed orientation of a pair of HGBLR centres with respect to their site symmetry vectors: the radius of the spherical hard core depending on the relative orientation of site symmetry vectors. Hard spheres do not of course exhibit liquid crystalline properties. In this respect therefore, single site HGBLR centres ignore the significant shape anisotropy of real liquid crystal molecules. The dispersive anisotropy in the potential is created by part of the Gay-Berne type energy scaling function $\varepsilon_2(\hat{\mathbf{u}}_1, \hat{\mathbf{u}}_2, \hat{\mathbf{r}})$ [1]. This function is dependent on the relative orientation of a pair of HGBLR centres with respect to the intermolecular vector joining their centres (see figure IV.1). Thus for constant relative orientation of two HGBLR site symmetry vectors $\hat{\mathbf{u}}_1$ and $\hat{\mathbf{u}}_2$ the angles θ_i of figure IV.1, can take all values in the range $0^\circ \rightarrow 360^\circ$. The ratio of end-end:side-side strength interactions $\varepsilon_e / \varepsilon_s$ determines χ' thus:

$$\chi' = (1 - \varepsilon_e / \varepsilon_s) / (1 + \varepsilon_e / \varepsilon_s) \quad \text{[IV.1]}$$

We have parameterised the HGBLR centres as (a) disc-like particles which favour interaction with the site symmetry vectors aligned end-end using a value $\varepsilon_e / \varepsilon_s = 5$ (i.e. the end-end interaction is five times as strong as the side-side interaction), and (b) as a system of rod-like particles with $\varepsilon_e / \varepsilon_s = 0.2$. These values were chosen after studies of Gay-Berne particles with these same $\varepsilon_e / \varepsilon_s$

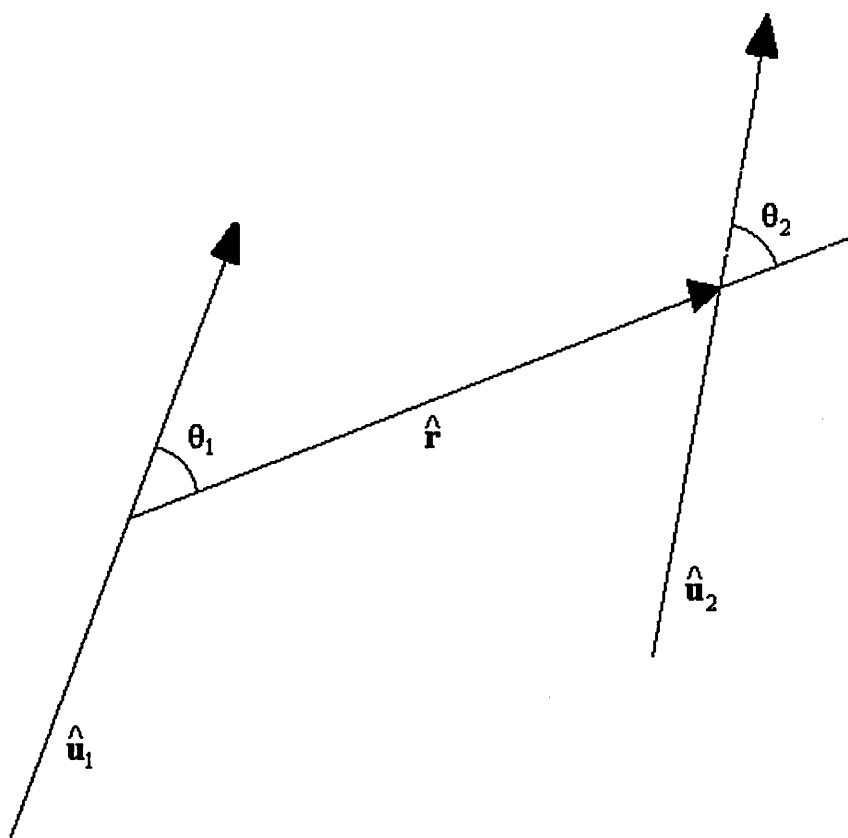


Figure IV.1

A schematic diagram illustrating the construction of the intermolecular vector between two site symmetry vectors of the HGBLR potential.

were shown to exhibit calamitic and discotic mesophases [2, 3]. For preliminary studies in both cases a value of $\lambda=0.15$, determined from earlier work with the Luckhurst-Romano potential was used [4].

Table IV.1 shows the values the function $\varepsilon_2(\hat{\mathbf{u}}_1, \hat{\mathbf{u}}_2, \hat{\mathbf{r}})$ takes for a few selected orientations. Clearly we can see that the energy scaling part of the Gay-Berne potential distinguishes between end-end and side-side interactions. Interestingly we note that the function $\varepsilon_2(\hat{\mathbf{u}}_1, \hat{\mathbf{u}}_2, \hat{\mathbf{r}})$ does not itself differentiate between side-side and X interactions. The HGBLR potential does discriminate between all four chosen idealised configurations as shown in figures IV.2 and IV.3 which illustrate the distance dependence of the HGBLR potential when parameterised with disc-like and rod-like interactions respectively. The distinction between side-side and X configurations now obtains because of the $\hat{\mathbf{u}}_1 \cdot \hat{\mathbf{u}}_2$ dependence of the Legendre P_2 term in the Luckhurst-Romano potential. It is not sufficient therefore, to merely scale a Lennard-Jones potential by $\varepsilon_2(\hat{\mathbf{u}}_1, \hat{\mathbf{u}}_2, \hat{\mathbf{r}})$ as dependence on the relative orientation of the intermolecular vector with respect to the site symmetry vector is clearly not enough to differentiate between the four chosen side-side, end-end, X and T configurations.

Examination of figures IV.2 and IV.3 shows that the HGBLR potential clearly distinguishes between rod-like and disc-like interactions. We note that in figure IV.3, the energy well depth minimum for the most favoured configuration is only 1/5 that for the most favoured end-end configuration of the disc like parameterisation, figure IV.2. This effect can also be seen in table IV.1, after taking account of the fact that the most favoured orientations, side-side and end-end are exchanged. Thus we would expect mesophases exhibited by the disc-like HGBLR centres to be more stable at higher temperatures than those formed from

Configuration	$\hat{\mathbf{u}}_1 \cdot \hat{\mathbf{u}}_2$	$\varepsilon_2(\hat{\mathbf{u}}_1, \hat{\mathbf{u}}_2, \hat{\mathbf{r}})$	$\varepsilon_e / \varepsilon_s = 5$	$\varepsilon_e / \varepsilon_s = 0.2$
end-end	1	$\varepsilon_e / \varepsilon_s$	5.0	0.2
side-side	1	1	1.0	1.0
X	0	1	1.0	1.0
T	0	$2 / (1 + \varepsilon_e / \varepsilon_s)$	5.0/3.0	1.0/3.0

Table IV.1

Values of the function $\varepsilon_2(\hat{\mathbf{u}}_1, \hat{\mathbf{u}}_2, \hat{\mathbf{r}})$ for a few selected orientations of HGBLR centres parameterised as disc-like ($\varepsilon_e / \varepsilon_s = 5$) and rod-like ($\varepsilon_e / \varepsilon_s = 0.2$). The angle between the two site symmetry vectors of HGBLR particles is represented by the dot product $\hat{\mathbf{u}}_1 \cdot \hat{\mathbf{u}}_2$. Explicit values for the two parameterizations are given in the final two columns.

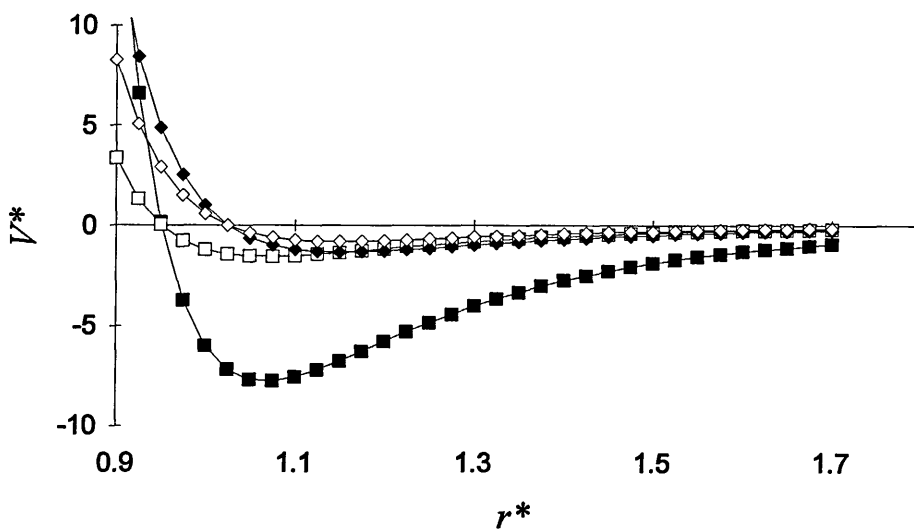


Figure IV.2

Distance dependence of the disc-like HGBLR potential parameterised with $\epsilon_e / \epsilon_s = 5$ and $\lambda = 0.15$. The Lennard-Jones parameters σ_0 and ϵ_0 take the value unity. Symbols: closed squares, end-end; open squares, side-side; closed diamonds, T-configuration; open diamonds, X-configuration.

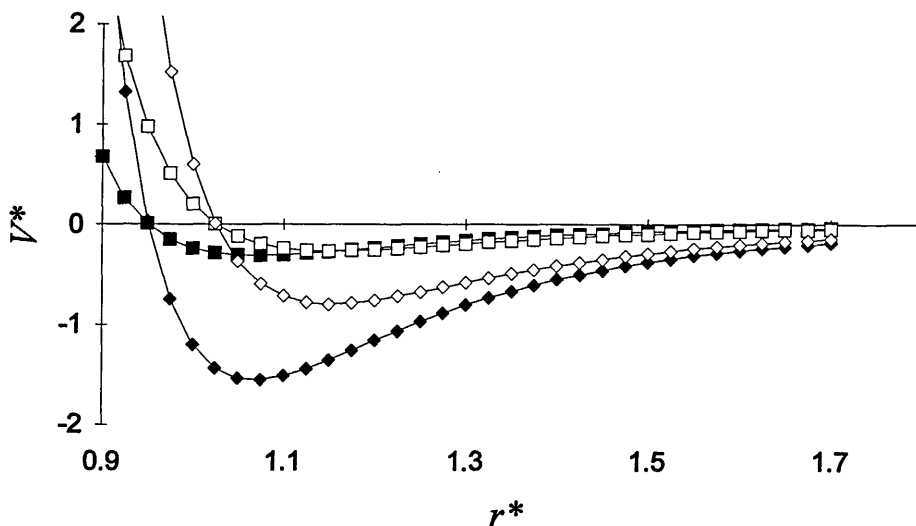


Figure IV.3

Distance dependence of the rod-like HGBLR potential. The parameters are as above (figure IV.2) but $\epsilon_e / \epsilon_s = 0.2$. Symbols: closed squares, end-end; open squares, T-configuration; closed diamonds, side-side; open diamonds, X-configuration.

rod-like parameterised centres. Further, the minimum of the potential energy occurs at the same separation in both cases. Changing the parameterisation through changing χ' , does not alter the position of the minimum well depth. Clearly this is the case as $\varepsilon_2(\hat{\mathbf{u}}_1, \hat{\mathbf{u}}_2, \hat{\mathbf{r}})$ is not a function dependent on the intermolecular separation r .

Figures IV.4 and IV.5, show energy contour plots for a pair of HGBLR centres, one rotated around the other in the same plane with site symmetry vectors constrained to be parallel. The inner most contour in each case represents the hard core of the molecule: defined at $r = \sigma_0$. This is spherical for constant relative orientation of the $\hat{\mathbf{u}}_i$. Clearly the surrounding attractive region is anisotropic. For the disc-like parameterised HGBLR particle the deepest well depths occur above and below the site centre along the direction of the site symmetry vector. Figure IV.5, shows that the rod-like parameterised centre has a deep well outside the hard core region around the site symmetry vector. Figure IV.6 and figure IV.7 further show the HGBLR sites presented in a topographical form depicting the potential energy surface in isometric projection.

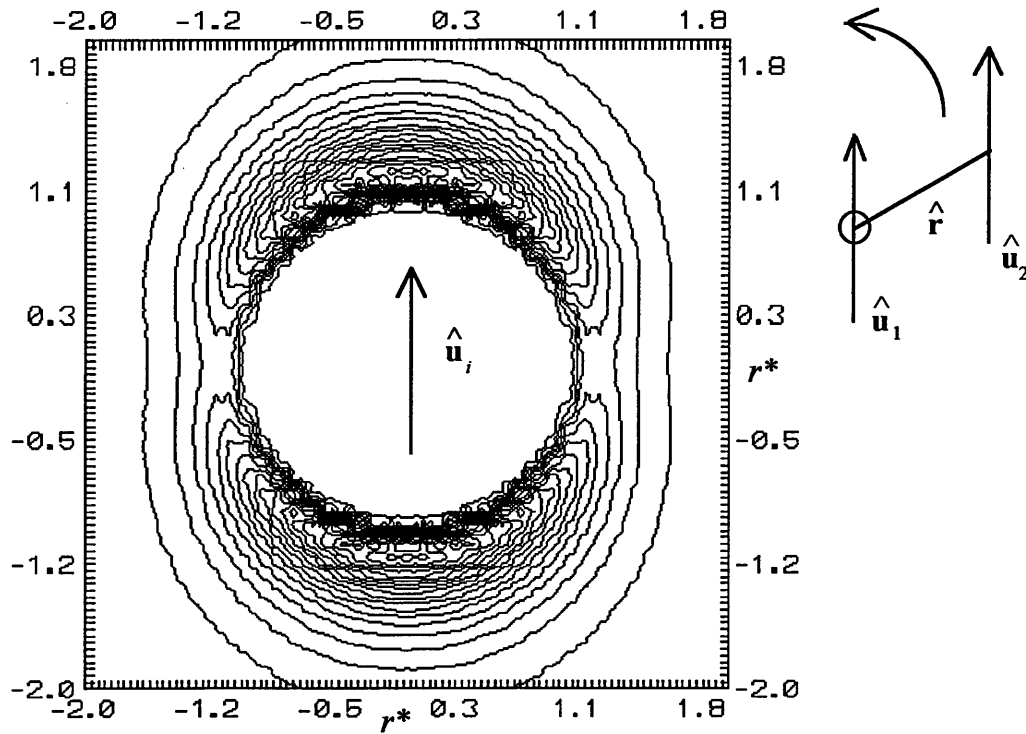


Figure IV.4

A two dimensional representation of the field of potential energy between a pair of disc-like HGBLR centres orientated as in the small schematic diagram. The centre with symmetry vector \hat{u}_1 is fixed at the origin, while the second centre is rotated around the first on the same plane: the plane of the paper. The \hat{u}_i remain constant and only the $\hat{r} \cdot \hat{u}_i$ and the intermolecular separation r^* are allowed to vary. The potential energy has been truncated at $V^* = 0$. The contours are plotted at intervals of $V^* = 0.2$. The spherical hard core extending to a radius $\sigma_0 = 1$ is clearly visible. The other parameters are $\epsilon_0 = 1$, $\chi' = -2/3$ corresponding to $\epsilon_e / \epsilon_s = 5$, and $\lambda = 0.15$.

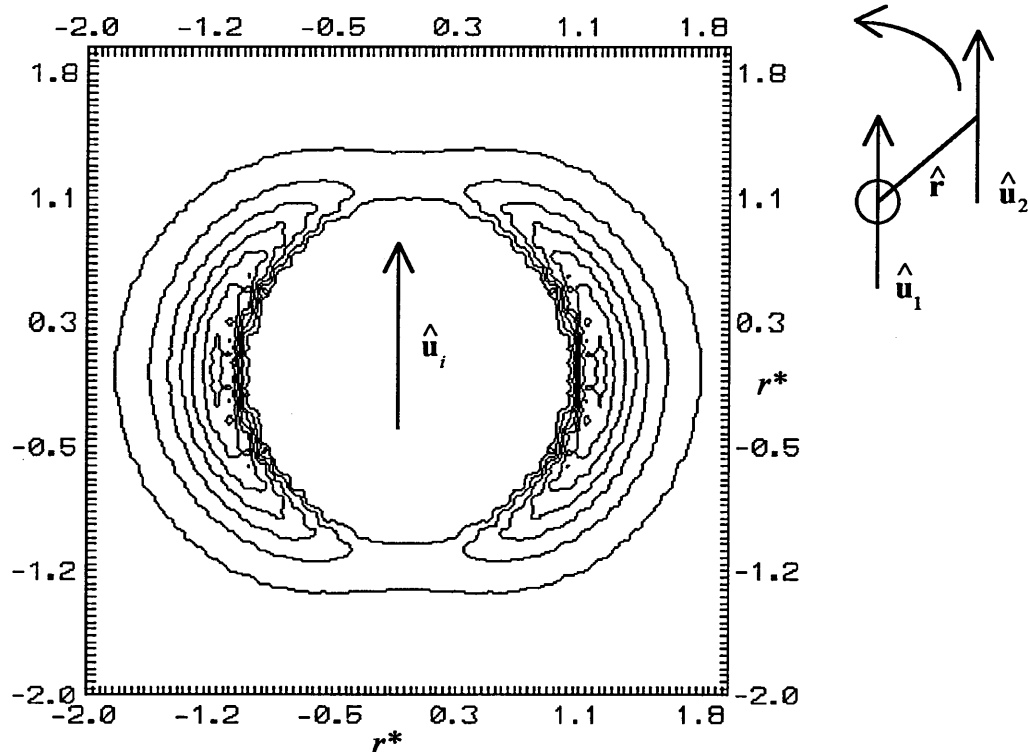


Figure IV.5

A two dimensional representation of the field of potential energy between a pair of rod-like HGBLR centres orientated as in the small schematic diagram. The centre with symmetry vector \hat{u}_1 is fixed at the origin, while the second centre is rotated around the first on the same plane: the plane of the paper. The \hat{u}_i remain constant and only the $\hat{r} \cdot \hat{u}_i$ and the intermolecular separation r^* are allowed to vary. The potential energy has been truncated at $V^* = 0$. The contours are plotted at intervals of $V^* = 0.1$. The spherical hard core extending to a radius $\sigma_0 = 1$ is clearly visible. The other parameters are $\epsilon_0 = 1$, $\chi' = 2/3$, corresponding to $\epsilon_e / \epsilon_s = 0.2$ and $\lambda = 0.15$. The rod like nature of the parameterisation is clearly distinguishable from the form of figure IV.4. Note in this figure the contours are plotted twice as frequently as in figure IV.4 demonstrating the reduced strength of the rod-rod interaction compared with that of the discs.

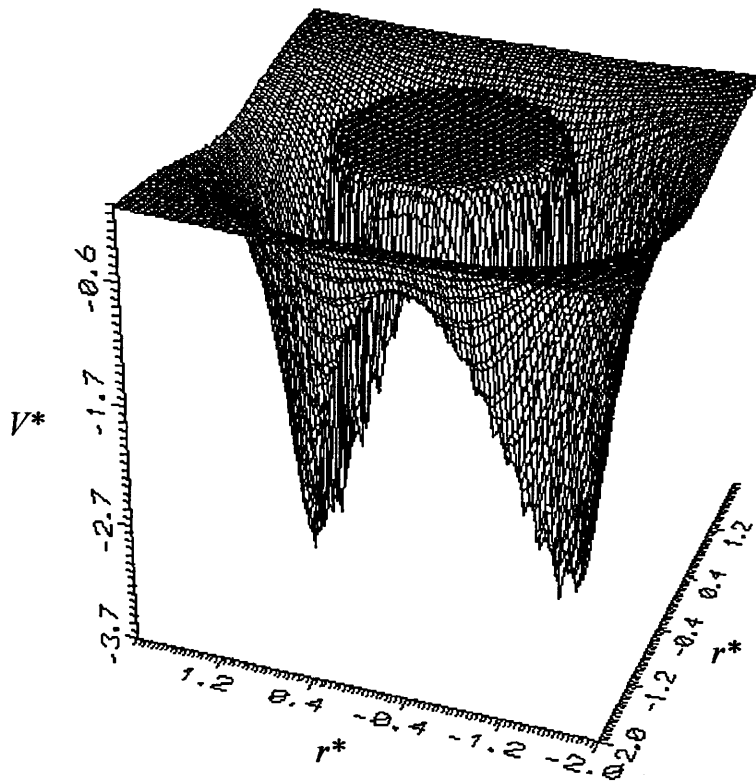


Figure IV.6

A three dimensional orthographic representation of the contour plot of figure IV.4. See figure IV.4 for details of the orientation and parameterisation of the HGBLR centres.

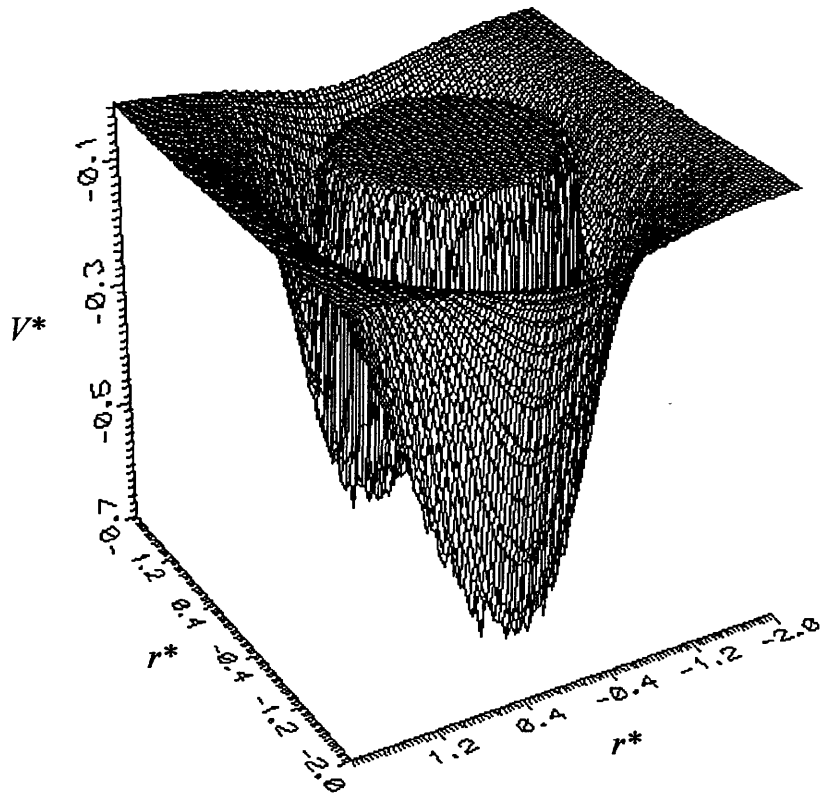


Figure IV.7

A three dimensional orthographic representation of the contour plot of figure IV.5. See figure IV.5 for details of the orientation and parameterisation of the HGBLR centres.

IV.3 Discotic HGBLR Simulations

IV.3.1 Details of the Discotic Simulations

With the parameters $\chi' = -2/3$ and $\sigma_0 = 1$, 256 particles were simulated in a cubic box in the microcanonical or constant NVE ensemble, i.e. particle number, volume and total internal energy. Full periodic boundary conditions (see section II.5.1) were implemented. The translational equations of motion were solved using the method of section II.5.6.3.

For ease of calculation and subsequent comparison with the calamitic results, the particles were taken to have unit mass $m^* = 1$ and unit moment of inertia magnitude. Consequently these values did not have to be included in the simulation. Such values enabled rapid system equilibration to obtain equipartition of the kinetic energies of rotation and translation.

As the aim of these preliminary calculations was to see if the HGBLR centres were capable of exhibiting liquid crystalline behaviour, results presented here concentrate on the structure and order parameters measured of the system. Discontinuities in the behaviour of the reduced potential energy $\langle V^* \rangle$, often more usefully presented as $\langle V^*/N \rangle$, the ensemble average of the reduced potential energy per particle, can be indicative of phase transitions occurring, so the behaviour of this variable is presented together with $\langle P_2 \rangle$, the second rank order parameter, $G_2(r^*)$, the second rank orientational pair correlation function, $g(r^*)$, the radial distribution function and $\langle |r^*(t) - r^*(0)| \rangle$, the mean square particle displacement. The two latter functions are also resolved into their components parallel and perpendicular to the nematic director.

The following should be stressed, as it is a point that often causes a degree of confusion in the literature. Within this report, when a function is presented resolved with respect to system director, it is the instantaneous director $\hat{\mathbf{n}}(t)$ that is referred to. For a given configuration P_2 (an average over particles only, and not an ensemble average here) is taken to be the largest eigenvalue of the diagonalised \mathbf{Q} tensor, and the corresponding eigenvector is taken as the direction of $\hat{\mathbf{n}}(t)$ [5]. Whenever components of a function resolved parallel and perpendicular to the system director for a given configuration are computed, it is the direction of the director of the same given configuration that is considered. Functions are not resolved with respect to an average director direction over the whole run. This method is chosen as in high temperature nematic phases the $\hat{\mathbf{n}}(t)$ have been observed to reorientate continuously.

At each state point, simulation runs consisted of typically 30,000 equilibration steps followed by 30,000 production run steps (where the data for ensemble averaging are collected). The length of a time step in conventional seconds then becomes 3.7×10^{-12} seconds; choosing unity for the fundamental parameters of length and mass and choosing $\varepsilon = 1/k_B$. The large equilibration times were chosen to ensure that the system had evolved to a suitable point from which ensemble averages could later be safely computed for the number of particles considered. This was monitored by observing the equipartition of rotational and translational kinetic energy: a ratio 3:2 obtains as there are three degrees of translational freedom, but only two degrees of rotational freedom: the cylindrically symmetric HGBLR centres being rotationally invariant about their principle symmetry axis. Typically this was achieved after only a few thousand time steps. This is not, though, a guarantee that equilibrium has been reached and we shall return to this point a little later (see section IV.4.2). Nevertheless,

because the single-site HGBLR is a relatively computationally inexpensive potential it was decided to continue the equilibration runs up to 30,000 steps in total.

During the production stage of the simulation, instantaneous configurations and relevant thermodynamic quantities such as $\langle E^* \rangle$, $\langle V^* \rangle$ and $\langle K^* \rangle$ etc., (previously defined in section II) were output at intervals of every 100 time steps. As successive system configurations do not change significantly from one to the next, it is statistically more efficient to sample from configurations at larger intervals. The correlation length of statistically significant configurations of a system of Lennard-Jones 12-6 centres with a time step of 0.0015 seconds (the smallest used here), was found to be approximately 80 configurations, using the method described in reference [6]. Whilst there is no reason to suppose a system of HGBLR centres would exhibit exactly the same correlation length, one would not expect the correlation length to vary tremendously. Without a full analysis therefore, a sampling interval of every 100 configurations was adopted. This was achieved by filing available thermodynamic data from the simulation, together with the vectors describing each particle's position, principle symmetry axis orientation, velocity, and angular velocity. These data were subsequently analysed to provide structural parameters. For example, the \mathbf{Q} tensor was assembled and diagonalised to calculate $\langle P_2 \rangle$ and $\hat{\mathbf{n}}(t)$ from the stored $\hat{\mathbf{u}}_i$ and likewise, $\langle |r^*(t) - r^*(0)| \rangle$ and $g(r^*)$ were computed from the stored \mathbf{r}_i ; the position vectors of the HGBLR centres with respect to the system origin. The particle velocity vectors and angular velocity vectors were stored for possible future analysis.

The system was initially started with a reduced density of $\rho^* = 0.84$ at high temperature on an α -fcc lattice. In the absence of further information the system density was chosen to be close to that of the triple point of liquid argon, which has been previously simulated using a Lennard-Jones potential [6]. Observation of the translational order parameter indicated that this structure rapidly melted. Additional analyses of $\langle P_2 \rangle$ and $g(r^*)$ indicated an isotropic liquid phase. However, visualisation of the contents of the simulation cell through the use of computer graphics revealed, that at lower temperatures cavities had formed in the system. Further investigations at higher densities showed that a value of $\rho^* = 1.1$ allowed equilibration of the system at all temperatures without cavities being formed.

The final configuration of a single state point simulation was taken as the input to the next state point simulation. The translational velocities were scaled by a factor of 0.8: the rotational velocities were left unchanged resulting in an overall kinetic energy scaling factor 0.88. During the equilibration cycle of the simulations, equipartition of the kinetic energy was restored once again. In this manner, the system was cooled from a reduced temperature of $\langle T^* \rangle = 10.0$ to $\langle T^* \rangle \approx 0.3$.

IV.3.2 Discotic Simulation Results

IV.3.2.1 Energy Fluctuations, Potential Energy and the Second Rank Orientational Order Parameter

Table IV.2 shows the values of reduced potential energy per particle $\langle V^*/N \rangle$ and order parameter $\langle P_2 \rangle$ for the state points simulated over the range $10.0 \geq \langle T^* \rangle \geq 0.3$. In the higher temperature region a time step of $\Delta t^* = 0.005$ was employed, giving acceptable energy conservation. The fluctuations in the

total energy of the system, $\langle E^* \rangle = \langle V^* \rangle + \langle K^* \rangle$, were observed at better than 1 part in 1000. However as $\langle P_2 \rangle$ began to rise at $\langle T^* \rangle \approx 6$, large fluctuations in the total energy began to appear. Acceptable energy conservation, according to the above criterion, was once more achieved by reducing the time step to $\Delta t^* = 0.0015$. Clearly this means that the simulations are no longer of equal time length. Close to subsequently observed phase transitions therefore, simulations were extended at appropriate state points for a further 150,000 steps.

Over such large runs, drifts in energy beyond the adopted criterion were observed. After much investigation, unacceptable drifts in energy were eventually eliminated by substituting a full-step Verlet for the half-step Verlet algorithm to solve the rotational equations of motion within the constraint method. The reason why this should be the case is not quite clear. In the full step Verlet algorithm, emphasis is placed on predicting new particle positions using previous positions and current accelerations derived in the force loop. With the half step Verlet, it is particle (angular) velocities from the previous half step that are used in conjunction with the present accelerations to predict future half step velocities, from which positions may be subsequently calculated. However, both algorithms are algebraically equivalent. This suggests that it is possibly a rounding error that was causing the energy instabilities observed. If the rounding error is caused by the addition of a small number to a large number (which may often cause errors in numerical computing), then it is, however, the full step Verlet that is most likely to suffer from such effects [6].

It is also possible that the use of angular velocities in the half step Verlet algorithm causes the calculation of particle orientations to depart from their true values. One could imagine such a situation obtaining if the angular velocities

$\langle T^* \rangle$	$\langle V^*/N \rangle$	$\langle P_2 \rangle$
10.0±0.2	-1.3±0.6	0.07±0.03
8.5±0.2	-2.7±0.5	0.08±0.03
7.3±0.2	-4.3±0.4	0.09±0.04
6.3±0.1	-5.7±0.4	0.12±0.05
5.5±0.2	-7.0±0.4	0.18±0.06
5.7±0.2	-7.6±0.4	0.31±0.06
5.1±0.2	-9.1±0.4	0.35±0.07
5.1±0.2	-12.1±0.4	0.64±0.03
4.7±0.1	-13.6±0.4	0.71±0.02
4.2±0.1	-15.2±0.3	0.76±0.02
3.9±0.1	-16.6±0.3	0.82±0.01
3.5±0.1	-17.8±0.3	0.85±0.01
3.19±0.09	-18.8±0.2	0.869±0.008
2.90±0.09	-19.8±0.2	0.893±0.006
2.61±0.08	-20.6±0.2	0.903±0.007
2.57±0.08	-21.9±0.2	0.908±0.007
2.59±0.07	-22.0±0.2	0.909±0.006
2.32±0.07	-22.7±0.2	0.923±0.004
2.09±0.06	-23.3±0.1	0.931±0.005
1.88±0.05	-23.9±0.1	0.939±0.003
1.68±0.05	-24.4±0.1	0.948±0.003
1.51±0.05	-24.8±0.1	0.955±0.003
1.34±0.04	-25.2±0.1	0.959±0.003
1.34±0.04	-25.2±0.1	0.962±0.003
1.20±0.04	-25.59±0.09	0.965±0.002
1.06±0.03	-25.92±0.07	0.969±0.002
0.94±0.03	-26.20±0.06	0.972±0.001
0.84±0.02	-26.44±0.06	0.977±0.001
0.75±0.02	-26.69±0.06	0.980±0.001
0.67±0.02	-26.87±0.05	0.982±0.001
0.59±0.02	-27.06±0.05	0.983±0.001
0.53±0.01	-27.22±0.04	0.986±0.001
0.47±0.01	-27.34±0.03	0.987±0.001
0.42±0.01	-27.48±0.03	0.989±0.001

Table IV.2

Average temperature $\langle T^* \rangle$, average potential energy per particle $\langle V^*/N \rangle$ and second rank order parameter $\langle P_2 \rangle$ for the disc-like HGCLR centres parameterised as described in the text. Errors are ± 1 standard deviation of the arithmetic mean.

were rapidly varying functions of time. Trying different length time steps did not improve the energy stability though. A smaller time step should stabilise the simulation eventually. But from another point of view, it is clear that the use of an estimator to calculate the kinetic energy of the form of equation II.44 is adequate to provide acceptable energy conservation in both cases, implying that the calculation of (angular) velocities is in fact sufficiently accurate.

The results of these extended runs are presented in table IV.3. Figure IV.8 and figure IV.9 illustrate the behaviour of the second rank order parameter $\langle P_2 \rangle$ and the potential energy per particle $\langle V^*/N \rangle$, respectively. The latter shows that the system is orientationally disordered at temperatures $\langle T^* \rangle > 6$; although $\langle P_2 \rangle$ maintains a value greater than zero due to the finite size of the system and the averaging of a positive quantity (see section II.4.2). We interpret these data as describing an isotropic system. As the system is cooled further $\langle P_2 \rangle$ begins to rise, sharply, over a short temperature range of about $5.5 \geq \langle T^* \rangle \geq 5.0$ to obtain $\langle P_2 \rangle = 0.64$. Thereafter $\langle P_2 \rangle$ tends, more slowly, to a value of unity. In the former figure, we note that as the temperature begins to fall the potential energy becomes increasingly negative, as one would expect. A change in the behaviour of the potential energy of the system is observed in the same temperature range.

A further change is observed at a lower temperature also. Immediately after the simulated state points at $\langle T^* \rangle = 5.3 \pm 0.2$ and $\langle T^* \rangle = 2.77 \pm 0.09$, a sudden fall in potential energy over a short temperature range is observed. Such discontinuities in the behaviour of the potential energy indicate that a change of phase may be occurring in the system.

$\langle T^* \rangle$	$\langle V^*/N \rangle$	$\langle P_2 \rangle$
5.3±0.2	-9.7±0.5	0.49±0.06
5.0±0.2	-11.7±0.4	0.62±0.03
2.88±0.08	-19.8±0.2	0.889±0.008
2.77±0.09	-21.1±0.2	0.901±0.007
2.58±0.07	-21.9±0.2	0.911±0.007

Table IV.3

Simulation averages of temperature $\langle T^* \rangle$, internal potential energy per particle $\langle V^*/N \rangle$ and order parameter $\langle P_2 \rangle$ obtained for the extended runs of the system of HGBLR centres parameterised as discs. Errors are quoted to plus or minus one standard deviation of the respective ensemble average.

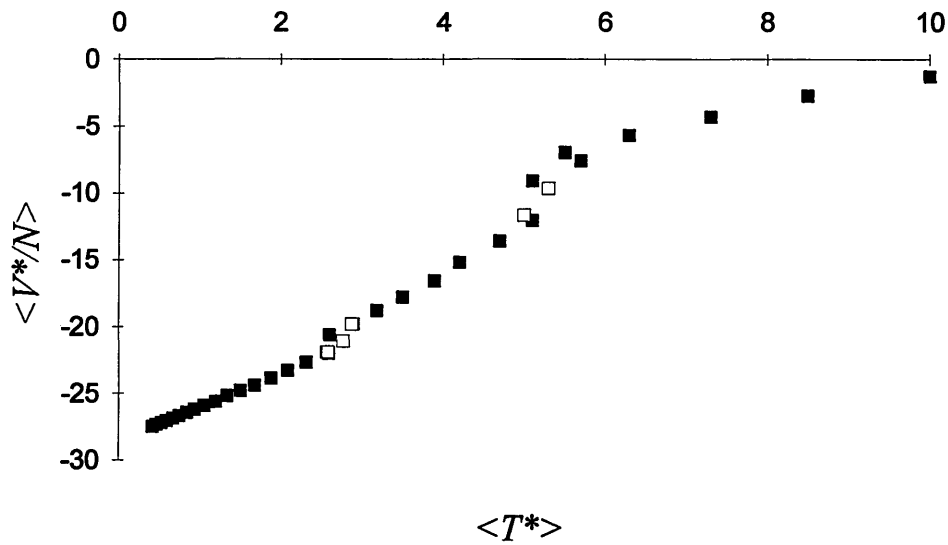


Figure IV.8

Average reduced potential energy per particle $\langle V^*/N \rangle$ against reduced temperature $\langle T^* \rangle$ for disc-like HGBLR centres parameterised as in the text. Additional values obtained from the extended runs are indicated with open squares.

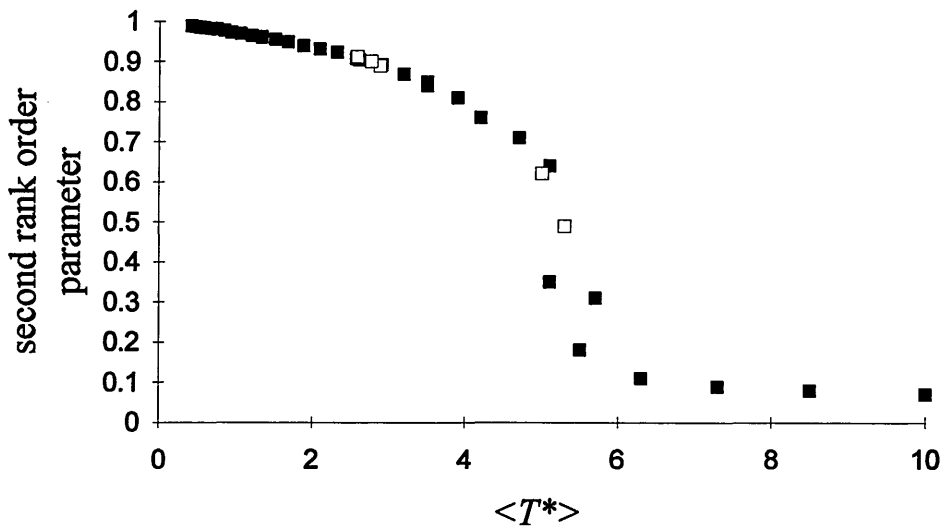


Figure IV.9

Order parameter $\langle P_2 \rangle$ against reduced temperature for the system of disc-like HGBLR centres parameterised as described in the text. The results obtained from extended runs are indicated with open squares.

It is possible to obtain an estimate of the change in entropy at the indicated temperatures, by approximating the curve of figure IV.8 to three straight lines. The change in entropy, from one branch to another was estimated at $\Delta\langle V^*/N \rangle / \langle T^* \rangle = 0.6$ in each case. In order to further our knowledge of what was happening to the system of HGBLR centres exhibiting such behaviour, we turned our attention to the radial distribution function $g(r^*)$.

IV.3.2.2 Radial Distribution Function and Second Rank Orientational Correlation Coefficient

Figures IV.10a to IV.10c show examples of the radial distribution function computed at three state points during the disc cooling runs. In these figures the radial distribution function is also presented resolved parallel and perpendicular with respect to the system director $\hat{n}(t)$. Figure IV.10a illustrates the behaviour of $g(r^*)$ after the first transition at a reduced temperature of $\langle T^* \rangle = 5.0$. Here $g(r^*)$ has the typical form expected of a liquid like structure. Further there appears to be no translational ordering of the HGBLR centres from the resolved components $g_{\parallel}(r_{\parallel}^*)$ and $g_{\perp}(r_{\perp}^*)$. Considering the large value of $\langle P_2 \rangle = 0.64$, these data are indicative of a discotic nematic phase.

The figure IV.10b obtained at a reduced temperature of $\langle T^* \rangle = 2.77$ shows that $g(r^*)$ again possesses a liquid like structure. The intensity of the peaks have increased implying a structure that is more regularly ordered, than that of figure IV.10a. It is, further, probable that this ordering persists at greater distances than in the system of figure IV.10a: the larger oscillations in $g(r^*)$ requiring a longer length before decaying to the ideal gas limit of $g(r^*) = 1$. This latter point is not verifiable though, because in all figures $g(r^*)$ and its components are only meaningful when considered at distances somewhat less than half the simulation

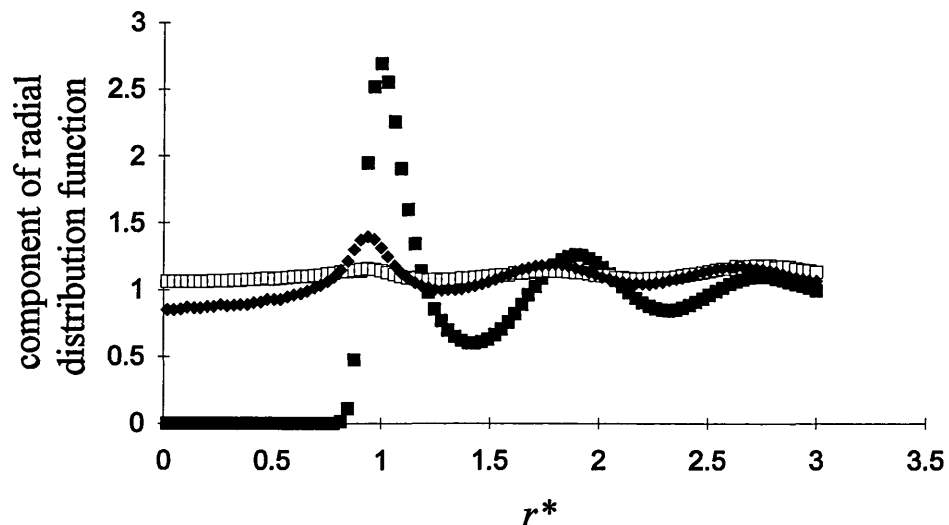


Figure IV.10a

The radial distribution function and components resolved parallel and perpendicular to the director for HGBLR discs at reduced temperature $\langle T^* \rangle = 5.0$. The symbols have the following meanings: closed squares, $g(r^*)$; open squares, $g_{\parallel}(\eta^*)$; closed diamonds, $g_{\perp}(r_{\perp}^*)$

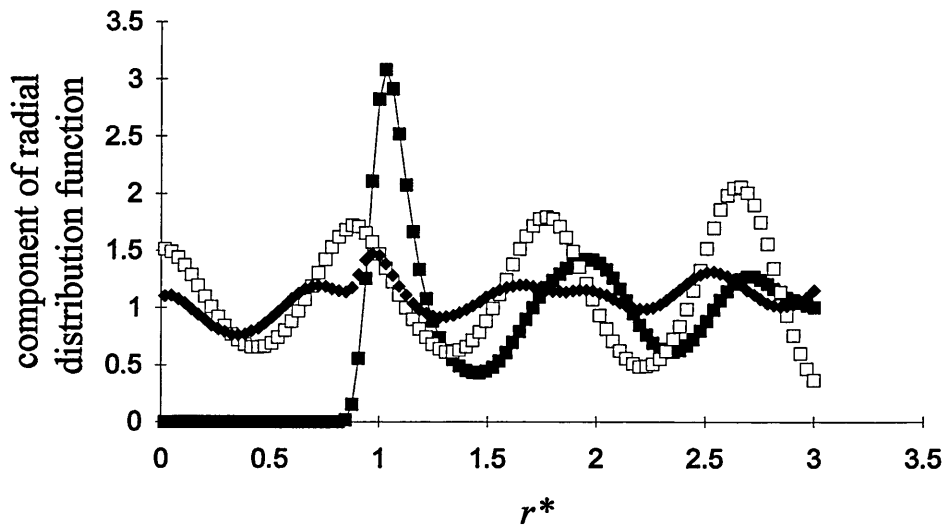


Figure IV.10b

As figure IV.10a at reduced temperature $\langle T^* \rangle = 2.77$. Lines joining data points have been introduced as a guide to the eye where it was considered appropriate.

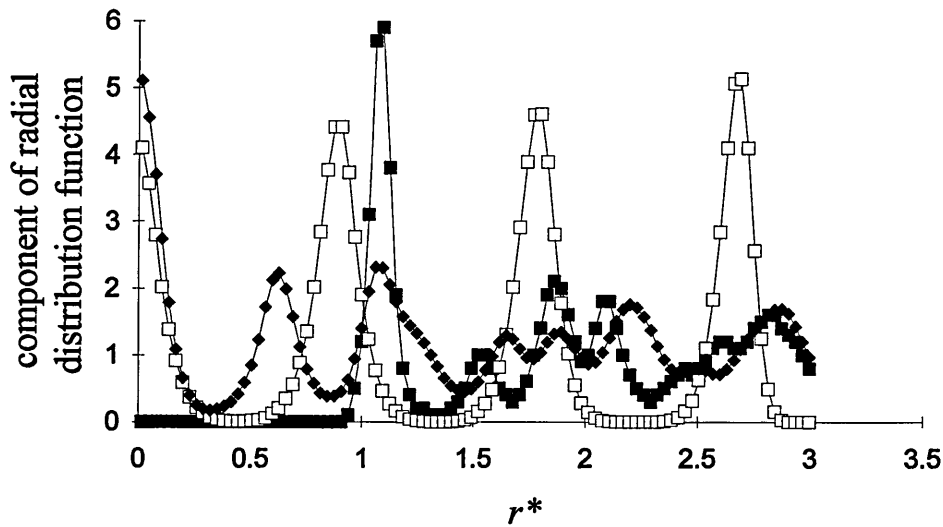


Figure IV.10c

As figure IV.10a at reduced temperature $\langle T^* \rangle = 0.47$. Lines joining data points have been introduced as a guide to the eye.

box length. For a given simulation density, this upper limit on $g(r^*)$ etc., may be overcome by simulating more particles or by changing the simulation box geometry. However, for the 256 particles that we have simulated, a maximum length of $r^* = 3.0$ (just under half the box length to avoid spurious contributions from particle self interactions), is sufficient for our purposes here, where we are only trying to identify the phases present in the simulations and not perform any quantitative analysis of the radial distribution function or its components.

Turning now to the resolved components of figure IV.10b, the function $g_1(\eta^*)$ exhibits a one dimensional density wave parallel to the system director. This result may be explained in terms of disc-like parameterised HGBLR centres tending to stack up in a regular layer like structure. The function $g_{\perp}(r_{\perp}^*)$ is also beginning to show the presence of some structure perpendicular to the system director. The first meaningful maximum in $g_1(\eta^*)$ occurs at $\eta^* \approx 0.9$ compared with the minimum in the disc-like pair potential which occurs at r^* slightly greater than 1 (see figure IV.2). This indicates that the HGBLR centres are closely stacked in the layered arrangement and indeed this may be the required arrangement at the relatively high reduced density of $\rho^* = 1.1$. At first sight this would seem a reasonable argument, but examination of figure IV.2 shows that the disc-like HGBLR potential is a rapidly varying function around $r^* = 0.9$, making it unlikely to find that the HGBLR particles have a spatial distribution such that nearest neighbours are peaked at $r^* = 0.9$. It is important to consider the evidence afforded through resolved components of structural order functions carefully. Although figure IV.10b presents strong evidence for HGBLR centres separated on average by $r^* = 0.9$ along the direction of the director, these centres may be far apart in the direction of planes perpendicular to the director. Because

of this we can only be sure that the first peak of the unresolved radial distribution function comes from nearest neighbour contributions.

An interesting feature of figure IV.10b is that as r^* increases, the amplitude of oscillations in $g_1(\eta^*)$ also increases. This would imply that at longer range HGBLR centres separated along the direction of the director are more correlated than near neighbour centres separated in the same direction. An effect like this intuitively seems most unlikely. Incorrect normalisation of the curves of $g_1(\eta^*)$ and $g_\perp(r_\perp^*)$ could help explain the unexpected increasing amplitudes of oscillations; especially with the former curve. The normalising function for $g_1(\eta^*)$ consists of computing the volume of equal volume pairs of successive slices of a sphere, stepping from the equator to the poles. Close to the equator the slices are of relatively large volume. However the slice volume rapidly decreases as one moves towards the poles of the sphere, making an accurate calculation of the volume of a slice difficult. In the case of $g_\perp(r_\perp^*)$ the normalising volume is a series of cylinders with hemispherical caps, whose radii increase (as one looks out further along planes perpendicular to the director), while they progressively shrink in length. However these corrections should be minimal, and we should look to other explanations of this effect.

When calculating the normalisation function for the $g(r^*)$ we have tacitly assumed a continuous particle distribution function: appropriate for liquids and gases. It is possible that particularly ordered arrangements, such as columns of disk-like particles do not suit such an interpretation. To illustrate this consider the schematic figure IV.11. Disc-like particles are represented as shaded ovals. The discs are arranged in columns with their principle symmetry axes coincident with the column axis indicated by the vertical straight lines. A circle is drawn

which represents the cross section of a sphere within which $g(r^*)$ is considered. The projection of three interparticle vectors on to the system director is represented by line segments labelled $r_{1\parallel}$ and $r_{2\parallel}$; $r_{0\parallel} = 0$. By examining the number of discs that contribute to the longitudinal distribution function at the selected values of $r_{i\parallel}$, considering the top right hand quadrant only, we find, $g(r_{0\parallel}) = g(r_{1\parallel}) = 3$ and $g(r_{2\parallel}) = 2$. The first two separations $r_{i\parallel}$ which are significantly different have the same number of particle contributions to the longitudinal distribution function. However at the larger separation of $r_{1\parallel}$ a smaller normalising factor applies. Thus the contribution to the longitudinal distribution function at this separation tends to be overestimated after normalisation. In actuality many such separations are considered in calculating $g_1(\eta^*)$, shifting the origin to the centre of a particle resulting in the same view of the system each time. Unless the system has formed a perfectly ordered crystal such an arrangement as described in figure IV.11 would not exist; disorder and thermal motion notwithstanding the effect will still be manifest though.

Figure IV.10c shows the radial distribution function and its resolved components at the very low reduced temperature of $\langle T^* \rangle = 0.47$. All curves exhibit well defined translational order characterised by sharp peaks separated by low or zero value minima. We note that increasing magnitude of the oscillations of $g_1(\eta^*)$ are once again present.

In order to investigate the nature of the relative orientations of HGBLR centres we may examine the behaviour of the second rank pair correlation function $G_2(r^*)$. Figure IV.12 shows $G_2(r^*)$ at $\langle T^* \rangle = 5.0$ and $\langle T^* \rangle = 2.77$ (the same values of temperature at which figures IV.10a and IV.10b are presented). At both temperatures $G_2(r^*)$ exhibits a peak around $r^* = 0.8$. The initial peak of each

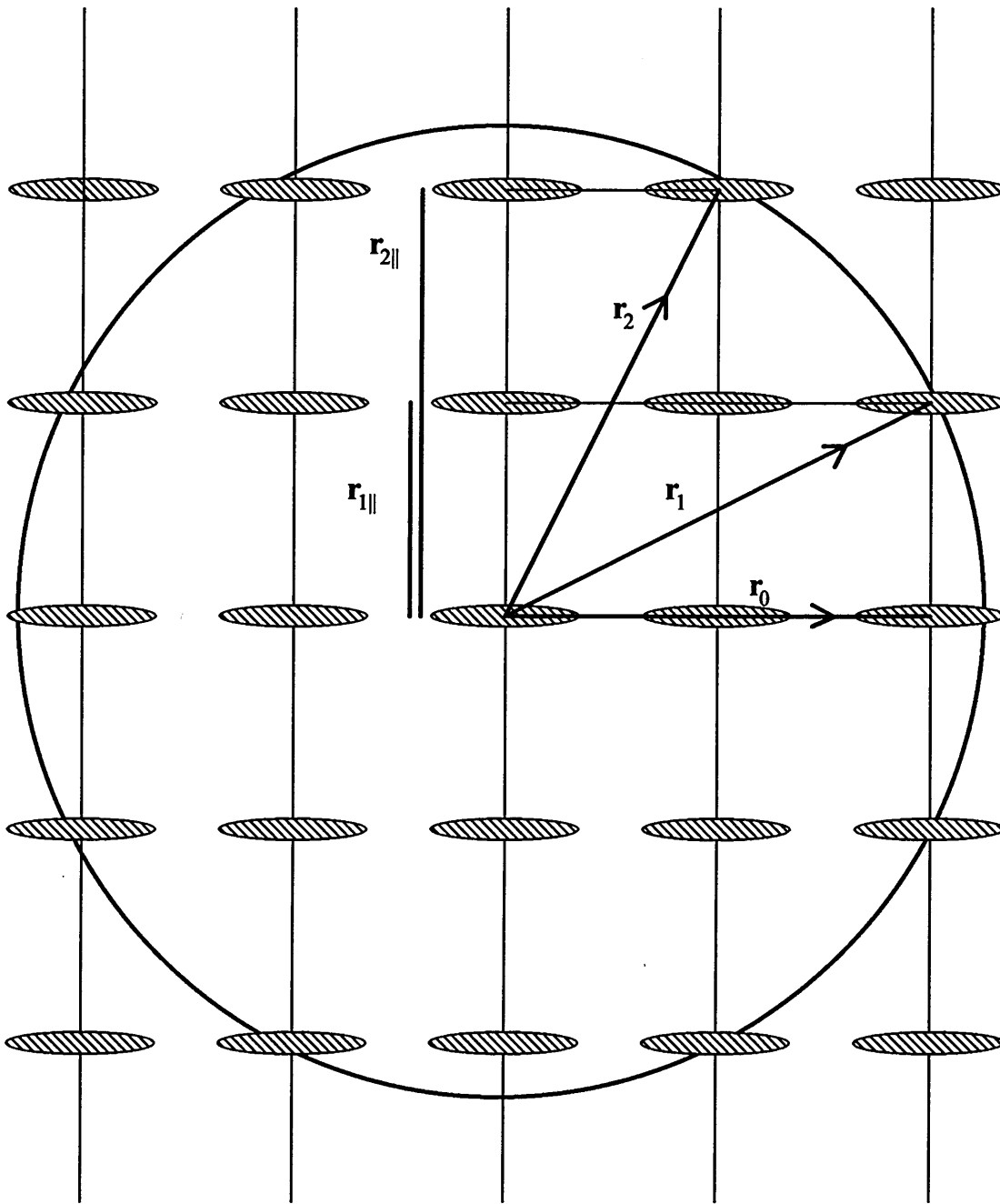


Figure IV.11

A schematic diagram illustrating how an example configuration of disc-like HGBLR centres may cause difficulties in the calculation of $g_1(\eta^*)$. See text for explanation.

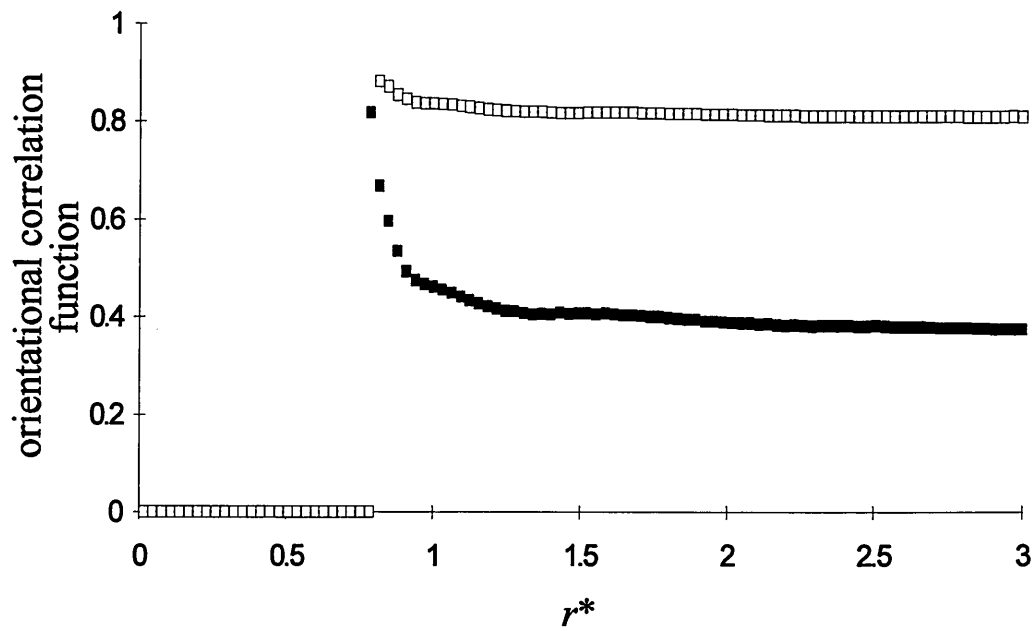


Figure IV.12

The second rank pair orientational correlation function $G_2(r^*)$ for disc-like parameterised HGBLR centres as described in the text. Closed squares $\langle T^* \rangle = 5.0$; open squares $\langle T^* \rangle = 2.77$.

curve of the function $G_2(r^*)$ provides an estimator for nearest neighbour HGBLR centres possessing the same orientation. However with the low temperature curve $G_2(r^*)$ quickly decays to a limiting value of approximately $G_2(r^*) = 0.4$ over a range of about $0.3r^*$. At long range $G_2(r^*)$ should adopt a limiting value of $\langle P_2 \rangle^2$ (see section II.6.2). For the state point simulated here the corresponding value of $\langle P_2 \rangle = 0.62$ such that $\langle P_2 \rangle^2 = 0.38$ and the agreement is excellent. The higher temperature curve illustrates that at short range HGBLR centres are highly likely to be orientationally correlated. This correlation decays very quickly over a short range to attain a plateau indicating the persistence of orientational order even at long range. At the lower temperature the orientational pair correlation function tends to $G_2(r^*) \approx 0.8$ indicating the presence of a highly orientated phase at long range.

IV.3.2.3 Preliminary Identification of Phases

With the information contained in figures IV.10a-c, together with the quantitative values of the second rank orientational order parameter $\langle P_2 \rangle$, internal potential energy per particle $\langle V^*/N \rangle$, and pair orientational correlation function we may provisionally identify four different phases for the system of HGBLR discs. These may be summarised as follows:

$\langle T^* \rangle \geq 5.5$	isotropic
$5.5 \geq \langle T^* \rangle \geq 2.8$	discotic-nematic
$2.8 \geq \langle T^* \rangle \geq 2.6$	highly ordered
$\langle T^* \rangle \leq 2.6$	crystal

IV.3.2.4 Mean Square Particle Displacement and Diffusion Coefficients

For the study of liquid crystal phases it is important to be able to check on the fluidity of a phase. Herein lies the advantage in carrying out MD simulations which allow us to examine some of the dynamic properties of the systems under study. The mean square particle displacement provides a measure of the particle self diffusion within a simulation. The gradient of a graph of mean square particle displacement against time t relates to the Einstein expression for the diffusion coefficient of molecules at long times (see section II.6.1, equation II.65). Results of the diffusion coefficients and their components resolved parallel and perpendicular to the director calculated by considering only the last two thirds of the extended runs are presented in table IV.4. In addition figures IV.13a and IV.13b illustrate the behaviour of the mean square displacement observed for the extended simulations (the whole run) recorded at the reduced temperatures $\langle T^* \rangle = 5.0$ and $\langle T^* \rangle = 2.77$.

In both figures the unresolved mean square diffusion shows a straight line behaviour at long time. This is characteristic of liquid like diffusion. In figure IV.13a recorded from a run with ensemble average $\langle P_2 \rangle = 0.62$ (well into the nematic phase) there does not appear to be a difference between the curves of mean square displacement resolved with respect to the system director. This is reflected in table IV.4 which shows that the particle self diffusion coefficients D_{\parallel}^* and D_{\perp}^* at this temperature is equal. At the lower temperature there is an obvious difference between the behaviour of the resolved components of the mean square displacement. The gradient of the component perpendicular to the director is greater than that parallel. Reference to table IV.4 reveals that the particle self diffusion coefficient in a direction perpendicular to the director is

$\langle T^* \rangle$	$6D^*$	$\langle P_2 \rangle$
5.3±0.2	57.84±0.02	0.49±0.06
5.0±0.2	51.74±0.02	0.62±0.02
2.88±0.08	19.30±0.02	0.889±0.008
2.77±0.09	5.36±0.01	0.901±0.007
2.58±0.07	0.662±0.001	0.911±0.007

$\langle T^* \rangle$	$6D_{\parallel}^*$	$6D_{\perp}^*$	$D_{\parallel}^*/D_{\perp}^*$
5.3±0.2	19.44±0.05	19.20±0.02	1.01
5.0±0.2	17.90±0.03	16.92±0.02	1.06
2.88±0.08	6.15±0.02	6.67±0.02	0.92
2.77±0.09	1.301±0.004	2.028±0.004	0.64
2.58±0.07	0.1106±0.0002	0.2757±0.0009	0.40

Table IV.4

The reduced diffusion coefficients D^* and components resolved parallel and perpendicular to the system director for the extended runs of disc-like parameterised single HGBLR centres. The fifth column presents the ratio of the parallel to perpendicular diffusion coefficients. The ensemble averaged order parameter $\langle P_2 \rangle$ calculated for each run is also indicated.

approximately one-and-a-half times greater than that parallel to the director. This indicates that the molecules move further and hence more freely in a direction perpendicular to the system director at this temperature.

Previous simulations of rod-like and disc-like mesogens have shown further displacement of the particles parallel and perpendicular to the director respectively, compared to other directions. Sometimes the coefficient of diffusion in the preferred direction is actually higher than for the isotropic phase just after the transition [7]. On moving through the isotropic-nematic phase transition we would expect mean particle displacement perpendicular to the director to be greater than that parallel to the director. This obtains because in the discotic nematic phase an arbitrary mesogen may move more easily perpendicular to the director as on average there is less likelihood of it encountering further discogens possessing an orientation perpendicular to itself impeding further motion in that direction. However in an isotropic phase there is an equal probability of all molecular orientations and thus an equal chance of other discogens presenting a large molecular surface to impede further displacement. Hence in the isotropic phase there is no preferred direction of displacement

However as clearly illustrated in figure IV.13a, there is no difference between the resolved components of mean square displacement in the nematic phase of HGBLR centres. This can be explained by taking into account the spherical hard core of the HGBLR centres. Mesogens are prevented from diffusing further when they encounter the repulsive hard core of another mesogen. If we assume, in the nematic phase, that the longer range dispersive forces play no role in the

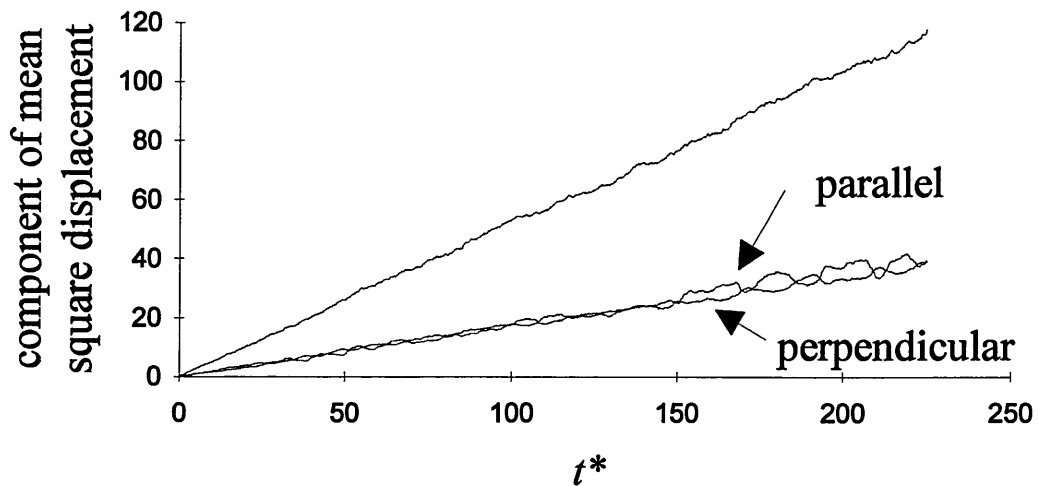


Figure IV.13a

Total and resolved components with respect to the system director of particle mean square displacement for the extended runs of the system of disc-like HGBLR centres at $\langle T^* \rangle = 5.0$. The resolved components are indicated, the unlabelled curve corresponds to the total mean square particle displacement.

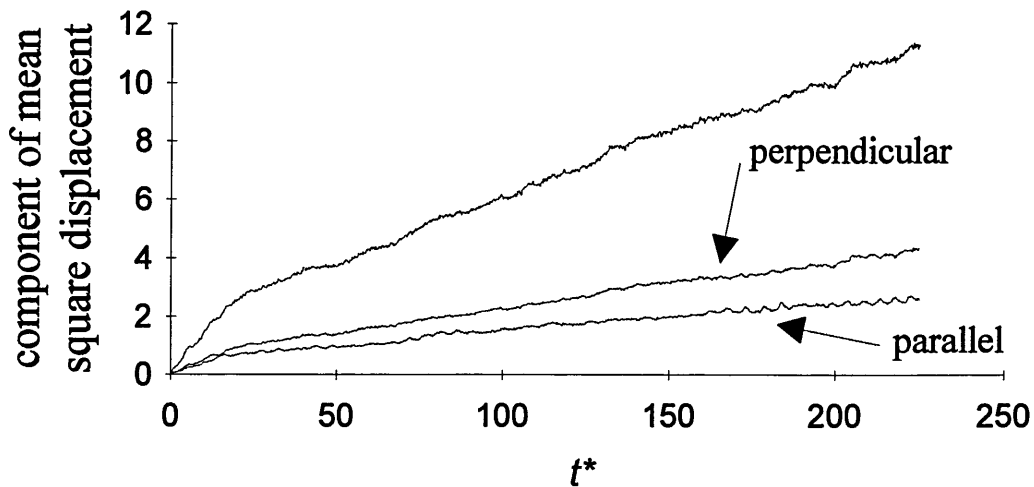


Figure IV.13b

As figure IV.13a but recorded at $\langle T^* \rangle = 2.77$

particle self diffusion process, then the orientated anisotropic attractive regions of HGBLR centres will not influence the diffusion process. The spherical hard core (for a fixed orientation of two HGBLR centres) then presents itself as an equal restriction to diffusion in all directions. Thus diffusion behaviour in the nematic phase is qualitatively the same as that expressed in the isotropic phase. We do observe an overall decrease in the magnitude of diffusion coefficient as the temperature is lowered.

As previously stated the radius of the spherical hard core depends on the fixed orientation of the HGBLR centres. However the difference between the minimum hard core radius and the maximum is small (see figures IV.2 and IV.3). Components of mean square displacement resolved with respect to the system director in the nematic phase essentially compare the ease of diffusion between side-side and end-end oriented centres. Examination of figures IV.2 and IV.3 shows that the HGBLR potential has the same hard core radius for these two orientations. Thus disc-like HGBLR centres trying to diffuse perpendicular to their symmetry axes would experience the same hard core radii presented by the surrounding molecules as they would experience trying to diffuse parallel to their symmetry axes.

A difference between the diffusion coefficients parallel and perpendicular to the director does emerge as the system enters the more highly ordered phase. This may be explained in terms of the environment that each particle finds itself. In the nematic phase each particle can be considered to be in identical surroundings as its neighbours: there is no positional ordering of the centres of mass, and on average the particles possess the same orientation. However when the particles enter the more highly ordered columnar phase, there is a distinction between

neighbours that belong to the same column and those that do not. Discs within columns are prevented from moving along the column axis because of the cooperative motion that would be required from the discs above and below. It is far easier for the discs to diffuse perpendicular to the director.

This observation is in contrast to what is seen in experimental columnar systems. These have been described as orientated one-dimensional liquids [8]. The translational disorder of the molecules occurs within the columns themselves. However, high resolution X-ray studies on columnar systems have shown although the flat discotic cores are orientated with respect to each other, the hydrocarbon chains surrounding the cores exhibit practically isotropic scattering patterns. A detailed model of discotic liquid crystals would necessarily have to include the conformational degrees of freedom of the hydrocarbon chains [8]. Consideration of these effects may yield a model that more appropriately describes columnar discotic systems.

IV.3.2.5 Graphical Representations of Discotic HGBLR Centres

Computer graphics has been employed to capture "snapshots" from typical configurations in order to represent the molecular arrangement. Figures IV.14a-IV.14f are examples of these. With the exception of figure IV.14f in each figure each disc-like HGBLR centre is represented by a line indicating the position and orientation of the site symmetry vector and a disc drawn perpendicular to this indicating the position and orientation of the site equatorial plane. For the sake of clarity in the diagrams the discs are drawn with a radius that is approximately half that of the average hard core radius and the site symmetry vectors are drawn with unit magnitude. In the case of figure IV.14f, only the centres of mass of the HGBLR centres are drawn. In all cases the direction of the instantaneous

director $\hat{n}(t)$ of each configuration is described by thick line running through the centre of the box.

Figures IV.14a and IV.14b are two snapshots taken from a configuration in the nematic phase for which $P_2 = 0.67$ (note this is no longer an ensemble averaged P_2). Figure IV.14a shows a view approximately perpendicular to the system director whilst figure IV.14b shows a view looking down the director. With regard to figure IV.14b it is clear that the majority of discs have their equatorial plane approximately perpendicular to the director. It is interesting to note that although the order parameter measured for this snapshot is relatively high, it is clear from figure IV.14a that the order within the system does not resemble the idealised representations of nematic liquid crystals so often presented in text books etc.

Figures IV.14c and IV.14d illustrate a snapshot of the system taken at the much higher order parameter of $P_2 = 0.91$. Compared with figures IV.14a and IV.14b the increase in ordering is apparent. Looking perpendicular to the director (figure IV.14c) there is not much evidence for the layered structure suggested by the density wave observed for $g_1(\eta^*)$ at low temperature. Looking down the director, it does not appear as though the HGBLR centres are organised in a regular columnar structure, as one may expect of a discotic mesogen as has been observed in previous simulations of soft discotic particles [3].

Figures IV.14e and IV.14f show two snapshots taken at the low reduced temperature of $\langle T^* \rangle = 0.47$ and the configuration shown has an order parameter corresponding to the previously identified crystal phase. Although not perfect, it is clear from these figures that three dimensional positional ordering is present

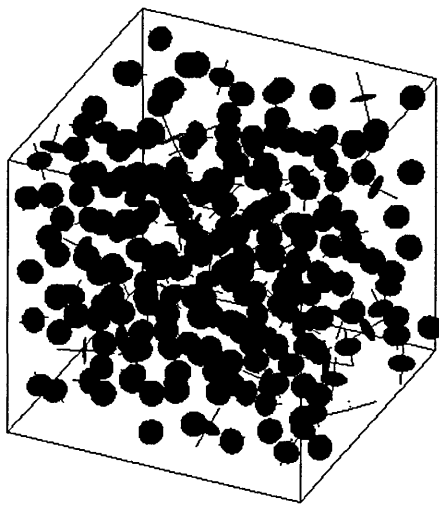
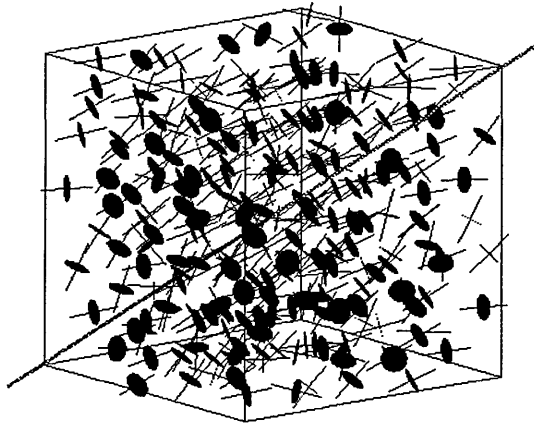


Figure IV.14a (top), figure IV.14b (bottom)

Two views of a discotic nematic configuration. Figure IV.14a is a view perpendicular to the director $\hat{n}(t)$, figure IV.14b is a view looking down the director. Each HGBLR disc is represented by a unit vector parallel to the site symmetry axis and a circle of radius approximately 50% of the hard core radius drawn in the disc equatorial plane. The system director is indicated as a thick line drawn through the box. The measured order parameter for both configurations is $P_2 = 0.67$.

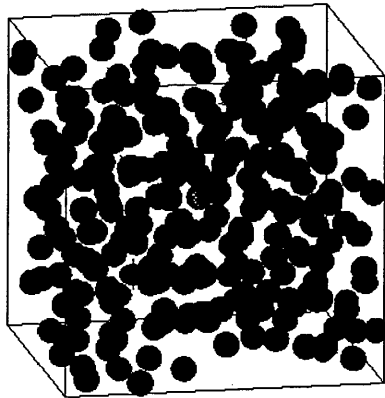
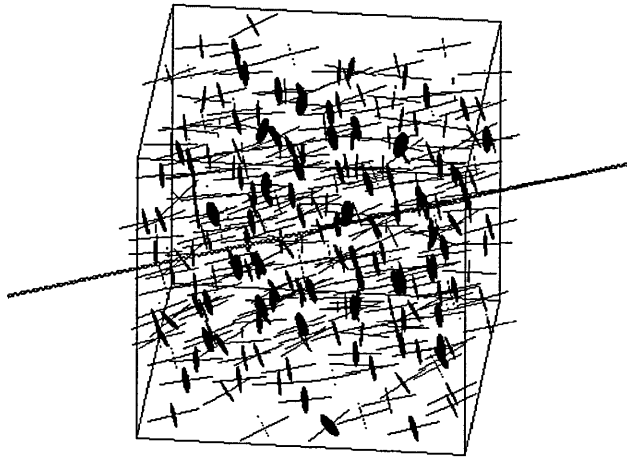


Figure IV.14c (top), figure IV.14d (bottom)

Two views of a highly ordered phase. Figure IV.14c is a view perpendicular to the director $\hat{n}(t)$, figure IV.14d is a view looking down the director. Each HGBLR disc is represented by a unit vector parallel to the site symmetry axis and a circle of radius approximately 50% of the hard core radius drawn in the disc equatorial plane. The system director is indicated as a thick line drawn through the box. The measured order parameter for both configurations is $P_2 = 0.91$.

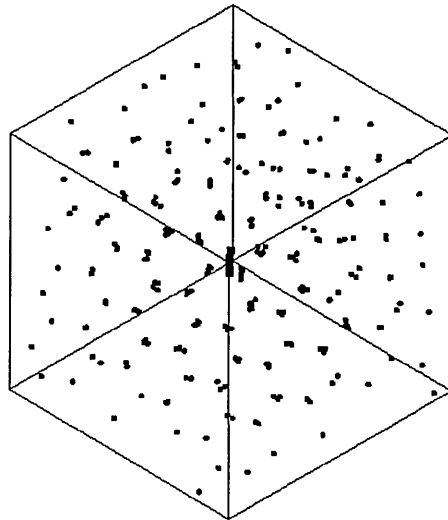
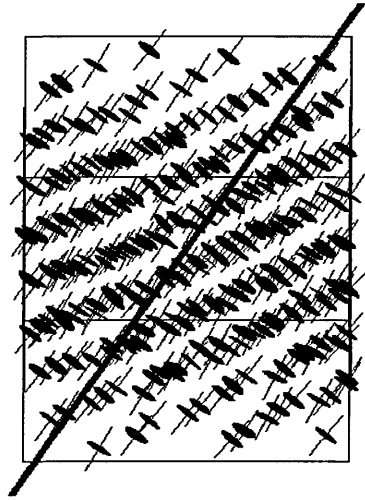


Figure IV.14e (top), figure IV.14f (bottom)

Two views of a crystal phase. Figure IV.14e is a view perpendicular to the director $\hat{\mathbf{n}}(t)$. Each HGBLR disc is represented by a unit vector parallel to the site symmetry axis and a circle approximately 50% of the hard core radius drawn in the equatorial plane. Figure IV.14f is a view looking down the director; the centres of mass of the HGBLR discs represented as dots. The director is shown as a thick line drawn through the box. The measured order parameter for both configurations is $P_2 = 0.99$.

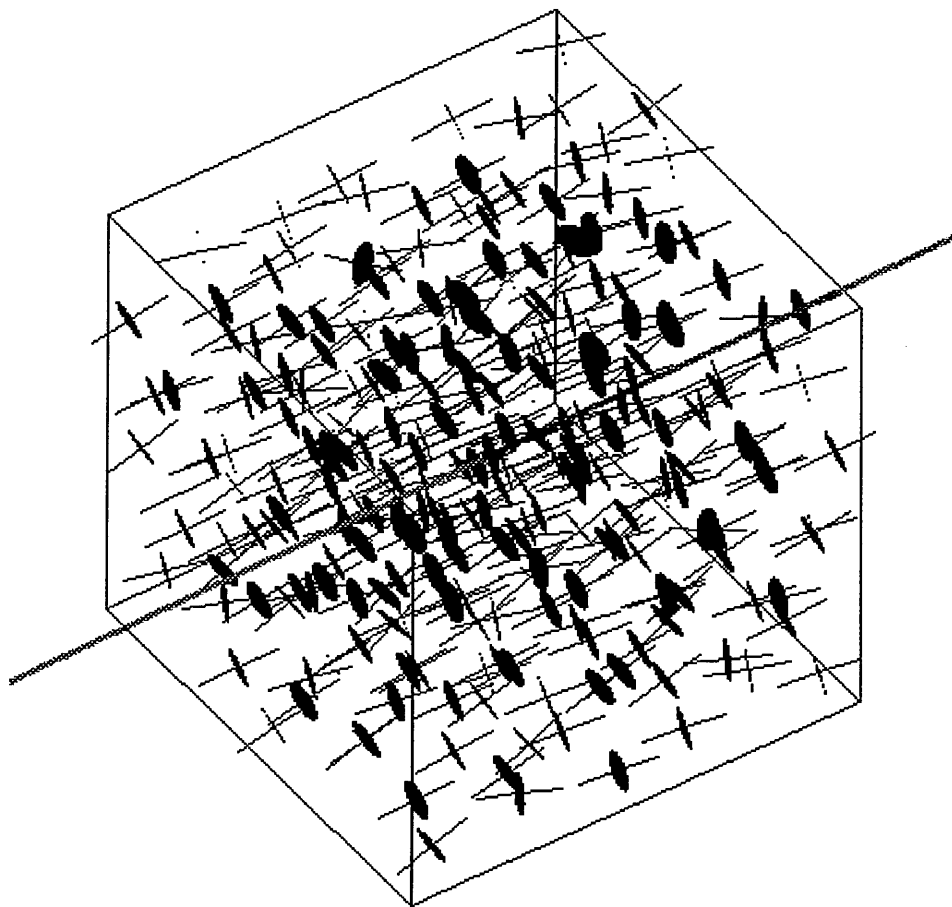


Figure IV.14g

An enlarged view of the highly ordered system of figures IV.14c and IV.14d, exhibiting examples of short stacks of discs. Each HGBLR disc is represented by a unit vector parallel to the site symmetry axis and a circle of radius approximately 50% of the hard core radius drawn in the disc equatorial plane. The system director is indicated as a thick line drawn through the box. The order parameter $P_2 = 0.91$.

here. The disc-like HGBLR centres are stacked in columns. The crystal appears to have a non close packed honeycomb structure with hexagonal symmetry. This may indicate that the system is stable at densities higher than $\rho^* = 1.1$, where a close packed structure may be realised. What is surprising in figure IV.14e is that we can see the HGBLR centres appear to be tilted with respect to the column axes.

The symmetry of the HGBLR potential does not at first sight appear to favour a tilted arrangement of discs in columns. Columns of tilted discs have not been observed before in computer simulations, although they have been observed in experimental systems [9]; the columns exhibiting a rectangular array where molecules in adjacent columns have alternate tilt, or a square array where the molecules are consistently tilted in the same direction. Calamitic Gay-Berne particles have been observed to form a tilted smectic B phase [10]. In previous simulations of discogens the resultant crystal phase has exhibited rectangular and hexagonal arrays: the rectangular array occurring at high density where discs in columns are staggered and interdigitated with respect to those in neighbouring columns [11].

IV.3.2.6 Discotic HGBLR Centres: Brief Summary

From analyses of the data presented thus far, we have evidence that the system of disc-like HGBLR centres exhibits three phases on cooling from an isotropic liquid. A discotic nematic phase forms after a sharp transition from the isotropic liquid. There is no distinction between the coefficients of diffusion resolved with respect to the director in the nematic phase. The discotic nematic phase is stable over a relatively large reduced temperature range but subsequent cooling yields a highly orientationally ordered phase, itself stable over only a relatively short

temperature range. This highly ordered phase is characterised by a one dimensional density wave running through the simulation box parallel to the system director $\hat{n}(t)$. This latter observation is consistent with the disc-like HGBLR centres arranging themselves in a layered structure. Figure IV.14g presents another enlarged view of the system of figures IV.14c and IV.14d: examples of the highly ordered phase. Close examination reveals the existence of short stacks of HGBLR discs. It is these short stacks that may be responsible for the density wave described by $g_1(\eta^*)$. In this respect the phase presents a degree of translational order, demonstrating some columnar features. This highly ordered phase remains fluid and is thus distinct from the crystal phase. We note that there is a greater tendency for the centres to diffuse perpendicular to the system director than parallel to it. Finally the diffusion of particles essentially ceases. A three dimensionally ordered, but non-close packed crystal phase results. In both the highly ordered phase and the crystal phase the constituent discs appear to be tilted within the columns.

IV.4 Calamitic HGBLR Simulations

IV.4.1 Details of the Calamitic Simulations

For the rod-like parameterised HGBLR centres the well depth anisotropy was chosen as $\varepsilon_e / \varepsilon_s = 0.2$ thus favouring a side-side interaction. In order to facilitate a ready comparison between the discotic and calamitic simulations the same reduced density of $\rho^* = 1.1$ was chosen. Results are presented here for 256 and 500 particles simulated in the microcanonical ensemble. The simulations were basically performed using the same methods outlined in section IV.3.1 above. There are some subtle differences and these are detailed below.

In order to investigate the possibility of hysteresis existing at phase transitions, both a series of cooling and a series of heating runs were performed with the $N = 256$ system. Firstly a system of rod-like HGBLR centres was cooled, by scaling just the translational velocities by a factor 0.8: the same method as employed for the discs, described in section IV.3.1. The final coolest configuration generated from these runs was then taken as the starting configuration for a series of heating runs, in which the particle translational velocities were scaled by a factor 1.2 between each simulated state point. At each state point the simulation consisted of an equilibration run of 15,000 steps followed by a production run of a further 15,000 steps employing a time step of $\Delta t^* = 0.003$ for both the heating and cooling runs; twice the value of $\Delta t^* = 0.0015$ used for the disc-like HGBLR centres.

It was possible to employ a higher time step with the rods whilst still maintaining fluctuations in the total energy of the systems at better than one part in 1000. The reason for this may be illustrated by considering figures IV.2 and IV.3. The rod-like parameterised HGBLR potential is less rapidly varying at its minimum

compared to the disc-like parameterised potential. Within the microcanonical ensemble, fluctuations in the total potential energy of the system necessarily produce opposing fluctuations in the total kinetic energy under the constraint that the total energy must remain constant. With a less rapidly varying potential function and therefore smaller fluctuations in kinetic energy, it is possible to employ a larger time step in solving the equations of motion without harming energy conservation.

Thermodynamic variables and instantaneous configurations were stored from the production runs every 50 steps. In this manner the rod-like systems were run for the same total length as the non-extended disc-like simulations, the subsequent ensemble averages being calculated over the same size interval as for the disc-like systems. The results from $N = 256$ disc-like HGBLR centres and $N = 256$ rod-like centres are thus directly comparable.

Further a series of cooling runs were performed with a similar system of rod-like HGBLR centres but with an increased system size of $N = 500$. These latter simulations were performed in an attempt to qualitatively estimate the effect of finite system sizes with small particle numbers.

The cooling simulations (256 and 500 particles) were started from an α -fcc lattice at high temperature. The particles were simulated in a cubic box with full periodic boundary conditions. Close to subsequently identified phase transitions some of the simulations were extended.

IV.4.2 Calamitic Simulation Results

IV.4.2.1 Energy Fluctuations, Potential Energy and the Second Rank Orientational Order Parameter

Values of the average potential energy per particle, $\langle V^*/N \rangle$ and the second rank order parameter $\langle P_2 \rangle$ for the both the cooling and heating $N = 256$ and $N = 500$ systems are presented in tables IV.5, IV.6 and IV.7 respectively. Figure IV.15a shows the behaviour of the potential energy as the smaller system is firstly cooled from $\langle T^* \rangle \approx 3.1$ to $\langle T^* \rangle = 0.34$. The final configuration of the cooling runs was taken as the input to a series of heating runs. The behaviour of the potential energy therefore, from $\langle T^* \rangle = 0.34$ to $\langle T^* \rangle = 5.5$ for the $N = 256$ system is presented in figure IV.15b (some higher temperature data are not presented in this figure, in order to improve the scale, but are included in table IV.6). Both these figures appear to show two discontinuities in the behaviour of the potential energy, although this is clearer in the figure IV.15a. As has been observed in the case of the disc-like simulations as the temperature moves to lower values the potential energy becomes increasingly negative. The decrease in potential energy seems to occur in three distinct phases. Up to and including $\langle T^* \rangle = 1.71$ the potential energy is decreasing with a relatively shallow gradient. A discontinuity in the behaviour of $\langle V^*/N \rangle$ is evidenced through an increasing (negative) gradient until about $\langle T^* \rangle = 0.88$ where there is a second discontinuity occurs and $\langle V^*/N \rangle$ continues to tend to lower values but less steeply.

By fitting straight lines to the branches of figure IV.15a, the entropy of observed transitions was estimated to be $\Delta\langle V^*/N \rangle / \langle T^* \rangle \approx 0.5$ each, using a method outlined in section IV.3.2.1. This is slightly less than was observed for the disc-like HGBLR centres where $\Delta\langle V^*/N \rangle / \langle T^* \rangle \approx 0.6$ was estimated.

$\langle T^* \rangle$	$\langle V^*/N \rangle$	$\langle P_2 \rangle$
3.14±0.07	-0.8±0.2	0.08±0.03
3.16±0.06	-0.9±0.2	0.07±0.02
2.66±0.06	-1.4±0.1	0.08±0.03
2.28±0.05	-1.8±0.1	0.08±0.03
1.98±0.04	-2.2±0.1	0.12±0.03
1.71±0.04	-2.7±0.1	0.16±0.05
1.60±0.04	-3.3±0.1	0.44±0.04
1.50±0.05	-3.9±0.1	0.58±0.03
1.39±0.04	-4.5±0.1	0.67±0.03
1.29±0.04	-4.9±0.09	0.73±0.02
1.18±0.03	-5.32±0.08	0.78±0.02
1.08±0.03	-5.71±0.08	0.81±0.01
0.97±0.03	-6.02±0.08	0.85±0.01
0.87±0.02	-6.32±0.06	0.874±0.008
0.88±0.02	-6.79±0.06	0.883±0.007
0.78±0.02	-7.02±0.06	0.894±0.006
0.70±0.02	-7.25±0.05	0.911±0.007
0.62±0.02	-7.45±0.04	0.922±0.005
0.55±0.02	-7.61±0.04	0.935±0.003
0.49±0.01	-7.76±0.03	0.941±0.004
0.43±0.01	-7.91±0.03	0.947±0.004
0.38±0.01	-8.02±0.03	0.954±0.002
0.34±0.01	-8.12±0.02	0.961±0.002

Table IV.5

Average temperature $\langle T^* \rangle$, average potential energy per particle $\langle V^*/N \rangle$ and second rank order parameter $\langle P_2 \rangle$ for the cooling runs with $N = 256$ rod-like HGBLR centres parameterised as described in the text. Errors are indicated to ± 1 standard deviation of the arithmetic mean.

$\langle T^* \rangle$	$\langle V^*/N \rangle$	$\langle P_2 \rangle$
0.341±0.009	-8.12±0.02	0.962±0.002
0.40±0.01	-7.99±0.03	0.953±0.002
0.46±0.01	-7.83±0.03	0.943±0.003
0.54±0.01	-7.65±0.04	0.934±0.004
0.63±0.02	-7.42±0.05	0.919±0.004
0.74±0.02	-7.15±0.06	0.904±0.006
0.84±0.02	-6.83±0.06	0.881±0.008
0.99±0.03	-6.40±0.07	0.84±0.01
1.12±0.04	-5.91±0.09	0.82±0.01
1.22±0.04	-5.17±0.09	0.76±0.02
1.39±0.04	-4.5±0.1	0.69±0.02
1.53±0.05	-3.8±0.1	0.54±0.04
1.64±0.05	-2.8±0.1	0.18±0.06
1.95±0.05	-2.3±0.1	0.12±0.04
2.41±0.06	-1.7±0.1	0.09±0.03
2.92±0.06	-1.0±0.2	0.07±0.03
3.60±0.08	-0.4±0.2	0.07±0.03
4.48±0.09	0.4±0.2	0.06±0.02
5.5±0.1	1.3±0.3	0.06±0.02

Table IV.6

Average temperature $\langle T^* \rangle$, average potential energy per particle $\langle V^*/N \rangle$ and second rank order parameter $\langle P_2 \rangle$ for the heating runs with $N = 256$ rod-like HGBLR centres. Errors are indicated to ± 1 standard deviation of the arithmetic mean.

$\langle T^* \rangle$	$\langle V^*/N \rangle$	$\langle P_2 \rangle$
2.11±0.03	-2.10±0.09	0.07±0.02
1.84±0.03	-2.52±0.08	0.10±0.04
1.61±0.03	-2.99±0.08	0.17±0.05
1.56±0.04	-3.75±0.09	0.51±0.04
1.44±0.03	-4.30±0.08	0.62±0.02
1.33±0.03	-4.82±0.07	0.70±0.02
1.22±0.03	-5.24±0.07	0.76±0.01
1.12±0.02	-5.63±0.06	0.807±0.009
1.01±0.02	-5.95±0.05	0.832±0.007
0.92±0.02	-6.23±0.05	0.855±0.006
0.83±0.02	-6.51±0.04	0.881±0.004
0.75±0.02	-6.75±0.04	0.896±0.004
0.74±0.02	-7.16±0.04	0.899±0.005
0.67±0.01	-7.38±0.04	0.913±0.004
0.60±0.01	-7.56±0.03	0.922±0.004
0.54±0.01	-7.73±0.02	0.933±0.003
0.48±0.01	-7.87±0.08	0.944±0.003
0.429±0.008	-7.99±0.02	0.949±0.003
0.383±0.008	-8.10±0.02	0.952±0.002

Table IV.7

Average temperature $\langle T^* \rangle$, average potential energy per particle $\langle V^*/N \rangle$ and second rank order parameter $\langle P_2 \rangle$ for the cooling runs of $N = 500$ rod-like HGBLR centres parameterised as described in the text. Errors are indicated to ± 1 standard deviation of the arithmetic mean.

The system of $N = 500$ HGBLR centres was cooled from $\langle T^* \rangle = 2.1$ to $\langle T^* \rangle = 0.38$ in the light of knowledge acquired from the smaller system. Figure IV.15c shows the potential energy per particle against temperature curve for the larger system. Again the same qualitative behaviour enables us to identify three distinct phases.

An easy comparison between the heating and cooling runs and between the different size cooling runs is afforded by figures IV.15d and IV.15e respectively, presenting the relevant data on the same axes. Close inspection of these figures reveals that the the curves are not coincident over their entire lengths. Close to the discontinuities in $\langle V^*/N \rangle$ especially at the lower temperature there is evidence of hysteresis between the two cooling runs. Further, we note the evidence for system size effects presented by figure IV.15e.

It is possible that hysteresis may occur as a natural consequence of a phase transition. For example, a first order phase transition may exhibit a degree of hysteresis around the transition temperature depending from which side the transition is approached. However, it is likely when simulating small systems, that first order phase transitions will manifest themselves as weak or higher order transitions [12].

Hysteresis would also be present should the systems have not been equilibrated properly. But, as stated before in all cases equipartition of the kinetic energies of translation and rotation was observed for all runs. However this is not proof that sufficient equilibration had been achieved. Of course thermodynamic equilibrium of any system, real or simulated, is only closely approached after very long time. The problem of incomplete equilibration has often plagued

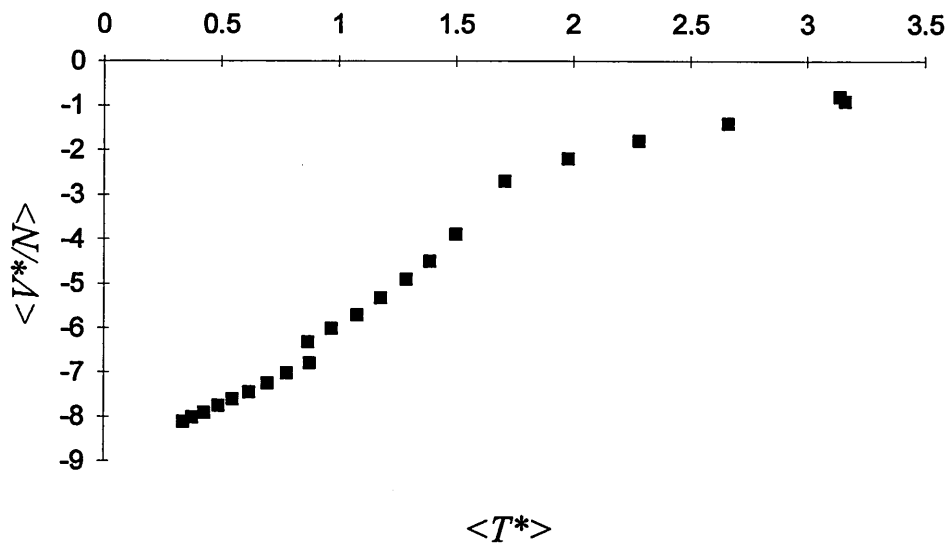


Figure IV.15a

Average potential energy per particle $\langle V^*/N \rangle$ against reduced temperature for the system of $N = 256$ rod-like parameterised HGBLR centres on cooling.

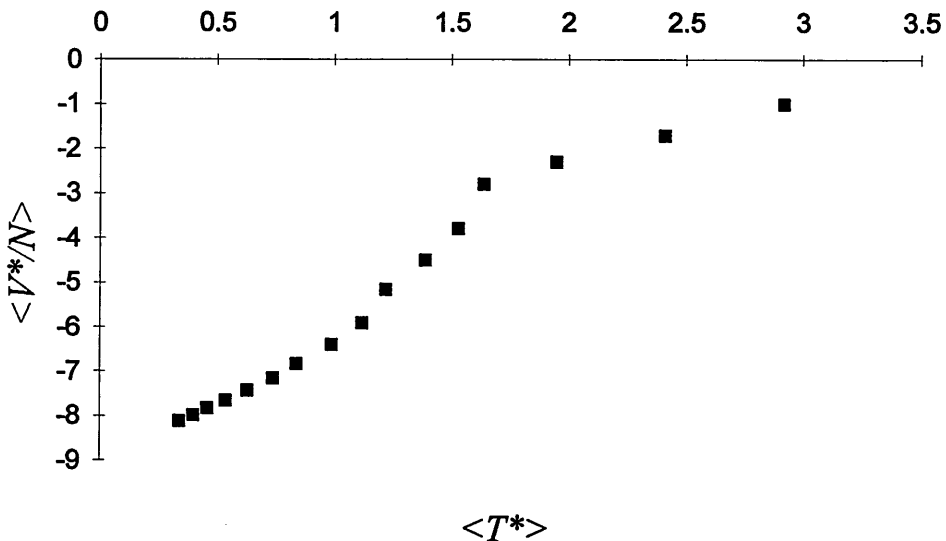


Figure IV.15b

As for figure IV.15a but for the heating runs. $N = 256$

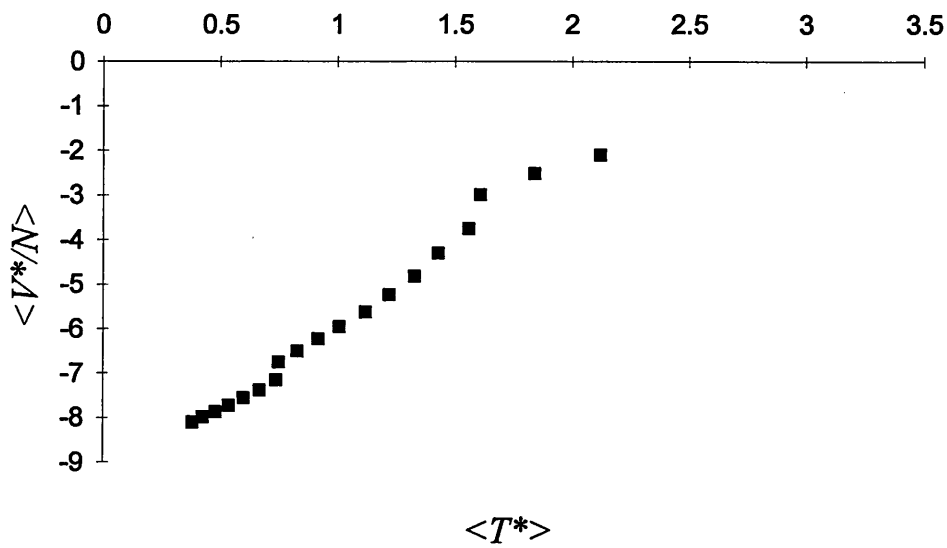


Figure IV.15c

As figure IV.15a but with system size $N = 500$.

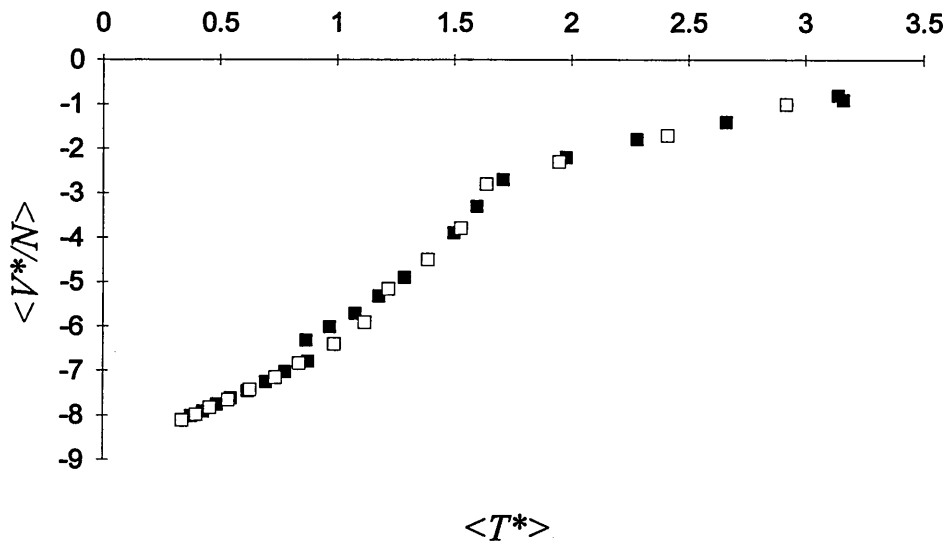


Figure IV.15d

Average internal energy per particle $\langle V^*/N \rangle$ against reduced temperature $\langle T^* \rangle$: a combination of results plotted on the same axes for ease of comparison of the heating and cooling systems: closed squares, $N = 256$ cooling runs; open squares, $N = 256$ heating runs.

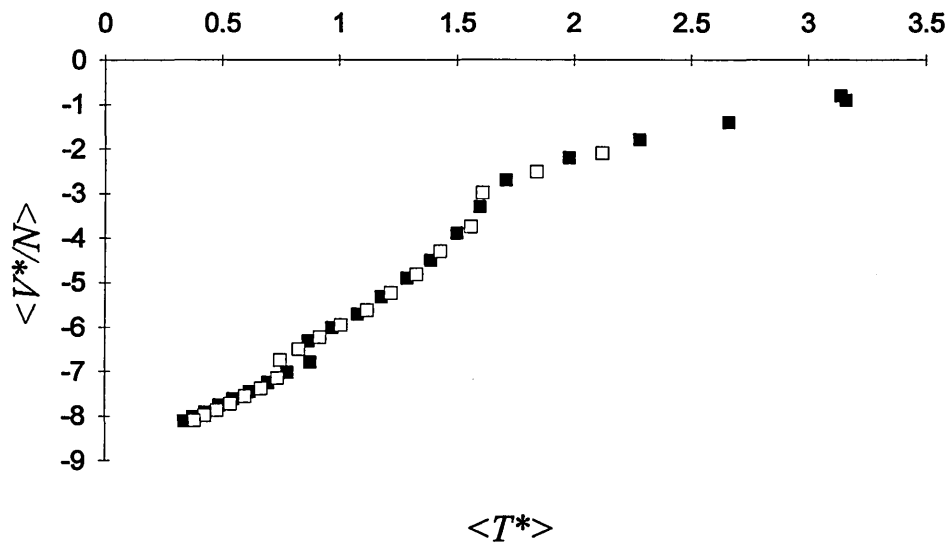


Figure IV.15e

Average internal energy per particle $\langle V^*/N \rangle$ against reduced temperature $\langle T^* \rangle$: a combination of results plotted on the same axes for ease of comparison of the different size systems: closed squares, $N = 256$ cooling runs; open squares, $N = 500$ cooling runs.

simulators. It is a factor that can only be truly overcome with long expensive simulations.

Simulation of a non-ergodic system can also cause hysteresis between successive "identical" runs to arise should the simulations become caught in cyclic regions of phase space, unable to sample different areas of phase space resulting in poor ensemble averaging.

Results of $\langle V^*/N \rangle$ against $\langle T^* \rangle$ for the $N = 500$ system, excepting points where hysteresis is apparent, are consistently lower compared to both the $N = 256$ simulations. In order to quantify finite size effects, a detailed study of different size systems would have to be undertaken. If enough information can be obtained, it may be possible to correct results from small systems by extrapolating to infinite system size. This however would be quite a time consuming process, especially at large system sizes, and this is not our aim nor desire here.

There is evidence therefore, that the simulated HGBLR centres exhibit a finite system size dependence. Hysteresis is present between cooling and heating runs of identical systems. However, such effects are small with the most likely consequences being a shifting of transition temperatures. They are not expected to affect the type of mesophases observed.

Figures IV.16a and IV.16b show the $\langle P_2 \rangle$ behaviour of the $N = 256$ system. The results of the $N = 500$ system are presented in figure IV.16c (some high temperature data have been left off this graph in order to enhance the detail in the transition region, although these data are included in table IV.6). Once again for

ease of comparison figure IV.16d and figure IV.16e respectively, present combined on the same axes, the results of the $N = 256$ heating and cooling runs and the different system size runs.

Consider figure IV.16a. We see that at high temperature above $\langle T^* \rangle = 1.71$, $\langle P_2 \rangle$ describes an orientationally disordered isotropic phase. As in the case of the disc-like HGBLR centres, $\langle P_2 \rangle$ retains a finite value due to the small size of the system under investigation. Below $\langle T^* \rangle = 1.71$, $\langle P_2 \rangle$ rapidly rises to a value of $\langle P_2 \rangle = 0.44$ indicating the onset of an orientationally ordered phase. $\langle P_2 \rangle$ continues rising less rapidly at first, before eventually tending to one, as the temperature is lowered. The same qualitative behaviour is observed for the heating runs, displayed in figure IV.16b.

Figure IV.16d shows that between the heating and cooling runs there is little evidence for significant hysteresis. A close examination of figure IV.16e presents evidence of some system size effects. Figure IV.16e shows that at high temperatures ($\langle T^* \rangle > 1.7$), $\langle P_2 \rangle$ obtains a value closer to zero for the $N = 500$ system compared to the $N = 256$ particle system. Naturally we would expect $\langle P_2 \rangle \rightarrow 0$ as $N \rightarrow \infty$ in the isotropic regime.

From our experience with the disc-like HGBLR centres there are two possible phase transitions present in both simulations, evidenced by the discontinuities in $\langle V^*/N \rangle$, occurring at lower temperatures than those seen in the system of disc-like HGBLR centres. This was anticipated in section IV.1, where the disc-like HGBLR centres were found to have a minimum energy well depth approximately five times deeper than the rod-like centres.

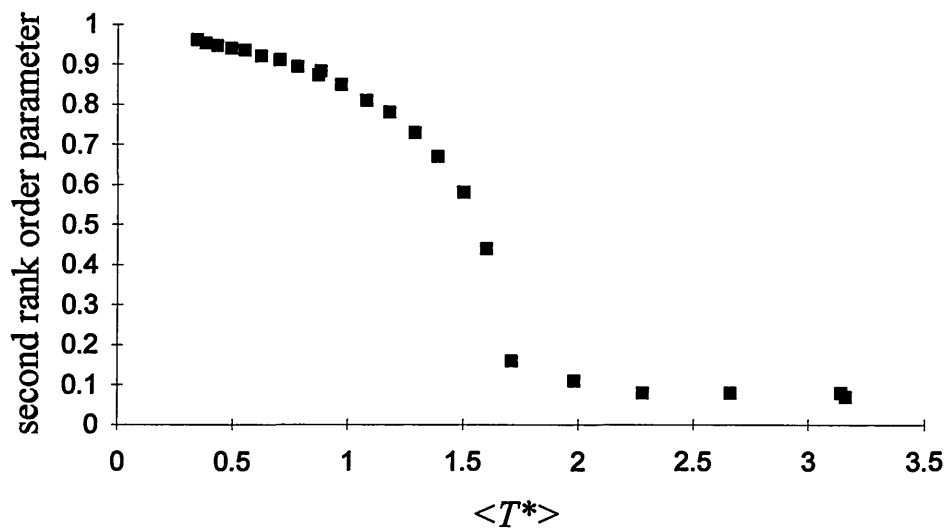


Figure IV.16a

Order parameter $\langle P_2 \rangle$ against reduced temperature $\langle T^* \rangle$ for the cooling runs of the rod-like HGBLR centres parameterised as described in the text. $N = 256$.

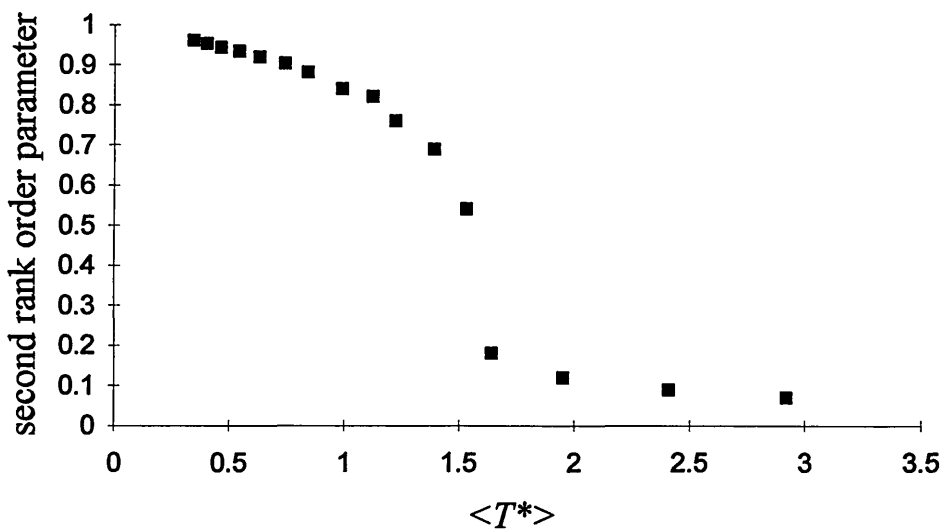


Figure IV.16b

Second rank order parameter $\langle P_2 \rangle$ against reduced temperature $\langle T^* \rangle$ for the heating runs of rod-like HGBLR centres parameterised as described in the text. $N = 256$.

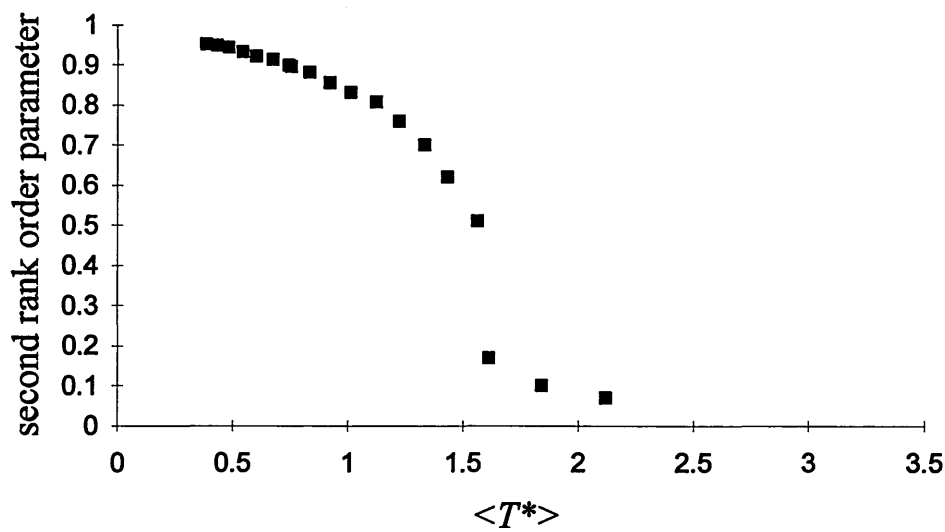


Figure IV.16c

As for the cooling runs of figure IV.16a but with system size $N = 500$.

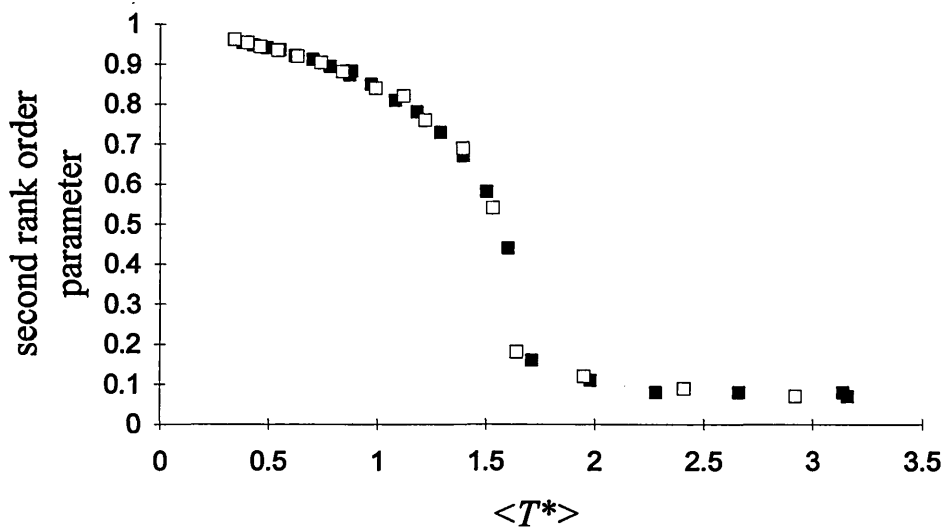


Figure IV.16d

Second rank order parameter $\langle P_2 \rangle$ against reduced temperature $\langle T^* \rangle$ plotted on the same axes for two systems of rod-like HGBLR centres considered for ease of comparison of heating and cooling systems. Closed squares, $N = 256$ cooling runs; open squares, $N = 256$ heating runs.

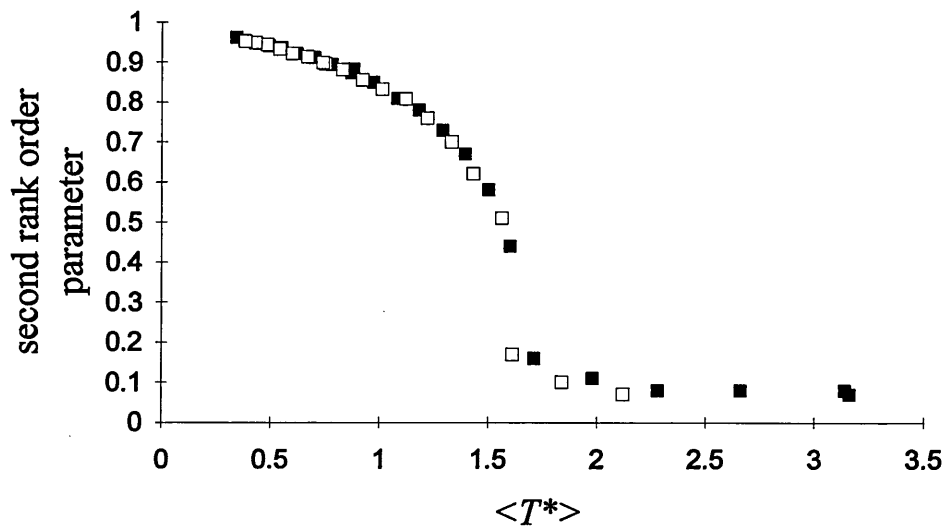


Figure IV.16e

Second rank order parameter $\langle P_2 \rangle$ against reduced temperature $\langle T^* \rangle$ plotted on the same axes for two systems of rod-like HGBLR centres considered for ease of comparison of the different system sizes. Closed squares, $N = 256$ cooling runs; open squares, $N = 500$ cooling runs.

As was undertaken for the disc-like HGBLR centres, six state points chosen close to the probable phase transitions were continued from the unscaled previous state points obtained from the $N = 256$ cooling runs, for an additional 60,000 steps recording thermodynamic data and configurations every 100 steps.

In the absence of a significant difference between the $N = 500$ and $N = 256$ cooling simulations it was decided to concentrate on the $N = 256$ cooling system. In order to better investigate the behaviour of the mean square displacement of the system of rod-like HGBLR centres it was decided at a later date to further extend three runs of the original $N = 256$ cooling simulations. Table IV.8 presents the $\langle T^* \rangle$, $\langle V^*/N \rangle$ and $\langle P_2 \rangle$ results from these extended runs. Thereafter these extended runs were themselves extended for an additional 60,000 steps, together with three simulation state points in the vicinity of the higher temperature transition which were continued from the original $N = 256$ cooling runs. The ensemble averages from these simulations are presented in table IV.9. Generally these latter data are used for the presentation of the structural and dynamic information which follows.

IV.4.2.2 Radial Distribution Function and Second Rank Orientational Correlation Coefficient

With the exception of the low temperature crystal phase, presentation of the radial distribution function together with resolved components and the second rank orientational correlation function, are based on data obtained from the runs presented in table IV.9. From the series of cooling runs with $N = 256$ the radial distribution function $g(r^*)$ and the components $g_1(\eta^*)$ and $g_\perp(r_\perp^*)$ are presented in figures IV.17 for a few judiciously chosen temperatures.

$\langle T^* \rangle$	$\langle V^*/N \rangle$	$\langle P_2 \rangle$
0.93±0.03	-6.46±0.07	0.863±0.008
0.84±0.03	-6.69±0.07	0.884±0.008
0.78±0.02	-7.02±0.06	0.889±0.007

Table IV.8

Temperature $\langle T^* \rangle$, potential energy per particle $\langle V^*/N \rangle$ and second rank order parameter $\langle P_2 \rangle$ for three simulations of table IV.5, close to the second transition extended for a further 45,000 steps. Errors are quoted to ± 1 standard deviation.

$\langle T^* \rangle$	$\langle V^*/N \rangle$	$\langle P_2 \rangle$
1.98±0.05	-2.3±0.1	0.12±0.04
1.72±0.05	-2.7±0.1	0.19±0.07
1.57±0.06	-3.3±0.2	0.38±0.08
0.93±0.03	-6.47±0.07	0.861±0.009
0.84±0.02	-6.71±0.06	0.879±0.009
0.78±0.02	-7.03±0.06	0.897±0.007

Table IV.9

Temperature $\langle T^* \rangle$, potential energy per particle $\langle V^*/N \rangle$ and second rank order parameter $\langle P_2 \rangle$ for the six runs close to observed transitions. The three higher temperature runs are continuations of state points of table IV.5, the later three are continued from table IV.8. Simulations runs were of length 60,000 steps. Errors are quoted to ± 1 standard deviation.

Figure IV.17a illustrates the radial distribution function and the components $g_1(\eta^*)$ and $g_\perp(r_\perp^*)$, corresponding to the extended run at $\langle T^* \rangle = 1.57$ and ensemble average $\langle P_2 \rangle = 0.38$; just after the sudden rise in order parameter shown in figure IV.16a. According to the value of $\langle P_2 \rangle$ the system is a low ordered nematic phase. This is corroborated by figure IV.17a which shows typical liquid like behavior for $g(r^*)$ and its components.

Figure IV.17b was computed from a run with ensemble averages $\langle T^* \rangle = 0.93$ and $\langle P_2 \rangle = 0.861$ just before the second lower temperature transition occurs. In contrast the following figure IV.17c, comes from a simulation just after the transition: $\langle T^* \rangle = 0.84$ and $\langle P_2 \rangle = 0.879$. The function $g(r^*)$ of figure IV.17b again displays behaviour typical of a liquid. The initial peak and subsequent oscillations have increased indicative of a more ordered short range structure present at the lower temperature. More interestingly the component $g_\perp(r_\perp^*)$ shows the presence of a one dimensional density wave perpendicular to the direction of the director. This is consistent with the rod like particles exhibiting short range order perpendicular to the molecular symmetry axis. Apart from a slight increase in the final peak magnitude perhaps due to incorrect normalisation as suggested in section IV.3.2.2, compared with figure IV.10b of the disc-like HGBLR simulations, the oscillations die away in the simulation box with increasing r_\perp^* as one would expect. The first significant peak of $g_\perp(r_\perp^*)$ occurs at $r_\perp^* = 1.0$ compared to $\eta^* = 0.9$ for the analogous function $g_1(\eta^*)$ in the case of the disc-like HGBLR centres. Subsequent peaks occur at distances somewhat less than $r_\perp^* = 1.0$. There appears to be no evidence for structure in the $g_1(\eta^*)$ function indicating that the HGBLR rods are uniformly distributed along the direction of the director.

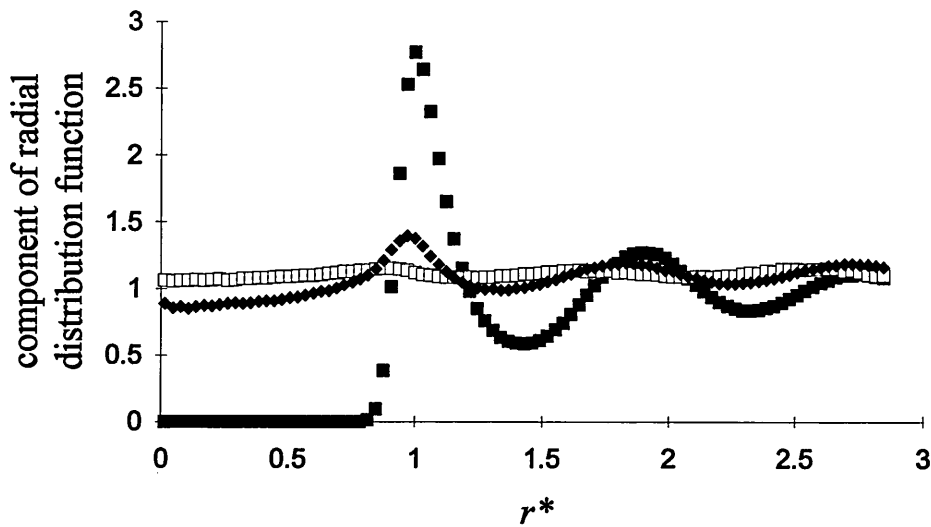


Figure IV.17a

The radial distribution function and components resolved parallel and perpendicular to the director for rod-like HGBLR centres at $\langle T^* \rangle = 1.57$. Symbols: closed squares, $g(r^*)$; open squares, $g_1(\eta^*)$; closed diamonds, $g_{\perp}(r_{\perp}^*)$.

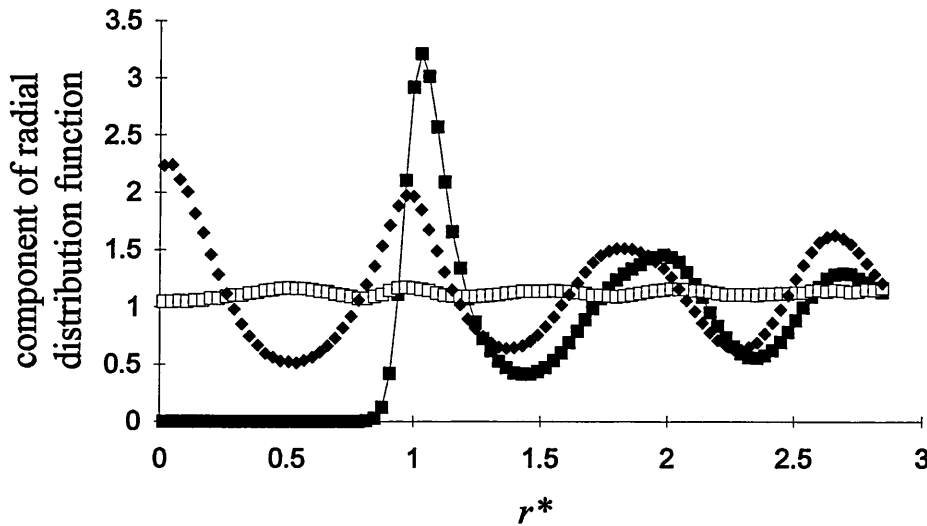


Figure IV.17b

As figure IV.17a but at temperature $\langle T^* \rangle = 0.93$. Lines have been introduced where it was thought appropriate as a guide to the eye.

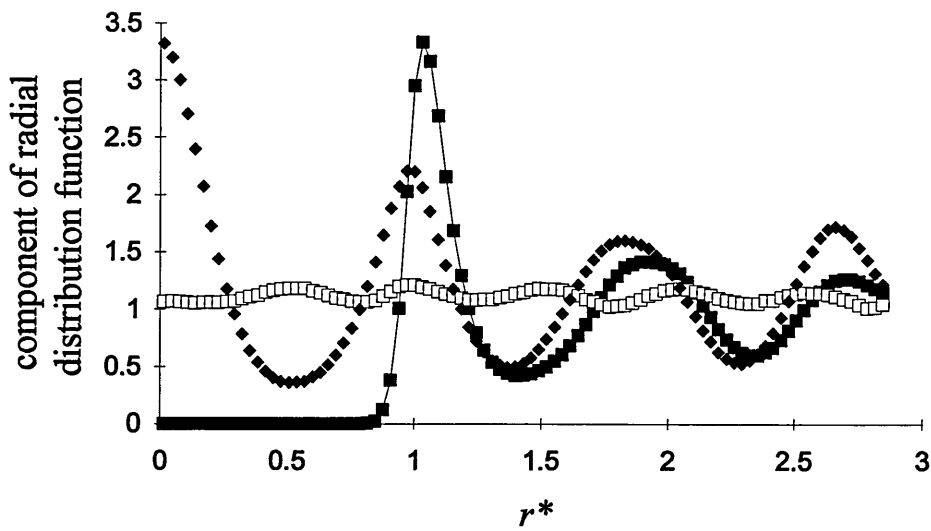


Figure IV.17c

As figure IV.17a but at temperature $\langle T^* \rangle = 0.84$. Lines have been introduced where it was thought appropriate as a guide to the eye.

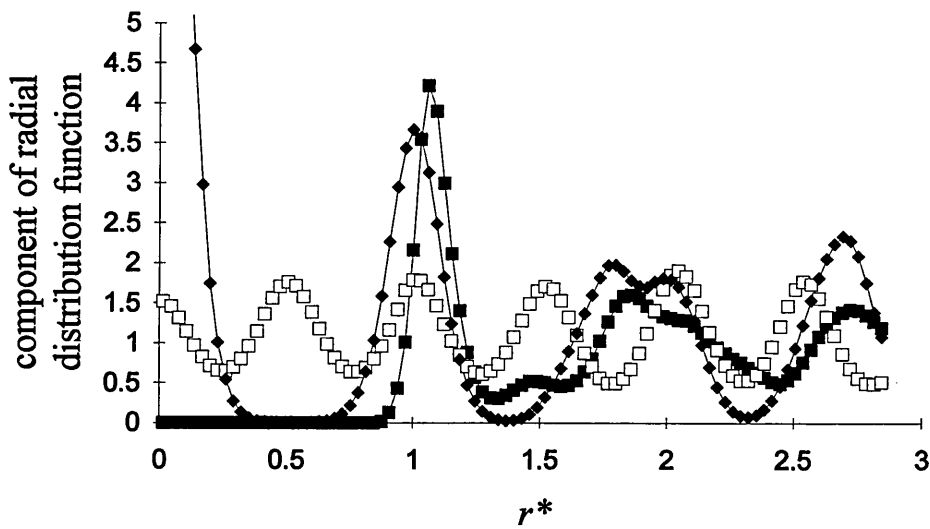


Figure IV.17d

As figure IV.17a but at temperature $\langle T^* \rangle = 0.34$. Lines have been introduced where it was thought appropriate as a guide to the eye.

The functions $g(r^*)$ and $g_{\perp}(r_{\perp}^*)$ of figure IV.17c at a slightly lower temperature exhibit a behaviour similar to that seen in figure IV.17b. The height of the peaks of both functions have increased. This is very apparent with the initial peaks, indicating an increased positional correlation between nearest neighbours. The resolved component $g_{\parallel}(\eta^*)$ now begins to exhibit a series of gentle oscillations with increasing r^* implying a degree of order beginning to develop in planes lying parallel to the director $\hat{n}(t)$.

Figure IV.17d shows the behaviour of $g(r^*)$, $g_{\parallel}(\eta^*)$ and $g_{\perp}(r_{\perp}^*)$ for the lowest temperature run of table IV.5. Here $\langle T^* \rangle = 0.34$ and $\langle P_2 \rangle = 0.961$; a very highly ordered system. Structure is present in all the functions shown.

Figure IV.18 shows the behaviour of the second rank orientational correlation function for the same four simulation runs considered in the previous section. The higher temperature curve displays a peak at about $G_2(r^*) = 0.8$ at around $r^* = 0.8$ then quickly decays to attain a limiting value of $G_2(r^*) \approx 0.14$. Note that the function does not decay to zero and indeed $(G_2(r^*)) \approx \langle P_2 \rangle^2 = 0.37$ in agreement with our observation of a nematic phase at $\langle T^* \rangle = 1.57$. At higher temperatures $G_2(r^*)$ exhibits a higher initial peak and subsequently attains a limiting value describing a highly orientationally ordered state.

IV.4.2.3 Mean Square Particle Displacement and Diffusion Coefficients

The mean square particle displacements have been calculated for the extended runs and are presented in figures IV.19. Figure IV.19a shows the behaviour of the extended run of 60,000 steps reported in table IV.9, just after the first transition at $\langle T^* \rangle = 1.57$ into the nematic phase. We note that the mean square

particle displacement exhibits straight line liquid like behaviour. The components of mean square displacement parallel and perpendicular to the system director, both exhibit straight line behaviour also. There appears to be no difference between the resolved displacement components.

The mean square displacement behaviour shown in figure IV.19b was recorded over 105,000 steps at the reduced temperature $\langle T^* \rangle = 0.93$ and consists of the combined runs of tables IV.8 and IV.9. This system state point is well into the nematic phase with an order parameter $\langle P_2 \rangle \approx 0.86$. The unresolved component shows liquid like behaviour once again. Yet even with such a high value of the second rank order parameter both the resolved components show the same behaviour. In the case of HGBLR centres though the absence of a preferred direction of diffusion in the nematic phase is attributed to the spherical hard core and has been discussed in section IV.3.2.4.

Figure IV.19c presents the same information as IV.19b but at the lower reduced temperature $\langle T^* \rangle = 0.84$ corresponding to the state point simulated just after the second transition between two highly orientationally ordered systems. Liquid like displacement is present at long time confirming the phase remains fluid. Moreover, in the same time interval the particles have moved further at the lower temperature than during the previous state point simulation. Compare the scales of figures IV.19b and IV.19c.

Table IV.10 presents values of the diffusion coefficients obtained from the gradients of mean square displacement curves for the simulations listed in table IV.9. Diffusion coefficients are calculated from a least squares regression fit to the last 30,000 steps of the resolved and unresolved mean square displacements

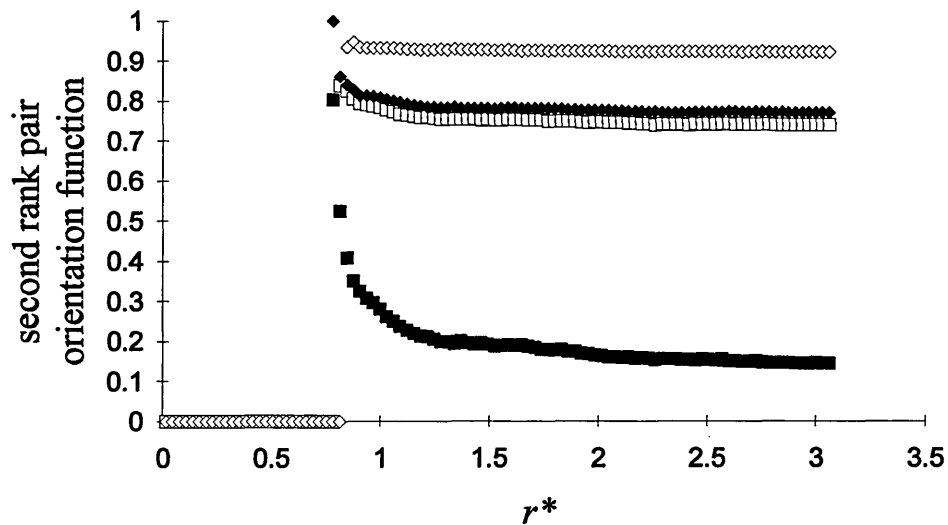


Figure IV.18

The second rank orientational correlation function $G_2(r^*)$ for the system of rod like HGBLR centres. Simulation runs are chosen to be the same as those represented in figures IV.17. Symbols correspond to the following ensemble averages: closed squares, $\langle T^* \rangle = 1.57$ and $\langle P_2 \rangle = 0.38$; open squares, $\langle T^* \rangle = 0.93$ and $\langle P_2 \rangle = 0.861$; closed diamonds, $\langle T^* \rangle = 0.84$ and $\langle P_2 \rangle = 0.879$; open diamonds, $\langle T^* \rangle = 0.34$ and $\langle P_2 \rangle = 0.961$.

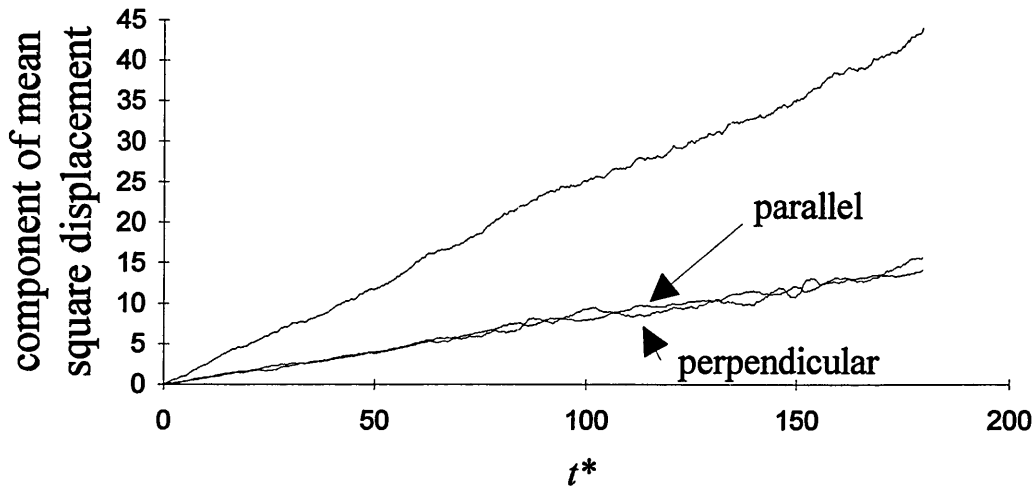


Figure IV.19a

Mean square displacement components, total and resolved with respect to the director for the 60,000 extended run of rod-like HGBLR centres as described in the text. $\langle T^* \rangle = 1.57$ and $\langle P_2 \rangle = 0.38$. The resolved components are indicated, the unlabelled curve corresponds to the total mean square displacement.

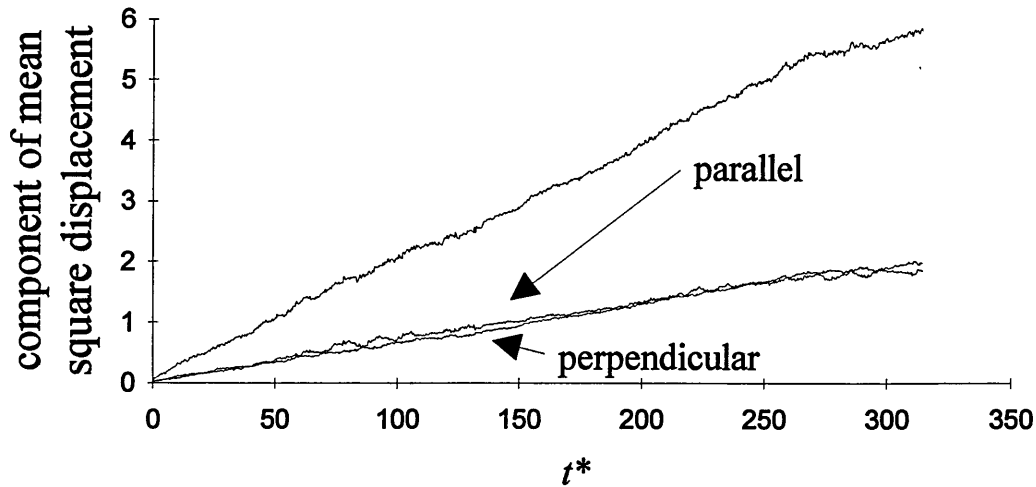


Figure IV.19b

As for figure IV.19a, but recorded over 105,000 steps, $\langle T^* \rangle = 0.93$ and $\langle P_2 \rangle = 0.861$.

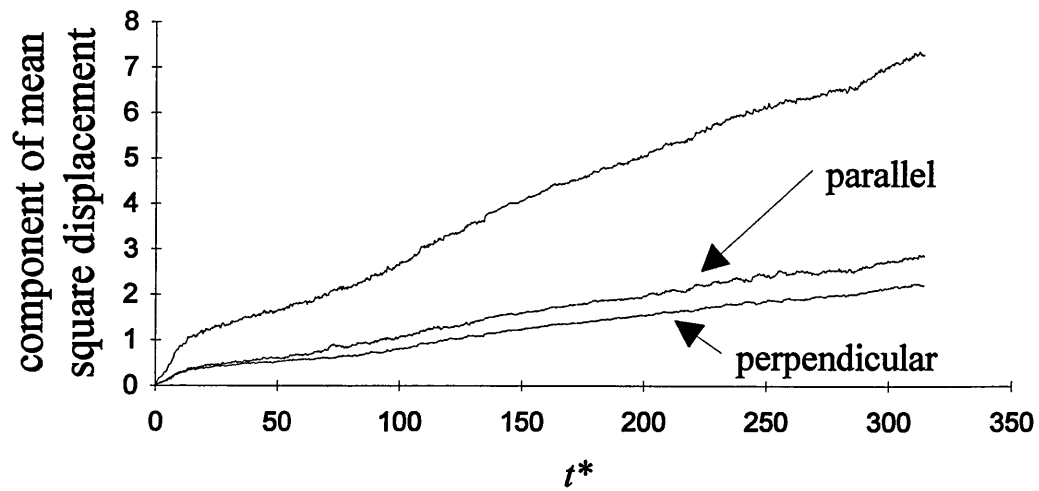


Figure IV.19c

As for figure IV.19a, but recorded over 105,000 steps, $\langle T^* \rangle = 0.84$ and $\langle P_2 \rangle = 0.879$.

$\langle T^* \rangle$	$6D^*$	$\langle P_2 \rangle$
1.98±0.05	0.3523±0.0003	0.12±0.04
1.72±0.05	0.323±0.0004	0.18±0.07
1.57±0.06	0.2399±0.0003	0.38±0.08
0.93±0.03	0.0195±0.00003	0.861±0.009
0.84±0.02	0.02384±0.00004	0.879±0.009

$\langle T^* \rangle$	$6D_{\parallel}^*$	$6D_{\perp}^*$	$D_{\parallel}^* / D_{\perp}^*$
1.98±0.05	0.1176±0.0004	0.1173±0.0003	1.00
1.72±0.05	0.108±0.0005	0.1075±0.0002	1.00
1.57±0.06	0.08±0.0003	0.08±0.0002	1.00
0.93±0.03	0.00637±0.00002	0.00657±0.00001	0.97
0.84±0.02	0.00932±0.00002	0.00726±0.00001	1.28

Table IV.10

Diffusion coefficients D^* and diffusion coefficients resolved parallel D_{\parallel}^* , and perpendicular D_{\perp}^* to the system director $\hat{n}(t)$, for the extended runs as detailed in the text. The coefficients for the higher three temperatures were calculated from a least squares regression fit to the last 30,000 steps of a 60,000 step simulation. The lower two temperatures correspond to a similar analysis performed on the last 30,000 steps of a 105,000 step simulation.

of the 60,000 or 105,000 step simulations. An increase in diffusion coefficient on transforming to the highly ordered phase is apparent from table IV.10 which shows a higher coefficient of diffusion, $6D^* = 0.02384$ at $\langle T^* \rangle = 0.84$ compared to only $6D^* = 0.0195$ at $\langle T^* \rangle = 0.93$: an increase of 22%. It is not known how long this effect persists as the temperature is lowered in the highly ordered phase. An increased coefficient of diffusion on entering a nematic phase from the isotropic liquid has been previously observed in simulations of hard ellipsoids [7].

Clearly we can see from table IV.10 that the resolved coefficients of diffusion are equal for the first three entries in the table. We note that the director does not have much meaning in the isotropic phases included in table IV.10. The direction of the director $\hat{n}(t)$ is most likely influenced by transient correlations that occur in small systems.

Interestingly for the simulation at $\langle T^* \rangle = 0.93$ just before the observed transition to the more highly ordered phase, D_{\perp}^* takes a value slightly higher than D_{\parallel}^* . This is in contrast to the result from the following simulation, after the transition, where the diffusion coefficient parallel to the director then takes a value approximately 30% higher than D_{\perp}^* . This could be the result of precursor effects, especially if the simulation at $\langle T^* \rangle = 0.93$ is very close to the actual transition temperature. We do note however the inconsistency of this observation. Perhaps one would expect such precursory fluctuations to provide for an increase in D_{\parallel}^* .

Below $\langle T^* \rangle \approx 0.8$ mean particle displacement virtually ceases. Certainly liquid like behaviour is not exhibited. Thus below $\langle T^* \rangle \approx 0.8$ the system is solid like.

IV.4.2.4 Preliminary Identification of Phases

With the information from the previous sections IV.4.2 we may attempt a preliminary identification of the phases exhibited by a system of rod-like parameterised HGBLR centres. We identify four distinct phases:

$\langle T^* \rangle > 1.57$	isotropic liquid
$1.57 \geq \langle T^* \rangle \geq 0.93$	calamitic nematic
$0.93 \geq \langle T^* \rangle \geq 0.80$	highly ordered columnar/smectic
$\langle T^* \rangle < 0.80$	crystal

Although the phases transition temperatures are not necessarily precise, a limitation of the NVE ensemble, it is clear that the highly ordered phase persists for only a short range of reduced temperature.

IV.4.2.5 Graphical Representation of Calamitic HGBLR Centres.

Figures IV.20 comprise a series of snapshots taken at different temperatures from the non-extended $N = 256$ cooling runs. The molecules are represented in two different ways in the diagrams. In some figures dots are used to represent to centres of mass of the HGBLR particles, whilst in other figures the HGBLR particles are represented by a line segment of correct relative orientation \hat{u} and length of unity i.e. σ_0 . The thick line running through the centre of the box represents the orientation of the director.

Figure IV.20a shows a view looking down the director of the nematic phase; $\langle T^* \rangle = 1.29$ and for this configuration $P_2 = 0.71$. Figure IV.20b shows a view of the same system looking perpendicular to the director. The nematic like

arrangement of the symmetry axes of the HGBLR centres is clearly visible in figures IV.20b and IV.20a. The particles are shown to be aligned along the director with no apparent ordering perpendicular to this direction. One again we note that at even this relatively high value of the second rank order parameter, the system does not reflect the often rather idealised representations of the nematic phase that are presented in text books.

Figure IV.20c shows the centre of mass positions of the HGBLR rods at the lower temperature of $\langle T^* \rangle = 0.88$ with a corresponding $P_2 = 0.90$ in the highly ordered phase, looking almost down the director. The centres of mass of the HGBLR particles appear to be approximately ordered with hexagonal symmetry. Figure IV.20d shows the same configuration but looking perpendicular to the director. The centres of mass are distributed in layers consistent with the HGBLR rods adopting a smectic phase but with a degree of positional ordering within the smectic layers. At this temperature the phase is still fluid. Figure IV.20e shows a similar view to that of figure IV.20d, but this time the orientations of the particles are demonstrated. From the radial distribution function of figure IV.17b it is clear that the appearance of a density wave perpendicular to the director precedes the formation of order parallel to the director. However it is clear that long range correlations parallel to the director begin to develop at lower temperatures. Thus it seems that the particles firstly tend to arrange into columns; the particles themselves being disordered within these columns. The arrangement of columns exhibits hexagonal symmetry, but this is not perfect due to the fluidity of the phase. The view of figure IV.20c is equivalent to projecting the centres of mass of the HGBLR particles on to a single plane. It is apparent that the best view of the approximate hexagonal

symmetry is obtained when this plane is not perpendicular to the director. Thus the columnar axes are not coincident with the director.

The final three figures IV.20f, g and h are similar representations as the previous three but at the lower temperature of $\langle T^* \rangle = 0.34$ and these views have $P_2 = 0.96$. Figure IV.20f shows a view looking down the system director. The hexagonal symmetry of the solid phase is clearly visible. The tilt of the columnar axes with respect to the system director has disappeared. Figure IV.20g shows a view of the centres of mass looking perpendicular to the director. Clearly the particles are arranged in layers lying parallel to the director. There is also ordering visible in planes running perpendicular to the director. Figure IV.20h is a similar view as figure IV.20g. but includes the orientation of the particles and confirms that the columns are now aligned along the direction of the director.

IV.4.2.6 Calamitic HGBLR Centres: Brief Summary

We identify four distinct phases formed by the system of rod-like HGBLR centres. As with the disc-like centres, cooling from the isotropic liquid yields a nematic phase, although this forms at a lower reduced temperature than for the former. The nematic phase is stable over a relatively large temperature range as seen for the disc-like centres. Similarly, subsequent cooling yields a highly orientationally ordered phase which also exhibits a degree of translational order, though it remains fluid. It appears that the rod-like particles initially form a columnar type structure, but as the rods within columns become more regularly ordered a layer like smectic phase develops. Eventually a crystal phase is formed which has hexagonal symmetry.

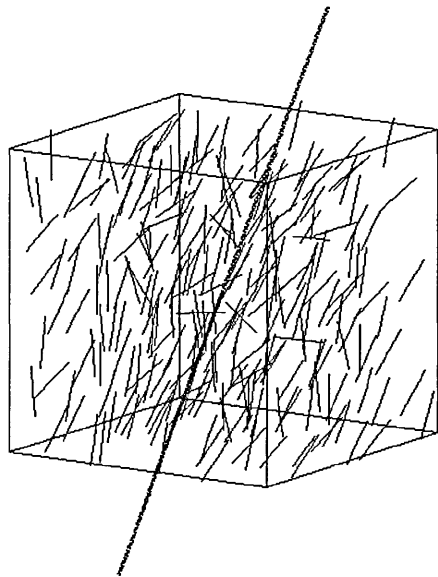
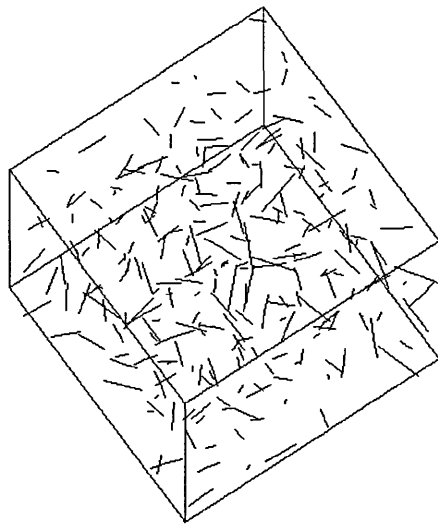


Figure IV.20a (top) and Figure IV.20b (bottom)

Two views of a nematic configuration. Figure IV.20a shows a view looking down the director $\hat{n}(t)$, whereas figure IV.20b shows a view looking perpendicular to the director. The rod-like HGBLR centres are represented by a line segment of length unity. The director is indicated as a thick line drawn through the simulation box. The measured order parameter for both configurations; $P_2 = 0.71$.

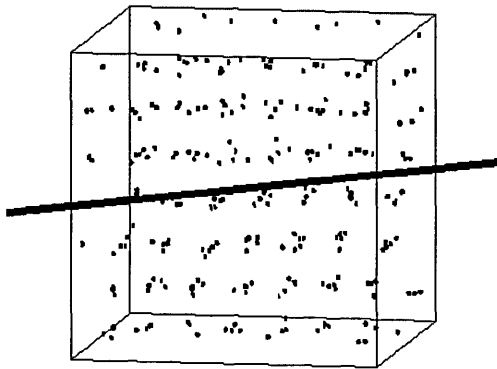
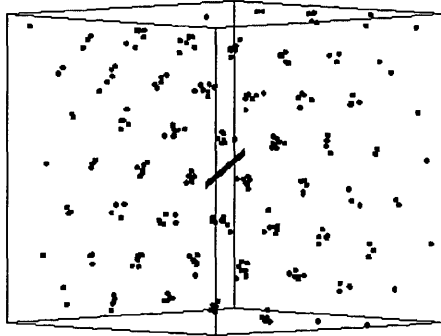


Figure IV.20c (top) and Figure IV.20d (bottom)

Two views of the centre of mass positions of the rod-like HGBLR centres in the highly ordered phase. Figure IV.20c shows a view looking down the columnar axes. Figure IV.20d shows a view approximately perpendicular to the director, showing the particles exhibiting a degree of positional ordering within the columns. Particles are represented by a line segment of length unity. The director is indicated as the thick line drawn through the simulation box. $P_2 = 0.90$ for both configurations.

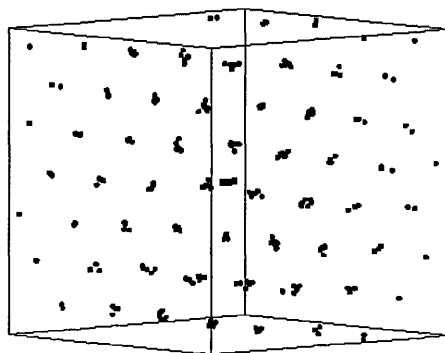
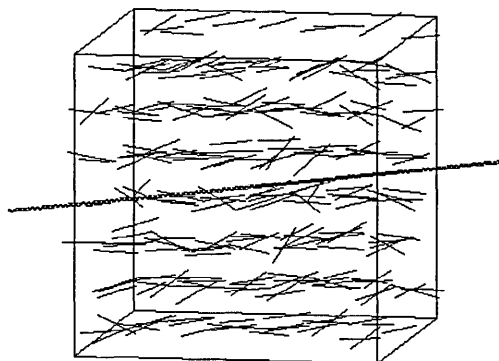


Figure IV.20e (top) and figure IV.20f (bottom)

Figure IV.20e presents the same view as figure IV.20d, but on this occasion the rod-like HGBLR centres are represented as line segments of length unity. Figure IV.20f shows a view of the crystal phase looking down the director. The centres of mass of the HGBLR centres are represented as dots. The hexagonal symmetry of the crystal is clearly visible. For this snapshot $P_2 = 0.96$

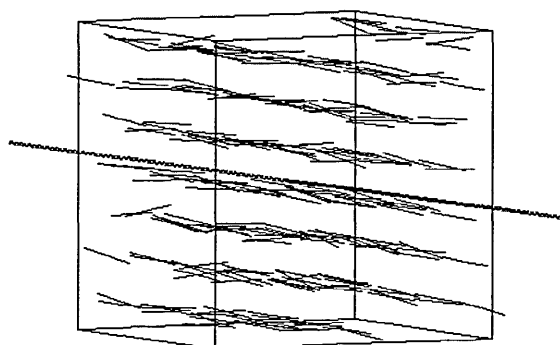
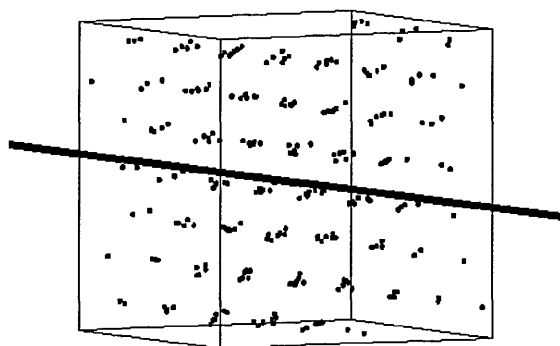


Figure IV.20g (top) and figure IV.20h (bottom)

Two views of the crystal phase seen perpendicular to the nematic director. Figure IV.20g shows the centres of mass of the HGBLR particles. Figure IV.20h shows the same view but this time the HGBLR rods are represented by line segments of length unity.

IV.5 Summary Comparison of Discotic and Calamitic HGBLR Centres

IV.5.1 Phase Transition Temperatures

Both the disc-like and rod-like single-site HGBLR centres showed four distinct phases. The approximate transition temperatures of these on cooling from the isotropic liquid are shown below.

<u>Discs</u>	<u>Rods</u>
isotropic	isotropic
↓ $\langle T^* \rangle = 5.5$ ↓	↓ $\langle T^* \rangle = 1.57$ ↓
discotic nematic	calamitic nematic
↓ $\langle T^* \rangle = 2.8$ ↓	↓ $\langle T^* \rangle = 0.93$ ↓
highly ordered/columnar	highly ordered columnar/smectic
↓ $\langle T^* \rangle = 2.6$ ↓	↓ $\langle T^* \rangle = 0.80$ ↓
non-close packed honeycomb crystal	crystal with hexagonal symmetry

It is immediately obvious that the mesophases formed by the disc-like centres are stable at higher temperatures than the rod-like particles. This was anticipated from the observation that the well depth of the disc-like HGBLR potential is five times deeper than that of the rod-like potential for the deepest well depth in each case. Both systems show the same qualitative behaviour of a relatively stable nematic, followed by a highly ordered fluid phase stable over a short temperature range before a crystal forms.

IV.5.2 Anisotropic Diffusion Effects

It is clear that in the nematic phases that no distinction exists between the coefficients of diffusion resolved parallel and perpendicular with respect to the nematic director $\hat{n}(t)$, contrary to what is observed in real liquid crystal systems.

This effect is attributed to the spherical hard core nature of the HGBLR centres. On entering more highly ordered phases a distinction does arise. The coefficient of diffusion perpendicular to the site symmetry axis is shown to be greatest in the case of disc-like parameterised centres, whereas it is the component parallel to the director which is enhanced in rod-like centres. This effect emerges due to the environment that the constituent particles find themselves in the highly ordered phases.

IV.5.3 Structural Effects

Both systems exhibit a true nematic phase characterised by long range orientational order in the absence of any translational order.

The onset of positional correlations in the disc-like system is characterised by a one dimensional density wave forming parallel to the director, indicative of discs stacking in columns. The discs are tilted within the columns. To a lesser degree positional ordering is also apparent perpendicular to the director. Nevertheless, the highly ordered phase remains fluid. In the eventual crystal phase the discs remain tilted with respect to the columnar axes.

Rod-like parameterised centres appear to order themselves firstly into columns; the rods being disordered within the columns and slightly tilted with respect to the columnar axis. With subsequent cooling the rods become organised within the columns to form a structure that resembles a smectic phase. The highly ordered phase is fluid. On further cooling a crystal phase forms. Within the crystal phase the initial tilt of the particles with respect to columnar axes has disappeared.

IV.6 Concluding Remarks

We have shown that the single site HGBLR centres are capable of exhibiting liquid crystal mesophases. As the HGBLR centres are characterised by a spherical hard core (for constant relative site orientation), the mesophases must be a consequence of the surrounding anisotropic attractive region. Thus we have shown that anisotropic dispersive forces are sufficient to form a variety of mesophases. This is most interesting, because it has also been shown that solely anisotropic repulsive interactions are capable of forming a variety of liquid crystalline phases [13]. It has been argued that the formation of real liquid crystal phases is due to a combination of these effects, and this view is enhanced by the evidence presented by this work.

Previous simulations of hard spheres with off-centre square well attractive regions have been attempted in order to investigate associating fluids [14], but no liquid crystal phases were observed. This is the first time simulations have been performed using a soft potential possessing a spherical hard core region but an anisotropic repulsive region.

The single-site HGBLR potential is of great interest from a theoretical point of view, and as such merits further investigation. However in the course of these studies it has not been possible to pursue such an inquiry. Rather, we have incorporated HGBLR centres into a rigid multisite model, thus recovering the shape anisotropy of real liquid crystals. The details of the molecular shape and the simulations performed on this model are presented in the following section; chapter V.

IV.7 References

- [1] Gay, J. G., and Berne, B. J., 1981, *Journal of Chemical Physics*, **74**, 3316-3319.
- [2] Adams, D. J., Luckhurst, G. R., and Phippen, R. W., 1987, *Molecular Physics*, **61**, 1575-1580.
- [3] Emerson, A. P. J., 1991, *PhD Thesis, Chapter VIII* (University of Southampton, UK).
- [4] Luckhurst, G. R., and Romano, S., 1980, *Proceedings of the Royal Society, London*, **A373**, 111-130.
- [5] Zannoni, C., 1979, *Distribution Functions and Order Parameters in The Molecular Physics of Liquid Crystals*, edited by Luckhurst, G. R., and Gray, G. W., (Academic Press, London, UK).
- [6] Allen, M. P., and Tildesley, D. J., 1987, *Computer Simulation of Liquids* (Clarendon Press, Oxford, UK).
- [7] Allen, M. P., 1990, *Physical Review Letters*, **65**, 2881- 2884.
- [8] Chandrashekar, S., 1992, *Liquid Crystals, second edition* (Cambridge University Press, Cambridge, UK).
- [9] Chandrasekhar, S., 1983, *Philosophical Transactions of The Royal Society, London*, **A309**, 93-103.
- [10] Chalam, M. K., Gubbins, K. E., de Miguel, E., and Rull, L. F., 1991, *Molecular Simulation*, **7**, 357-385.
- [11] Emerson, A. P. J., Luckhurst, G. R., and Whatling S. G., 1994, *Molecular Physics*, **82**, 113-124.
- [12] Zannoni, C., 1991 *An Introduction to the Molecular Dynamics Method and to Orientational Dynamics in Liquid Crystals* in *Molecular Dynamics of Liquid Crystals*, edited by Luckhurst, G. R., (NATO ASI, Reidel, New York, USA).
- [13] Frenkel, D., 1988, *Journal of Physical Chemistry*, **92**, 3280-3284;
Frenkel, D., 1989, *Liquid Crystals*, **5**, 929-940.
- [14] Jackson, G., Chapman, W. G., and Gubbins, K. E., 1988, *Molecular Physics*, **65**, 1-31.

CHAPTER V

SIMULATION OF THE NEMATOGEN *PARA*-TERPHENYL USING A MULTI-HYBRID-GAY-BERNE-LUCKHURST-ROMANO-SITE SITE POTENTIAL

V.1 Introduction

In this chapter we describe a methodology which may be suitable for parameterising a multi-HGBLR-site site potential to represent a realistic nematogen via comparison with a realistic atom-atom model. We have chosen a 3-HGBLR-site site potential to represent the nematogen *para*-terphenyl and in this chapter we legitimise this choice. Suitable parameters are selected and justification of the choice of these parameters is discussed.

Results are subsequently presented from molecular dynamics simulations of two models: (a) a 3-HGBLR-site site model in which the central HGBLR site is twisted about the molecular long axis with respect to the coplanar end sites in accord with a minimum energy conformation of the benzene rings of *para*-terphenyl; and (b) an all coplanar 3-HGBLR-site site model.

V.2 A 32-Lennard-Jones-Site Site Representation of an Energy Minimised Conformer of the Nematogen *Para*-Terphenyl.

Para-terphenyl has been chosen as this will allow comparison with results of an earlier study [1] in which a single-site Gay-Berne potential was parameterised to represent *para*-terphenyl. In this original study *para*-terphenyl was chosen because of its rigidity and non-polar nature. Furthermore a virtual nematic-

isotropic phase transition has been located for *para*-terphenyl at $360\pm 3\text{K}$, and is referenced in this work [1].

The energy minimised conformer of the *para*-terphenyl molecule has been calculated using the MMX [2] force field in the molecular mechanics package PCMODEL [3]. The ground state configuration has the two end benzene rings coplanar, with the central ring twisted through a dihedral angle of 39° . This compares favourably with the result of Luckhurst and Simmonds [1], who obtained the centre benzene ring twisted through 36° with respect to the coplanar end rings using a different software package. In this study we aim to consider two representations of *para*-terphenyl. One representation with the centre benzene ring twisted through 39° and another where all three benzene rings are coplanar. The parameters of the 3-HGBLR-site model to be used will be those selected to represent the twisted ring model of *para*-terphenyl in each case, i.e. the only difference between the two models will be a twist of the centre ring. This will allow us to compare the effects of the two models with respect to the location, stability and types of mesophase they may exhibit.

In order to obtain a function with which we may fit the multi-HGBLR-site potential, a *para*-terphenyl molecule was represented as a collection of 32 Lennard-Jones 12-6 sites. Three views of this molecule are shown in figure V.1. The sites were placed at the atomic centre of mass positions of the ground state *para*-terphenyl molecule as calculated using MMX above. The Lennard-Jones parameters σ_{LJ} and ϵ_{LJ} were given the values $\sigma_{LJC} = 3.35\text{\AA}$, $\sigma_{LJH} = 2.81\text{\AA}$ and $\epsilon_{LJC} = 51.2k_B\text{K}$, $\epsilon_{LJH} = 8.6k_B\text{K}$ for the carbon and hydrogen atomic sites respectively (k_B is the Boltzmann constant) [4]. Pair interactions between like atoms are easily calculated using the above parameters. Approximate

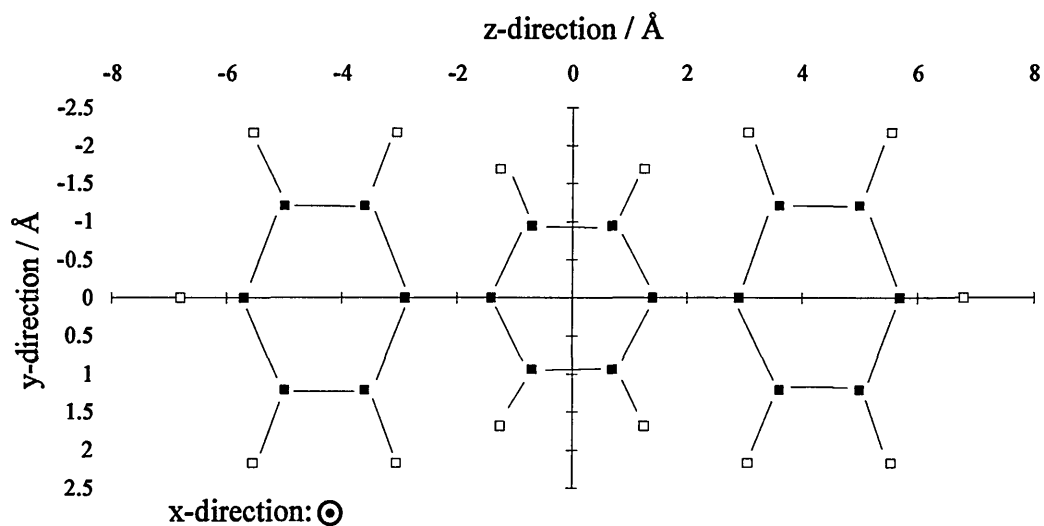


Figure V.1a

32-Lennard-Jones-site representation of the nematogen *para*-terphenyl. The molecule is shown in the y -, z -plane with the coplanar benzene ring symmetry vectors coming out of the page as indicated by the sense of the dart symbol. Solid black squares indicate carbon atoms, open squares represent hydrogen atoms. Where visible, atomic bonds have been represented as thin lines to guide the eye. The Cartesian convention established in this figure will be subsequently used when referring to the *para*-terphenyl molecule throughout this chapter.

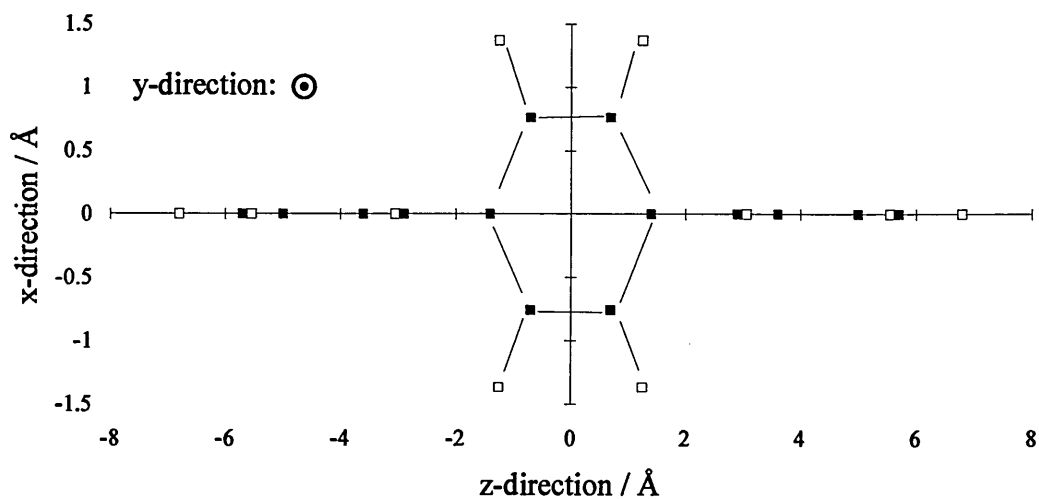


Figure V.1b

32-Lennard-Jones-site representation of the nematogen *para*-terphenyl. The molecule is shown in the x-, z-plane. The sense of the y-direction is as indicated. For key see figure V.1a.

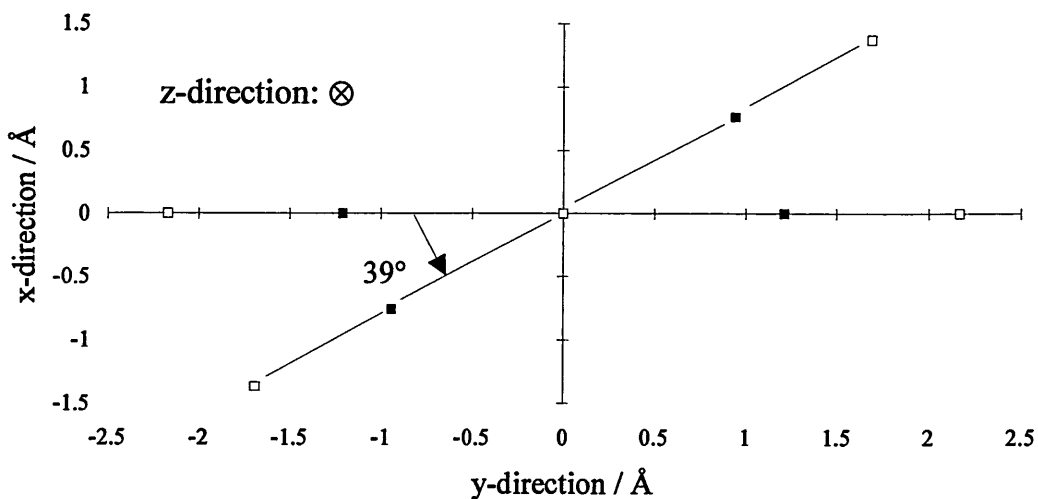


Figure V.1c

32-Lennard-Jones-site representation of the nematogen *para*-terphenyl. The molecule is shown in the x-, y-plane. The sense of the z-direction is as indicated. For key see figure V.1a.

interactions between unlike atoms, provided they do not greatly differ in electronegativity, may be evaluated using the Lorentz-Berthelot mixing rules:

$$\sigma_{\text{LJCH}} = \frac{1}{2}[\sigma_{\text{LJC}} + \sigma_{\text{LJH}}]; \quad [\text{V.1}]$$

$$\varepsilon_{\text{LJCH}} = [\varepsilon_{\text{LJC}}\varepsilon_{\text{LJH}}]^{1/2}; \quad [\text{V.2}]$$

yielding the results $\sigma_{\text{LJCH}} = 3.08\text{\AA}$ and $\varepsilon_{\text{LJCH}} = 21.0k_{\text{B}}\text{K}$ for the pair interactions between hydrogen and carbon atoms. The pair potential between two 32-Lennard-Jones-site *para*-terphenyl molecules was calculated for four different parallel configurations: a, side by side where the benzene rings lie one on top of each other; b, side by side in a T configuration in which one molecule has been rotated by 90° about its molecular long axis; c, side by side where the benzene rings lie in the same plane; d, an end to end configuration. These configurations are presented schematically in figure V.2.

It is necessary to consider separately the a, b and c side by side configurations because of the biaxiality of the *para*-terphenyl molecule. These parallel configurations have been chosen because of their importance in the formation of a nematic phase where molecules tend on average to orientate themselves with their principle symmetry axes parallel. At the virtual nematic-isotropic phase transition molecular conformations other than the ground state will be thermally accessible. However it is for the sake of simplicity that we only consider the ground state here. The form of the 32-Lennard-Jones-site site representation is shown in figure V.3 for the four configurations considered. We shall return to this figure shortly.

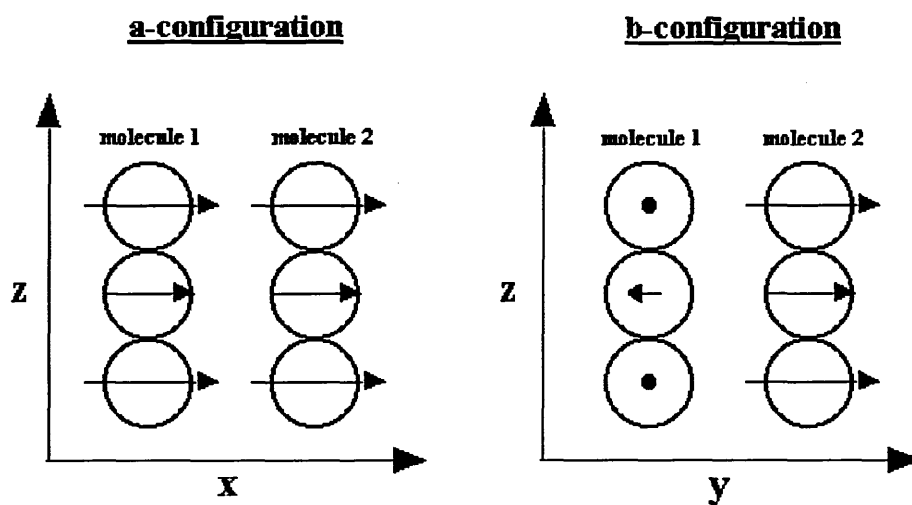


Figure V.2a

Two schematic drawings illustrating the difference between an 'on top' and a 'T' side by side configuration (configurations a and b). The circles represent the locations of the three benzene rings of each *para*-terphenyl molecule. The arrow serves to represent the orientation of the benzene rings and coincides with the principle symmetry axis of each individual benzene ring. A twisted benzene ring is represented by a reduction in the length of the arrow. The sense of the arrow shows the direction of twist. Dots in the centre of rings represent the benzene ring principle symmetry axis pointing straight up through the page, and thus the ring lies in the plane of the page. Cartesian coordinates are shown on the axes with respect to the orientation of molecule 1, as an aid to distinguishing the different configurations. These coordinates are chosen consistent with the coplanar rings of molecule 1 lying in the x-, y-plane, with the molecular long axis parallel to the z-direction as in the convention of figure V.1.

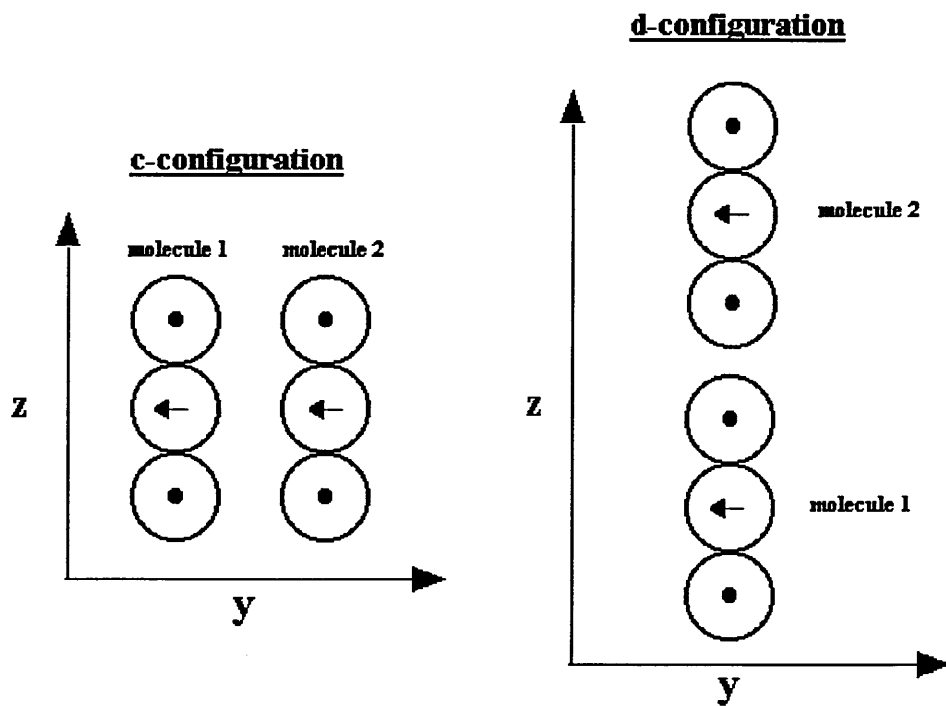


Figure V.2b

Schematic representations of configurations c and d. For a key to the meaning of the scheme see figure V.2a.

V.3 Choosing the Number of Sites and Type of Site Parameterisation of the Multi-HGBLR-Site Site Model of *Para*-Terphenyl

A rigid 3-HGBLR-site model will be used to represent each *para*-terphenyl molecule. The reasoning here is that each site will represent a single benzene ring. With three sites we hope to closely reproduce the structure of *para*-terphenyl using a minimum number of sites. The computational effort required for a multisite model interacting in a pairwise manner scales as $n^2N(N-1)$, where N is the number of molecules consisting of n sites. Clearly an increase in n causes a significant increase in the amount of time required to solve a given model.

Using three rigidly joined HGBLR sites to preserve the rigidity of the *para*-terphenyl molecule we must further decide how to; (a) parameterise the individual sites, as rods, discs or a combination of the two and (b) how we arrange the sites constituting the whole molecule.

If three rod parameterised sites are used with the site symmetry vectors pointing along the molecular long axis of *para*-terphenyl, then this model will not distinguish between configuration a and configuration c for an all coplanar three site model. In this case the scalar products of the HGBLR potential are $\hat{u}_1 \cdot \hat{u}_2 = 1$ and $\hat{r} \cdot \hat{u}_1 = \hat{r} \cdot \hat{u}_2 = 0$ for both these configurations. An alternative approach would be to have the (rod parameterised) site symmetry vectors perpendicular to the *para*-terphenyl long axis in the plane of the benzene rings. However such a rod parameterisation would be unrepresentative of *para*-terphenyl as the energy well depth minima would occur at the ends of the molecule and in between the ring systems.

Fortunately a 3-HGBLR-site disc parameterisation with the site symmetry axes perpendicular to the plane of the benzene rings does indeed distinguish between all the considered configurations a, b, c and d. Furthermore a disc-like parameterisation of the individual HGBLR sites seems a natural choice to represent the benzene rings.

Presently the possibility of using a combination of rod-like and disc-like parameterised sites complicates the model. A cross interaction between two differently parameterised sites would have to be identified within the force loop computation. Once identified the interaction would have to be characterised and the appropriate potential energy function calculated together with the corresponding derivative terms. In future however, more complex models may incorporate such cross interactions, perhaps together with an elegant method of solution. Very recently such a generalisation of the Gay-Berne potential function has been proposed [5].

With 3-HGBLR-sites parameterised as discs we may easily model a twisted centre ring by rotating its site symmetry vector about the molecular long axis. It is sufficient that an individual *para*-terphenyl molecule is represented by a position vector to the centre of mass and a unit vector describing the relative orientation of the molecular long axis, with respect to the laboratory axis system. The position of the individual sites may then be located through simple geometric translations along the direction of the unit vector. The centre site is identified and in addition it is rotated through 39° about the molecular long axis (z-direction according to the convention used in figure V.1).

Thus we shall choose to use three disc-like parameterised HGBLR sites to model *para*-terphenyl. A linear arrangement of the three HGBLR sites with the site centres coinciding with the benzene ring centres seems an appropriate starting point at which to begin to parameterise our model. Such an arrangement correctly represents the geometry of the *para*-terphenyl molecule.

Figure V.3 shows the behaviour of two 32-Lennard-Jones-site representations of *para*-terphenyl as they approach each other according to the configurations a, b, c and d. Inspection of figure V.3 shows that it is the side by side on top dimer configuration a that is the most favoured. In this configuration the benzene rings coincide leading to a very deep minimum in the potential energy at a distance of approach of 3.9Å. In the side by side configuration c the distance of closest approach is hindered by the hydrogens which stick out in the plane of the benzene rings and the energy well minimum is found at 6.9Å. The T-configuration, b, obtains a well depth minimum at a separation of 5.4Å. Because of the spherically symmetric hard core nature of individual HGBLR sites however, the distance of closest approach of 3-HGBLR-site side by side configurations are governed by the parameter σ_0 for given values of λ and χ' . With the HGBLR potential we may therefore choose only one σ_0 which will necessarily dictate the distance of closest approach of all side by side configurations. Further we note that the end to end configuration achieves a well depth minimum at 16.2Å. The values of the minimum well depths and the separations at which they occur are listed in table V.1

At the virtual nematic-isotropic transition temperature of 360K, the molecules will possess a degree of rotational motion. Rotation about the molecular long axis (which has a correspondingly relatively low principle moment of inertia I_{zz} see

section V.5) will lead to a cylindrically symmetric time averaged volume for each *para*-terphenyl molecule. This suggests the use of the larger of the side by side separation as the choice for the distance of closest approach in the 3-HGBLR-site model. Further, the distance of closest approach of the a configuration as represented by the 32-Lennard-Jones-site model is likely to be in error. Such a model does not take into consideration the large quadrupole moment associated with the delocalized conjugated π -electron systems perpendicular to the plane of the benzene rings [6]. For such a configuration the real distance of closest approach is likely to be greater than that predicted by the 32-Lennard-Jones-site model for configuration a, and may favour the T-type b configuration as in the crystalline form of triphenylene which has a large delocalised conjugated π -electron system [7]. Again this suggests the choice of the larger of the two distances of closest approach in order that we may assign a value to σ_0 for our model.

Although the inclusion of the three quadrupoles may result in a more correct description of the interaction of the 32-Lennard-Jones-site site pair potential such a representation of *para*-terphenyl was not used to parameterise the 3-HGBLR-site potential model owing to the following points. Originally *para*-terphenyl was chosen to allow comparison with the work of Luckhurst and Simmonds [1]. They fitted their Gay-Berne overlap model using a 32-Lennard-Jones-site site representation of *para*-terphenyl without a quadrupole term. It was necessary in this case however to project out the biaxiality of the of the 32-Lennard-Jones-site model in order to fit the cylindrically symmetric Gay-Berne overlap model. The choice of σ_0 in the 3-HGBLR-site site model necessarily restricts the distance of closest approach of the HGBLR sites. This reflects the increased

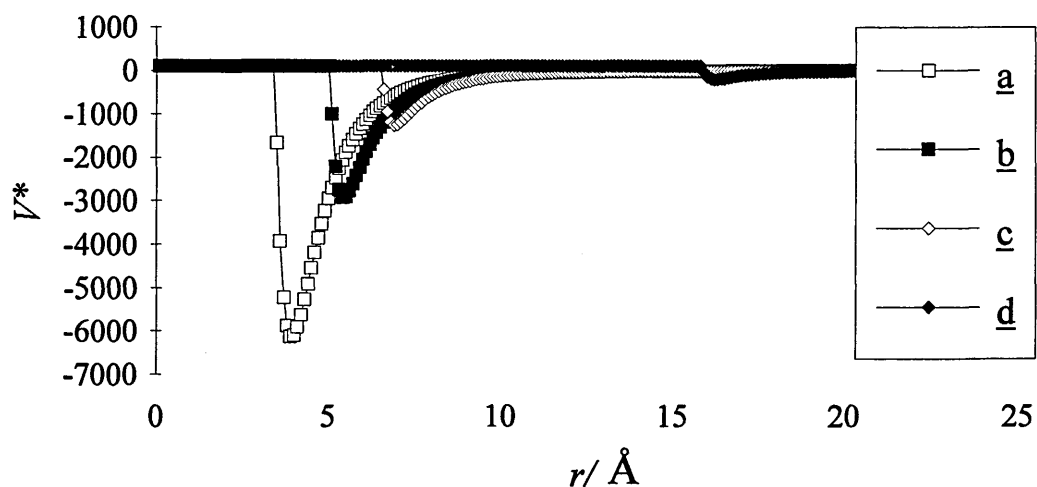


Figure V.3

A 32-Lennard-Jones-site site representation of *para*-terphenyl. Four configurations are shown. The legend corresponds to the configurations illustrated in figure V.2 For the sake of clarity values of $V > 100$ have been truncated to $V = 100$.

configuration	32-Lennard-Jones-site site		twisted central site 3-HGBLR-site site		all coplanar 3-HGBLR-site site	
	$V_{\min} / k_B K$	$r / \text{Å}$	$V_{\min} / k_B K$	$r / \text{Å}$	$V_{\min} / k_B K$	$r / \text{Å}$
<u>a</u>	-6122	3.9	-6121	6.9	-8166	6.8
<u>b</u>	-2921	5.4	-2443	6.5	-2281	6.5
<u>c</u>	-1260	6.9	-1692	6.8	-888	6.8
<u>d</u>	-205	16.2	-200	16.2	-198	16.2

Table V.1

A comparison of the locations and values of the energy well depth minimum in the pair potential between the 32-Lennard-Jones-site site model and the two 3-HGBLR-site site models for the four considered configurations of figure V.2.

distance of closest approach to be expected from benzene rings possessing a quadrupole moment in a side by side on top configuration. So a contribution to this effect is already included although it is to be noted that the position of the reduced attractive well depth minimum in this configuration expected from the inclusion of the quadrupole moment may not be well represented.

V.4 Parameterisation of a 3-HGBLR-Site Site model of *Para*-Terphenyl

Having decided which version of the 32-Lennard-Jones-site site model to use, we shall now attempt to fit the remaining parameters. By calculating the ratio of minimum well depths for the four selected configurations of the 3-HGBLR-site site model we may compare these with the ratios obtained from the 32-Lennard-Jones-site site model. For the 32-Lennard-Jones-site site model these are, corresponding to configurations a:b:c:d, equivalent to 30·0:19·5:6·2:1·0.

The interdependency of λ and χ' of the 3-HGBLR-site site model is not *a priori* obvious. A preliminary investigation into the behaviour of λ and χ' revealed that the positions of the well depth minimum for the considered configurations a, b, c and d varies depending on the values of λ and χ' (see appendix B.1). Thus it was important to adopt a tractable method for deciding on an initial value of σ_0 . In order to accomplish this the following procedure was employed. The three HGBLR sites were originally located at the site centres of the benzene rings of the 32-Lennard-Jones-site representation of *para*-terphenyl. In this case the centres of the coplanar rings are located in linear array 4·3Å either side of the centre of the twisted central ring. Having established the site-site separation an initial value of σ_0 consistent with the value of the zero crossing of the 32-Lennard-Jones-site site configuration c was chosen yielding $\sigma_0 = 6·6\text{Å}$. These values were used in an exploratory search of the available λ and χ' parameter

space. The results of which are presented in appendix B.1 A schematic representation of the 3-HGBLR-site model where the site separation is less than σ_0 is presented in figure V.4.

In order to parameterise the HGBLR potential as a disc $-1.0 \leq \chi' < 0.0$, and λ is free to take the range $-1.0 \leq \lambda \leq 1.0$. When λ or χ' take extreme values such as $\lambda > 0.9$ or $\chi' < -0.9$ the function is no longer well behaved. Thus the ranges of λ and χ' considered were altered to $-1.0 \leq \lambda \leq 0.9$ and $-0.9 \leq \chi' \leq 0.0$. Both λ and χ' were incremented in steps of 0.1 yielding what is effectively a coarse grid search over the available parameter space. For every combination of the parameters λ and χ' the potential energy function for each considered configuration was computed over a range of values of separation $0 < r \leq 30 \text{ \AA}$ in steps of 0.1 \AA. The numerical values of the location and value of the minimum well depth energy and the ratio of well depth minimum for configurations a, b and c with respect to that of configuration d are listed in appendix B.1 These data were subsequently used to create the contour plots of figure V.5.

Examination of figure V.5, the contour map corresponding to the configuration d (see figure V.5d) shows the value of the well depth minimum is constant for a given value of λ and does not depend on χ' . For all other configurations considered λ and χ' do not have such a simple relationship.

A closer inspection identifies a range of values λ which appear promising, namely, $-0.2 \leq \lambda \leq 0.2$, with χ' ranging $-0.90 \geq \chi' \geq -0.80$. Two further similar searches were performed with λ taking the above range of values with resolution $\Delta\lambda = 0.1$ and χ' taking the above range with resolution $\Delta\chi' = 0.01$.

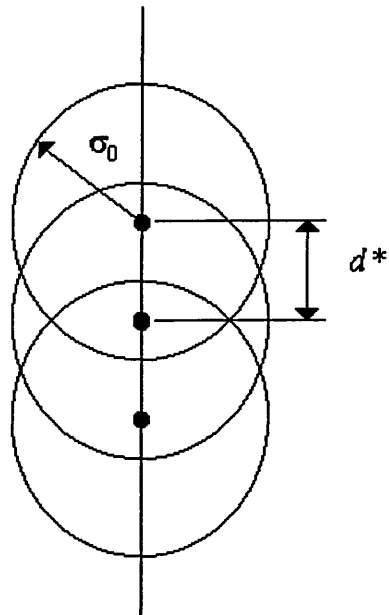


Figure V.4

A schematic representation of the 3-HGBLR-site model. The sites are arranged in linear array, each represented by a circle here. This diagram illustrates the axial ratio of the 3-HGBLR-site model where the sites are separated such that $d^* < \sigma_0$.

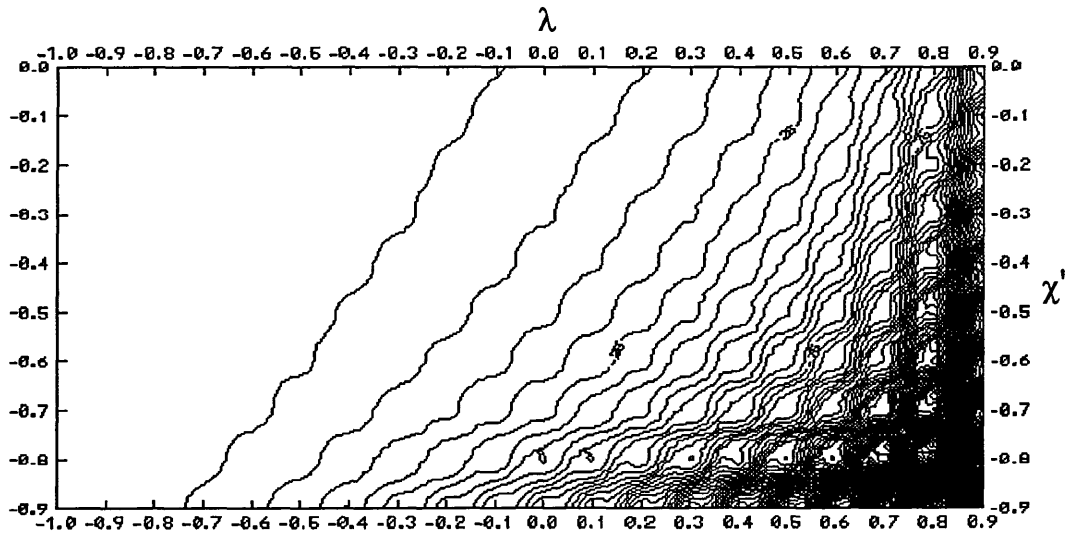


Figure V.5a

A contour map showing contours of constant well depth minimum for configuration a of figure V.2. The map is drawn in the λ, χ' plane. The minimum contour value plotted is $V^* = -1825$ and the maximum is $V^* = 0$; contours are plotted at intervals $\Delta V^* = 5$.

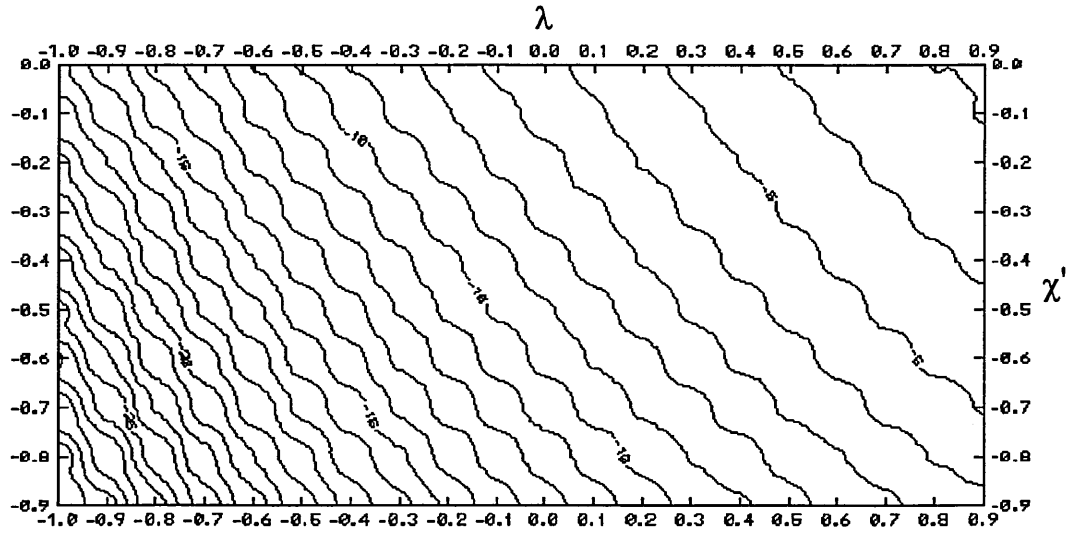


Figure V.5b

A contour map showing contours of constant well depth minimum for configuration b of figure V.2. The map is drawn in the λ, χ' plane. The minimum contour value plotted is $V^* = -30$ and the maximum is $V^* = 0$; contours are plotted at intervals $\Delta V^* = 1$.

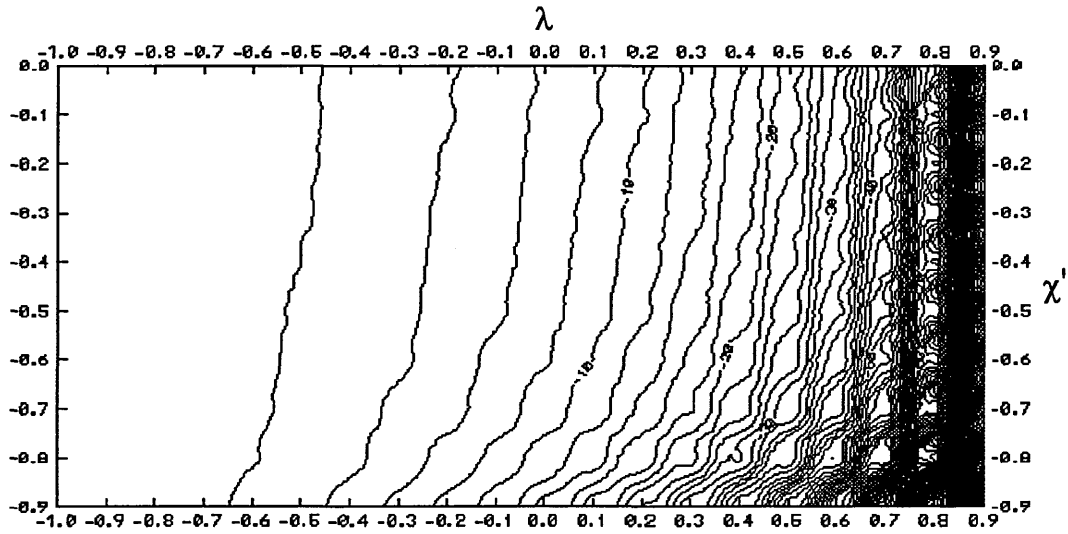


Figure V.5c

A contour map showing contours of constant well depth minimum for configuration c of figure V.2. The map is drawn in the λ, χ' plane. The minimum contour value plotted is $V^* = -370$ and the maximum is $V^* = 0$; contours are plotted at intervals $\Delta V^* = 2$.

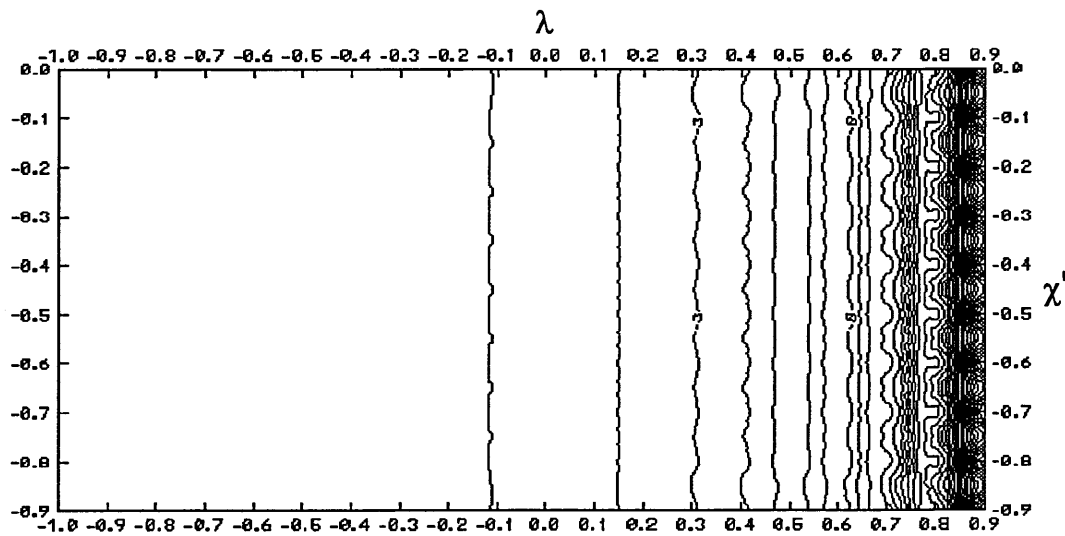


Figure V.5d

A contour map showing contours of constant well depth minimum for configuration d of figure V.2. The map is drawn in the λ , χ' plane. The minimum contour value plotted is $V^* = -38$ and the maximum is $V^* = 0$; contours are plotted at intervals $\Delta V^* = 1$.

Each search is discriminated according to the value of λ investigated. The site-site separation between HGBLR centres is chosen to be consistent with the distance of the energy well depth minimum in the end to end separation (configuration d) of 16.2\AA obtained from the 32-Lennard-Jones-site model because it is not affected by λ over the reduced range of χ' investigated. This yields a site site separation value $d = 4.65\text{\AA}$. Subsequently the value of σ_0 was adjusted to bring the most favoured configuration, a, to the adopted distance of closest approach accepted for the 32-Lennard-Jones-site site model due to the arguments presented in section V.3, *viz.* 6.9\AA , according to the value of λ investigated.

The ratios of these well depth minima and the positions at which they occur have been similarly calculated as before and are presented in appendix B.2. Through inspection values of $\lambda = -0.1$ and $\chi' = -0.83$ were selected; the corresponding minimum well depth ratios being $30.6:12.2:8.5:1.0$ for configurations a:b:c:d occurring at separations 6.9\AA , 6.5\AA , 6.8\AA and 16.2\AA respectively and the single site hard core radius taking a value $\sigma_0 = 6.0\text{\AA}$. This potential is illustrated in figure V.6, and was the parameterisation used in the ensuing simulations.

Finally, the last parameter to be fitted is the well depth parameter ε_0 . This simply scales the well depths linearly. Thus it is a simple matter to choose a value $\varepsilon_0 = 219.0 k_B K$, leading to a minimum well depth of $V^* = 6121$ comparing very favourably with that of the 32-Lennard-Jones-site site (see table V.1) for the preferred configuration a.

The potential function for the four considered configurations of the 3-HGBLR-site site potential with the parameters we have found above is shown in figure

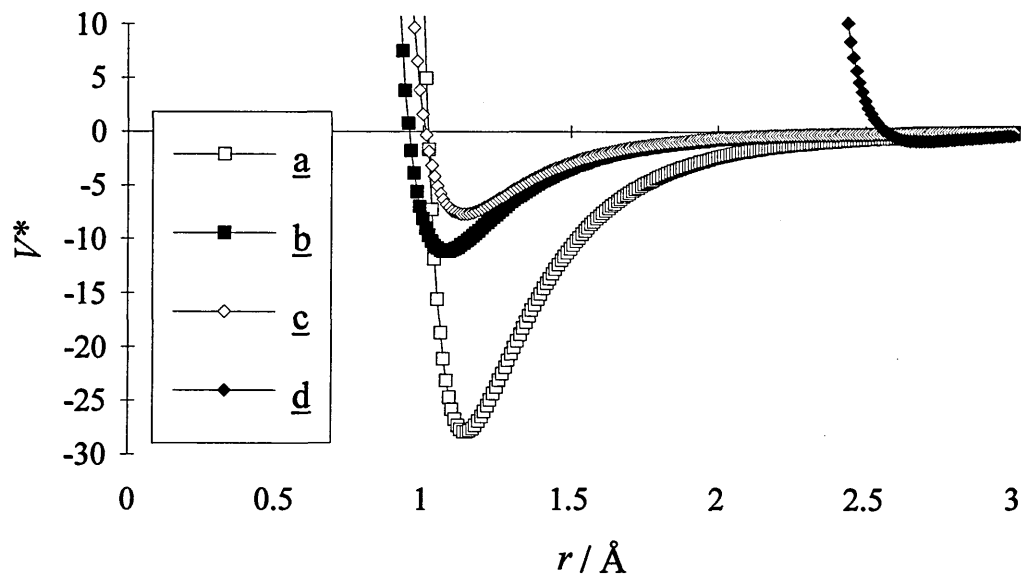


Figure V.6

A 3-HGBLR-site site representation of *para*-terphenyl as employed in the simulation: $\sigma_0 = 1.0$ and $\varepsilon_0 = 1.0$. The configurations identified in the legend correspond to the configurations described in the text and illustrated in figure V.2.

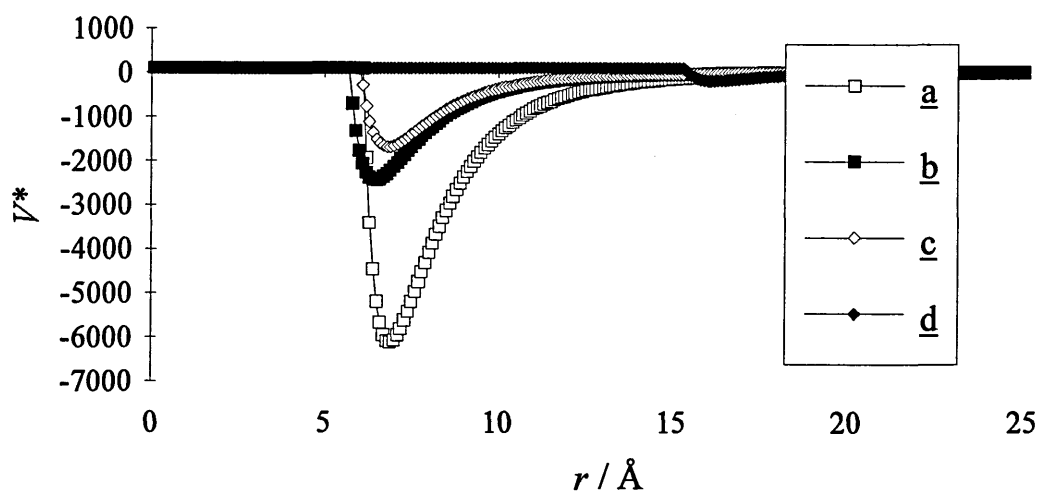


Figure V.7

A 3-HGBLR-site representation of *para*-terphenyl. The parameters used in this model are those as described in the text. For the sake of clarity values of $V > 100$ have been truncated to $V = 100$. For a key to the orientations see figure V.6 above.

V.7 Comparison of figure V.3 with figure V.7 shows that with the exception of the \underline{c} configuration, after correcting for location, the well depth minima compare very favourably with those of the 32-Lennard-Jones-site model. On closer inspection it is clear that the well widths though, are not in such good agreement. The HGBLR potential well widths are wider than those for the 32-Lennard-Jones-site model. There are several approaches that we may try to compensate for this discrepancy.

One approach may be to include a power term ν in the scaling function ϵ' , as is included in the Gay-Berne potential [10], such that the modified HGBLR potential becomes;

$$V_{\text{modified HGBLR}}(\hat{\mathbf{u}}_1, \hat{\mathbf{u}}_2, \hat{\mathbf{r}}, r) = \epsilon'^{\nu}(\hat{\mathbf{u}}_1, \hat{\mathbf{u}}_2, \hat{\mathbf{r}})\{V_O(r) + V_A(\hat{\mathbf{u}}_1, \hat{\mathbf{u}}_2, r)\}. \quad [\text{V.6}]$$

Here altering the value of ν again has an effect on the well widths, but when the well depth is corrected the width returns to its original value. So it appears that such an approach to scaling the well widths is fruitless.

Secondly, in the original Lennard-Jones 12-6 potential the energy well width may be modified by the distance of closest approach σ_0 for constant ϵ_0 . In the case of the HGBLR model for *para*-terphenyl the value of σ_0 has already been chosen, so we do not have the freedom to reassign a value to σ_0 here.

For constant σ_0 and constant ϵ_0 in a Lennard-Jones type potential, the well width results from competition between the short range repulsive and long range attractive components. A Lennard-Jones type potential may be written;

$$V_{LJ} = 4\epsilon_o \left\{ \left(\frac{\sigma_o}{r} \right)^\nu - \left(\frac{\sigma_o}{r} \right)^\mu \right\}. \quad [V.7]$$

The repulsive part of the potential becomes progressively harder as the power ν in V.7 is raised. The long range attractive tail becomes progressively longer as the index μ is lowered. A degree of control over the potential energy well width may therefore be exercised through a judicious choice of the parameters ν and μ . However, for historical reasons the values $\nu = 12$ and $\mu = 6$ have been used and are those we have used in the HGBLR potential.

More significantly perhaps, with the above parameters the length to breadth ratio of the 3-HGBLR-site molecule is merely 2.2 to 1 compared to an axial ratio of 4.4 to 1 obtained for the Gay-Berne representation of *para*-terphenyl [1]. Both with hard and soft ellipsoids it is generally considered the repulsive core of these potentials should have an axial ratio of at least 3 to 1 before mesogenic ordering is observed [11, 12]. It will be seen that the shape of the 3-HGBLR-site site model hard core is spherocylindrical. Hard core models of unconstrained spherocylinders do not exhibit any orientationally ordered phases unless they have an axial ratio of $L/D > 3$ [13]. Thus we may at first suppose it unlikely that we would observe liquid crystal phases with the 3-HGBLR-site site model. This of course would be an unwise conclusion. Indeed, we have shown through earlier simulations that both single site rod-like and disc-like HGBLR centres (with an aspect ratio close to unity) form orientationally ordered phases.

Thus we have presented a tractable methodical approach which we have used to parameterise the 3-HGBLR-site site model to represent the 32-Lennard-Jones site model of *para*-terphenyl. It may be possible to arrive at a better parameter set

using say, the method of least squares but this has not been attempted. Alternatively a simple approach which yields not altogether unreasonable well depth minima and locations has been employed. The following values are obtained:

$$\begin{aligned}\sigma_0 &= 6.0 \text{ \AA}; \\ \text{site-site separation } d &= 4.65 \text{ \AA}; \\ \lambda &= -0.1; \\ \chi' &= -0.83; \\ \varepsilon_0 &= 219.0 \text{ k}_B\text{K};\end{aligned}$$

where k_B is the Boltzmann constant and the other symbols have their usual meaning. The equivalent reduced site-site separation is $d^* = 0.775$. The same parameter set has been employed in both simulations i.e. (a) with the twisted central site with respect to the coplanar end sites, and (b), the all coplanar site model. It is interesting to see what difference removing the twist of the central site has on the potential function. These differences may be illustrated by comparing figures in the range of V.6 to V.15 and additionally a numerical comparison of the well depth minima and locations is provided in table V.1.

Examining table V.1 reveals that only the location of the well depth minimum of the preferred configuration a is displaced by having an all coplanar site configuration, with a slightly reduced distance of closest approach of 6.8 \AA . We may have anticipated this result, because the HGBLR potential has the smallest hard core radius when the site symmetry vectors and intermolecular vector scalar products all take the value unity. This situation obtains for configuration a of an all coplanar model. However, inclusion of the twisted site destroys the higher symmetry of the 3-HGBLR-site model causing some scalar products to take

values other than unity, thus increasing the effective hard core radius of these interactions.

The values of the well depth minima have altered in all cases. The preferred configuration a has a well depth minimum 33% deeper than that of the twisted site model. Interestingly, for the remaining configurations the well depth of the all coplanar model is not less than that of the twisted central site model. For configuration b, the well depth minimum is almost 7% greater, for configuration c it is almost 48% greater than that of the twisted central site model, there only being a small difference between the two configurations d.

Figures V.6 and V.7 show graphs of potential energy against distance for the twisted central site model in terms of the reduced units actually employed in the simulations and for the same fully parameterised model respectively. Figures V.8 and V.9 show similar graphs for the all coplanar site model. The deeper well depth of the all coplanar configuration as expressed in table V.1 is clearly visible in figures V.8 and V.9.

In order to examine the shape of the hard core of the two 3-HGBLR-site site models we have plotted their potential of interaction in terms of a contour map both in the y-, z-planes and x-, y-planes using the Cartesian convention adopted in figure V.1. These plots can be found as figures V.10-V.13. Furthermore, we have also visualized each potential as a three dimensional orthographic projection; figures V.14 and V.15.

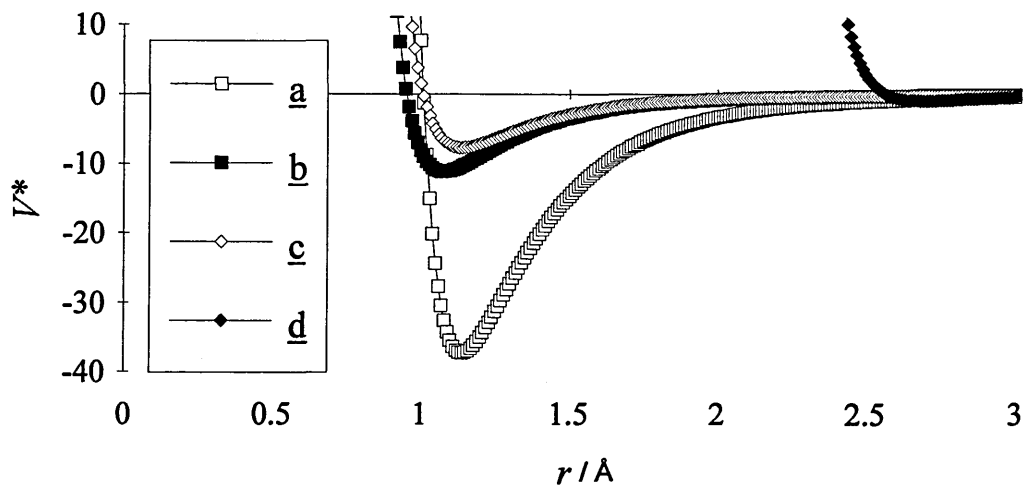


Figure V.8

As for figure V.6 but the potential displayed is a representation of the all coplanar 3-HGBLR-site site model.

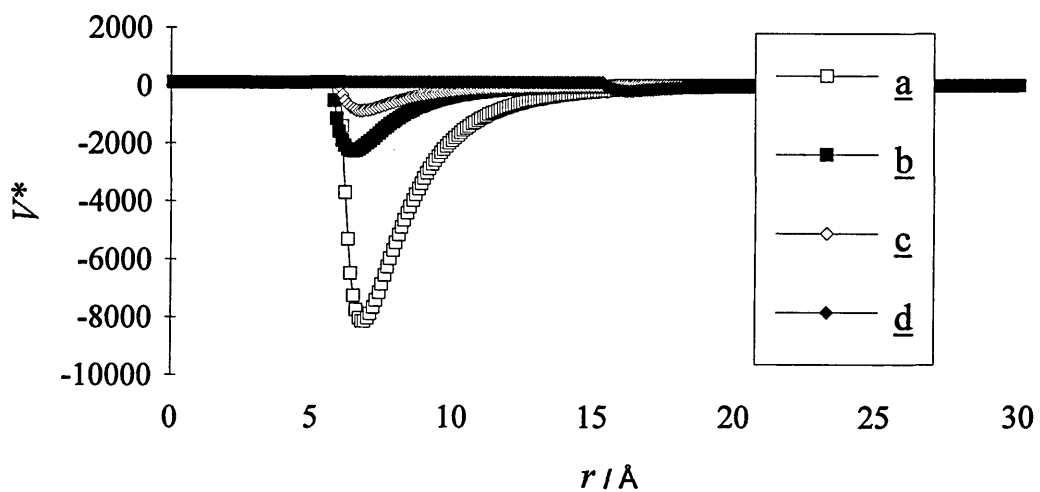


Figure V.9

As for figure V.7 but the potential displayed is a representation of the all coplanar 3-HGBLR-site site model.

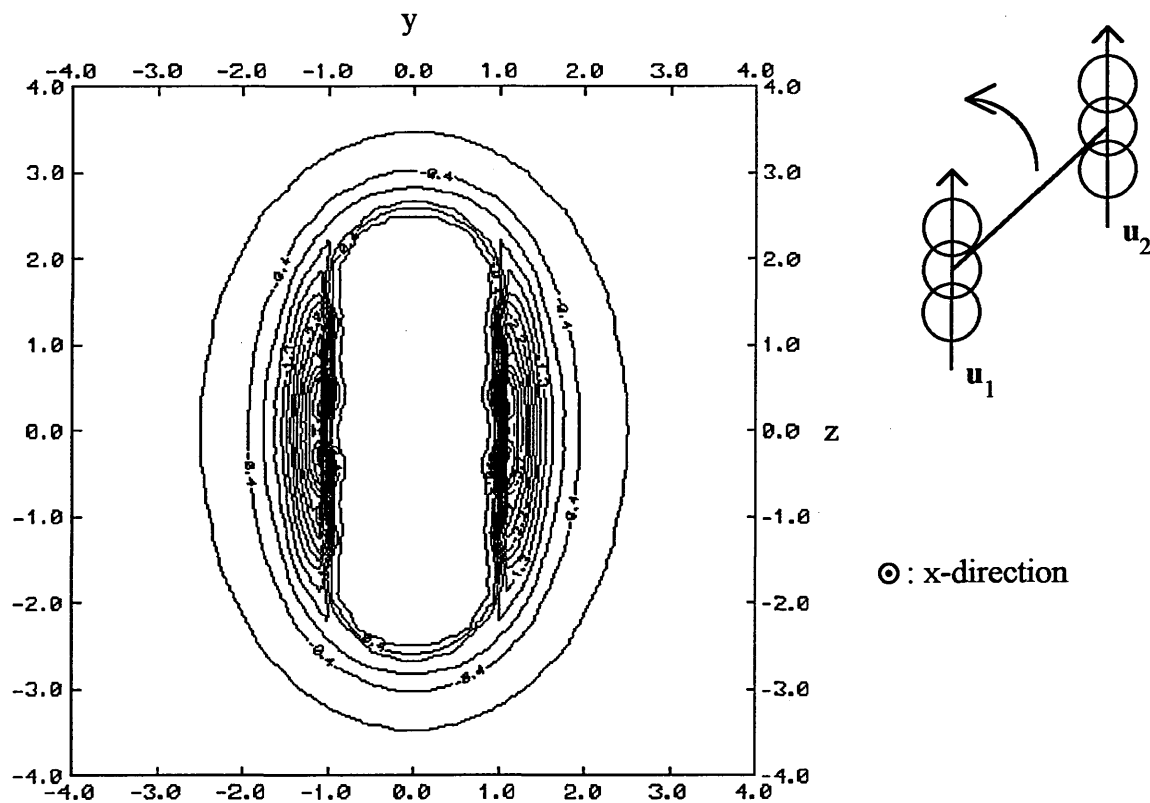


Figure V.10

A contour map of the field of potential energy between a pair of 3-HGBLR-site molecules, with the central site twisted with respect to the coplanar end sites, as described in the text. The contours are drawn in the y -, z -plane, using the Cartesian convention applied in figure V.1, and the x -direction out of the paper as indicated. One molecule is held with its centre of mass fixed at the origin while the other is rotated around the former in the plane of the paper as indicated by the small schematic diagram. Contours are drawn at intervals of $\Delta V^* = 0.3$ in the range $V^* = -4.0$ to $V^* = -0.1$. The parameters are those described in the text and used in the 3-HGBLR-site site simulation. Knowing that individual HGBLR centres have an approximately spherical hard core, the spherocylindrical shape of the 3-HGBLR-site hard core is apparent in this contour plot.

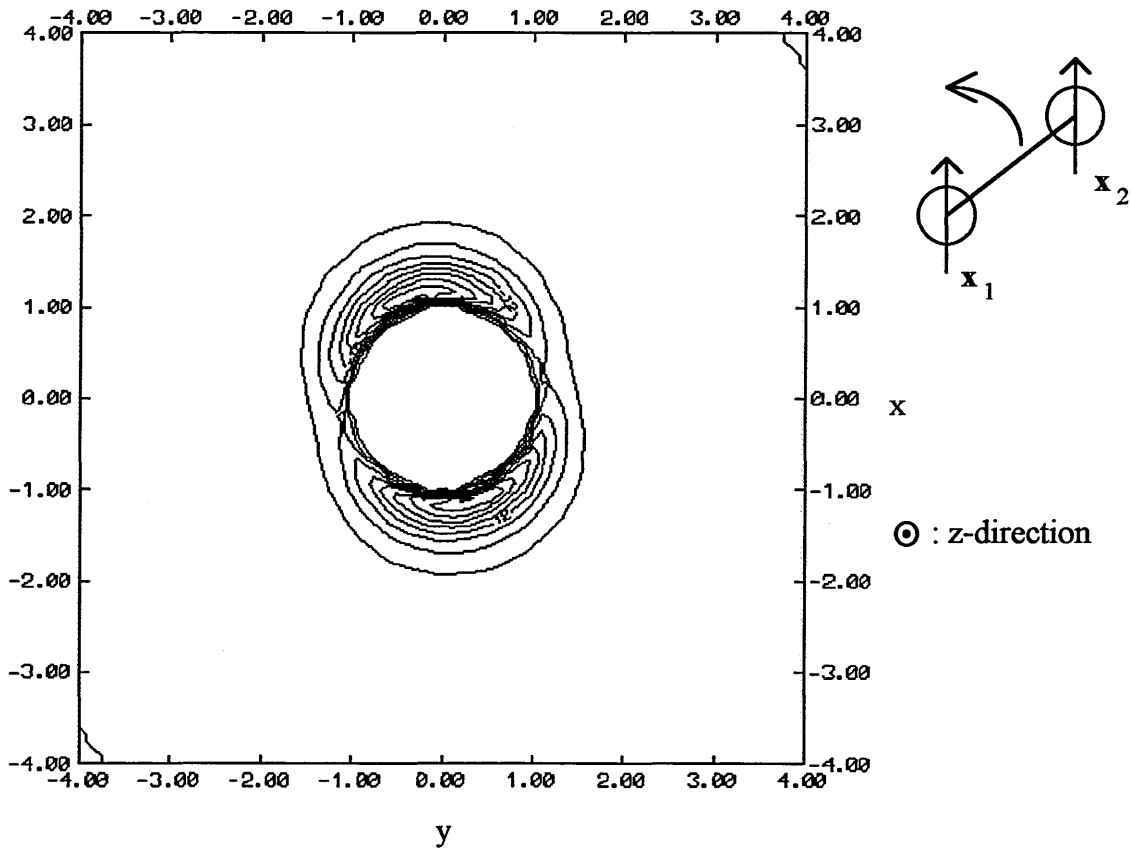


Figure V.11

A contour map of the field of potential energy between a pair of 3-HGBLR-site molecules, with the central site twisted with respect to the coplanar end sites, as described in the text. The contours are drawn in the x -, y -plane, using the Cartesian convention applied in figure V.1, and the z -direction is out of the paper is indicated. One molecule is held with its centre of mass fixed at the origin while the other is rotated around the former's molecular long axis as indicated in the small schematic diagram. In this schematic diagram the sense of the coplanar (only) HGBLR site symmetry axes are denoted x_i for molecules 1 and 2 respectively, according to the adopted convention, to aid visualisation of the molecular configuration. Contours are drawn at intervals of $\Delta V^* = 3.0$ in the range $V^* = -27.0$ to $V^* = 0.0$. The parameters are those described in the text and used in the 3-HGBLR-site site simulation. The approximately spherical hard core of the HGBLR single site model is clearly seen extending to a radius of $\sigma_0 = 1.0$.

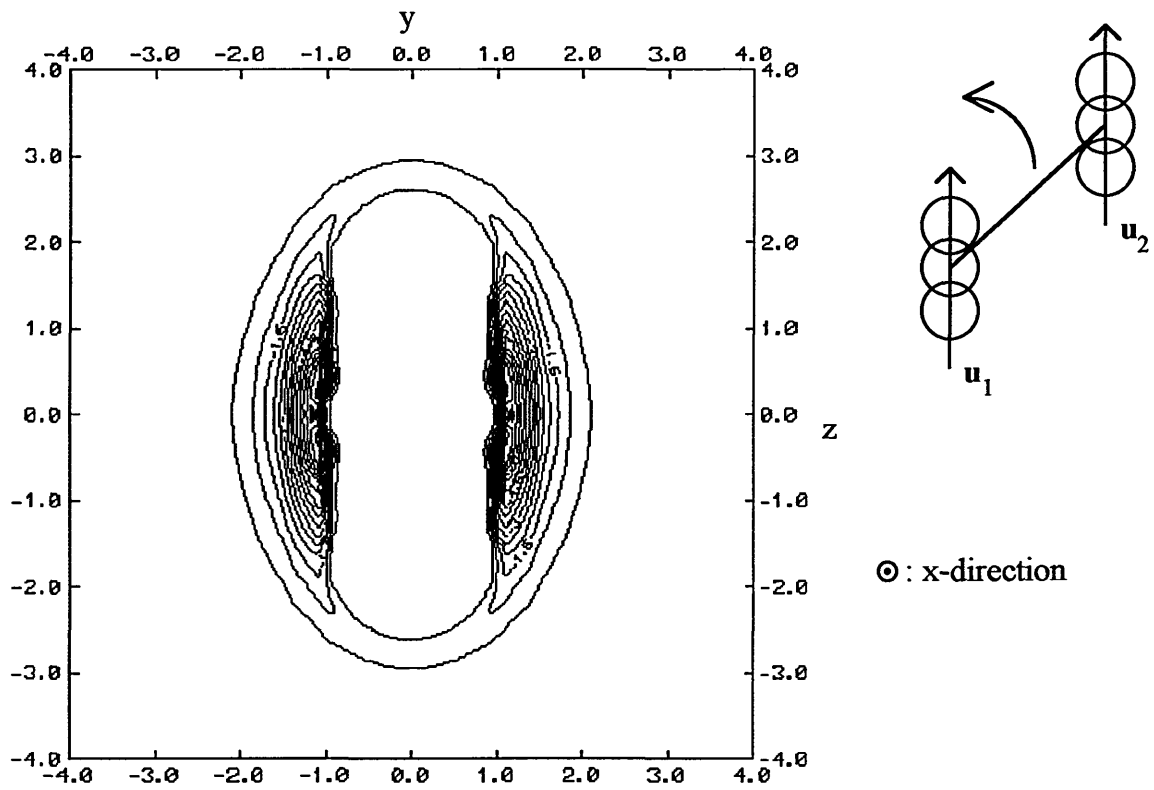


Figure V.12

A contour map similar to figure V.10 but with all the HGBLR sites oriented coplanar. Contours are drawn at intervals of $\Delta V^* = 0.5$ in the range $V^* = -7.5$ to $V^* = -0.5$. For an explanation of the small schematic diagram and axes convention see figure V.10.

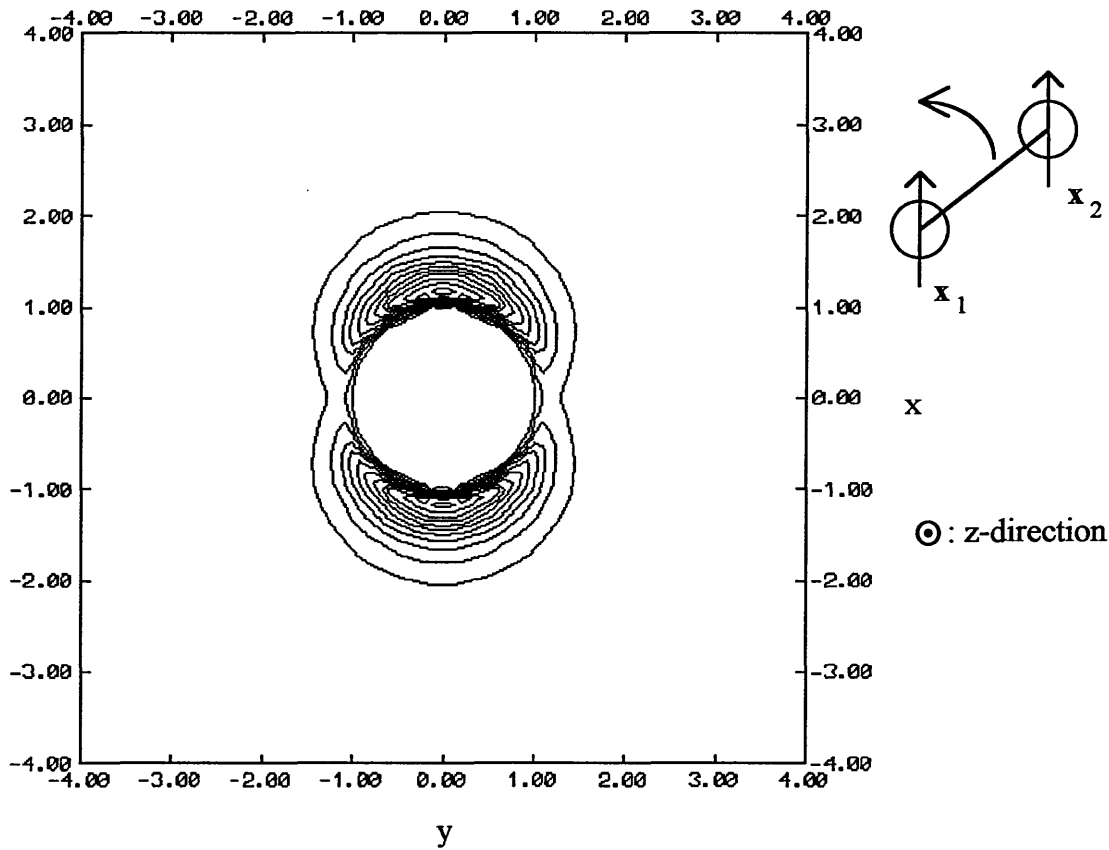


Figure V.13

A contour map similar to figure V.11 but with all 3-HGBLR-sites per molecule oriented coplanar. Contours are drawn at intervals of $\Delta V^* = 3.0$ in the range $V^* = -33.0$ to $V^* = 0.0$. For an explanation of the small schematic diagram and axes convention see figure V.11.

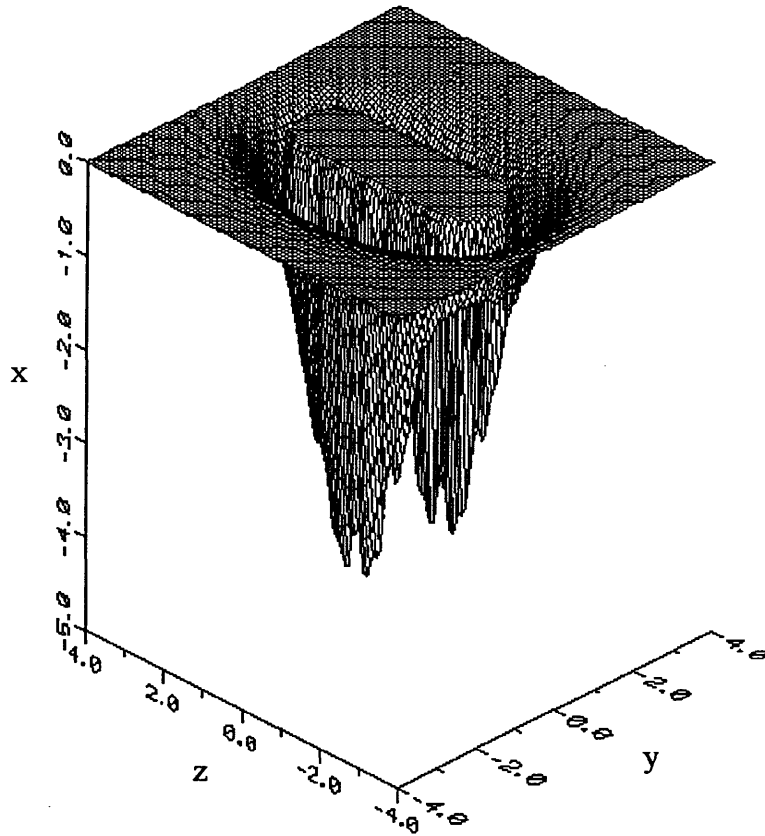


Figure V.14

A three dimensional orthographic representation of figure V.10. See figure V.10 for details of the orientation and parameterisation of the 3-HGBLR-site site model.

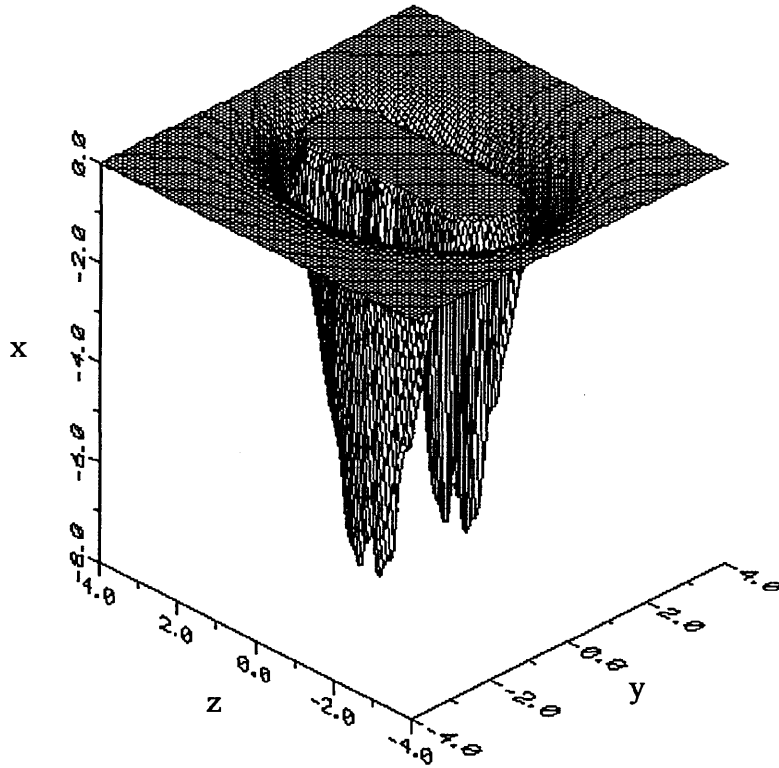


Figure V.15

A three dimensional orthographic representation of figure V.12. See figure V.12 for details of the orientation and parameterisation of the 3-HGBLR-site site model.

V.5 Calculating the Reduced Moment of Inertia Tensor

In order that we may represent the dynamics of a *para*-terphenyl molecule correctly by our 3-HGBLR-site potential, we need to know its moment of inertia tensor \mathbf{I} given by equation [V.8] below;

$$\mathbf{I} = \begin{bmatrix} I_{xx} & I_{xy} & I_{xz} \\ I_{yx} & I_{yy} & I_{yz} \\ I_{zx} & I_{zy} & I_{zz} \end{bmatrix}. \quad [\text{V.8}]$$

If we use the following notation convention:

$$\begin{aligned} x &\rightarrow x_1; \\ y &\rightarrow x_2; \\ z &\rightarrow x_3, \end{aligned} \quad [\text{V.9}]$$

then the components of a general rigid body expressed with respect to a fixed Cartesian reference frame within the body may be denoted;

$$I_{jk} = \int_{\text{Volume}} \rho(\mathbf{r})(r^2\delta_{jk} - x_jx_k)d\text{Volume}, \quad [\text{V.10}]$$

where ρ is the density of the rigid body as a function of the position vector \mathbf{r} and δ is the Kronecker delta function. For our 32-Lennard-Jones-site representation if we represent the carbon and hydrogen atoms as discrete mass entities at the atomic centre of mass positions equation [V.7] reduces to;

$$I_{jk} = \sum_{\text{carbons}} m_c(r^2\delta_{jk} - x_jx_k) + \sum_{\text{hydrogens}} m_h(r^2\delta_{jk} - x_jx_k), \quad [\text{V.11}]$$

where m_c and m_h are the mass of carbon and hydrogen atoms respectively and take the values $m_c = 12.0$ umu and $m_h = 1.0$ umu. Similarly the mass of the 32-

Lennard-Jones site model of *para*-terphenyl may be readily computed from the expression;

$$m = \sum_{\text{carbons}} m_c + \sum_{\text{hydrogens}} m_h. \quad [\text{V.12}]$$

The initials "umu" stand for unified mass units. A conversion to SI units is provided by the relationship;

$$1\text{umu} = 1.66 \times 10^{-27} \text{kg}. \quad [\text{V.13}]$$

Using equations [V.12] and [V.13] the mass of the 32-Lennard-Jones-site representation of *para*-terphenyl is found to be $m = 3.82 \times 10^{-25} \text{kg}$. Using a Cartesian coordinate reference frame equivalent to that of figure V.1 applying equation [V.11], the moment of inertia tensor corresponding to the 32-Lennard-Jones-site *para*-terphenyl molecule was found to be;

$$\mathbf{I} = \begin{bmatrix} 3281.30 & 46.52 & 0 \\ 46.52 & 3083.27 & 0 \\ 0 & 0 & 273.35 \end{bmatrix} \text{umu } \text{\AA}^2. \quad [\text{V.14}]$$

Clearly the moment of inertia tensor in this reference frame is not diagonal. For ease of calculating the angular velocities from angular momenta it is convenient to have the moment of inertia tensor in a diagonal form. This corresponds to rotating the reference frame used in the calculation of [V.11] to one in which the products of inertia (the off diagonal components of [V.8]) vanish. Diagonalising the inertia tensor and computing the respective eigenvectors of the solution is found to correspond to a rotation of the original reference frame of 12.5° about the molecular long or z-axis. This now becomes the body fixed axes system for

the representation of the *para*-terphenyl molecules with respect to the original reference frame of figure V.1. Molecules represented in this manner have the diagonal inertia tensor;

$$\mathbf{I}' = \begin{bmatrix} 3291.68 & 0 & 0 \\ 0 & 3072.89 & 0 \\ 0 & 0 & 273.35 \end{bmatrix} \text{ umu } \text{\AA}^2. \quad [\text{V.15}]$$

The equivalent reduced moment of inertia may be calculated from the relationship;

$$I^*_{ij} = I'_{ij} / m\sigma_o^2. \quad [\text{V.16}]$$

Using [V.16] the reduced moment of inertia tensor in diagonal form is found to be;

$$\mathbf{I}^* = \begin{bmatrix} 0.366 & 0 & 0 \\ 0 & 0.342 & 0 \\ 0 & 0 & 0.030 \end{bmatrix}. \quad [\text{V.17}]$$

Thus the principle moments of inertia of the 32-Lennard-Jones-site model are found to be $I_{xx} = 0.366$, $I_{yy} = 0.342$ and $I_{zz} = 0.030$. These values have been used in both 3-HGBLR-site site simulations in solving the rotational equations of motion.

V.6 Preliminary Simulation of the 3-HGBLR-Site Representation of Para-Terphenyl.

Preliminary simulations were performed with $N = 108$ particles in order to find an appropriate density where, at low temperature, cavities did not form in the simulation box. Both the 3-HGBLR-site models were simulated using the method of Price et al [14]. Mathematical details specific to the HGBLR potential are explicated in appendix A. The other simulation techniques used were those as described in section II for molecules of arbitrary symmetry. Both models were parameterised as described in section V.4. Some further details of the simulations are described in the subsections below.

V.6.1 Implementation of a Cutoff

In order to save time it was decided to implement a cutoff in the multisite simulations: the multisite simulations were run on scalar machines. It is necessary to apply the cutoff to the central site in deciding whether to include a molecule in a calculation or not. If a cutoff is simply applied to all sites there is a chance that the molecular separation will allow some sites to be encompassed within the cutoff, while others of the same molecule are not. Subsequent application of the PBCs and nearest image convention (see section II.3.1) may cause some molecules to become fragmented, sometimes resulting in non-bonded sites being mapped quite close to each other leading to high contributions to the potential energy or alternatively incorrect forces and torques being calculated.

For the reasons outlined in section II.3.4, the cutoff was chosen to be half the simulation box edge and the potential was shifted to $V^* = 0$ at the cutoff.

V.6.2 Choice of Time Step

At high temperatures with the initial chosen time step of $\Delta t^* = 0.001$ the system did not stay on the same constant energy hypersurface. Consequently the time step was reduced to $\Delta t^* = 0.00075$ equivalent to a real time of $t = 5.06 \times 10^{-15}$ s. This was found to give tolerable energy conservation based on a criterion of fluctuations of not more than 1 part in 1000 of the total energy being considered acceptable away from phase transitions. We note that this value is half the previous lowest time step used for the single-site simulations: the moment of inertia about the molecular long axis will allow rapid rotation of this axis, the correspondingly high angular velocities will require a shorter time step in order to solve the finite difference equations of motion to sufficient accuracy.

V.6.3 Choice of Density

It was necessary to run some preliminary simulations to arrive at a reasonable density at which to simulate the system. As before with the single-site simulations a density too low resulted in cavities being formed in the simulation box when the system had been cooled sufficiently. Alternatively, and not observed in the single-site simulations, at a density too high, the system was found to have an unacceptably high $\langle P_2 \rangle$ order parameter (the simulations were started from an ordered system, see section V.7), even at high temperature. These systems were not found to exhibit an isotropic phase. Therefore an intermediate density was selected; $\rho^* = 0.33$ which is equivalent to 584 kgm^{-3} . This is somewhat less than the density at which typical calamitic mesophases form [15]. However, at this simulation density, even at low temperatures cavities were not observed forming in the simulation box.

Interestingly the value of the density selected for the 3-HGBLR-site model is very nearly one third of that used for a single-site model. While we would expect the value to be lower, being close to a third is almost certainly fortuitous.

V.7 Details of of *Para*-Terphenyl Simulations

After identifying a suitable simulation parameter set: $\rho^* = 0.33$; $\Delta t^* = 0.00075$; equivalent simulations of $N = 256$ particles with (a), a system with the central HGBLR site twisted as described in section V.2 and (b), an all coplanar ring system were performed in the microcanonical ensemble. The simulations were each run for a total of 40,000 steps during which simulation averages were collected every 100 steps for the final 20,000 steps.

The simulations were started from an fcc lattice with each particle orientated at 20° to the simulation cell z -direction by rotating the space fixed molecular x - and z -axes according to the Cartesian convention adopted in figure V.1. The tilt was applied in order to start the simulation at the appropriate density. With long molecules it is found that the system can be started at the density of interest by inclining the molecules to the simulation box edge, thus eliminating the need to scale the system density followed by a necessary equilibration period. The simulations were started from an ordered system so that the subsequent evolution of the system to an isotropic phase could be confirmed. The particles were given sufficient translational and angular velocity (not constrained perpendicular to the molecular long axis in this case) that the original lattice rapidly melted.

The output of one simulation was used as the input to another after the translational velocities, only, had been scaled by a factor 0.9, using the same method as described in section IV.3.1 Scaling the translational velocities alone

allows identification of the re-attainment of equipartition of the kinetic energies of rotation and translation, providing a guide to the state of equilibration of the system.

In the following sections we present the results of these simulations, paying particular attention to the structure of the phases observed. Specifically we have individually calculated the degree of ordering of all three molecular semi-axes as defined in the convention adopted in figure V.1, i.e. $\langle P_2(x_i) \rangle$ where x_i represents the z-, x- or y-molecular semi-axes. Additionally when presenting the structural distribution functions based on $g(r^*)$ we have resolved these with respect to the average molecular semi-axes directions. We shall denote these functions $g_1(r^*(\hat{n}(x_i)))$ for $g(r^*)$ resolved parallel with respect to the directions $\hat{n}(z)$, $\hat{n}(x)$ and $\hat{n}(y)$. The reasons behind such a detailed investigation of the structural distribution functions and mean square displacements shall become apparent as we examine the results of the simulations in sections V.8 and V.9 following.

V.8 Para-Terphenyl Simulation Results: Comparison of the Twisted Central Site and All Coplanar Site 3-HGBLR-Site Site models.

V.8.1 Potential Energy and the Second Rank Orientational Order Parameter

Values of the average potential energy per particle, $\langle V^*/N \rangle$ and the second rank orientational order parameter, $\langle P_2(x_i) \rangle$ (as a function of each of the three orthogonal molecular semi-axes), for the twisted central site and all coplanar site 3-HGBLR-site site models are presented in tables V.2 and V.3 respectively.

Figures V.16 and V.17 illustrate the behaviour of $\langle V^*/N \rangle$ with respect to the reduced temperature of each system. Figure V.16 presents evidence for a strong first order phase transition in the discontinuity of the potential energy curve. The potential energy function decays approximately linearly from high temperature until $\langle T^* \rangle \approx 4.5$. Thereafter there occurs a sharp discontinuity with evidence of hysteresis effects until $\langle T^* \rangle = 4.0$. Examination of table V.2 and figure V.16 shows that after cooling to $\langle T^* \rangle = 4.5$ at the onset of the transition the temperature is seen to rise again despite a continuing decrease in the potential energy. After the transition period $\langle V^*/N \rangle$ continues to decay in a linear fashion as the temperature is reduced.

Figure V.17 shows that for the all coplanar site model from high temperature $\langle V^*/N \rangle$ decays approximately linearly until $\langle T^* \rangle \approx 6.3$. At lower temperatures strong evidence for a first order type phase transition is presented via the van der Waals loop exhibited by the variation of $\langle V^*/N \rangle$ against $\langle T^* \rangle$. After the transition, $\langle V^*/N \rangle$ appears to decrease approximately linearly once again upon further cooling below $\langle T^* \rangle \approx 6.0$.

$\langle T^* \rangle$	$\langle V^*/N \rangle$	$\langle P_2(z) \rangle$	$\langle P_2(x) \rangle$	$\langle P_2(y) \rangle$
10.0±0.2	-28.9±0.6	0.06±0.02	0.06±0.02	0.05±0.02
9.5±0.2	-29.9±0.6	0.07±0.02	0.06±0.02	0.06±0.02
8.9±0.2	-30.6±0.5	0.05±0.02	0.06±0.02	0.05±0.02
8.3±0.1	-31.4±0.4	0.08±0.03	0.07±0.03	0.06±0.02
7.8±0.2	-32.2±0.5	0.07±0.02	0.07±0.02	0.06±0.02
7.3±0.2	-33.3±0.5	0.06±0.02	0.07±0.02	0.05±0.02
6.9±0.1	-33.8±0.4	0.08±0.03	0.07±0.02	0.06±0.02
6.5±0.1	-34.5±0.4	0.09±0.03	0.08±0.03	0.06±0.02
6.1±0.2	-35.3±0.5	0.10±0.03	0.09±0.03	0.06±0.02
5.7±0.1	-36.0±0.4	0.08±0.03	0.10±0.03	0.07±0.02
5.4±0.1	-36.7±0.4	0.09±0.03	0.12±0.04	0.06±0.02
5.2±0.1	-37.3±0.4	0.10±0.03	0.12±0.04	0.07±0.03
4.9±0.1	-37.9±0.4	0.10±0.04	0.11±0.04	0.07±0.02
4.7±0.1	-38.7±0.4	0.14±0.05	0.20±0.07	0.08±0.03
4.5±0.1	-39.2±0.4	0.11±0.04	0.18±0.06	0.08±0.03
4.5±0.1	-40.6±0.4	0.18±0.02	0.37±0.05	0.12±0.03
4.6±0.2	-42.2±0.5	0.23±0.03	0.53±0.04	0.17±0.03
4.6±0.1	-43.4±0.4	0.26±0.05	0.59±0.03	0.20±0.03
4.3±0.1	-44.0±0.4	0.27±0.05	0.60±0.03	0.22±0.03
4.4±0.1	-45.3±0.4	0.34±0.04	0.67±0.02	0.29±0.04
4.3±0.1	-46.3±0.4	0.27±0.03	0.72±0.02	0.23±0.02
4.3±0.1	-47.5±0.4	0.28±0.03	0.76±0.03	0.24±0.03
4.3±0.1	-48.7±0.3	0.36±0.04	0.79±0.02	0.31±0.03
4.3±0.1	-50.0±0.4	0.38±0.04	0.82±0.02	0.33±0.04
4.2±0.1	-50.8±0.3	0.43±0.03	0.85±0.01	0.38±0.03
4.2±0.1	-52.1±0.4	0.57±0.03	0.86±0.01	0.51±0.03
4.2±0.1	-53.4±0.4	0.69±0.02	0.87±0.01	0.62±0.02

Table V.2

Average temperature $\langle T^* \rangle$, average potential energy per particle $\langle V^*/N \rangle$ and molecular axes order parameters $\langle P_2(z) \rangle$, $\langle P_2(x) \rangle$ and $\langle P_2(y) \rangle$ for the rotated central site 3-HGBLR-site site model (continued overleaf).

$\langle T^* \rangle$	$\langle V^*/N \rangle$	$\langle P_2(z) \rangle$	$\langle P_2(x) \rangle$	$\langle P_2(y) \rangle$
4.3±0.1	-54.6±0.4	0.81±0.01	0.88±0.01	0.73±0.02
4.3±0.1	-55.5±0.3	0.83±0.01	0.89±0.01	0.76±0.01
4.0±0.1	-56.2±0.3	0.83±0.01	0.896±0.009	0.77±0.01
3.8±0.1	-57.0±0.3	0.86±0.01	0.90±0.01	0.80±0.01
3.7±0.09	-57.6±0.3	0.871±0.007	0.910±0.007	0.814±0.009
3.58±0.09	-58.2±0.3	0.876±0.005	0.920±0.006	0.823±0.008
3.39±0.08	-58.8±0.2	0.877±0.004	0.924±0.007	0.828±0.007
3.25±0.08	-59.3±0.2	0.877±0.004	0.930±0.005	0.833±0.005
3.10±0.08	-59.8±0.2	0.880±0.004	0.932±0.006	0.835±0.007
2.95±0.08	-60.2±0.2	0.880±0.004	0.937±0.005	0.840±0.006
2.83±0.07	-60.6±0.2	0.884±0.004	0.940±0.005	0.845±0.006
2.70±0.07	-61.0±0.2	0.883±0.003	0.943±0.004	0.846±0.005
2.60±0.07	-61.4±0.2	0.883±0.003	0.948±0.005	0.850±0.005
2.47±0.06	-61.8±0.2	0.886±0.004	0.951±0.004	0.855±0.005
2.35±0.06	-62.1±0.2	0.882±0.003	0.954±0.004	0.852±0.004
2.29±0.06	-62.5±0.2	0.887±0.003	0.955±0.004	0.858±0.005
2.19±0.06	-62.8±0.2	0.886±0.003	0.957±0.004	0.859±0.004
2.13±0.06	-63.2±0.2	0.884±0.003	0.958±0.004	0.857±0.005
2.03±0.05	-63.6±0.2	0.885±0.003	0.961±0.003	0.860±0.004
2.32±0.07	-63.8±0.2	0.886±0.003	0.964±0.004	0.863±0.004
1.95±0.05	-63.9±0.2	0.885±0.003	0.963±0.003	0.861±0.004
1.87±0.05	-64.2±0.1	0.886±0.003	0.964±0.003	0.862±0.004
1.79±0.05	-64.5±0.1	0.885±0.002	0.996±0.003	0.863±0.004

Table V.2 (continued)

$\langle T^* \rangle$	$\langle V^*/N \rangle$	$\langle P_2(z) \rangle$	$\langle P_2(x) \rangle$	$\langle P_2(y) \rangle$
9.9±0.2	-29.9±0.6	0.06±0.03	0.07±0.02	0.06±0.02
9.4±0.2	-30.8±0.6	0.07±0.02	0.07±0.02	0.06±0.02
8.7±0.2	-31.6±0.6	0.07±0.03	0.08±0.03	0.06±0.02
8.3±0.2	-32.7±0.5	0.07±0.02	0.07±0.02	0.06±0.02
7.8±0.2	-33.5±0.5	0.07±0.02	0.08±0.03	0.06±0.02
7.4±0.2	-34.5±0.5	0.06±0.02	0.08±0.03	0.07±0.02
7.0±0.2	-35.5±0.5	0.08±0.03	0.10±0.03	0.07±0.03
6.7±0.2	-36.3±0.5	0.09±0.02	0.14±0.06	0.08±0.03
6.3±0.2	-37.2±0.5	0.09±0.03	0.11±0.04	0.07±0.03
6.2±0.2	-38.4±0.5	0.11±0.03	0.23±0.05	0.10±0.03
6.3±0.3	-40±1	0.16±0.03	0.4±0.1	0.13±0.03
6.3±0.2	-42.0±0.7	0.18±0.03	0.49±0.05	0.17±0.03
6.4±0.3	-44.4±0.8	0.21±0.04	0.60±0.05	0.20±0.03
6.5±0.2	-46.7±0.7	0.26±0.04	0.68±0.03	0.24±0.04
6.4±0.2	-48.0±0.7	0.22±0.02	0.71±0.03	0.21±0.03
6.7±0.2	-50.7±0.7	0.28±0.03	0.79±0.02	0.27±0.03
6.6±0.2	-52.2±0.7	0.29±0.02	0.82±0.02	0.27±0.02
6.6±0.2	-53.9±0.7	0.28±0.03	0.85±0.02	0.27±0.03
6.6±0.2	-55.9±0.6	0.29±0.02	0.88±0.01	0.27±0.02
6.5±0.2	-57.4±0.6	0.29±0.03	0.91±0.01	0.27±0.02
6.3±0.2	-58.6±0.6	0.29±0.02	0.92±0.01	0.28±0.02
6.1±0.2	-59.7±0.6	0.28±0.02	0.927±0.009	0.27±0.02
6.0±0.2	-61.0±0.5	0.36±0.04	0.941±0.006	0.35±0.04
5.8±0.2	-61.9±0.5	0.35±0.04	0.945±0.006	0.33±0.04
5.7±0.2	-63.1±0.5	0.46±0.03	0.947±0.006	0.44±0.03
5.5±0.1	-64.1±0.4	0.29±0.02	0.955±0.004	0.28±0.02
5.3±0.1	-64.9±0.4	0.32±0.04	0.960±0.004	0.31±0.03

Table V.3

Average temperature $\langle T^* \rangle$, average potential energy per particle $\langle V^*/N \rangle$ and molecular axes order parameters $\langle P_2(z) \rangle$, $\langle P_2(x) \rangle$ and $\langle P_2(y) \rangle$ for the all coplanar 3-HGBLR-site site model (continued overleaf).

$\langle T^* \rangle$	$\langle V^*/N \rangle$	$\langle P_2(z) \rangle$	$\langle P_2(x) \rangle$	$\langle P_2(y) \rangle$
5.1±0.1	-65.7±0.4	0.36±0.02	0.963±0.003	0.35±0.02
4.8±0.1	-67.3±0.4	0.31±0.03	0.966±0.003	0.30±0.03
4.7±0.1	-67.1±0.4	0.33±0.03	0.968±0.003	0.32±0.03
4.6±0.1	-68.1±0.4	0.42±0.02	0.968±0.003	0.41±0.02
4.5±0.1	-69.0±0.3	0.40±0.02	0.971±0.002	0.39±0.02
4.4±0.1	-69.9±0.3	0.36±0.01	0.971±0.002	0.36±0.01
4.2±0.1	-70.6±0.4	0.37±0.02	0.973±0.002	0.36±0.02
4.0±0.1	-71.2±0.3	0.40±0.03	0.975±0.002	0.40±0.03
3.9±0.1	-71.8±0.3	0.46±0.01	0.976±0.002	0.45±0.01
3.7±0.1	-72.4±0.3	0.501±0.009	0.978±0.002	0.495±0.009
3.51±0.09	-72.9±0.3	0.50±0.01	0.979±0.002	0.50±0.01
3.38±0.09	-73.4±0.3	0.468±0.006	0.980±0.002	0.463±0.006
3.24±0.09	-73.9±0.3	0.50±0.02	0.981±0.002	0.50±0.02
3.17±0.09	-74.7±0.3	0.51±0.01	0.982±0.001	0.51±0.01
3.06±0.09	-75.1±0.3	0.515±0.007	0.983±0.001	0.511±0.007
2.99±0.08	-75.7±0.2	0.517±0.005	0.984±0.001	0.512±0.005
2.82±0.08	-76.0±0.2	0.515±0.004	0.985±0.001	0.511±0.004
2.76±0.07	-76.6±0.2	0.527±0.007	0.985±0.001	0.524±0.007
2.67±0.08	-77.1±0.2	0.534±0.008	0.986±0.001	0.530±0.009
2.55±0.06	-77.5±0.2	0.530±0.006	0.986±0.001	0.526±0.006
2.47±0.07	-78.0±0.2	0.535±0.005	0.988±0.001	0.532±0.005
2.37±0.07	-78.3±0.2	0.532±0.005	0.988±0.001	0.529±0.005
2.28±0.05	-78.7±0.2	0.538±0.006	0.988±0.001	0.535±0.006

Table V.3 (continued)

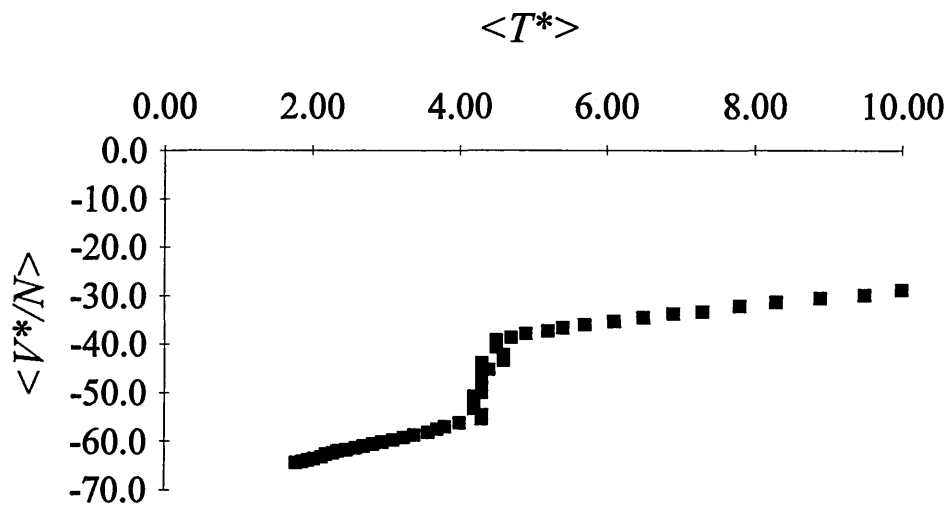


Figure V.16

Average reduced energy per particle $\langle V^*/N \rangle$ against reduced temperature for the twisted central site system of $N = 256$ 3-HGBLR-site site particles on cooling.

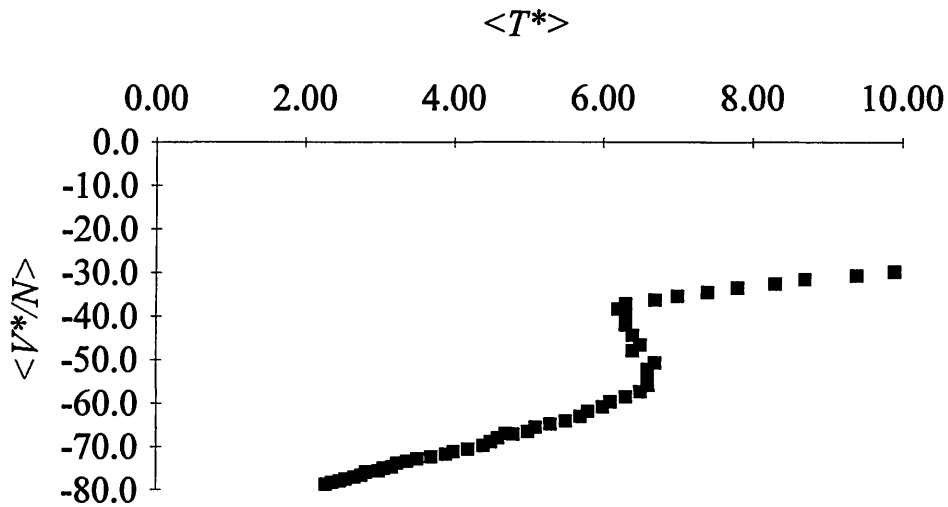


Figure V.17

Average reduced energy per particle $\langle V^*/N \rangle$ against reduced temperature for the all coplanar site system of $N = 256$ 3-HGBLR-site site particles on cooling.

Figures V.18 and V.19 illustrate the behaviour of the $\langle P_2(x_i) \rangle$ against $\langle T^* \rangle$ on cooling for both systems studied. Examining both figures V.18 and V.19 we note that initially at high temperature there is no ordering of the average molecular semi-axes directions apart from a small residual value due to system size effects and the averaging of a positive quantity (see section II.4.2).

Examining figure V.18 we observe, that around the same temperature of the indicated transition in figure V.16, all the $\langle P_2(x_i) \rangle$ begin to rise rapidly. The change is first observed in the ordering of $\langle P_2(x) \rangle$. Examination of table V.2 indicates a degree of hysteresis with $\langle P_2(x) \rangle$ fluctuating between approximately $\langle P_2(x) \rangle = 0.2$ and $\langle P_2(x) \rangle = 0.6$ over the temperature range $4.6 \geq \langle T^* \rangle \geq 4.5$. Thereafter as the potential energy of the system is lowered $\langle P_2(x) \rangle$ rises more slowly but consistently to obtain a value $\langle P_2(x) \rangle \approx 0.9$ at $\langle T^* \rangle = 4.3$. Similar behaviour is indicated for $\langle P_2(z) \rangle$ and $\langle P_2(y) \rangle$, the onset of ordering occurring at lower temperatures.

At first sight it may seem quite disturbing that the degree of ordering of each molecular semi-axis is different at many state points. As the three semi-axes are mutually orthogonal a degree of redundancy is provided by the third semi-axis. We would therefore expect two coplanar semi-axes to show identical ordering results. However this is not observed in figure V.18. This is because of the way in which the ordering of each of the semi-axes is calculated. The direction of each molecular semi-axis is known at the initial configuration. Subsequently, coordinates describing the evolution of the orientation of each molecular semi-axis vector are recorded at regular intervals (every $100\Delta t$). A separate \mathbf{Q} tensor is then constructed for each semi-axis at each saved configuration. It is the average of the largest eigenvalues of each of these \mathbf{Q} tensors per average semi-

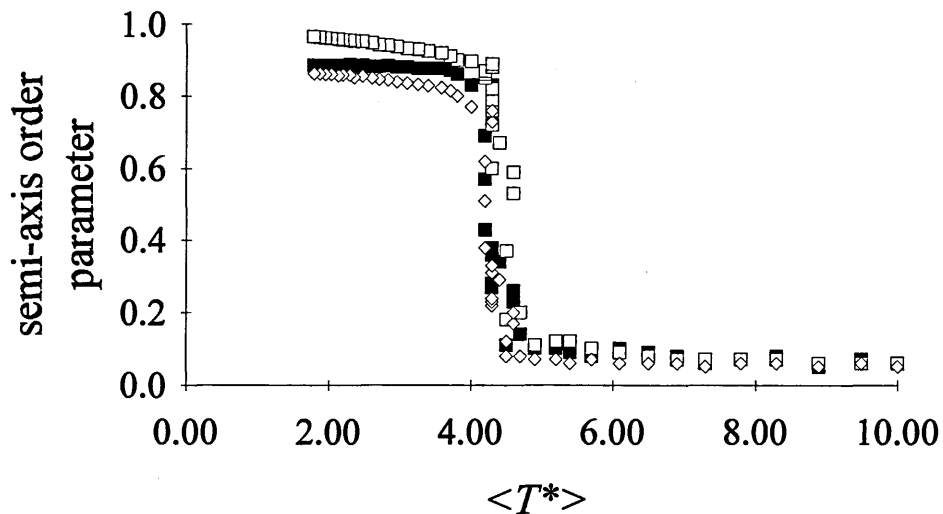


Figure V.18

Second rank orientational order parameter applied to the molecular long axis and both orthogonal molecular semi-axes for the twisted central site system of $N = 256$ 3-HGBLR-site particles. The following key applies: closed squares, $\langle P_2(z) \rangle$; open squares, $\langle P_2(x) \rangle$; open diamonds, $\langle P_2(y) \rangle$ according to the Cartesian convention of figure V.1.

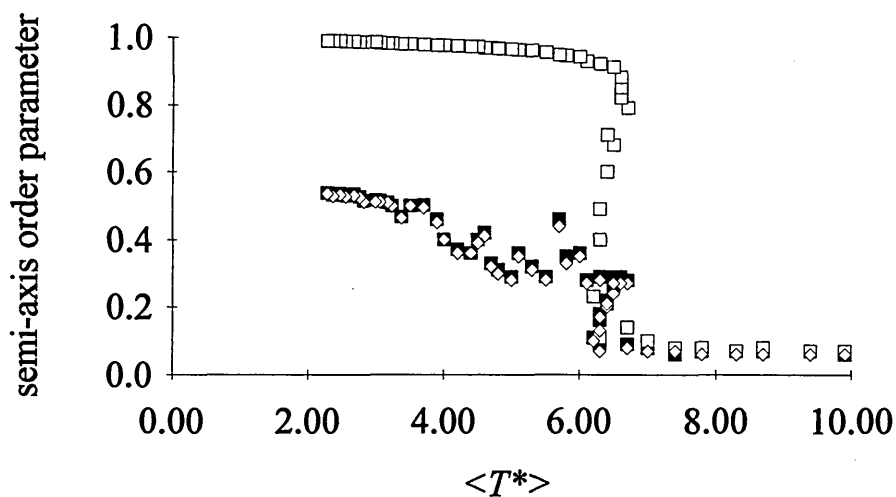


Figure V.19

As figure V.18 but for the all coplanar 3-HGBLR-site system. For legend see figure V.18.

axis direction over the entire state point simulation run that provides the semi-axis order parameter $\langle P_2(x_i) \rangle$. The observed differences between the degree of ordering of each molecular semi-axis can be explained according to the statistical nature of each measurement. Although the three semi-axes are orthogonal in an individual molecule, there is no requirement for the three rotations yielding the semi-axes directors $\hat{\mathbf{n}}(z)$, $\hat{\mathbf{n}}(x)$ and $\hat{\mathbf{n}}(y)$ to be orthogonal. Indeed, except in highly ordered systems, the effective averaging performed over all molecules for each separate semi-axis makes this unlikely. In fact, it can be seen from figure V.18 that as the system becomes more ordered $\langle P_2(y) \rangle \rightarrow \langle P_2(z) \rangle$; $\langle P_2(x) \rangle$ however always remains more ordered.

Similarly near to the approximate transition temperature indicated in figure V.17, we observe fluctuations in the behaviour of $\langle P_2(x) \rangle$ in figure V.19, closely followed by fluctuations in $\langle P_2(z) \rangle$ and $\langle P_2(y) \rangle$ as the system is cooled. Into the indicated transition the nature of the van der Waals loop leads to an erratic temperature behaviour of the system as the potential energy is reduced as can be seen from table V.3. The second rank order parameter $\langle P_2(\hat{\mathbf{n}}(x)) \rangle$ rises abruptly over a very small temperature range with evidence of hysteresis consistent with the van der Waals loop exhibited in the behaviour of $\langle V^*/N \rangle$. After this rapid rise in $\langle P_2(\hat{\mathbf{n}}(x)) \rangle$ the function then tends more slowly towards a value $\langle P_2(\hat{\mathbf{n}}(x)) \rangle = 1.0$. In stark contrast to that observed with the twisted central site model, ordering of the HGBLR site symmetry axes clearly dominates the ordering of the other molecular semi-axes. $\langle P_2(\hat{\mathbf{n}}(z)) \rangle$ and $\langle P_2(\hat{\mathbf{n}}(y)) \rangle$ behave very erratically at the transition temperature and thereafter for a range of $\langle T^* \rangle \approx 3$ on cooling. These latter two axes have an average degree of equivalent order at all temperatures converging on a maximum value of $\langle P_2 \rangle \approx 0.54$.

It appears therefore that in both cases we have evidence for a phase transition from an orientationally disordered to ordered phase. It is difficult to identify the precise transition temperature when employing the microcanonical ensemble for reasons outlined in chapter IV. However, it is clear from the data presented in table V.2 and figure V.16 that the transition occurs in the range $4.0 < \langle T^* \rangle < 5.0$ for the twisted central site model. Despite lacking a precise location of the phase transition we may make a rough estimate of the entropy of transition. By approximating straight lines to the potential energy curve we estimate the entropy of transition to be approximately $\Delta \langle V^* / N \rangle / \langle T^* \rangle \approx 4.4$ taking the transition temperature as $\langle T^* \rangle = 4.5$.

For the all coplanar model we note that a transition is indicated in the range $6.0 < \langle T^* \rangle < 7.0$. Applying the same method as above, taking the transition temperature as $\langle T^* \rangle = 6.5$, estimated at the centre of the van der Waals loop, we find $\Delta \langle V^* / N \rangle / \langle T^* \rangle \approx 3.5$ for the all coplanar site model.

With the information presented above we may begin to point out some differences between the two models investigated. Firstly, the transition temperature of $\langle T^* \rangle \approx 4.5$ for the twisted central site model compared to $\langle T^* \rangle \approx 6.5$. Looking at the evidence provided by table V.1 we might expect the onset of ordering to occur at a higher temperature for the all coplanar site model due to the magnitude of the well depth minimum, of molecules approaching in configuration a, compared to the twisted central site model.

Additionally, a comparison of the entropies of transition of each system may be made. However, these results are only very approximate. A strong first order transition is indicated by the van der Waals loop of figure V.17 and the entropy

of transition is estimated as $\Delta\langle V^*/N \rangle / \langle T^* \rangle \approx 3.5$ for the all coplanar system compared to $\Delta\langle V^*/N \rangle / \langle T^* \rangle \approx 4.4$ for the twisted central site system which does not appear to exhibit the van der Waals loop. It is clear though, that in both cases we are looking at a first order transition.

Perhaps the most striking difference between the two systems is recorded in the behaviour of the molecular semi-axes order parameters $\langle P_2(x_i) \rangle$ as a comparison of figures V.18 and V.19 clearly illustrates. In order to investigate the differences between the structure of the two ordered systems we have evaluated the radial distribution function and the second rank orientational correlation coefficients. These are presented, for selected state points, in the next section.

V.8.2 Radial Distribution Function and Second Rank Orientational Correlation Coefficient

Due to fluctuations in the temperature it is not possible to obtain a precise measurement of this variable as an inspection of tables V.2 and V.3 reveals. Where two similar state points with respect to temperature are concerned therefore, the potential energy per particle is additionally quoted in order to remove any ambiguity about the state point under consideration.

Figure V.20 shows examples of the radial distribution function at $\langle T^* \rangle = 4.7$ and $\langle T^* \rangle = 4.2$ ($\langle V^*/N \rangle = -52.1$) and $\langle T^* \rangle = 1.79$. Note in both figures V.20 and V.21 the first peak in $g(r^*)$ recorded at the lowest temperature has been truncated so that detailed structure is not swamped due to an inappropriate choice of scale.

Curves recorded at $\langle T^* \rangle = 4.7$ and $\langle T^* \rangle = 4.2$ ($\langle V^*/N \rangle = -52.1$) both exhibit liquid-like behaviour. The first peak in these curves occurring at $r^* \approx \sigma_0$ corresponds to the first shell of nearest neighbours surrounding a given molecule. On decreasing the temperature the first peak in all $g(r^*)$ of figure V.20 is seen to increase. At the highest temperature there appears to be a weak second peak occurring just before $r^* = 2\sigma_0$. The origins of this peak are not quite clear. However, the peak is not strong and may be due to a tendency towards weak hexagonal ordering whereby a second shell of nearest neighbours would form at a distance $1.73\sigma_0$. Little further structure is to be seen in $g(r^*)$ recorded at $\langle T^* \rangle = 4.7$. At $\langle T^* \rangle = 4.2$ ($\langle V^*/N \rangle = -52.1$) the second peak in $g(r^*)$ at $r^* < 2\sigma_0$ is seen to disappear as the temperature is lowered. The $g(r^*)$ now takes on a regular decaying periodic wave structure characteristic of a dense liquid. A second peak is now seen to form at $r^* \approx 2.3\sigma_0$ which may be due to a second shell of nearest neighbours, but contributions to this peak may also come from molecules arranged in an end-to-end configuration. For molecules close packed in this configuration a peak at close to $r^* = 2.2\sigma_0$ is to be expected.

Certainly at $\langle T^* \rangle = 1.79$ a sharp peak is observed at $r^* \approx 2.2\sigma_0$ and most probably corresponds to molecules in an end-to-end configuration. At this lowest temperature $g(r^*)$ now begins to show detailed structure. Interestingly the original second peak in the high temperature $g(r^*)$ occurring at $r^* < 2\sigma_0$ has been replaced by a deep trough which has been displaced to higher r^* at lower temperature. It may be that the likelihood of molecules adopting this separation at low temperature is small for an ordered system. This behaviour also occurs for the all coplanar model as evidenced by figure V.21.

Figure V.21 illustrates the behaviour of $g(r^*)$ recorded for the all coplanar system at temperatures $\langle T^* \rangle = 6.3$ ($\langle V^*/N \rangle = -37.2$), $\langle T^* \rangle = 5.3$ and $\langle T^* \rangle = 2.28$. The same behaviour observed for the two highest temperatures $\langle T^* \rangle = 4.7$ and $\langle T^* \rangle = 4.2$ ($\langle V^*/N \rangle = -52.1$) of figure V.20, described above is seen for the $g(r^*)$ recorded at $\langle T^* \rangle = 6.3$ ($\langle V^*/N \rangle = -37.2$) and $\langle T^* \rangle = 5.3$ in figure V.21 respectively.

Differences between the two models are seen in the detail recorded in the $g(r^*)$ at low temperature. Peaks at longer range than those corresponding to the first three or so shells of nearest neighbours of molecules in $g(r^*)$ are difficult to assign and may be composed of contributions from many different arrangements of molecules. Comparing the low temperature $g(r^*)$ of figures V.20 and V.21 however, we can observe that the all coplanar model displays fine structure at long range compared to the twisted central site model. Qualitatively, though, the short range structure up to $r^* \approx 2.6$, is noticeably similar in both figures, although the first trough occurring in $g(r^*)$ at $\langle T^* \rangle = 1.79$ is broader than that occurring in the low temperature $g(r^*)$ of figure V.21, and additionally the second peak of these respective curves is broader in figure V.21 than in figure V.20.

In order to compare the structure exhibited by the two models further we have examined components of the radial distribution function resolved along the average semi-axes directions $\hat{n}(z)$, $\hat{n}(x)$ and $\hat{n}(y)$. Figures V.22 and V.23 present the resolved functions $g_1(\eta^*(\hat{n}(x_i)))$ at temperatures $\langle T^* \rangle = 4.7$ and $\langle T^* \rangle = 6.3$ ($\langle V^*/N \rangle = -37.2$) for the twisted central site and all coplanar site models respectively. Clearly little structure is presented parallel to the average molecular semi-axes directions at high temperature. However, this is not so

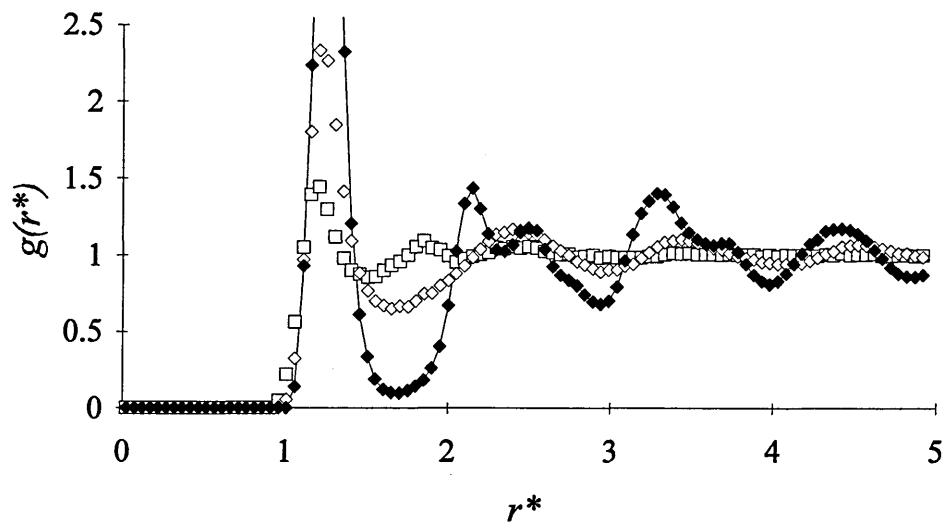


Figure V.20

Radial distribution function, $g(r^*)$ for the twisted central site 3-HGBLR-site model at selected temperatures: open squares, $\langle T^* \rangle = 4.7$; open diamonds, $\langle T^* \rangle = 4.2$ ($\langle V^*/N \rangle = -52.1$); closed diamonds, $\langle T^* \rangle = 1.79$.

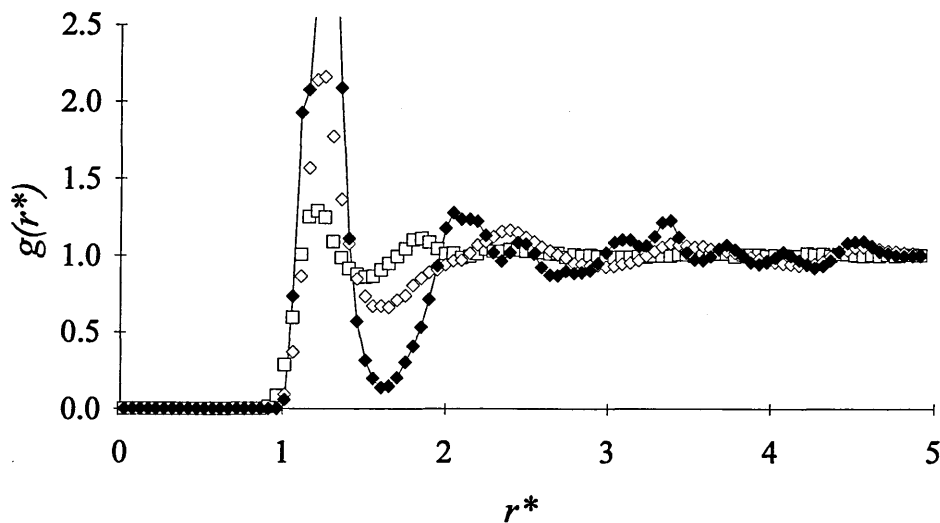


Figure V.21

Radial distribution function, $g(r^*)$ for the all coplanar 3-HGBLR-site model at selected temperatures: open squares, $\langle T^* \rangle = 6.3$ ($\langle V^*/N \rangle = -37.2$); open diamonds, $\langle T^* \rangle = 5.3$; closed diamonds, $\langle T^* \rangle = 2.28$.

surprising when the average directions $\hat{\mathbf{n}}(z)$, $\hat{\mathbf{n}}(x)$ and $\hat{\mathbf{n}}(y)$ are not well defined we would expect to see little structure in functions resolved along these directions. These figures are included here for completeness.

Figure V.24 illustrates the behaviour of the $g_l(\eta^*(\hat{\mathbf{n}}(x_i)))$ at lower temperature when $\langle P_2(x) \rangle = 0.60$ for the twisted central site system. Examination of figure V.24 reveals the appearance of small oscillations in all the $g_l(\eta^*(\hat{\mathbf{n}}(x_i)))$. The effect is most pronounced in the average direction parallel to the site symmetry axes which has the highest degree of order; $\langle P_2(z) \rangle = 0.27$ and $\langle P_2(y) \rangle = 0.22$. The oscillations are weak in amplitude ranging approximately $0.9 \leq g_l(r^*) \leq 1.1$, with the exception of the final peaks. These are of increased magnitude and one possible reason for this anomaly has been put forward in chapter IV, section IV.3.2.2. The oscillations in the $g_l(\eta^*(x_i))$ indicate the development of a layered structure along all the directions $\hat{\mathbf{n}}(z)$, $\hat{\mathbf{n}}(x)$ and $\hat{\mathbf{n}}(y)$. We note that this ordering is most apparent along the direction $\hat{\mathbf{n}}(x)$ and less intense along $\hat{\mathbf{n}}(y)$ and then $\hat{\mathbf{n}}(z)$ respectively. It would seem reasonable to expect a more well defined layered structure parallel to those directions that exhibit a higher degree of order. However, figure V.24 reveals that $g_l(\eta^*(\hat{\mathbf{n}}(y)))$ seems to be exhibiting a more well defined layer structure than $g_l(\eta^*(\hat{\mathbf{n}}(z)))$. It should be stressed that the interpretation of figure V.24 is that it shows only a tendency for the system to form layers over the duration of the simulation run. The apparent layers illustrated in the figure are weak. Due to the large value of $\langle P_2(x) \rangle = 0.60$, on average the site symmetry axes are orientated with a degree of order typical of a nematic liquid crystal, whereas the order along the remaining molecular semi-axes, although not zero, is very small. This phase most closely resembles that of a uniaxial discotic nematic. Indeed in a larger system values the $\langle P_2(z) \rangle$ and $\langle P_2(y) \rangle$ would take values closer to zero.

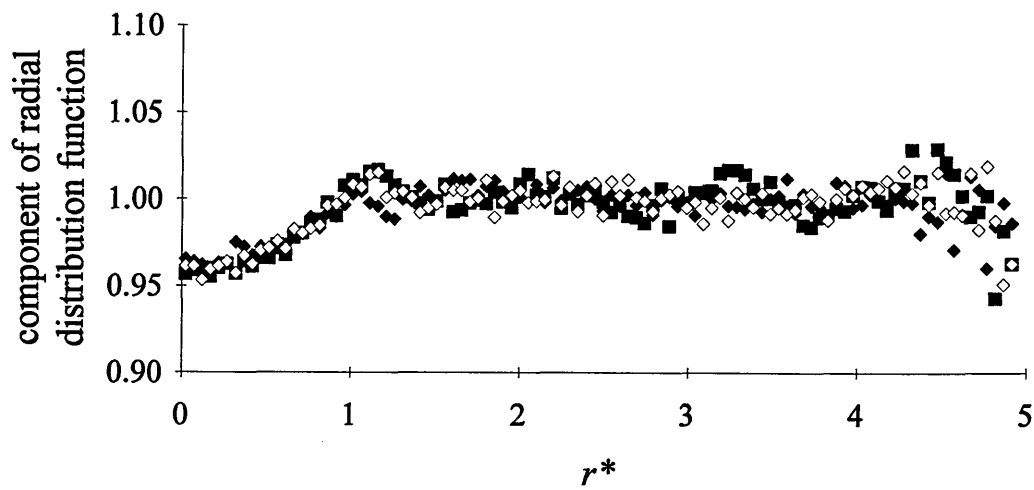


Figure V.22

Components of the radial distribution function for the twisted central site model at reduced temperature $\langle T^* \rangle = 4.7$: closed squares, $g_1(\eta^*(\hat{n}(z)))$; closed diamonds, $g_1(\eta^*(\hat{n}(x)))$; open diamonds, $g_1(\eta^*(\hat{n}(y)))$.

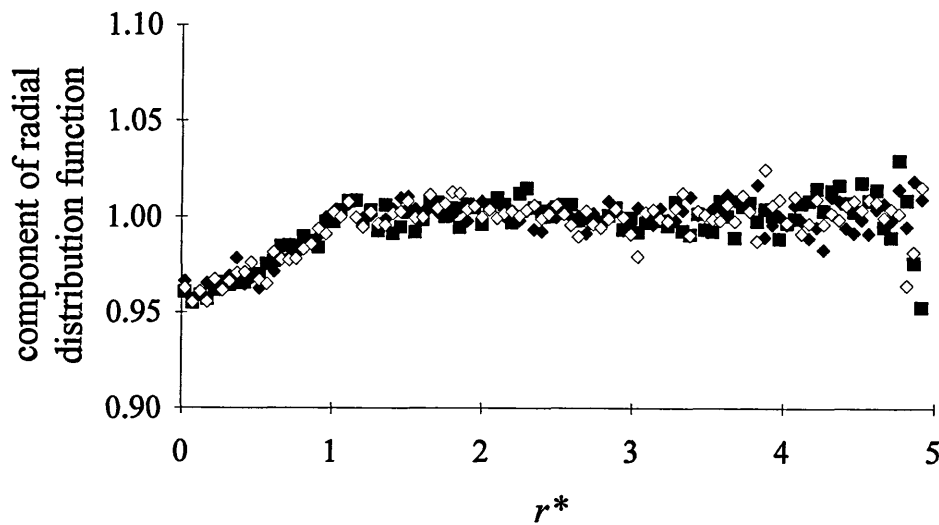


Figure V.23

Components of the radial distribution function for the all coplanar model at temperature $\langle T^* \rangle = 6.3$ ($\langle V^*/N \rangle = -37.2$). For legend see figure V.22.

As the system is cooled still further the $g_1(\eta^*(x_i))$ confirm the appearance of a layered structure with greater amplitude well defined oscillations as exhibited in figure V.25. The strength of definition order of the layers is not maintained; and now layers parallel to $\hat{n}(x)$ are more defined than those parallel $\hat{n}(z)$ which in turn are more defined than those parallel to $\hat{n}(y)$. Looking at the information provided in table V.2 we see that at this state point we have the following values for the $\langle P_2(x_i) \rangle$; $\langle P_2(x) \rangle = 0.86$, $\langle P_2(z) \rangle = 0.57$ and $\langle P_2(y) \rangle = 0.51$, the values being ordered in the same way as we find the evidence for layers appearing in the $g_1(\eta^*(x_i))$. The value of $\langle P_2(x_i) \rangle$ reflects the number of molecules, on average, adopting an orientation such that the molecular semi-axis x_i is aligned along the direction $\hat{n}(x_i)$. A relatively lower value for $\langle P_2(x_i) \rangle$ implies that the direction $\hat{n}(x_i)$ is not so well defined as for higher values $\langle P_2(x_i) \rangle$. Or rather, distribution properties resolved along these $\hat{n}(x_i)$ are subject to a more diffuse directional interpretation. This is what we are observing in figure V.25 and to a lesser extent in figure V.24 where the directions $\hat{n}(z)$ and $\hat{n}(y)$ are not so well defined.

The separation between the layers is found to be a little over σ_0 in all directions. The turning points of all curves occur at the same locations. Such a periodicity in $g_1(\eta^*(\hat{n}(x_i)))$ is easily comprehended parallel to the directions $\hat{n}(x)$ and $\hat{n}(y)$ if we are observing a discotic nematic phase where the coplanar site symmetry axes are tending to align. However in terms of alignment of the z-molecular semi-axes we would expect the function $g_1(\eta^*(\hat{n}(z)))$ to have a minimum periodicity of about $2 \cdot 2\sigma_0$, assuming the molecular hard cores do not overlap significantly. Each density wave appears to indicate the existence of four layers across half the box in the directions $\hat{n}(x_i)$.

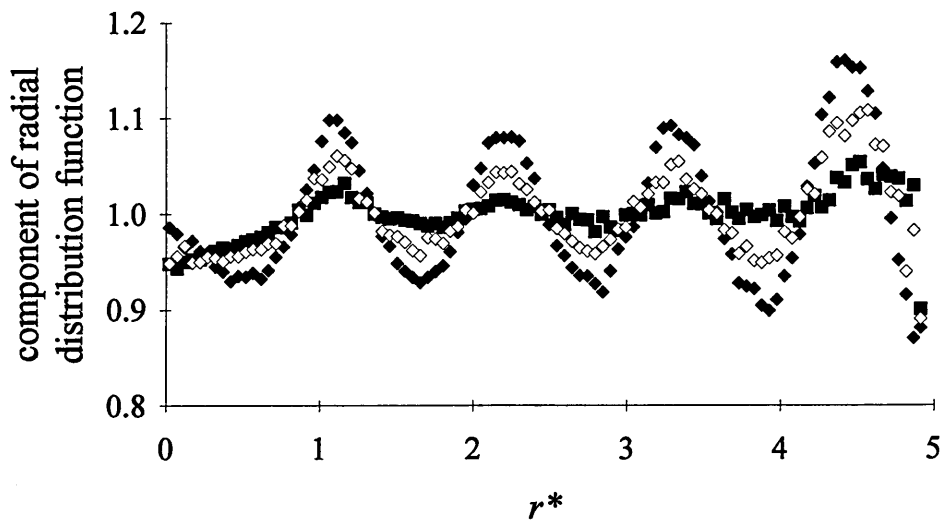


Figure V.24

Components of the radial distribution function for the twisted central site model at reduced temperature $\langle T^* \rangle = 4.3$ ($\langle V^*/N \rangle = -44.0$): closed squares, $g_1(\eta^*(\hat{n}(z)))$; closed diamonds, $g_1(\eta^*(\hat{n}(x)))$; open diamonds, $g_1(\eta^*(\hat{n}(y)))$.

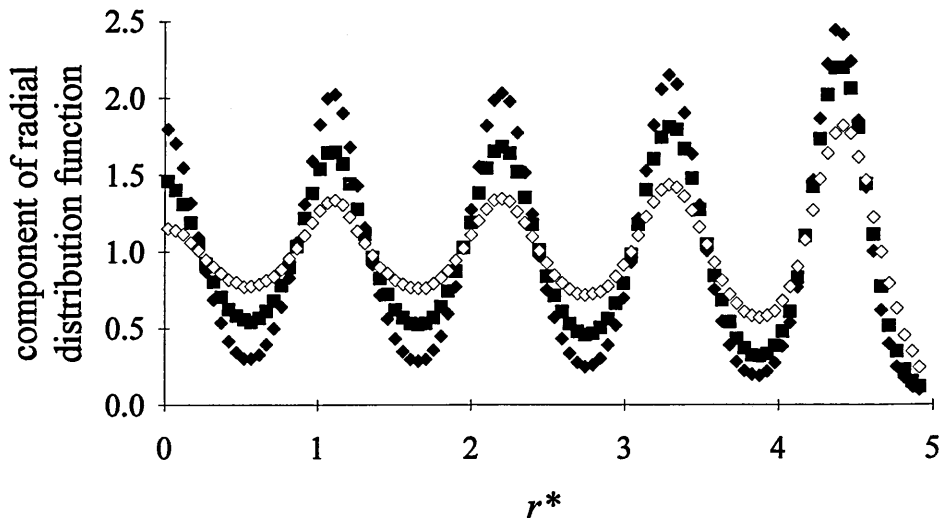


Figure V.25

Components of the radial distribution function for the twisted central site model at reduced temperature $\langle T^* \rangle = 4.2$ ($\langle V^*/N \rangle = -52.1$). For legend see figure V.24.

Turning to the all coplanar site model figure V.26 illustrates the behaviour of the $g_1(\eta^*(x_i))$ when the molecular semi-axes are ordered with $\langle P_2(x) \rangle = 0.85$, $\langle P_2(z) \rangle = 0.28$ and $\langle P_2(y) \rangle = 0.27$ with the higher temperature $\langle T^* \rangle = 6.6$ but with lower potential energy $\langle V^*/N \rangle = -53.9$ than those presented in figure V.23. In this figure we can see the emergence of structure parallel to the average direction of the HGBLR site symmetry axes. We note that this is qualitatively similar to that observed for $g_1(\eta^*(\hat{n}(x)))$ with the twisted central site model in figure V.24. However, we do not observe any ordering parallel to the other molecular semi-axes in figure V.26 yet these semi-axes are ordered with values comparable to those presented in figure V.24.

At lower temperature, $\langle T^* \rangle = 5.3$ (corresponding to $\langle V^*/N \rangle = -64.9$), figure V.27 we note enhanced layering parallel to the average HGBLR site symmetry axes direction but in stark contrast to the twisted central site model, there is no structure to $g_1(\eta^*(\hat{n}(z)))$ and $g_1(\eta^*(\hat{n}(y)))$ at all. The structure described by $g_1(\eta^*(\hat{n}(x)))$ is similar to that presented in figure V.26, but here the density wave is much stronger with zero minima appearing between the peaks which are separated by $\approx 1.1\sigma_0$.

It is clear that the structures described by figure V.24 and V.25 are different from those described by figures V.26 and V.27.

Once again with figure V.26 and to a lesser extent with figure V.27 we note the increasing amplitude of oscillations of $g_1(\eta^*(\hat{n}(x)))$ parallel to the direction $\hat{n}(x)$ with increasing η^* and allude to the explanation offered in section IV.3.2.2.

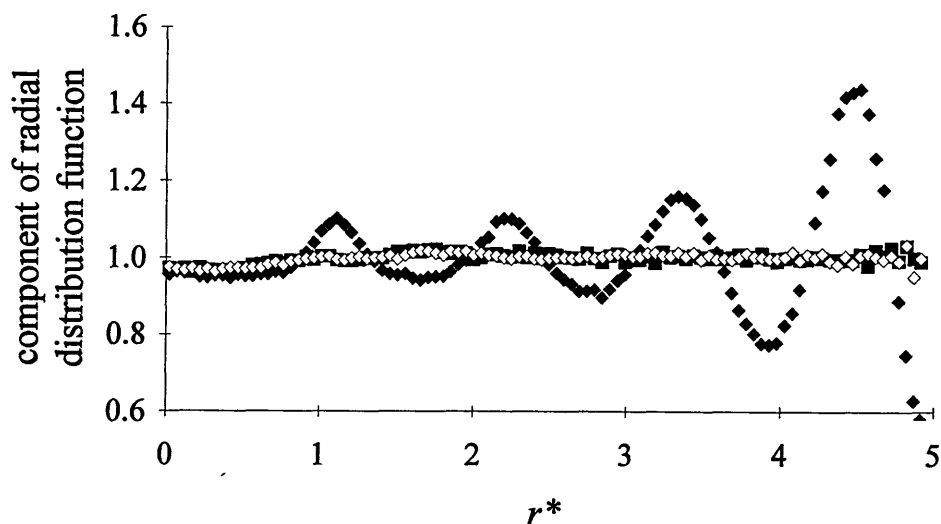


Figure V.26

Components of the radial distribution function for the all coplanar site model at temperature $\langle T^* \rangle = 6.6$ ($\langle V^*/N \rangle = -53.9$): closed squares, $g_1(\eta^*(\hat{n}(z)))$; closed diamonds, $g_1(\eta^*(\hat{n}(x)))$; open diamonds, $g_1(\eta^*(\hat{n}(y)))$.

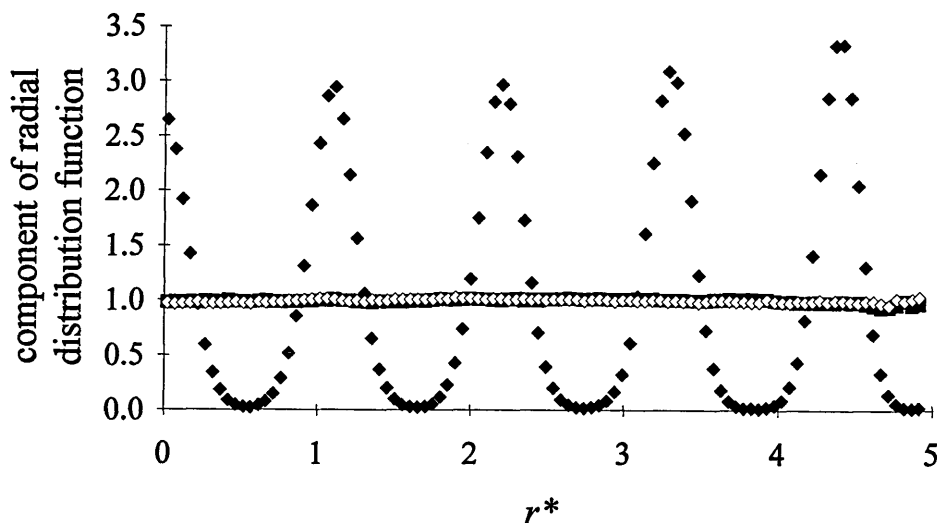


Figure V.27

Components of the radial distribution function for the all coplanar site model at temperature $\langle T^* \rangle = 5.3$. For legend see figure V.26.

In order to probe the structure of these two different models as the temperature is reduced further we have chosen to examine the $g_1(\eta^*(x_i))$ from two further state points for each model. Figure V.28 illustrates the behaviour exhibited for the twisted central site model at the temperature $\langle T^* \rangle = 4.2$, with $\langle V^*/N \rangle = -53.4$, the state point simulated just after that of figure V.26 on cooling the system. Comparing the two figures we note that the oscillations in $g_1(\eta^*(\hat{n}(x)))$ are now of increased magnitude in the latter figure, though they still occupy the same locations. Moreover the oscillations in $g_1(\eta^*(\hat{n}(z)))$ and $g_1(\eta^*(\hat{n}(y)))$ have all but disappeared. Clearly there are some correlations at the end of the range scale, these however, are most likely caused by the reasons explained in section IV.3.2.2.

At the lower temperature of $\langle T^* \rangle = 1.79$, exhibited in figure V.29, the oscillations in $g_1(\eta^*(\hat{n}(x)))$ have increased in magnitude so that they now have zero minima. Furthermore we see the positive reintroduction of structure in the distribution functions resolved along the directions $\hat{n}(z)$ and $\hat{n}(y)$. This time however, the structure is not as was previously observed in figure V.25 and to a lesser extent in figure V.24. The maxima and minima in $g_1(\eta^*(\hat{n}(z)))$ appear more erratic in amplitude. They appear to be weaker, equally spaced with shorter period; there are five periods observed in figure V.29 compared to just four in figure V.25.

Such a change in structure is not displayed by the all coplanar site model. Figure V.30 presents the behaviour of the components $g_1(\eta^*(x_i))$ for this model recorded at temperature $\langle T^* \rangle = 5.1$, and figure V.31 presents the behaviour of those components recorded at $\langle T^* \rangle = 2.28$. We note there appears to be little evidence for the development of structure present along the directions $\hat{n}(z)$ and

$\hat{n}(y)$. Parallel to $\hat{n}(x)$ however, the evidence of a layered structure remains. The density wave along $\hat{n}(x)$ in both figures have zero value minima as observed in figure V.27. This is typical of a well ordered layered structure with spaces in between the layers not filled with molecules. As the temperature is lowered further, the density wave becomes more distinct, the intensities of the maxima grow and the ranges of the minima become larger in figure V.31 indicating the presence of a more ordered layer structure parallel to $\hat{n}(x)$.

We note further that the layered structures exhibited by both models parallel to $\hat{n}(x)$ display the same periodicity of $\approx 1.1\sigma_0$ which is just slightly larger than the HGBLR hard core radius of σ_0 .

Turning to the second rank orientational correlation coefficients, $G_2(r^*)$, these have been recorded with respect to the molecular long axis. The results for both the twisted central site and all coplanar site model are presented in figures V.32 and V.33 respectively at a variety of temperatures. Examination of figure V.32 reveals that at $\langle T^* \rangle = 4.7$ $G_2(r^*)$ quickly decays to zero, indicating no long range ordering of the molecular long axes. However, at all other temperatures presented in figure V.32 $G_2(r^*)$ decays to some finite value at long range.

Similar behaviour is found for the all coplanar model presented in figure V.33.

A comparison of the two figures reveals a distinct difference between the degree of ordering of the molecular long axes of both models. As the temperature is reduced, the long range behaviour of $G_2(r^*)$ decays to a higher value for the twisted central site model as evidenced in figure V.33.

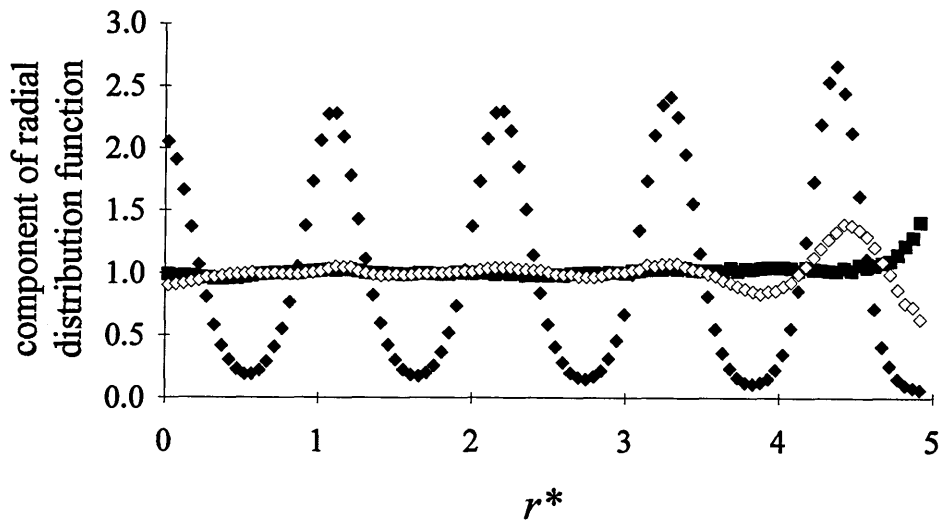


Figure V.28

Components of the radial distribution function for the twisted central site model at reduced temperature $\langle T^* \rangle = 4.2$ ($\langle V^* / N \rangle = -53.4$): closed squares, $g_1(\eta^*(\hat{n}(z)))$; closed diamonds, $g_1(\eta^*(\hat{n}(x)))$; open diamonds, $g_1(\eta^*(\hat{n}(y)))$.

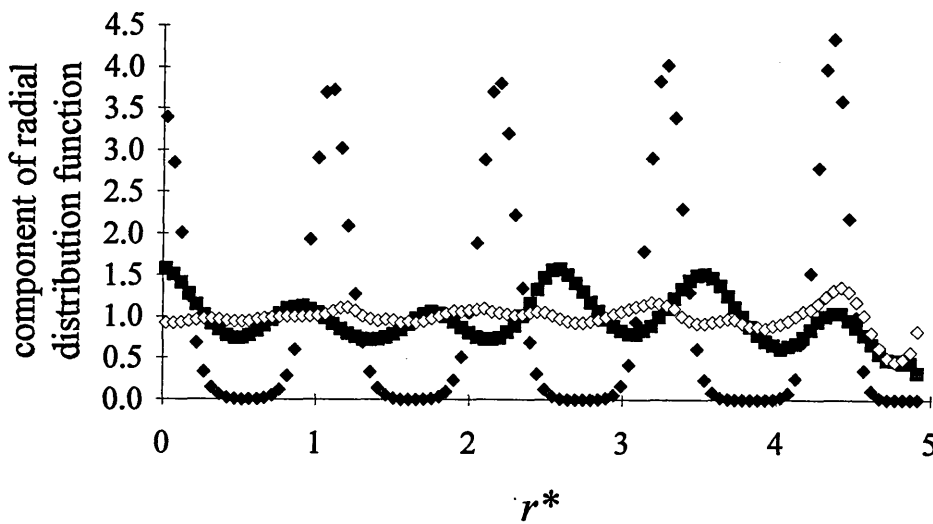


Figure V.29

Components of the radial distribution function for the twisted central site model at reduced temperature $\langle T^* \rangle = 1.79$. For legend see figure V.28.

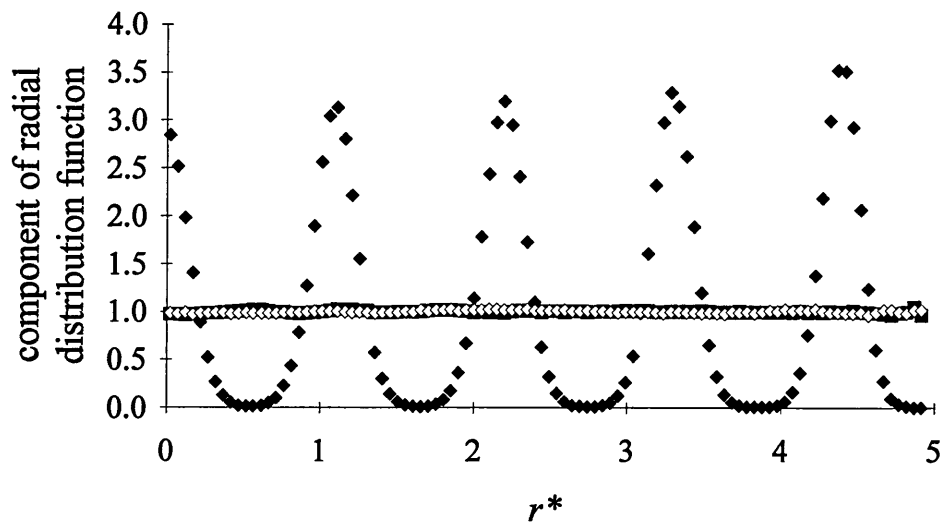


Figure V.30

Components of the radial distribution function for the all coplanar site model at temperature $\langle T^* \rangle = 5.3$: closed squares, $g_1(\eta^*(\hat{n}(z)))$; closed diamonds, $g_1(\eta^*(\hat{n}(x)))$; open diamonds, $g_1(\eta^*(\hat{n}(y)))$.

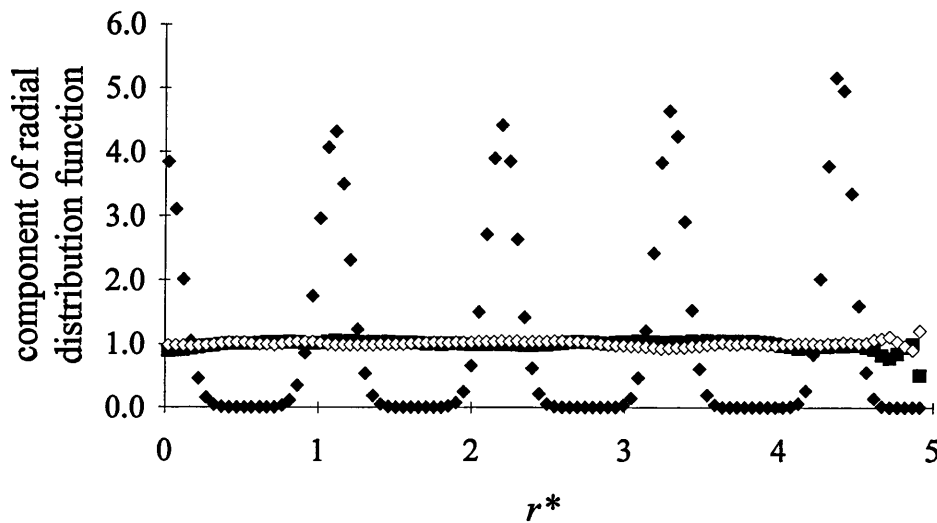


Figure V.31

Components of the radial distribution function for the all coplanar site model at reduced temperature $\langle T^* \rangle = 2.28$. For legend see figure V.31.

The values obtained at long range for $G_2(r^*)$ are consistent with $\langle P_2(z) \rangle^2$ for the temperatures indicated and indeed provide a check on the second rank order parameter for these temperatures. For the all coplanar model, though, the second rank orientational correlation coefficient tends towards a limiting value such that $G_2(r^*) \rightarrow 0.3$. Once again this is entirely consistent with the behaviour exhibited by the second rank order parameter of this system, illustrated in figure V.19.

V.8.3 Mean Square Particle Displacement

Although the behaviour exhibited by the radial distribution functions at higher temperatures are typical of liquid-like behaviour they do not confirm it: it is possible to observe similar behaviour in a glass, say. Thus it is instructive to examine the behaviour of the mean square particle displacement from initial positions. The behaviour of the mean square displacement for the twisted central site model is illustrated at four state points in figure V.34. All but the curve recorded at $\langle T^* \rangle = 1.79$ exhibit straight line liquid-like behaviour at the temperatures investigated. Thus we can be sure that down to $\langle T^* \rangle = 4.2$ the twisted central site system remains fluid. We note that the gradient of each curve decreases indicating a reduction in particle self diffusion with decreasing temperature.

Similar behaviour is indicated for the all coplanar model in figure V.35, and here we can be sure that down to $\langle T^* \rangle = 4.6$ that this system also remains fluid.

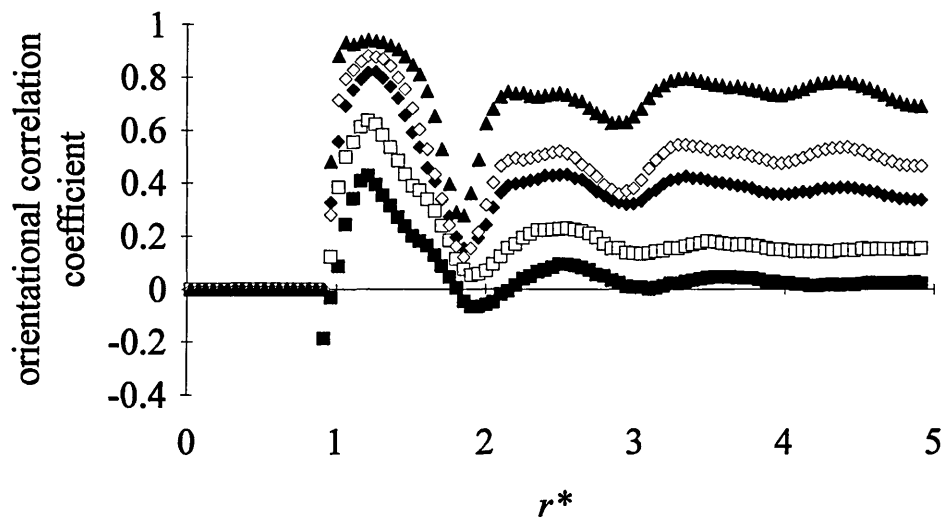


Figure V.32

$G_2(r^*)$ for the twisted central site model: closed squares, $\langle T^* \rangle = 4.7$; open squares, $\langle T^* \rangle = 4.3$ ($\langle V^*/N \rangle = -44.0$); closed diamonds, $\langle T^* \rangle = 4.2$ ($\langle V^*/N \rangle = -52.1$); open diamonds, $\langle T^* \rangle = 4.2$ ($\langle V^*/N \rangle = -53.4$); closed triangles, $\langle T^* \rangle = 3.8$.

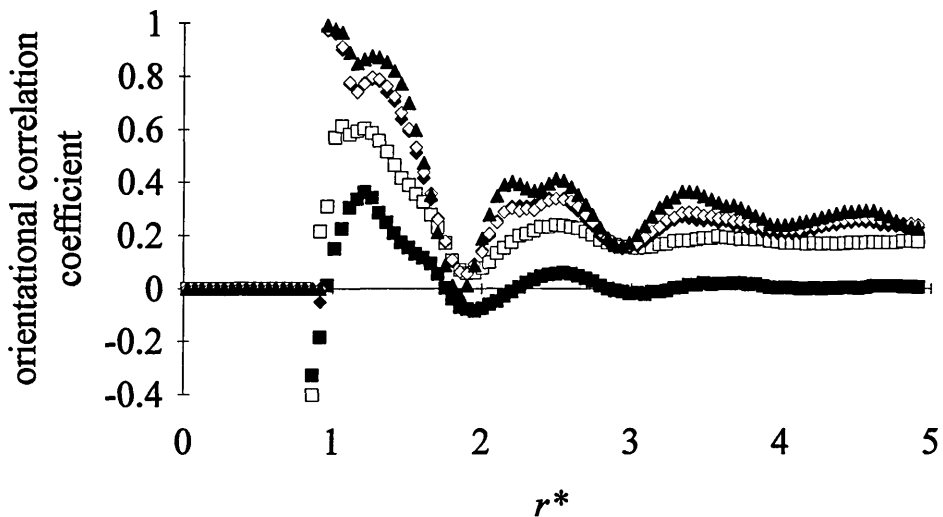


Figure V.33

$G_2(r^*)$ for the all coplanar site model: closed squares, $\langle T^* \rangle = 6.3$ ($\langle V^*/N \rangle = -37.2$); open squares, $\langle T^* \rangle = 6.6$ ($\langle V^*/N \rangle = -53.9$); closed diamonds, $\langle T^* \rangle = 5.3$; open diamonds, $\langle T^* \rangle = 5.1$; closed triangles, $\langle T^* \rangle = 4.6$.

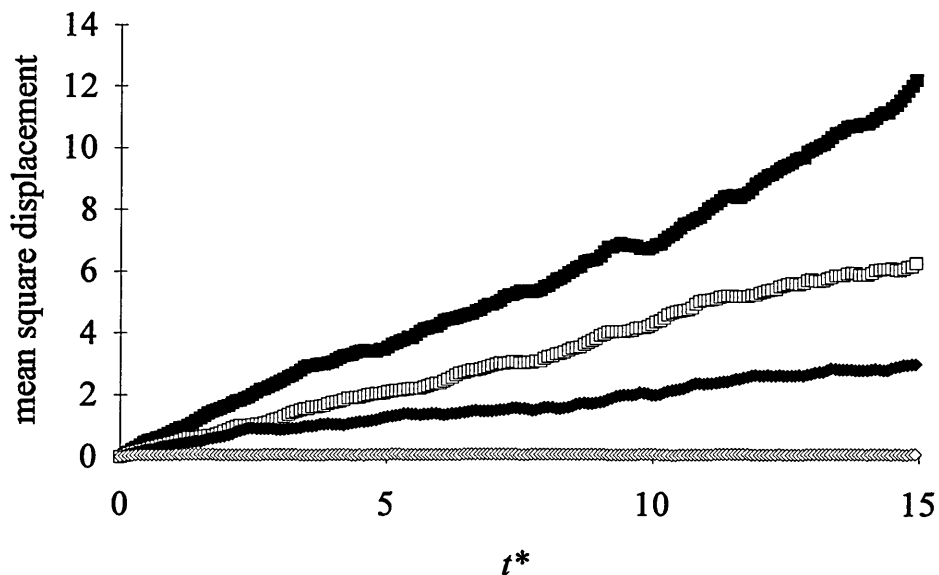


Figure V.34

Mean square displacement for the twisted central site model: closed squares, $\langle T^* \rangle = 4.7$; open squares, $\langle T^* \rangle = 4.3$ ($\langle V^*/N \rangle = -44.0$); closed diamonds, $\langle T^* \rangle = 4.2$ ($\langle V^*/N \rangle = -52.1$); open diamonds, $\langle T^* \rangle = 1.79$.

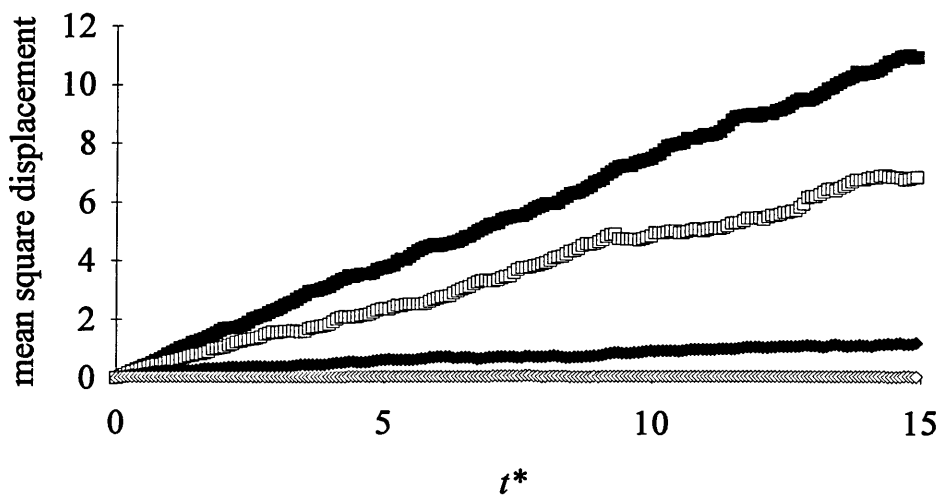


Figure V.35

Mean square displacement for the all coplanar site model: closed squares, $\langle T^* \rangle = 6.3$ ($\langle V^*/N \rangle = -37.2$); open squares, $\langle T^* \rangle = 6.6$ ($\langle V^*/N \rangle = -53.9$); closed diamonds, $\langle T^* \rangle = 4.6$; open diamonds, $\langle T^* \rangle = 2.28$.

V.8.4 Graphical Representations

We have used computer graphics to capture snapshots from system configurations in an attempt to complement the data provided from structural and orientational correlation functions to provide a comprehensive picture of the phases of the 3-HGBLR-site models we have investigated. Figures V.36 and V.37 present a series of images taken from configurations of the twisted central site and all coplanar site models respectively. In these figures single molecules are represented by coplanar squares in linear array along the molecular long axis. The squares are centred on the HGBLR site centres. They are drawn with correct orientation in the y-, z-planes of each molecule indicating the position and orientation of the site equatorial planes in accord with the convention adopted in figure V.1. The twisted central site is not represented in figure V.36 as it is found that this obscures the visual information presented by images of highly ordered phases. The side of each square is $0.7\sigma_0$; the molecules being drawn somewhat smaller than their actual size to facilitate viewing the images. In some images it is possible to see a black line drawn through the simulation box representing the director $\hat{\mathbf{n}}(\mathbf{x},t)$: the average direction of the coplanar HGBLR site symmetry axes for that single configuration.

Figure V.36a represents a snapshot taken from the simulation with average temperature $\langle T^* \rangle = 4.7$ and average molecular order parameters $P_2(\hat{\mathbf{n}}(z),t) = 0.07$, $P_2(\hat{\mathbf{n}}(x),t) = 0.16$ and $P_2(\hat{\mathbf{n}}(y),t) = 0.08$. Clearly the system appears to lack any orientational order and corresponds to an isotropic phase.

Figures V.36b and V.36c correspond to two images captured from the simulations with $\langle T^* \rangle = 4.3$ ($\langle V^*/N \rangle = -44.0$). In these views $P_2(\hat{\mathbf{n}}(z),t) = 0.30$, $P_2(\hat{\mathbf{n}}(x),t) = 0.62$ and $P_2(\hat{\mathbf{n}}(y),t) = 0.25$. Figure V.36b

illustrates the ordering of the coplanar HGBLR site symmetry axes along $\hat{\mathbf{n}}(\mathbf{x},t)$ clearly visible through the white space observed in the figure. There does not appear to be any layering of the molecules although we know from figure V.24 that over the entire simulation slightly rippled density waves exist parallel to all three molecular semi-axes directions to a small extent. Of course, the information presented by the structural order parameters is a time average over the simulation state point, whereas the snapshots simply refer to a single time step. We might therefore only expect to see a well defined layered structure presented in snapshots of well ordered low temperature state points. Looking approximately along the direction $\hat{\mathbf{n}}(\mathbf{x},t)$ we note that many of the HGBLR sites are orientated with their site symmetry axes pointing out of the plane of the page. We note further that the molecular long axes are essentially disordered. The phase is fluid at this temperature and is identified as a discotic nematic. The molecules have their site symmetry axes ordered with $P_2(\hat{\mathbf{n}}(\mathbf{x},t)) = 0.62$ which is typical of such an order parameter for a discotic nematic. Further there appears to be a little evidence of layering along the direction $\hat{\mathbf{n}}(\mathbf{x},t)$ and this is consistent with the evidence afforded by figure V.24.

When the system has been cooled to $\langle T^* \rangle = 4.2$ ($\langle V^*/N \rangle = -52.1$), figure V.36d exhibits a degree of layering perpendicular to $\hat{\mathbf{n}}(\mathbf{x},t)$: $P_2(\hat{\mathbf{n}}(\mathbf{z}),t) = 0.52$, $P_2(\hat{\mathbf{n}}(\mathbf{x}),t) = 0.87$ and $P_2(\hat{\mathbf{n}}(\mathbf{y}),t) = 0.48$. The layers are diffuse with some molecules appearing in-between layers. Figure V.36e shows a view of the same system looking approximately along the direction $\hat{\mathbf{n}}(\mathbf{x},t)$. Clearly many of the coplanar HGBLR site planes lie approximately in the plane of the paper. Closer inspection of figure V.36e reveals the orientational correlation of the molecular long axes visible at the top and bottom simulation box faces with relatively few molecules protruding through the side faces of the simulation box.

Once the system has been cooled to $\langle T^* \rangle = 3.8$ as illustrated in figures V.36f and V.36g possessing molecular semi-axes order parameters $P_2(\hat{\mathbf{n}}(z), t) = 0.84$, $P_2(\hat{\mathbf{n}}(x), t) = 0.91$ and $P_2(\hat{\mathbf{n}}(y), t) = 0.79$ we can see the high order present in the system. The layering along $\hat{\mathbf{n}}(x, t)$ is very well defined as exhibited in figure V.36f. In figure V.36f there do not appear to be any particles positioned in-between layers. However over the course of the simulation molecules may move into the interlayer spaces: particle mean square displacements indicate that molecular diffusion does occur at this temperature but it is of relatively low magnitude. The HGBLR site symmetry axes are now highly ordered as shown in figure V.36g. Close inspection of figure V.36g reveals that the HGBLR sites are stacked on top of each other to some extent. The system resembles that of a discotic-columnar phase. The positions of the individual columns are restricted by the rigid nature of the 3-HGBLR-site molecules. Due to the layered structure and high degree of ordering of the molecular semi-axes $\langle P_2(z) \rangle$ and $\langle P_2(y) \rangle$ this phase is perhaps more correctly described as a biaxial smectic with defects.

For completeness images of the low temperature simulation are presented in figures V.36h and V.36i. Molecular diffusion has ceased at $\langle T^* \rangle = 1.79$ (see figure V.34) and this system is highly ordered with $P_2(\hat{\mathbf{n}}(z), t) = 0.88$, $P_2(\hat{\mathbf{n}}(x), t) = 0.96$ and $P_2(\hat{\mathbf{n}}(y), t) = 0.86$. Figure V.36h illustrates the very regular layers along $\hat{\mathbf{n}}(x)$. Examination of figure V.36i reveals an additional layer like ordering along $\hat{\mathbf{n}}(z)$, and this reflects the behaviour of $g_1(\eta^*(\hat{\mathbf{n}}(z)))$ of figure V.29. This system is certainly a crystal due to the high degree of ordering and lack of diffusion present.

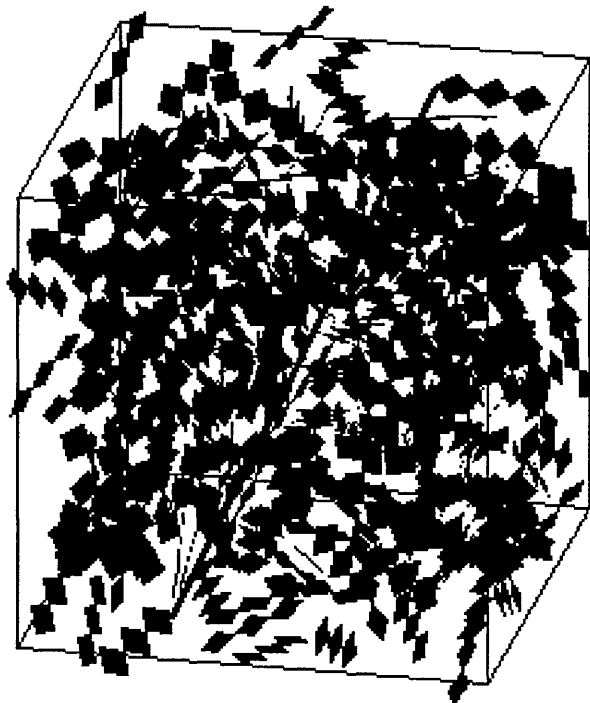


Figure V.36a

A view of an isotropic system from the simulation with average temperature $\langle T^* \rangle = 4.7$ and molecular semi-axes order parameters $P_2(\hat{\mathbf{n}}(z), t) = 0.07$, $P_2(\hat{\mathbf{n}}(z), t) = 0.16$ and $P_2(\hat{\mathbf{n}}(z), t) = 0.08$. Individual sites are represented as squares of side $0.7\sigma_0$ centred on the site symmetry axes and drawn in linear array with the same orientation as the molecular coplanar sites.

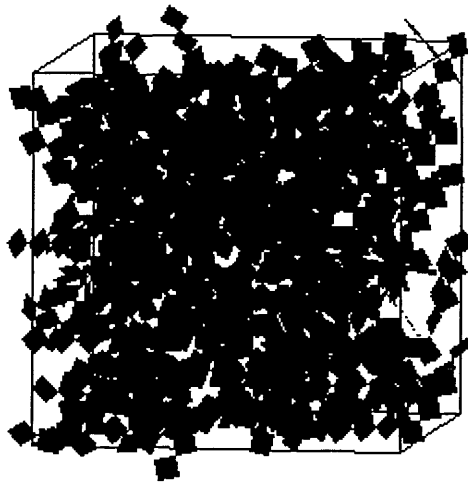
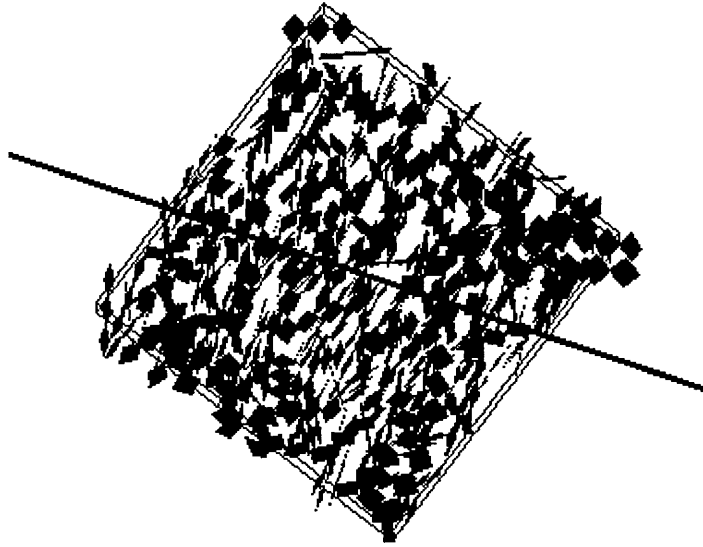


Figure V.36b (top) and V.36c (bottom)

Two views taken from the simulation with average temperature $\langle T^* \rangle = 4.3$ ($\langle V^* / N \rangle = -44.0$) with molecular semi-axes order parameters $P_2(\hat{n}(z), t) = 0.30$, $P_2(\hat{n}(x), t) = 0.62$ and $P_2(\hat{n}(y), t) = 0.25$. For a key to the molecular representation see figure V.36a and the main text.

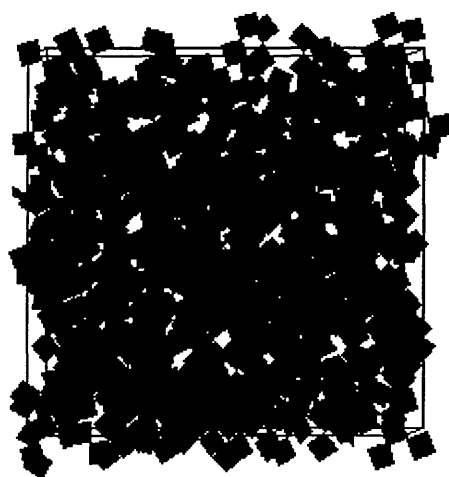
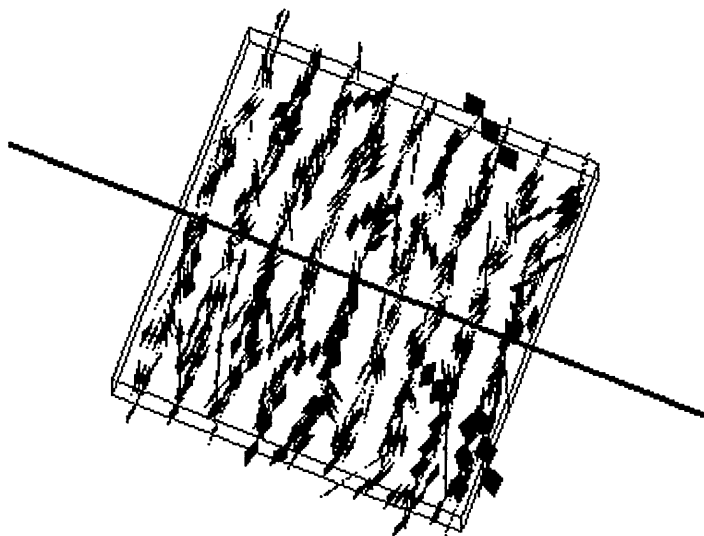


Figure V.36d (top) and V.36e (bottom)

Two views taken from the simulation with average temperature $\langle T^* \rangle = 4.2$ ($\langle V^*/N \rangle = -52.1$) with molecular semi-axes order parameters $P_2(\hat{\mathbf{n}}(z), t) = 0.52$, $P_2(\hat{\mathbf{n}}(x), t) = 0.87$ and $P_2(\hat{\mathbf{n}}(y), t) = 0.48$. For a key to the molecular representation see figure V.36a and the main text.

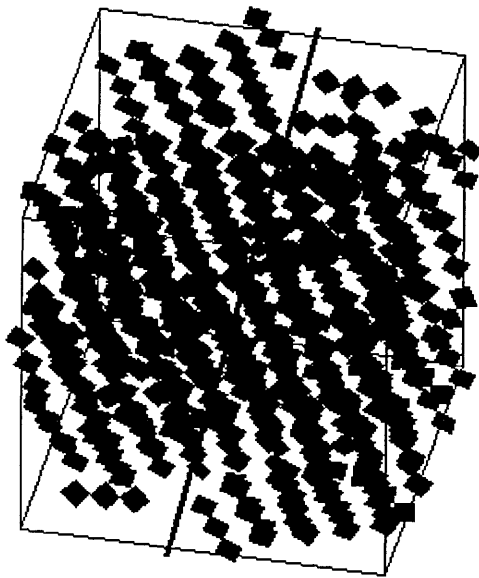
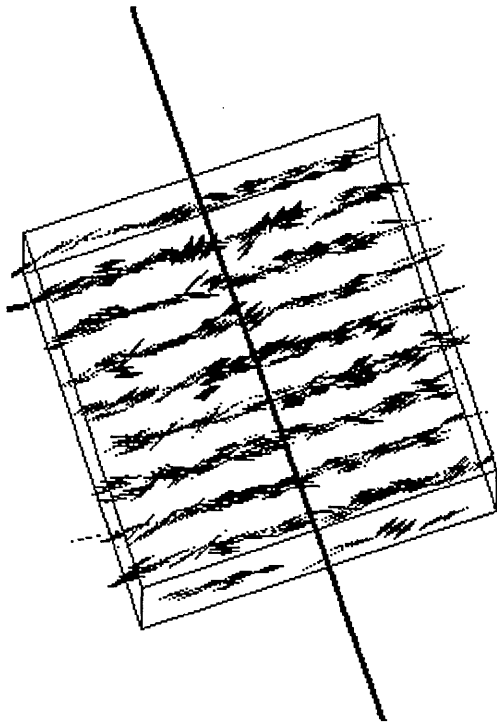


Figure V.36f (top) and V.36g (bottom)

Two views taken from the simulation with average temperature $\langle T^* \rangle = 3.8$ with molecular semi-axes order parameters $P_2(\hat{\mathbf{n}}(z), t) = 0.84$, $P_2(\hat{\mathbf{n}}(x), t) = 0.91$ and $P_2(\hat{\mathbf{n}}(y), t) = 0.79$. For a key to the molecular representation see figure V.36a and the main text.

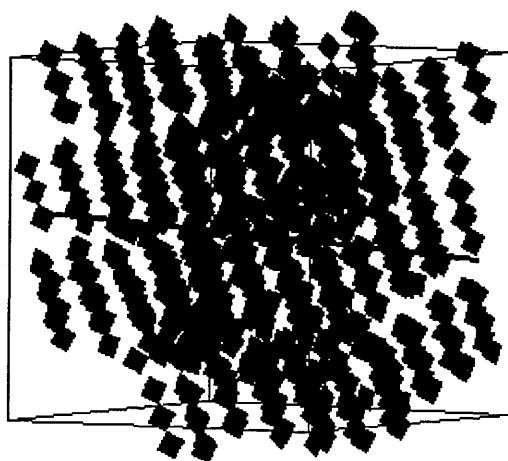
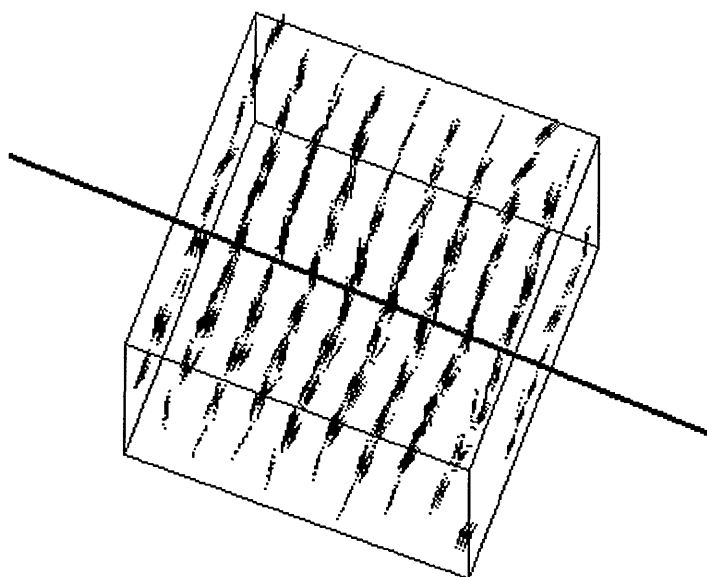


Figure V.36h (top) and V.36i (bottom)

Two views taken from the simulation with average temperature $\langle T^* \rangle = 1.79$ with molecular semi-axes order parameters $P_2(\hat{n}(z), t) = 0.88$, $P_2(\hat{n}(x), t) = 0.96$ and $P_2(\hat{n}(y), t) = 0.86$. For a key to the molecular representation see figure V.36a and the main text.

Graphical representations of the all coplanar site model are presented in figure V.37. Figure V.37a represents a snapshot taken from the simulation with average temperature $\langle T^* \rangle = 6.3$ ($\langle V^*/N \rangle = -37.2$) and the corresponding instantaneous order parameters are $P_2(\hat{\mathbf{n}}(z), t) = 0.09$, $P_2(\hat{\mathbf{n}}(x), t) = 0.17$ and $P_2(\hat{\mathbf{n}}(y), t) = 0.07$. Examination of figure V.37a reveals an essentially disordered phase and the magnitude of the order parameters identify the phase as isotropic.

Figures V.37b and V.37c represent two images recorded from the simulation with average temperature $\langle T^* \rangle = 6.6$ ($\langle V^*/N \rangle = -53.9$). Although this average temperature is higher than that of the simulation from which figure V.50a is presented, the average potential energy per particle is less. The molecules forming the images of figures V.37b and V.37c lead to instantaneous order parameters of $P_2(\hat{\mathbf{n}}(z), t) = 0.22$, $P_2(\hat{\mathbf{n}}(x), t) = 0.84$ and $P_2(\hat{\mathbf{n}}(y), t) = 0.22$. Clearly the HGBLR site symmetry axes are highly ordered whereas the degree of orientational ordering of the remaining molecular semi-axes is minimal. There appears to be little layering of the molecules as evidenced in figure V.50b. However the orientational ordering of the HGBLR site symmetry axes is clearly apparent on comparing figures V.37b and V.37c illustrated approximately perpendicular to the direction $\hat{\mathbf{n}}(x, t)$ and approximately parallel to that direction respectively. The component of the radial distribution function $g_1(r_1(\hat{\mathbf{n}}(x)))$ presented in figure V.26 does show a tendency for the molecules to prefer a weakly layered structure over the length of the simulation although the density wave does not afford particularly strong oscillations. Despite this tendency for a small degree of layering the phase more closely resembles a uniaxial discotic nematic.

Snapshots taken from the simulation with lower average temperature $\langle T^* \rangle = 5.3$ with $P_2(\hat{\mathbf{n}}(z), t) = 0.26$, $P_2(\hat{\mathbf{n}}(x), t) = 0.95$ and $P_2(\hat{\mathbf{n}}(y), t) = 0.26$ are presented as figures V.37d and V.37e. Figure V.37d now clearly illustrates the layered structure along $\hat{\mathbf{n}}(x, t)$ suggested by figure V.27. The increased orientational ordering of the site symmetry axes over those illustrated in figure V.37b is apparent. Figure V.37e presented looking approximately along the direction $\hat{\mathbf{n}}(x, t)$ shows little evidence of orientational ordering of the z- and y-molecular semi-axes. The phase resembles a discotic-smectic with each smectic layer possessing uniaxial symmetry about $\hat{\mathbf{n}}(x)$.

Figures V.37f and V.37g provide two images taken from the simulation with average temperature $\langle T^* \rangle = 4.6$ illustrating the molecular ordering with semi-axes order parameters $P_2(\hat{\mathbf{n}}(z), t) = 0.42$, $P_2(\hat{\mathbf{n}}(x), t) = 0.97$ and $P_2(\hat{\mathbf{n}}(y), t) = 0.42$. Clearly the increased orientational ordering of the molecular z- and y- semi-axes over figures V.37d and V.37e is apparent. Interestingly, figure V.37d shows one molecule, close to the line representing the site symmetry director, $\hat{\mathbf{n}}(x, t)$, which is not consistent with the general ordering observed amongst the remaining molecules. However, this is not surprising for a liquid phase. Although the mean square particle displacement recorded throughout the duration of the simulation run at $\langle T^* \rangle = 4.6$ is small it is not zero, as illustrated in figure V.37. Consequently we may expect the action of molecular diffusion to cause the odd molecule to orient itself against the prevailing trend. Indeed, such a phenomenon has been recently suggested as a reorientation mechanism for the liquid crystal [16]. Through examination of figure V.37g it appears that there may be a tendency for the molecules to arrange themselves in a rough herringbone type pattern although this is not conclusive.

Once again two views of the low temperature crystal phase are presented as figures V.37h and V.37i: $\langle T^* \rangle = 2.28$; $P_2(\hat{n}(z), t) = 0.54$, $P_2(\hat{n}(x), t) = 0.99$ and $P_2(\hat{n}(y), t) = 0.54$. Clearly the phase is highly ordered. The layering along the direction of the site symmetry axes is particularly apparent in figure V.37i. Figure V.37h shows evidence for strong correlations between the site symmetry axes of molecules from neighbouring layers, although this is not complete and the occasional approximate 90° angle can be observed.

V.9 Conclusions

We have performed MD simulations of two rigid 3-HGBLR-site site models, the two models differing only in the orientation of the central site with respect to the two coplanar end sites. At sufficiently low temperature both models exhibit orientationally ordered phases at the density investigated. It appears that the structure of the ordered phases differs for each model. The twisted central site model indicates a transition to an orientationally ordered phase at $\langle T^* \rangle \approx 4.5$ whereas for the all coplanar site model this transition is indicated at $\langle T^* \rangle \approx 6.5$, corresponding to $T = 986\text{K}$ and $T = 1424\text{K}$ respectively, taking $\epsilon_0 = 219$. These temperatures are somewhat higher than the virtual isotropic-nematic transition temperature of *para*-terphenyl of $T = 360\text{K}$ [1]. In an earlier study a Gay-Berne representation of *para*-terphenyl exhibited a transition to a nematic phase at $T = 4300\text{K}$ although the phase behaviour of this system was found to be very sensitive to ρ^* , and for other Gay-Berne systems the temperature of the isotropic-nematic transition is found to decrease rapidly with decreasing number density [1]. It is likely that simulations of 3-HGBLR-site site models at different number density will be similarly affected.

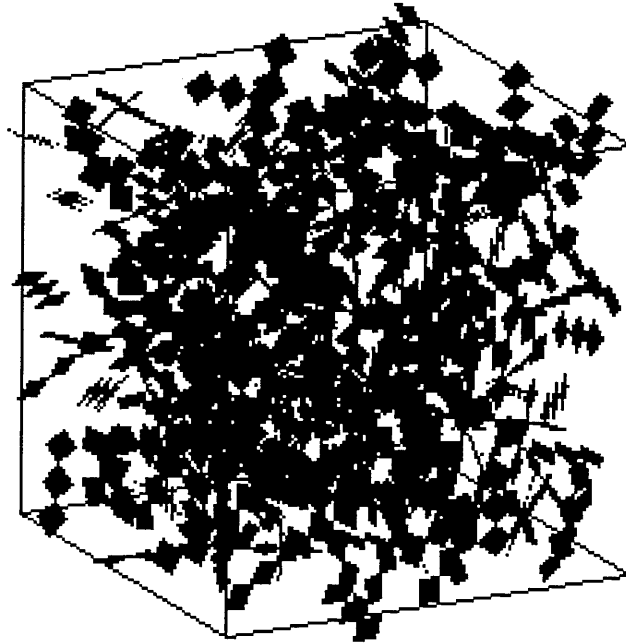


Figure V.37a

A view of an isotropic system from the simulation with average temperature $\langle T^* \rangle = 6.3$ ($\langle V^*/N \rangle = -37.2$), and molecular semi-axes order parameters $P_2(\hat{\mathbf{n}}(z), t) = 0.09$, $P_2(\hat{\mathbf{n}}(z), t) = 0.17$ and $P_2(\hat{\mathbf{n}}(z), t) = 0.07$. Individual sites are represented as squares of side $0.7\sigma_0$ centred on the site symmetry axes and drawn in linear array with the same orientation as the molecular coplanar sites.

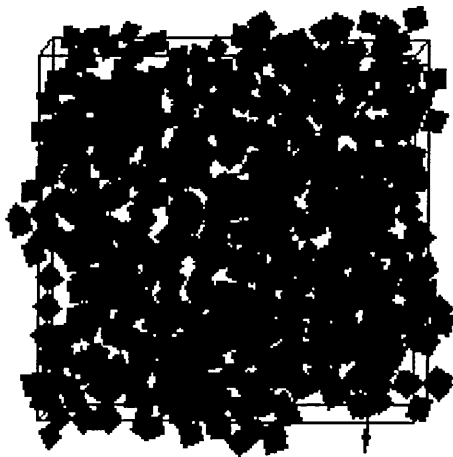
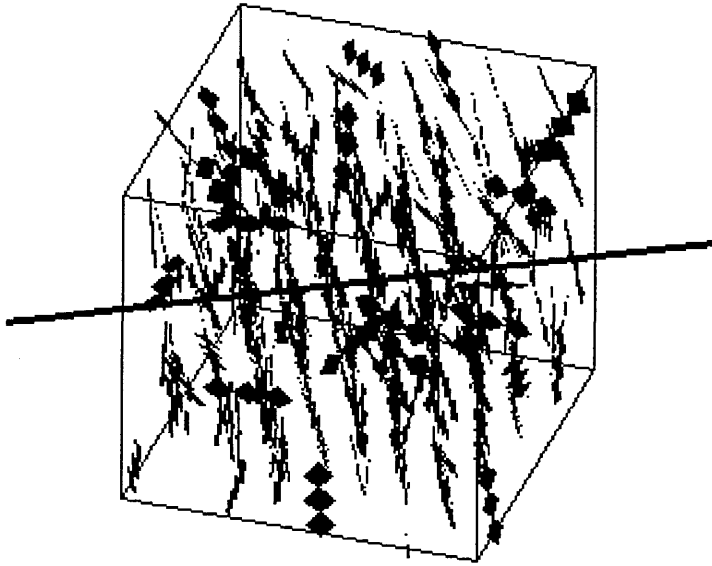


Figure V.37b (top) and V.37c (bottom)

Two views taken from the simulation with average temperature $\langle T^* \rangle = 6.6$ ($\langle V^*/N \rangle = -53.9$) with molecular semi-axes order parameters $P_2(\hat{\mathbf{n}}(z), t) = 0.22$, $P_2(\hat{\mathbf{n}}(x), t) = 0.84$ and $P_2(\hat{\mathbf{n}}(y), t) = 0.22$. For a key to the molecular representation see figure V.37a and the main text.

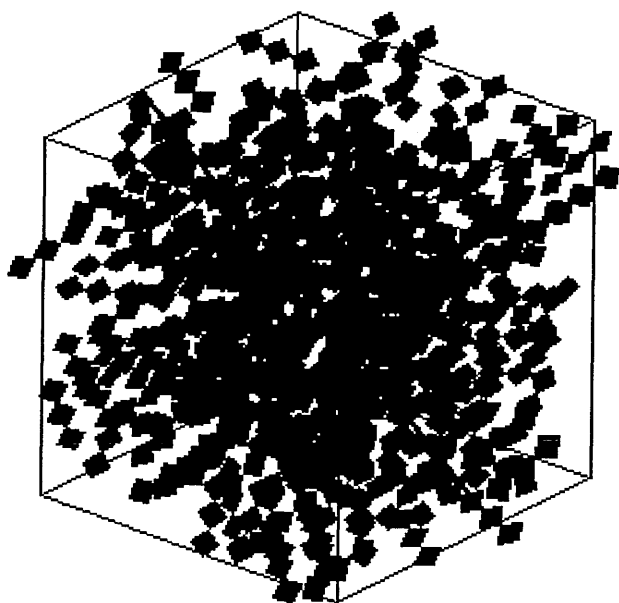
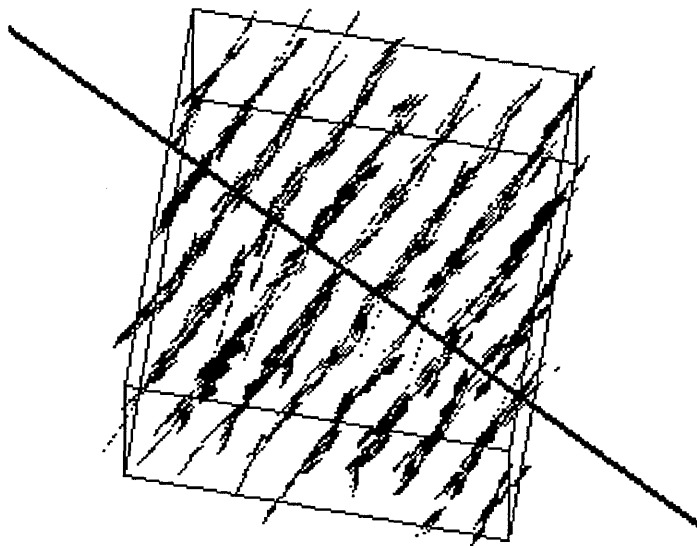


Figure V.37d (top) and V.37e (bottom)

Two views taken from the simulation with average temperature $\langle T^* \rangle = 5.3$ with molecular semi-axes order parameters $P_2(\hat{n}(z), t) = 0.26$, $P_2(\hat{n}(x), t) = 0.95$ and $P_2(\hat{n}(y), t) = 0.26$. For a key to the molecular representation see figure V.37a and the main text.

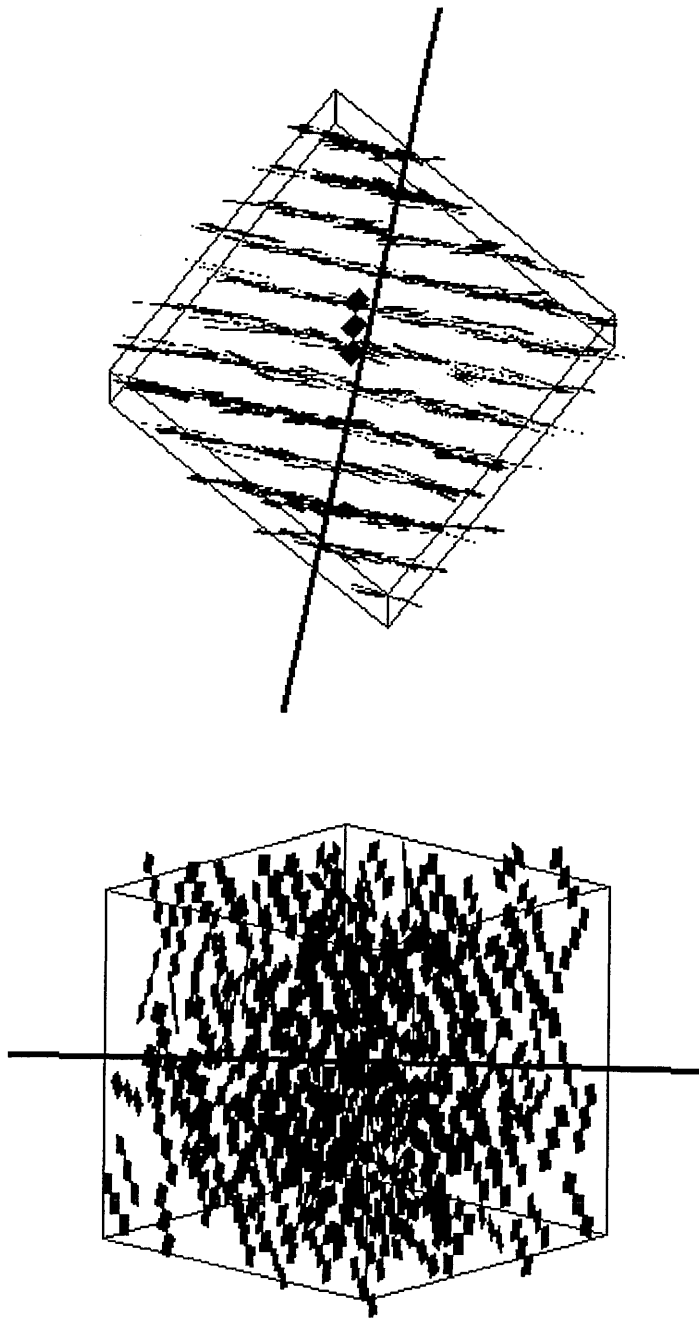


Figure V.37f (top) and V.37g (bottom)

Two views taken from the simulation with average temperature $\langle T^* \rangle = 4.6$ with molecular semi-axes order parameters $P_2(\hat{\mathbf{n}}(z), t) = 0.42$, $P_2(\hat{\mathbf{n}}(x), t) = 0.97$ and $P_2(\hat{\mathbf{n}}(y), t) = 0.42$. For a key to the molecular representation see figure V.37a and the main text.

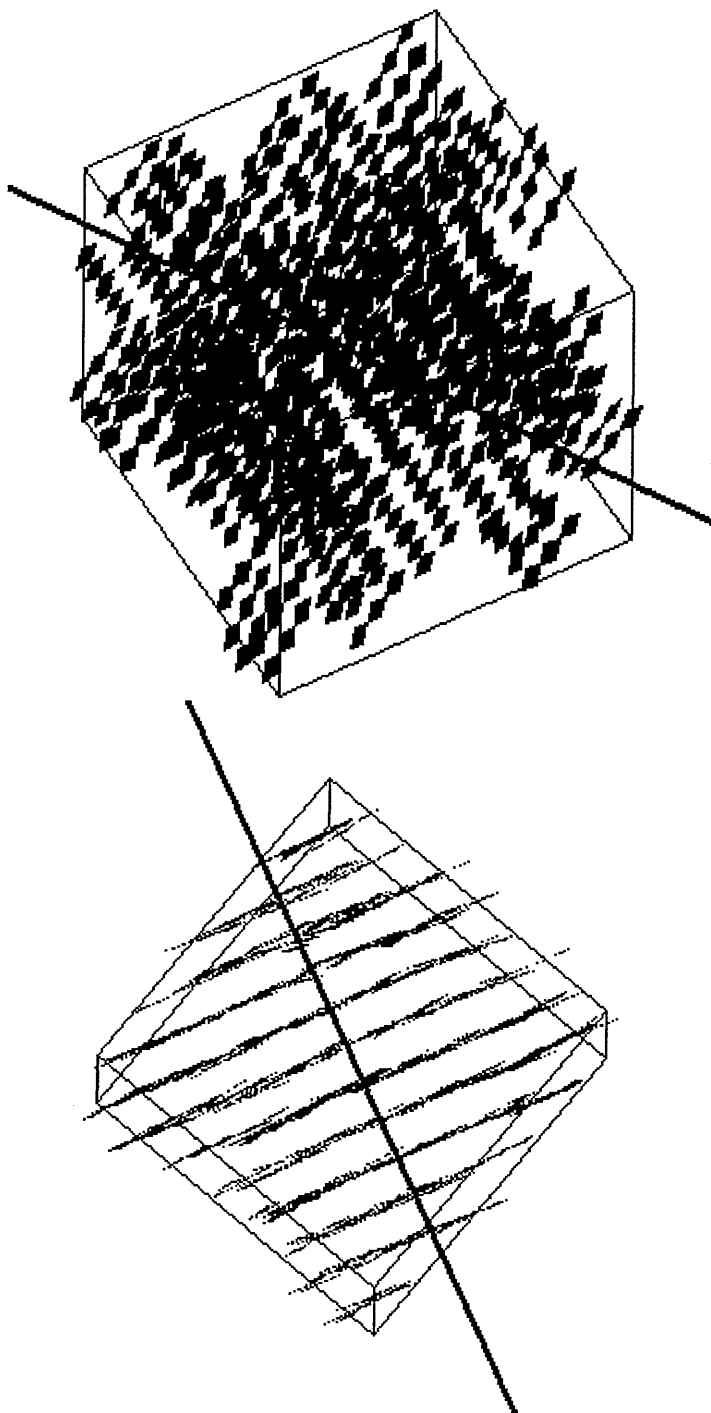


Figure V.37h (top) and V.37i (bottom)

Two views taken from the simulation with average temperature $\langle T^* \rangle = 2.28$ with molecular semi-axes order parameters $P_2(\hat{\mathbf{n}}(z), t) = 0.54$, $P_2(\hat{\mathbf{n}}(x), t) = 0.99$ and $P_2(\hat{\mathbf{n}}(y), t) = 0.54$. For a key to the molecular representation see figure V.37a and the main text.

We may tentatively identify five phases for the twisted central site model on cooling from $\langle T^* \rangle \approx 10$: isotropic \rightarrow uniaxial nematic \rightarrow biaxial nematic \rightarrow biaxial smectic \rightarrow crystal. Similarly we identify five phases for the all coplanar model on cooling from approximately the same temperature: isotropic \rightarrow uniaxial nematic \rightarrow uniaxial smectic \rightarrow biaxial smectic \rightarrow crystal. Inclusion of the twisted central site, which reduces the well depth of the most favoured configuration, appears to promote the formation of biaxial phases. In both cases the isotropic to uniaxial-nematic phase transition appears to be strongly first order. It is stressed however, that some of the phases identified above may not be thermodynamically stable and it is possible that the simulation results have been obtained from a metastable region of the phase diagram that would evolve to an alternative preferred state given sufficient length of simulation.

Luckhurst and Simmonds identify isotropic, nematic and smectic phases for their Gay-Berne model of *para*-terphenyl [1]. The formation of the smectic phase is found to be critically dependent on the long range anisotropic interactions, whereas the structure of the nematic and isotropic phases is dominated by excluded volume effects. The 3-HGBLR-site site models differ from single site HGBLR models in having anisotropic short range interactions provided by the geometrical disposition of the individual sites. The hard cores of both 3-HGBLR-site site models are spherocylindrical in shape and do not differ greatly. It is clear though, that the longer range anisotropic interactions do have an influence on the formation of the nematic phase as indicated by the different transition temperatures for each model. Similarly for the single site HGBLR centres it is the long range anisotropic interactions that allow the formation of the nematic phase.

It appears that immediately after the transition on cooling, the nematic phase exhibited by both models possesses uniaxial symmetry. Further cooling of the twisted central site model introduces a degree of ordering of the z- and y-molecular semi-axes. Owing to the large values of $\langle P_2(x_i) \rangle$ at $\langle T^* \rangle = 4.2$ ($\langle V^*/N \rangle = -52.1$), this phase may be more correctly described as a biaxial nematic. Biaxial nematic phases have been simulated before using hard particles [17]. With the all coplanar site model a significant degree of ordering of the z- and y-molecular semi-axes does not occur until well defined layers appear in the system. It may be possible that a biaxial nematic phase does not exist for this system, but instead the deep attractive well of configuration a enables the formation of a layered system along $\hat{n}(x)$ to pre-empt significant ordering of the molecular z- and y-semi-axes directions. On further cooling these axes do order but do not attain the same degree of ordering as those of the twisted central site model. It seems that incorporation of the twisted central site delays the onset of smectic-like layering and allows the biaxial nematic to form.

Alternatively, the biaxial nematic phase may not be thermodynamically stable and given sufficient length of simulation may resort to a uniaxial nematic or to the smectic-like layered system that occurs on further cooling. Apart from the differing transition temperatures it is the potential formation of the biaxial nematic phase and the structure of the final crystal phase that distinguishes the twisted central site model from the all coplanar site model.

Both 3-HGBLR-site models exhibit a layered structure. This structure is closely similar to the smectic-A mesophase of calamitic mesogens but the constituent molecules have the coplanar HGBLR site symmetry axes lying perpendicular to the plane of the smectic layers. In this respect the phase also

resembles that of a discotic lamellar phase. Indeed attempts at modelling such phases have been tried before using the Gay-Berne potential parameterised as a disc to favour edge-to-edge alignment [18]. However, the resultant highly ordered phase formed was columnar and no evidence of a lamellar phase was found.

The layered structure exhibited by the twisted central site model also exhibits a degree of ordering of the z- and y-molecular semi-axes. In this respect the system forms a biaxial smectic phase. The smectic-like phase presented by the all coplanar model does not display the same degree of ordering of the z- and y-molecular semi-axes, although these semi-axes are not completely disordered. It appears, therefore, that inclusion of the twisted central site promotes the formation of biaxial phases.

V.10 References

- [1] Luckhurst, G. R., and Simmonds, P. S. J., 1993, *Molecular Physics*, **80**, 233-252.
- [2] Gajewski, J.J., Gilbert, K.E., and Mckelvey, J., 1990, *Advances in Molecular Modelling*, **2**, 65-92.
- [3] Serena Software, 1990, *PCMODEL Manual 4th Edition* (Bloomington, USA: Serena Software, Box 3076, IN 47402-3076 USA).
- [4] Allen, M. P., and Tildesley, D.J., 1987, *Computer Simulation of Liquids* (Clarendon Press, Oxford, UK).
- [5] Cleaver, D. J., Care, C. M., Allen, M. P., and Neal, M. P., 1995, *Physical Review E*, **54**, 559-657.
- [6] Price, S. L., 1985, *Chemical Physics Letters*, **114**, 359-364.
- [7] Klug, A., 1950, *Acta Crystallographica*, **3**, 165-175.
- [8] Claessens, M., Ferrario, M., and Ryckaert, J-P., 1983, *Molecular Physics*, **50**, 217-227.
- [9] Battaglia, M. R., Buckingham, A. D., and Williams, J. H., 1981, *Chemical Physics Letters*, **78**, 421-423.

- [10] Gay, J. G., and Berne, B. J., 1981, *Journal of Chemical Physics*, **74**, 3316- 3319.
- [11] Frenkel, D., and Mulder, B. M., 1985, *Molecular Physics*, **55**, 1171-1192.
- [12] Luckhurst, G. R., Stephens, R. A., and Phippen, R. W., 1990, *Liquid Crystals*, **8**, 451-464.
- [13] Veerman, J. A. C., and Frenkel, D., 1990, *Physical Review A*, **41**, 3237-3244.
- [14] Price, S. L., Stone, A. J., and Alderton, M., 1984, *Molecular Physics*, **52**, 987-1001.
- [15] de Gennes, P. G., and Prost, J., 1994, *The Physics of Liquid Crystals* (Clarendon Press, Oxford, UK).
- [18] Allen, M. P., *private communication*.
- [17] Allen, M. P., 1990, *Liquid Crystals*, **8**, 499-511.
- [18] Bates, M. A., Luckhurst, G. R., and Whatling, S. G., 1994, *Presented at the 9th Annual British Liquid Crystal Society Conference, Hull, UK*.

CHAPTER VI

SUMMARY AND FUTURE WORK

We have developed a single-site soft potential based upon a potential proposed by Luckhurst and Romano and scaled by part of the well depth formalism employed in the Gay-Berne potential: The hybrid Gay-Berne Luckhurst-Romano (HGBLR) potential. The HGBLR potential is characterised by an approximately spherical hard core surrounded by a longer range anisotropic attractive region. by varying the anisotropy parameter χ' the anisotropic attractive region can be made to represent discotic mesogens which favour an end-to-end alignment or calamitic mesogens favouring side-by-side alignment. Changing χ' allows a smooth change from discotic to calamitic mesogen to be accomplished. We have chosen values for χ' that have been used previously in simulations of discotic and calamitic Gay-Berne particles.

The single-site HGBLR model is an easily differentiable anisotropic potential and has the advantage of computational simplicity. In order to be able to model the subtleties of real liquid crystal mesogens realistic models incorporating such factors as molecular flexibility and electronic charge distribution will have to be considered. Presently, such models may be just within reach of today's computational resources. In the light of this the HGBLR potential provides a convenient alternative which may be readily used in liquid crystal simulations with current resources.

We have performed molecular dynamics simulations in the microcanonical ensemble on single-site HGBLR centres. The model has been shown to exhibit a

range of mesophases when parameterised to represent calamitic and discotic mesogens. The single-site HGBLR particles have been shown to exhibit orientationally ordered phases despite their spherical hard core. The orientationally ordered phases formed therefore, are due to the anisotropic long range attractive forces in the potential. In contrast to hard particle models and the Gay-Berne potential, the nematic phases exhibited by single-site HGBLR centres are not due to excluded volume effects. In real liquid crystals it is expected that both short range repulsive and long range attractive forces influence the formation of mesophases. Simulations of single-site HGBLR centres are therefore of interest in their own right for the information that they can provide on the importance of anisotropic dispersion forces in the formation of liquid crystal phases. A return to single-site simulations would be beneficial, enabling different parameterisations of HGBLR centres to be investigated. It would be of interest to discover how anisotropic the attractive forces surrounding HGBLR centres have to be in order to observe orientationally ordered phases. Investigations into the effects of varying λ and χ' are required if we are to gain an understanding of the role these parameters play in the HGBLR model.

Previous simulations of Gay-Berne particles have shown the systems to be critically dependent on the choice of number density. The indications from preliminary simulations show that the HGBLR potential may be similarly affected. A study of similarly parameterised single-site HGBLR centres at differing densities would lead to a phase diagram so that we could investigate the influence of density.

Real mesogenic molecules do not have a spherical shape and by rigidly joining HGBLR centres a more realistic model of a liquid crystal mesophase may be constructed. This is not without complications as has been encountered in the 3-

HGBLR-site site model. Because the sites were arranged in linear array a restriction was placed on the distance of closest approach that two side-by-side molecules may achieve. This restriction may be overcome by employing a greater number of sites, however this is expensive computationally. Further, in the model of *para*-terphenyl each site was chosen to represent a benzene ring in the original molecule. The use of a greater number of sites may not be desirable where there is a natural mapping of HGBLR sites to represent components of mesogenic molecules. For longer molecules this restriction is not so severe and multisite-HGBLR-site site models may be more adept at simulating such systems.

A tractable approach to parameterising a multisite HGBLR model by comparison with an atom-atom Lennard-Jones representation has been presented. The distance of closest approach restriction notwithstanding, this provides an accessible method for arriving at parameters to represent real mesogens. Construction of the 3-HGBLR-site site model resulted in a multi-site soft biaxial model of a liquid crystal. This model was subsequently shown to exhibit biaxial mesophases. It is proposed that a thorough investigation of the nature of biaxial phases formed by these type of models be undertaken. Such an investigation may involve the application of novel structural distribution functions in order to probe thoroughly the biaxial phase.

Most liquid crystal forming molecules are not uniaxial, yet more often the phases they exhibit are. This requires a comprehensive investigation and the multi-site biaxial HGBLR models could realistically act as a starting point in looking at such systems.

Due to the lack of computational resources the systems simulated in this project have been relatively small in size. Simulations of larger systems, perhaps with

longer run times would be welcome. In the case of the biaxial phases identified with the 3-HGBLR-site site models, prolonged simulation in the region of the phase transitions would be desirable in order to identify metastable phases. Ensembles such as the isothermal-isobaric ensemble allow for changes in the volume of the system being investigated and thus the systems are less likely to become trapped in a metastable region of a first order phase transition. The use of such an ensemble in the simulation of the 3-HGBLR-site site models may help to clarify the nature of the transitions and perhaps enable a more precise location of the transition temperatures.

To investigate the usefulness of the multisite HGBLR models they should be employed in further simulations perhaps representing other real mesogens. It is proposed that several HGBLR centres be rigidly joined together to represent a discogen, such as a derivative of triphenylene. It is known that the long alkyl chains of such derivatives are important in the formation of liquid crystal phases as triphenylene itself is not a mesogen. Such an investigation would prove to be of great interest and may shed further light on our understanding of the formation of liquid crystal phases.

APPENDIX A

SINGLE-SITE AND MULTI-SITE HGBLR DERIVATIONS

This appendix contains details of the mathematics employed to implement both the single-HGBLR-site potential and the multi-HGBLR-site potential. It is broken down into the two following subsections:

Appendix A.1

This section contains details of the derivation of the HGBLR potential so that it can be used in the MD simulations of single-site HGBLR particles detailed in chapter IV

Appendix A.2

This section describes the mathematics necessary to implement the multi-HGBLR-site models using the method of Price et al described in chapter V and Price, S. L., Stone, A. J., and Alderton, M, 1984, *Molecular Physics*, **52**, 987-1001.

Appendix A.1 Derivation of the Single-Site HGBLR potential

In chapter II the HGBLR potential was written as follows:

$$V_{\text{HGBLR}}(\hat{\mathbf{u}}_1, \hat{\mathbf{u}}_2, \mathbf{r}) = \varepsilon_2(\hat{\mathbf{u}}_1, \hat{\mathbf{u}}_2, \hat{\mathbf{r}})(V_0(r) + V_A(\hat{\mathbf{u}}_1, \hat{\mathbf{u}}_2, r)) \quad [\text{A.1.1}]$$

Where in expression A.1.1 the terms have the following meanings

$$V_0(r) = 4\varepsilon \left(\left(\frac{\sigma}{r} \right)^{12} - \left(\frac{\sigma}{r} \right)^6 \right) \quad [\text{A.1.2}]$$

$$V_A(\hat{\mathbf{u}}_1, \hat{\mathbf{u}}_2, r) = -4\varepsilon\lambda \left(\left(\frac{\sigma}{r} \right)^{12} + \left(\frac{\sigma}{r} \right)^6 \right) P_2(\hat{\mathbf{u}}_1, \hat{\mathbf{u}}_2); \quad [\text{A.1.3}]$$

$$\varepsilon_2(\hat{\mathbf{u}}_1, \hat{\mathbf{u}}_2, \hat{\mathbf{r}}) = 1 - \frac{\chi'}{2} \left(\frac{(\hat{\mathbf{r}} \cdot \hat{\mathbf{u}}_1 + \hat{\mathbf{r}} \cdot \hat{\mathbf{u}}_2)^2}{1 + \chi'(\hat{\mathbf{u}}_1 \cdot \hat{\mathbf{u}}_2)} + \frac{(\hat{\mathbf{r}} \cdot \hat{\mathbf{u}}_1 - \hat{\mathbf{r}} \cdot \hat{\mathbf{u}}_2)^2}{1 - \chi'(\hat{\mathbf{u}}_1 \cdot \hat{\mathbf{u}}_2)} \right) \quad [\text{A.1.4}]$$

We now obtain the spatial partial derivative of this potential with respect to say, the x -direction.

$$\frac{\partial V}{\partial x} = \frac{\partial \varepsilon_2[(\chi')(V_0 + V_A)]}{\partial x} = \frac{\varepsilon_2(\chi') \partial(V_0 + V_A)}{\partial x} + \frac{(V_0 + V_A) \partial \varepsilon_2(\chi')}{\partial x} \quad [\text{A.1.5}]$$

Taking the $V_0 + V_A$ terms first,

$$\frac{\partial V_0}{\partial x} = 4\varepsilon_0 \left(\frac{-12\sigma_0^{12}}{r^{13}} + \frac{6\sigma_0^6}{r^7} \right) \frac{\partial r}{\partial x} \quad [\text{A.1.6}]$$

But;

$$r = (x^2 + y^2 + z^2)^{\frac{1}{2}} \quad [\text{A.1.7}]$$

$$\therefore \frac{\partial r}{\partial x} = \frac{1}{2} (x^2 + y^2 + z^2)^{-\frac{1}{2}} 2x \quad [\text{A.1.8}]$$

i.e.;

$$\frac{\partial r}{\partial x} = \frac{x}{r} \quad [\text{A.1.9}]$$

Thus;

$$\frac{\partial V_0}{\partial x} = 4\varepsilon \left(\frac{-12\sigma^{12}}{r^{14}} + \frac{6\sigma^6}{r^8} \right) x. \quad [\text{A.1.10}]$$

Similarly;

$$\frac{\partial V_A}{\partial x} = 4\lambda\varepsilon \left(\frac{12\sigma^{12}}{r^{14}} - \frac{6\sigma^6}{r^8} \right) x P_2(\mathbf{u}_1 \cdot \mathbf{u}_2) \quad [\text{A.1.11}]$$

Thus,

$$\frac{\partial [V_0 + V_A]}{\partial x} = 4\varepsilon \left(\frac{-12\sigma^{12}}{r^{14}} + \frac{6\sigma^6}{r^8} + \lambda \left(\frac{12\sigma^{12}}{r^{14}} - \frac{6\sigma^6}{r^8} \right) P_2(\mathbf{u}_1 \cdot \mathbf{u}_2) \right) x \quad [\text{A.1.12}]$$

Now for the anisotropic well depth term. Making this term explicitly dependent on the separation r : $\hat{\mathbf{r}} = \mathbf{r}/r$.

$$\frac{\partial \varepsilon_2}{\partial x} = \frac{-\chi'}{r^2} \left(\frac{(\mathbf{r} \cdot \hat{\mathbf{u}}_1 + \mathbf{r} \cdot \hat{\mathbf{u}}_2)^2}{1 + \chi'(\hat{\mathbf{u}}_1 \cdot \hat{\mathbf{u}}_2)} \left(\frac{\partial [\mathbf{r} \cdot \hat{\mathbf{u}}_1]}{\partial x} + \frac{\partial [\mathbf{r} \cdot \hat{\mathbf{u}}_2]}{\partial x} \right) + \frac{(\mathbf{r} \cdot \hat{\mathbf{u}}_1 - \mathbf{r} \cdot \hat{\mathbf{u}}_2)^2}{1 - \chi'(\hat{\mathbf{u}}_1 \cdot \hat{\mathbf{u}}_2)} \left(\frac{\partial [\mathbf{r} \cdot \hat{\mathbf{u}}_1]}{\partial x} - \frac{\partial [\mathbf{r} \cdot \hat{\mathbf{u}}_2]}{\partial x} \right) \right) + \frac{x\chi'}{r^4} \left(\frac{(\mathbf{r} \cdot \hat{\mathbf{u}}_1 + \mathbf{r} \cdot \hat{\mathbf{u}}_2)^2}{1 + \chi'(\hat{\mathbf{u}}_1 \cdot \hat{\mathbf{u}}_2)} + \frac{(\mathbf{r} \cdot \hat{\mathbf{u}}_1 - \mathbf{r} \cdot \hat{\mathbf{u}}_2)^2}{1 - \chi'(\hat{\mathbf{u}}_1 \cdot \hat{\mathbf{u}}_2)} \right) \quad [\text{A.1.13}]$$

We note;

$$\frac{\partial(\mathbf{r} \cdot \hat{\mathbf{u}}_1)}{\partial x} = \hat{u}_{1x} \quad [\text{A.1.14}]$$

$$\frac{\partial(\mathbf{r} \cdot \hat{\mathbf{u}}_2)}{\partial x} = \hat{u}_{2x} \quad [\text{A.1.15}]$$

as for example;

$$\mathbf{r} \cdot \hat{\mathbf{u}}_1 = r_x \hat{u}_{1x} + r_y \hat{u}_{1y} + r_z \hat{u}_{1z} \quad [\text{A.1.16}]$$

where \hat{u}_{1x} stands for the x -component of the orientational unit vector. So finally;

$$\frac{\partial \varepsilon_2}{\partial x} = \frac{-\chi'}{r^2} \left(\frac{(\mathbf{r} \cdot \hat{\mathbf{u}}_1 + \mathbf{r} \cdot \hat{\mathbf{u}}_2)^2}{1 + \chi'(\hat{\mathbf{u}}_1 \cdot \hat{\mathbf{u}}_2)} (\hat{u}_{1x} + \hat{u}_{2x}) + \frac{(\mathbf{r} \cdot \hat{\mathbf{u}}_1 - \mathbf{r} \cdot \hat{\mathbf{u}}_2)^2}{1 - \chi'(\hat{\mathbf{u}}_1 \cdot \hat{\mathbf{u}}_2)} (\hat{u}_{1x} - \hat{u}_{2x}) \right) + \frac{x\chi'}{r^4} \left(\frac{(\mathbf{r} \cdot \hat{\mathbf{u}}_1 + \mathbf{r} \cdot \hat{\mathbf{u}}_2)^2}{1 + \chi'(\hat{\mathbf{u}}_1 \cdot \hat{\mathbf{u}}_2)} + \frac{(\mathbf{r} \cdot \hat{\mathbf{u}}_1 - \mathbf{r} \cdot \hat{\mathbf{u}}_2)^2}{1 - \chi'(\hat{\mathbf{u}}_1 \cdot \hat{\mathbf{u}}_2)} \right) \quad [\text{A.1.17}]$$

Similar terms obtain for the partial derivatives with respect to ∂y and ∂z . Turning now to the orientation dependent terms. Consider the derivative of the HGBLR potential with respect to, say, the x -component of the orientational unit vector;

$$\frac{\partial V}{\partial \hat{u}_{1x}} = \frac{\partial \varepsilon_2 [(\chi')(V_0 + V_A)]}{\partial \hat{u}_{1x}} = \frac{\varepsilon_2 (\chi') \partial (V_0 + V_A)}{\partial \hat{u}_{1x}} + \frac{(V_0 + V_A) \partial \varepsilon_2 (\chi')}{\partial \hat{u}_{1x}} \quad [\text{A..1.18}]$$

The Lennard-Jones potential is not orientationally dependent, thus;

$$\frac{\partial V_0}{\partial \hat{u}_{1x}} = 0. \quad [\text{A.1.19}]$$

But;

$$\frac{\partial V_A}{\partial \hat{u}_{1x}} = -4\lambda\varepsilon \left(\left(\frac{\sigma}{r} \right)^{12} + \left(\frac{\sigma}{r} \right)^6 \right) \frac{\partial [P_2(\hat{\mathbf{u}}_1 \cdot \hat{\mathbf{u}}_2)]}{\partial \hat{u}_{1x}}. \quad [\text{A.1.20}]$$

$$\frac{\partial [P_2(\hat{\mathbf{u}}_1 \cdot \hat{\mathbf{u}}_2)]}{\partial \hat{u}_{1x}} = \frac{1}{2} \frac{\partial}{\partial \hat{u}_{1x}} [3(\hat{\mathbf{u}}_1 \cdot \hat{\mathbf{u}}_2)^2 - 1] = 3(\hat{\mathbf{u}}_1 \cdot \hat{\mathbf{u}}_2) \hat{u}_{2x} \quad [\text{A.1.21}]$$

as

$$\frac{\partial [\hat{\mathbf{u}}_1 \cdot \hat{\mathbf{u}}_2]}{\partial \hat{u}_{1x}} = \frac{\partial}{\partial \hat{u}_{1x}} [\hat{u}_{1x} \hat{u}_{2x} + \hat{u}_{1y} \hat{u}_{2y} + \hat{u}_{1z} \hat{u}_{2z}] = \hat{u}_{2x} \quad [\text{A.1.22}]$$

Thus

$$\frac{\partial [V_0 + V_A]}{\partial \hat{u}_{1x}} = 4\varepsilon \left(\left(\frac{\sigma}{r} \right)^{12} - \left(\frac{\sigma}{r} \right)^6 - \lambda \left(\left(\frac{\sigma}{r} \right)^{12} + \left(\frac{\sigma}{r} \right)^6 \right) 3(\hat{\mathbf{u}}_1 \cdot \hat{\mathbf{u}}_2) \hat{u}_{2x} \right) \quad [\text{A.1.23}]$$

Turning to the original definition of the orientational dependent well depth scaling term equation [A.1.4] this may be re-written in terms of the products;

$$\varepsilon_2(\hat{\mathbf{u}}_1, \hat{\mathbf{u}}_2, \hat{\mathbf{r}}) = 1 - \frac{\chi'}{2} \left((\hat{\mathbf{r}} \cdot \hat{\mathbf{u}}_1 + \hat{\mathbf{r}} \cdot \hat{\mathbf{u}}_2)^2 (1 + \chi'(\hat{\mathbf{u}}_1 \cdot \hat{\mathbf{u}}_2))^{-1} + (\hat{\mathbf{r}} \cdot \hat{\mathbf{u}}_1 - \hat{\mathbf{r}} \cdot \hat{\mathbf{u}}_2)^2 (1 - \chi'(\hat{\mathbf{u}}_1 \cdot \hat{\mathbf{u}}_2))^{-1} \right) \quad [\text{A.1.24}]$$

leading to;

$$\frac{\partial}{\partial \hat{u}_{1x}} [\varepsilon_2(\hat{\mathbf{u}}_1, \hat{\mathbf{u}}_2, \hat{\mathbf{r}})] = \frac{-\chi'}{2} \left(\left(\frac{2(\hat{\mathbf{r}} \cdot \hat{\mathbf{u}}_1 + \hat{\mathbf{r}} \cdot \hat{\mathbf{u}}_2)}{1 + \chi'(\hat{\mathbf{u}}_1 \cdot \hat{\mathbf{u}}_2)} + \frac{2(\hat{\mathbf{r}} \cdot \hat{\mathbf{u}}_1 - \hat{\mathbf{r}} \cdot \hat{\mathbf{u}}_2)}{1 - \chi'(\hat{\mathbf{u}}_1 \cdot \hat{\mathbf{u}}_2)} \right) \hat{r}_x \right. \\ \left. + \left(\frac{(\hat{\mathbf{r}} \cdot \hat{\mathbf{u}}_1 - \hat{\mathbf{r}} \cdot \hat{\mathbf{u}}_2)^2}{(1 - \chi'(\hat{\mathbf{u}}_1 \cdot \hat{\mathbf{u}}_2))^2} - \frac{2(\hat{\mathbf{r}} \cdot \hat{\mathbf{u}}_1 + \hat{\mathbf{r}} \cdot \hat{\mathbf{u}}_2)^2}{(1 + \chi'(\hat{\mathbf{u}}_1 \cdot \hat{\mathbf{u}}_2))^2} \right) \chi' \hat{u}_{2x} \right) \quad [\text{A.1.25}]$$

as

$$\frac{\partial}{\partial \hat{u}_{1x}} [\hat{\mathbf{r}} \cdot \hat{\mathbf{u}}_1] = \frac{\partial}{\partial \hat{u}_{1x}} [\hat{r}\hat{u}_{1x} + \hat{r}\hat{u}_{1y} + \hat{r}\hat{u}_{1z}] = \hat{r}_x, \quad [\text{A.1.26}]$$

$$\frac{\partial}{\partial \hat{u}_{1x}} [\hat{\mathbf{r}} \cdot \hat{\mathbf{u}}_2] = 0 \quad [\text{A.1.27}]$$

and we know

$$\frac{\partial}{\partial \hat{u}_{1x}} [\hat{\mathbf{u}}_1 \cdot \hat{\mathbf{u}}_2] = \hat{u}_{2x}. \quad [\text{A.1.28}]$$

Similar terms obtain for the partial derivatives with respect to \hat{u}_{1y} and \hat{u}_{1z} . The partial derivatives of the energy well depth scaling terms with respect to $\hat{\mathbf{u}}_2$ involves a subtle change of sign due to the preceding negative in the second $(\mathbf{r} \cdot \hat{\mathbf{u}}_2)$ term. The correct expression is given in equation [A.1.29]:

$$\frac{\partial}{\partial \hat{u}_{2x}} [\varepsilon_2(\hat{\mathbf{u}}_1, \hat{\mathbf{u}}_2, \hat{\mathbf{r}})] = \frac{-\chi'}{2} \left(\begin{array}{l} \left(\frac{2(\hat{\mathbf{r}} \cdot \hat{\mathbf{u}}_1 + \hat{\mathbf{r}} \cdot \hat{\mathbf{u}}_2)}{1 + \chi'(\hat{\mathbf{u}}_1 \cdot \hat{\mathbf{u}}_2)} - \frac{2(\hat{\mathbf{r}} \cdot \hat{\mathbf{u}}_1 - \hat{\mathbf{r}} \cdot \hat{\mathbf{u}}_2)}{1 - \chi'(\hat{\mathbf{u}}_1 \cdot \hat{\mathbf{u}}_2)} \right) \hat{r}_x \\ + \left(\frac{(\hat{\mathbf{r}} \cdot \hat{\mathbf{u}}_1 - \hat{\mathbf{r}} \cdot \hat{\mathbf{u}}_2)^2}{(1 - \chi'(\hat{\mathbf{u}}_1 \cdot \hat{\mathbf{u}}_2))^2} - \frac{2(\hat{\mathbf{r}} \cdot \hat{\mathbf{u}}_1 + \hat{\mathbf{r}} \cdot \hat{\mathbf{u}}_2)^2}{(1 + \chi'(\hat{\mathbf{u}}_1 \cdot \hat{\mathbf{u}}_2))^2} \right) \chi' \hat{u}_{1x} \end{array} \right) \quad [\text{A.1.29}]$$

Appendix A.2 Derivation of the Multi-Site HGBLR Potential

Consider two molecules with centre of mass position vectors \mathbf{A} for molecule 1 and \mathbf{B} for molecule 2, as illustrated in figure A.2.1. Each molecule has an additional vector \mathbf{a} and \mathbf{b} respectively which describes the location of a site on that molecule with respect to the centre of mass. The molecules have arbitrary orientation x, y and z as shown by the sense of the dotted lines in figure A.2.1.

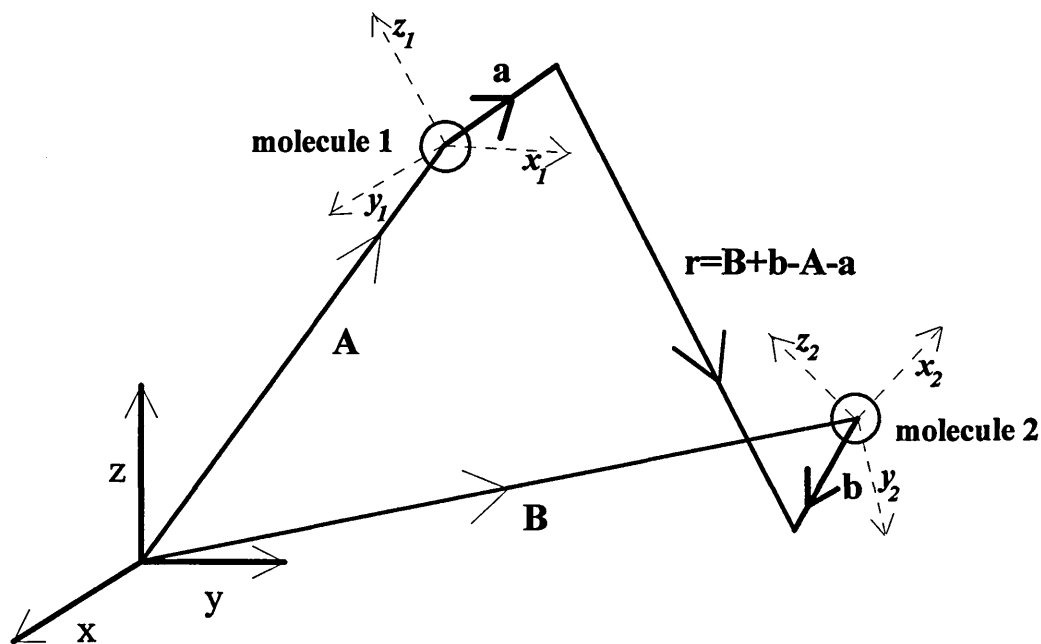


Figure A.2.1

The intersite vector \mathbf{r} is given by the expression $\mathbf{r} = \mathbf{B} + \mathbf{b} - \mathbf{A} - \mathbf{a}$. Then the force on the centre of mass of the molecule at \mathbf{B} is denoted $\mathbf{F}_2 = -\nabla_{\mathbf{B}}V$ where V is the potential of interaction. This can be re-expressed in terms of scalar products of \mathbf{r} by invocation of the chain rule for partial derivatives:

$$\mathbf{F}_2 = -\sum_{\mathbf{s}} \frac{\partial V}{\partial(\mathbf{s} \cdot \mathbf{r})} \nabla_{\mathbf{B}}(\mathbf{s} \cdot \mathbf{r}) \quad [\text{A.2.1}]$$

The notation $\sum_{\mathbf{s}}$ indicates that this expression is evaluated and summed for all scalar products of \mathbf{r} that occur in the potential V , including $r = (\mathbf{r} \cdot \mathbf{r})^{1/2}$. We seek

to find an expressions for $\sum_{\mathbf{s}} \nabla_{\mathbf{B}}(\mathbf{s} \cdot \mathbf{r})$:

$$\nabla_{\mathbf{B}}(\mathbf{s} \cdot \mathbf{r}) = \nabla_{\mathbf{B}}[\mathbf{s} \cdot (\mathbf{B} + \mathbf{b} - \mathbf{A} - \mathbf{a})] = \mathbf{s}; \quad [\text{A.2.2}]$$

$$\nabla_{\mathbf{B}}\mathbf{r} = \nabla_{\mathbf{B}}(\mathbf{r} \cdot \mathbf{r})^{1/2} = \nabla_{\mathbf{B}}[(\mathbf{B} + \mathbf{b} - \mathbf{A} - \mathbf{a}) \cdot (\mathbf{B} + \mathbf{b} - \mathbf{A} - \mathbf{a})]^{1/2}; \quad [\text{A.2.3}]$$

$$\nabla_{\mathbf{B}}\mathbf{r} = \frac{1}{2}[(\mathbf{B} + \mathbf{b} - \mathbf{A} - \mathbf{a}) \cdot (\mathbf{B} + \mathbf{b} - \mathbf{A} - \mathbf{a})]^{-1/2} 2(\mathbf{B} + \mathbf{b} - \mathbf{A} - \mathbf{a}). \quad [\text{A.2.4}]$$

Thus,

$$\nabla_{\mathbf{B}}\mathbf{r} = r^{-1}\mathbf{r} \quad [\text{A.2.5}]$$

Generally;

$$\nabla_{\mathbf{B}}\mathbf{r}^n = nr^{n-1}\nabla_{\mathbf{B}}\mathbf{r} = nr^{n-1}(r^{-1}\mathbf{r}) = nr^{n-2}\mathbf{r}. \quad [\text{A.2.6}]$$

Thus for the a multisite-HGBLR potential the force on the centre of mass of molecule 2 arising from a site-site interaction at site **b** is given by the expression;

$$-\mathbf{F}_2 = \nabla_{\mathbf{B}}[\varepsilon_2(V_0 + V_A)] = \varepsilon_2\nabla_{\mathbf{B}}(V_0 + V_A) + (V_0 + V_A)\nabla_{\mathbf{B}}\varepsilon_2. \quad [\text{A.2.7}]$$

But $(V_0 + V_A)$ has only one scalar product with \mathbf{r} : $(\mathbf{r} \cdot \mathbf{r})^{1/2}$, thus:

$$\nabla_{\mathbf{B}}(V_0 + V_A) = 4\varepsilon \left[\left\{ \frac{-12\sigma^{12}}{r^{14}} + \frac{6\sigma^6}{r^8} \right\} - \lambda \left\{ \frac{-12\sigma^{12}}{r^{14}} + \frac{6\sigma^6}{r^8} \right\} P_2(\hat{\mathbf{u}}_1 \cdot \hat{\mathbf{u}}_2) \right] \mathbf{r}. \quad [\text{A.2.8}]$$

The ε' term has three scalar products to contend with

$$\sum_{\mathbf{s}} \frac{\partial \varepsilon_2}{\partial(\mathbf{s} \cdot \mathbf{r})} \nabla_{\mathbf{B}}(\mathbf{s} \cdot \mathbf{r}) = \frac{\partial \varepsilon_2}{\partial(\mathbf{r} \cdot \mathbf{r})^{1/2}} \nabla_{\mathbf{B}}(\mathbf{r} \cdot \mathbf{r})^{1/2} + \frac{\partial \varepsilon_2}{\partial(\mathbf{r} \cdot \hat{\mathbf{u}}_1)^{1/2}} \nabla_{\mathbf{B}}(\mathbf{r} \cdot \hat{\mathbf{u}}_1)^{1/2} + \frac{\partial \varepsilon_2}{\partial(\mathbf{r} \cdot \hat{\mathbf{u}}_2)^{1/2}} \nabla_{\mathbf{B}}(\mathbf{r} \cdot \hat{\mathbf{u}}_2)^{1/2} \quad [\text{A.2.9}]$$

Now

$$\frac{\partial \varepsilon_2}{\partial (\mathbf{r} \cdot \mathbf{r})^{1/2}} \nabla_{\mathbf{B}} (\mathbf{r} \cdot \mathbf{r})^{1/2} = \frac{\chi'}{r^4} \left\{ \frac{(\mathbf{r} \cdot \hat{\mathbf{u}}_1 + \mathbf{r} \cdot \hat{\mathbf{u}}_2)^2}{1 + \chi'(\hat{\mathbf{u}}_1 \cdot \hat{\mathbf{u}}_2)} + \frac{(\mathbf{r} \cdot \hat{\mathbf{u}}_1 - \mathbf{r} \cdot \hat{\mathbf{u}}_2)^2}{1 - \chi'(\hat{\mathbf{u}}_1 \cdot \hat{\mathbf{u}}_2)} \right\} \mathbf{r} \quad [\text{A.2.10}]$$

and

$$\begin{aligned} \frac{\partial \varepsilon_2}{\partial (\mathbf{r} \cdot \hat{\mathbf{u}}_1)^{1/2}} \nabla_{\mathbf{B}} (\mathbf{r} \cdot \hat{\mathbf{u}}_1)^{1/2} + \frac{\partial \varepsilon_2}{\partial (\mathbf{r} \cdot \hat{\mathbf{u}}_2)^{1/2}} \nabla_{\mathbf{B}} (\mathbf{r} \cdot \hat{\mathbf{u}}_2)^{1/2} = \\ \frac{-\chi'}{2r^2} \left\{ \frac{2(\mathbf{r} \cdot \hat{\mathbf{u}}_1 + \mathbf{r} \cdot \hat{\mathbf{u}}_2)}{1 + \chi'(\hat{\mathbf{u}}_1 \cdot \hat{\mathbf{u}}_2)} (\hat{\mathbf{u}}_1 + \hat{\mathbf{u}}_2) + \frac{2(\mathbf{r} \cdot \hat{\mathbf{u}}_1 - \mathbf{r} \cdot \hat{\mathbf{u}}_2)}{1 - \chi'(\hat{\mathbf{u}}_1 \cdot \hat{\mathbf{u}}_2)} (\hat{\mathbf{u}}_1 - \hat{\mathbf{u}}_2) \right\} \end{aligned} \quad [\text{A.2.11}]$$

Collecting the terms together gives minus the force on the centre of mass of molecule 2, due to the interaction of the sites at $\mathbf{A}+\mathbf{a}$ and $\mathbf{B}+\mathbf{b}$ which is in fact the force on the centre of mass of the molecule at \mathbf{A} , i. e.,

$$\mathbf{F}_2 = -\nabla_{\mathbf{B}} V = -\mathbf{F}_1 \quad [\text{A.2.12}]$$

Now we turn our attention to calculating the torques. The torque is expressed in the potential in terms of scalar products of vectors which are either fixed in a direction in space, \mathbf{s} , or rotate with the molecule \mathbf{t} : $(\mathbf{s} \cdot \mathbf{t})$. If both are fixed or both are rotating then the scalar product is independent of orientation and does not contribute to the torque. For example in the determination of the torque on molecule 1 the vectors \mathbf{x}_1 , \mathbf{y}_1 and \mathbf{z}_1 and the site vector \mathbf{a} all rotate while \mathbf{x}_2 , \mathbf{y}_2 , \mathbf{z}_2 , \mathbf{b} , and $\mathbf{B} - \mathbf{A}$ (the centre of mass intermolecular vector) remain fixed. If $\hat{\mathbf{G}}$ is the differential operator that yields the torques then invocation of the chain rule similar to equation [A.2.1] yields:

$$\hat{\mathbf{G}}V = \sum \frac{\partial V}{\partial (\mathbf{s} \cdot \mathbf{t})} \hat{\mathbf{G}}(\mathbf{s} \cdot \mathbf{t}). \quad [\text{A.2.13}]$$

The expression $\frac{\partial V}{\partial(\mathbf{s} \cdot \mathbf{t})}$ can be calculated directly by differentiating the potential.

What we require here is an expression for $\hat{\mathbf{G}}(\mathbf{s} \cdot \mathbf{t})$. Writing the dot product in terms of the elements of a transformation matrix \mathbf{T} which rotates a vector in the molecular frame to the space fixed frame we may say,

$$\mathbf{s} \cdot \mathbf{t} = s_{\alpha} T_{\alpha\beta} t'_{\beta} \quad [\text{A.2.14}]$$

If the molecular frame is defined by the unit vectors \mathbf{x} , \mathbf{y} , and \mathbf{z} then we have simply,

$$\mathbf{T} = (\mathbf{x} \ \mathbf{y} \ \mathbf{z}) \quad [\text{A.2.15}]$$

Consider an infinitesimal rotation of the molecule $\delta\gamma$ about the \mathbf{z} axis thus,

$$\mathbf{T} + \delta\mathbf{T} = (\mathbf{x} + \mathbf{y}\delta\gamma \ \mathbf{y} - \mathbf{x}\delta\gamma \ \mathbf{z}) \quad [\text{A.2.16}]$$

So that the change in \mathbf{T} due to $\delta\gamma$ becomes,

$$\frac{\partial\mathbf{T}}{\partial\gamma} = (\mathbf{y} \ -\mathbf{x} \ 0) = (\mathbf{z} \times \mathbf{x} \ \mathbf{z} \times \mathbf{y} \ \mathbf{z} \times \mathbf{z}) \quad [\text{A.2.17}]$$

The z component of the torque in the molecular frame is then given,

$$\frac{-\partial}{\partial\gamma}(\mathbf{s} \cdot \mathbf{t}) = -\mathbf{s} \cdot \mathbf{z} \times \mathbf{t} = -s_{\alpha} \epsilon_{\alpha\beta\gamma} T_{\beta z} t'_{\gamma}. \quad [\text{A.2.18}]$$

Dealing with other components similarly yields,

$$\hat{\mathbf{G}}'_{\delta}(\mathbf{s} \cdot \mathbf{t}) = -s_{\alpha} \epsilon_{\alpha\beta\gamma} T_{\beta\delta} t'_{\gamma} (\mathbf{s} \times \mathbf{t})_{\beta} T_{\beta\delta}. \quad [\text{A.2.19}]$$

Because \mathbf{T} is the transformation matrix from the space fixed frame to the molecular frame the torque in the space fixed frame is given by,

$$\hat{\mathbf{G}}(\mathbf{s} \cdot \mathbf{t}) = (\mathbf{s} \times \mathbf{t}). \quad [\text{A.2.20}]$$

And thus equation A.2.13 becomes

$$\hat{\mathbf{G}}V = \sum_{\mathbf{s}, \mathbf{t}} \frac{\partial V}{\partial (\mathbf{s} \cdot \mathbf{t})} \mathbf{s} \times \mathbf{t} \quad [\text{A.2.21}]$$

Where the notation refers to a sum of the contributions of all scalar products formed from a vector that is fixed in space, \mathbf{s} , and another that rotates with the molecule, \mathbf{t} , the result is the torque about the centre of mass. There are four different combinations to consider, and we shall now evaluate these expressions for the torque on molecule 2. In this case only vector \mathbf{b} on molecule 2 rotates.

Consider two vectors fixed in the molecular frame, \mathbf{x}_1 on molecule 1 and \mathbf{z}_2 on molecule 2 say;

$$\hat{\mathbf{G}}_2(\mathbf{x}_1 \cdot \mathbf{z}_2) = \mathbf{x}_1 \times \mathbf{z}_2. \quad [\text{A.2.22}]$$

Consider the scalar product with the intersite vector:

$$\begin{aligned} \hat{\mathbf{G}}_2(\mathbf{r} \cdot \mathbf{t}) &= \hat{\mathbf{G}}_2[(\mathbf{B} + \mathbf{b} - \mathbf{A} - \mathbf{a}) \cdot \mathbf{t}] \\ &= (\mathbf{B} - \mathbf{A} - \mathbf{a}) \times \mathbf{t} \\ &= (\mathbf{r} - \mathbf{b}) \times \mathbf{t}. \end{aligned} \quad [\text{A.2.23}]$$

Consider;

$$\begin{aligned} \hat{\mathbf{G}}_2(\mathbf{s} \cdot \mathbf{r}) &= \hat{\mathbf{G}}_2[\mathbf{s} \cdot (\mathbf{B} + \mathbf{b} - \mathbf{A} - \mathbf{a})] \\ &= \mathbf{s} \times \mathbf{b}. \end{aligned} \quad [\text{A.2.24}]$$

And;

$$\begin{aligned} \hat{\mathbf{G}}_2(\mathbf{r} \cdot \mathbf{r}) &= \hat{\mathbf{G}}_2[(\mathbf{B} + \mathbf{b} - \mathbf{A} - \mathbf{a}) \cdot (\mathbf{B} + \mathbf{b} - \mathbf{A} - \mathbf{a})] \\ &= 2(\mathbf{B} - \mathbf{A} - \mathbf{a}) \times \mathbf{b} \\ &= 2(\mathbf{r} \times \mathbf{b}). \end{aligned} \quad [\text{A.2.25}]$$

Generally then;

$$\begin{aligned}
 \hat{\mathbf{G}}_2 \mathbf{r}^n &= \hat{\mathbf{G}}_2 (\mathbf{r} \cdot \mathbf{r})^{n/2} \\
 &= \frac{1}{2} n (\mathbf{r} \cdot \mathbf{r})^{n/2-1} 2(\mathbf{r} \times \mathbf{b}) \\
 &= n \mathbf{r}^{n-2} (\mathbf{r} \times \mathbf{b}).
 \end{aligned}
 \tag{A.2.26}$$

The torque on molecule 1 is not (necessarily) the same as that on molecule 2. Here then we simply reconsider the above four conditions, [A.2.22] to [A.2.26]. Now though \mathbf{t} is a vector rotating with molecule 1, thus;

$$\hat{\mathbf{G}}_1 (\mathbf{s} \cdot \mathbf{t}) = \mathbf{s} \times \mathbf{t}.
 \tag{A.2.27}$$

Remembering it is molecule 1 which is rotating:

$$\hat{\mathbf{G}}_1 (\mathbf{x}_1 \cdot \mathbf{z}_2) = \mathbf{z}_2 \times \mathbf{x}_1.
 \tag{A.2.28}$$

And for the other terms;

$$\begin{aligned}
 \hat{\mathbf{G}}_1 (\mathbf{r} \cdot \mathbf{t}) &= \hat{\mathbf{G}}_1 [(\mathbf{B} + \mathbf{b} - \mathbf{A} - \mathbf{a}) \cdot \mathbf{t}] \\
 &= (\mathbf{B} + \mathbf{b} - \mathbf{A}) \times \mathbf{t} \\
 &= (\mathbf{r} + \mathbf{a}) \times \mathbf{t};
 \end{aligned}
 \tag{A.2.29}$$

$$\begin{aligned}
 \hat{\mathbf{G}}_1 (\mathbf{s} \cdot \mathbf{r}) &= \hat{\mathbf{G}}_1 [\mathbf{s} \cdot (\mathbf{B} + \mathbf{b} - \mathbf{A} - \mathbf{a})] \\
 &= \mathbf{s} \times -\mathbf{a} \\
 &= -\mathbf{s} \times \mathbf{a};
 \end{aligned}
 \tag{A.2.30}$$

$$\begin{aligned}
 \hat{\mathbf{G}}_1 (\mathbf{r} \cdot \mathbf{r}) &= \hat{\mathbf{G}}_1 [(\mathbf{B} + \mathbf{b} - \mathbf{A} - \mathbf{a}) \cdot (\mathbf{B} + \mathbf{b} - \mathbf{A} - \mathbf{a})] \\
 &= 2(\mathbf{B} + \mathbf{b} - \mathbf{A}) \times \mathbf{b} \\
 &= 2(\mathbf{r} \times -\mathbf{a}) \\
 &= -2(\mathbf{r} \times \mathbf{a}).
 \end{aligned}
 \tag{A.2.31}$$

Generally then;

$$\hat{\mathbf{G}}_1 \mathbf{r}^n = \hat{\mathbf{G}}_1 (\mathbf{r} \cdot \mathbf{r})^{n/2}$$

$$\begin{aligned}
&= \frac{1}{2}n(\mathbf{r} \cdot \mathbf{r})^{n/2-1} - 2(\mathbf{r} \times \mathbf{a}) \\
&= -n\mathbf{r}^{n-2}(\mathbf{r} \times \mathbf{a}).
\end{aligned}
\tag{A.2.32}$$

The whole expression for the torque about the centre of mass owing to a site on molecule 2 due to another site on molecule 1 is then given by:

$$\begin{aligned}
\sum_{\mathbf{s}, \mathbf{t}} \frac{\partial V}{\partial(\mathbf{s}, \mathbf{t})}(\mathbf{s} \times \mathbf{t}) &= \varepsilon_2 \left\{ \frac{\partial[V_0 + V_A]}{\partial(\mathbf{r} \cdot \mathbf{r})}(\mathbf{r} \times \mathbf{b}) + \frac{\partial[V_0 + V_A]}{\partial(\hat{\mathbf{u}}_1 \cdot \hat{\mathbf{u}}_2)}(\hat{\mathbf{u}}_1 \times \hat{\mathbf{u}}_2) \right\} + \\
[V_0 + V_A] &\left\{ \frac{\partial \varepsilon_2}{\partial(\mathbf{r} \cdot \mathbf{r})}(\mathbf{r} \times \mathbf{b}) + \frac{\partial \varepsilon_2}{\partial(\mathbf{r} \cdot \hat{\mathbf{u}}_1)}(\hat{\mathbf{u}}_1 \times \mathbf{b}) + \frac{\partial \varepsilon_2}{\partial(\mathbf{r} \cdot \hat{\mathbf{u}}_2)}(\mathbf{r} - \mathbf{b}) \times \hat{\mathbf{u}}_2 + \frac{\partial \varepsilon_2}{\partial(\hat{\mathbf{u}}_1 \cdot \hat{\mathbf{u}}_2)}(\hat{\mathbf{u}}_1 \times \hat{\mathbf{u}}_2) \right\}
\end{aligned}
\tag{A.2.33}$$

The equivalent expression for the similar torque on molecule 1 due to a site on molecule 2 is given;

$$\begin{aligned}
\sum_{\mathbf{s}, \mathbf{t}} \frac{\partial V}{\partial(\mathbf{s}, \mathbf{t})}(\mathbf{s} \times \mathbf{t}) &= \varepsilon_2 \left\{ \frac{\partial[V_0 + V_A]}{\partial(\mathbf{r} \cdot \mathbf{r})}(-\mathbf{r} \times \mathbf{a}) + \frac{\partial[V_0 + V_A]}{\partial(\hat{\mathbf{u}}_1 \cdot \hat{\mathbf{u}}_2)}(\hat{\mathbf{u}}_2 \times \hat{\mathbf{u}}_1) \right\} + \\
[V_0 + V_A] &\left\{ \frac{\partial \varepsilon_2}{\partial(\mathbf{r} \cdot \mathbf{r})}(-\mathbf{r} \times \mathbf{a}) + \frac{\partial \varepsilon_2}{\partial(\mathbf{r} \cdot \hat{\mathbf{u}}_1)}(\mathbf{r} + \mathbf{a}) \times \hat{\mathbf{u}}_1 + \frac{\partial \varepsilon_2}{\partial(\mathbf{r} \cdot \hat{\mathbf{u}}_2)}(-\hat{\mathbf{u}}_2 \times \mathbf{a}) + \frac{\partial \varepsilon_2}{\partial(\hat{\mathbf{u}}_1 \cdot \hat{\mathbf{u}}_2)}(\hat{\mathbf{u}}_2 \times \hat{\mathbf{u}}_1) \right\}
\end{aligned}
\tag{A.2.34}$$

So for the HGBLR potential, consider the torque on molecule 2 caused by a site on molecule 1. There are four scalar products to consider $(\hat{\mathbf{u}}_1 \cdot \hat{\mathbf{u}}_2)$, $(\mathbf{r} \cdot \hat{\mathbf{u}}_1)$, $(\mathbf{r} \cdot \hat{\mathbf{u}}_2)$ and $(\mathbf{r} \cdot \mathbf{r})$ for which we now know the answer when these are operated on by $\hat{\mathbf{G}}_2$, the differential operator that yields the torque. Remember molecule 1 remains stationary and molecule 2 rotates.

$$\hat{\mathbf{G}}_2(\hat{\mathbf{u}}_1 \cdot \hat{\mathbf{u}}_2) = \hat{\mathbf{u}}_1 \times \hat{\mathbf{u}}_2; \tag{A.2.35}$$

$$\hat{\mathbf{G}}_2(\mathbf{r} \cdot \hat{\mathbf{u}}_2) = (\mathbf{r} - \mathbf{b}) \times \hat{\mathbf{u}}_2; \tag{A.2.36}$$

$$\hat{\mathbf{G}}_2(\mathbf{r} \cdot \hat{\mathbf{u}}_1) = \hat{\mathbf{G}}_2(\hat{\mathbf{u}}_1 \cdot \mathbf{r}) = \hat{\mathbf{u}}_1 \times \mathbf{b}; \quad (\hat{\mathbf{u}}_1 \text{ remains fixed}) \tag{A.2.37}$$

$$\hat{\mathbf{G}}_2(\mathbf{r}^{-12}) = -12\mathbf{r}^{-14}(\mathbf{r} \times \mathbf{b}); \quad [\text{A.2.38}]$$

$$\hat{\mathbf{G}}_2(\mathbf{r}^{-6}) = -6\mathbf{r}^{-6}(\mathbf{r} \times \mathbf{b}). \quad [\text{A.2.39}]$$

And so we may write:

$$\begin{aligned} \frac{\partial[V_0 + V_A]}{\partial(\mathbf{r} \cdot \mathbf{r})}(\mathbf{r} \times \mathbf{r}) = \\ 4\epsilon \left[\left\{ \frac{-12\sigma^{12}}{r^{14}} + \frac{6\sigma^6}{r^8} \right\}(\mathbf{r} \times \mathbf{b}) - \lambda \left\{ \frac{-12\sigma^{12}}{r^{14}} - \frac{6\sigma^6}{r^8} \right\}(\mathbf{r} \times \mathbf{b}) P_2(\hat{\mathbf{u}}_1 \cdot \hat{\mathbf{u}}_2) \right], \end{aligned} \quad [\text{A.2.40}]$$

$$\frac{\partial[V_0 + V_A]}{\partial(\hat{\mathbf{u}}_1 \cdot \hat{\mathbf{u}}_2)}(\hat{\mathbf{u}}_1 \times \hat{\mathbf{u}}_2) = -4\lambda\epsilon \left\{ \frac{\sigma^{12}}{r^{12}} + \frac{\sigma^6}{r^6} \right\} 3(\hat{\mathbf{u}}_1 \cdot \hat{\mathbf{u}}_2)(\hat{\mathbf{u}}_1 \times \hat{\mathbf{u}}_2) \quad [\text{A.2.41}]$$

$$\frac{\partial\epsilon_2}{\partial(\mathbf{r} \cdot \mathbf{r})}(\mathbf{r} \times \mathbf{r}) = \frac{\chi'}{r^4} \left(\frac{(\hat{\mathbf{r}} \cdot \hat{\mathbf{u}}_1 + \hat{\mathbf{r}} \cdot \hat{\mathbf{u}}_2)^2}{1 + \chi'(\hat{\mathbf{u}}_1 \cdot \hat{\mathbf{u}}_2)} + \frac{(\hat{\mathbf{r}} \cdot \hat{\mathbf{u}}_1 - \hat{\mathbf{r}} \cdot \hat{\mathbf{u}}_2)^2}{1 - \chi'(\hat{\mathbf{u}}_1 \cdot \hat{\mathbf{u}}_2)} \right) (\mathbf{r} \times \mathbf{b}) \quad [\text{A.2.42}]$$

$$\frac{\partial\epsilon_2}{\partial(\mathbf{r} \cdot \hat{\mathbf{u}}_1)}(\mathbf{r} \times \hat{\mathbf{u}}_1) = \frac{-\chi'}{2r^2} \left(\frac{2(\hat{\mathbf{r}} \cdot \hat{\mathbf{u}}_1 + \hat{\mathbf{r}} \cdot \hat{\mathbf{u}}_2)}{1 + \chi'(\hat{\mathbf{u}}_1 \cdot \hat{\mathbf{u}}_2)} + \frac{2(\hat{\mathbf{r}} \cdot \hat{\mathbf{u}}_1 - \hat{\mathbf{r}} \cdot \hat{\mathbf{u}}_2)}{1 - \chi'(\hat{\mathbf{u}}_1 \cdot \hat{\mathbf{u}}_2)} \right) (\hat{\mathbf{u}}_1 \times \mathbf{b}) \quad [\text{A.2.43}]$$

$$\frac{\partial\epsilon_2}{\partial(\mathbf{r} \cdot \hat{\mathbf{u}}_2)}(\mathbf{r} \times \hat{\mathbf{u}}_2) =$$

$$\frac{-\chi'}{2r^2} \left(\frac{2(\hat{\mathbf{r}} \cdot \hat{\mathbf{u}}_1 + \hat{\mathbf{r}} \cdot \hat{\mathbf{u}}_2)}{1 + \chi'(\hat{\mathbf{u}}_1 \cdot \hat{\mathbf{u}}_2)} - \frac{2(\hat{\mathbf{r}} \cdot \hat{\mathbf{u}}_1 - \hat{\mathbf{r}} \cdot \hat{\mathbf{u}}_2)}{1 - \chi'(\hat{\mathbf{u}}_1 \cdot \hat{\mathbf{u}}_2)} \right) (\mathbf{r} - \mathbf{b}) \times \hat{\mathbf{u}}_2 \quad [\text{A.2.44}]$$

$$\frac{\partial\epsilon_2}{\partial(\hat{\mathbf{u}}_1 \cdot \hat{\mathbf{u}}_2)}(\hat{\mathbf{u}}_1 \times \hat{\mathbf{u}}_2) =$$

$$\frac{-\chi'}{2r^2} \left(\frac{-(\hat{\mathbf{r}} \cdot \hat{\mathbf{u}}_1 + \hat{\mathbf{r}} \cdot \hat{\mathbf{u}}_2)^2}{(1 + \chi'(\hat{\mathbf{u}}_1 \cdot \hat{\mathbf{u}}_2))^2} - \frac{(\hat{\mathbf{r}} \cdot \hat{\mathbf{u}}_1 - \hat{\mathbf{r}} \cdot \hat{\mathbf{u}}_2)^2}{(1 - \chi'(\hat{\mathbf{u}}_1 \cdot \hat{\mathbf{u}}_2))^2} \right) (\hat{\mathbf{u}}_1 \times \hat{\mathbf{u}}_2) \quad [\text{A.2.45}]$$

And similarly, consider the torque on molecule 1 caused by a site on molecule 2. This time molecule 1 rotates and molecule 2 remains stationary. The solutions for the differential operator that we require are:

$$\hat{G}_1(\hat{\mathbf{u}}_1 \cdot \hat{\mathbf{u}}_2) = \hat{\mathbf{u}}_1 \times \hat{\mathbf{u}}_2 \quad [\text{A.2.46}]$$

$$\hat{G}_1(\mathbf{r} \cdot \hat{\mathbf{u}}_1) = (\mathbf{r} + \mathbf{a}) \times \hat{\mathbf{u}}_1 \quad [\text{A.2.47}]$$

$$\hat{G}_1(\mathbf{r} \cdot \hat{\mathbf{u}}_2) = \hat{G}_1(\hat{\mathbf{u}}_2 \cdot \mathbf{r}) = -\hat{\mathbf{u}}_2 \times \mathbf{a} \quad [\text{A.2.48}]$$

$$\hat{G}_1(r^{-12}) = 12r^{-14}(\mathbf{r} \times \mathbf{a}) \quad [\text{A.2.49}]$$

$$\hat{G}_1(r^{-6}) = 6r^{-8}(\mathbf{r} \times \mathbf{a}) \quad [\text{A.2.50}]$$

Thus

$$\frac{\partial[V_0 + V_A]}{\partial(\mathbf{r} \cdot \mathbf{r})}(\mathbf{r} \times \mathbf{r}) = 4\varepsilon \left[\left\{ \frac{-12\sigma^{12}}{r^{14}} + \frac{6\sigma^6}{r^8} \right\} (\mathbf{r} \times \mathbf{a}) - \lambda \left\{ \frac{-12\sigma^{12}}{r^{14}} - \frac{6\sigma^6}{r^8} \right\} (\mathbf{r} \times \mathbf{b}) P_2(\hat{\mathbf{u}}_1 \cdot \hat{\mathbf{u}}_2) \right] \quad [\text{A.2.51}]$$

$$\frac{\partial[V_0 + V_A]}{\partial(\hat{\mathbf{u}}_1 \cdot \hat{\mathbf{u}}_2)}(\hat{\mathbf{u}}_1 \times \hat{\mathbf{u}}_2) = -4\lambda\varepsilon \left\{ \frac{\sigma^{12}}{r^{12}} + \frac{\sigma^6}{r^6} \right\} 3(\hat{\mathbf{u}}_1 \cdot \hat{\mathbf{u}}_2)(\hat{\mathbf{u}}_2 \times \hat{\mathbf{u}}_1) \quad [\text{A.2.52}]$$

$$\frac{\partial\varepsilon_2}{\partial(\mathbf{r} \cdot \mathbf{r})}(\mathbf{r} \times \mathbf{r}) = \frac{\chi'}{r^4} \left(\frac{(\hat{\mathbf{r}} \cdot \hat{\mathbf{u}}_1 + \hat{\mathbf{r}} \cdot \hat{\mathbf{u}}_2)^2}{1 + \chi'(\hat{\mathbf{u}}_1 \cdot \hat{\mathbf{u}}_2)} + \frac{(\hat{\mathbf{r}} \cdot \hat{\mathbf{u}}_1 - \hat{\mathbf{r}} \cdot \hat{\mathbf{u}}_2)^2}{1 - \chi'(\hat{\mathbf{u}}_1 \cdot \hat{\mathbf{u}}_2)} \right) (\mathbf{r} \times \mathbf{a}) \quad [\text{A.2.53}]$$

$$\frac{\partial\varepsilon_2}{\partial(\mathbf{r} \cdot \hat{\mathbf{u}}_1)}(\mathbf{r} \times \hat{\mathbf{u}}_1) =$$

$$\frac{-\chi'}{2r^2} \left(\frac{2(\hat{\mathbf{r}} \cdot \hat{\mathbf{u}}_1 + \hat{\mathbf{r}} \cdot \hat{\mathbf{u}}_2)}{1 + \chi'(\hat{\mathbf{u}}_1 \cdot \hat{\mathbf{u}}_2)} - \frac{2(\hat{\mathbf{r}} \cdot \hat{\mathbf{u}}_1 - \hat{\mathbf{r}} \cdot \hat{\mathbf{u}}_2)}{1 - \chi'(\hat{\mathbf{u}}_1 \cdot \hat{\mathbf{u}}_2)} \right) (\mathbf{r} + \mathbf{a}) \times \hat{\mathbf{u}}_1 \quad [\text{A.2.54}]$$

$$\frac{\partial\varepsilon_2}{\partial(\mathbf{r} \cdot \hat{\mathbf{u}}_2)}(\mathbf{r} \times \hat{\mathbf{u}}_2) = \frac{-\chi'}{2r^2} \left(\frac{2(\hat{\mathbf{r}} \cdot \hat{\mathbf{u}}_1 + \hat{\mathbf{r}} \cdot \hat{\mathbf{u}}_2)}{1 + \chi'(\hat{\mathbf{u}}_1 \cdot \hat{\mathbf{u}}_2)} + \frac{2(\hat{\mathbf{r}} \cdot \hat{\mathbf{u}}_1 - \hat{\mathbf{r}} \cdot \hat{\mathbf{u}}_2)}{1 - \chi'(\hat{\mathbf{u}}_1 \cdot \hat{\mathbf{u}}_2)} \right) (\hat{\mathbf{u}}_2 \times \mathbf{a}) \quad [\text{A.2.55}]$$

$$\frac{\partial \varepsilon_2}{\partial (\hat{\mathbf{u}}_1 \cdot \hat{\mathbf{u}}_2)} (\hat{\mathbf{u}}_1 \times \hat{\mathbf{u}}_2) =$$

$$\frac{-\chi' \left(\frac{-(\hat{\mathbf{r}} \cdot \hat{\mathbf{u}}_1 + \hat{\mathbf{r}} \cdot \hat{\mathbf{u}}_2)^2}{(1 + \chi'(\hat{\mathbf{u}}_1 \cdot \hat{\mathbf{u}}_2))^2} - \frac{(\hat{\mathbf{r}} \cdot \hat{\mathbf{u}}_1 - \hat{\mathbf{r}} \cdot \hat{\mathbf{u}}_2)^2}{(1 - \chi'(\hat{\mathbf{u}}_1 \cdot \hat{\mathbf{u}}_2))^2} \right)}{2r^2} (\hat{\mathbf{u}}_2 \times \hat{\mathbf{u}}_1)$$

[A.2.56]

APPENDIX B

λ AND χ' PARAMETER SPACE OF THE 3-HGBLR-SITE SITE MODEL

Appendix B.1

Numerical results of the coarse grid search over the ranges $-1.0 \leq \lambda \leq 0.9$ and $-0.9 \leq \chi' \leq 0.0$ with resolutions $\Delta\lambda = 0.1$ and $\Delta\chi' = 0.1$ for the values of well depth minimum (denoted V^*_{\min}), and location of the minimum (denoted $r/\text{\AA}$), for each of the configurations a, b, c and d of figure V.2, together with the values of the well depth minima ratios for configurations: a/d, b/d and c/d.

Appendix B.2

Numerical results of the finer grid search in the range $-0.90 \leq \chi' \leq -0.80$ with resolution $\Delta\chi' = 0.01$ at selected values of λ for the values of well depth minimum (denoted V^*_{\min}), and location of the minimum (denoted $r/\text{\AA}$), for each of the configurations a, b, c and d of figure V.2, together with the values of the well depth minima ratios for configurations: a/d, b/d and c/d. The hard core radii chosen to fit configuration d to the 32-Lennard-Jones-site site model for the selected values λ , are as follows:

table B.2.1	$\sigma_0 = 5.8\text{\AA}$
table B.2.2	$\sigma_0 = 6.0\text{\AA}$
table B.2.3	$\sigma_0 = 6.2\text{\AA}$
table B.2.4	$\sigma_0 = 6.4\text{\AA}$
table B.2.5	$\sigma_0 = 6.6\text{\AA}$

λ	χ'	<u>config., a</u>		<u>config., b</u>		<u>config., c</u>		<u>config., d</u>		ratios:		
		r/Å	V*min	r/Å	V*min	r/Å	V*min	r/Å	V*min	<u>a/d</u>	<u>b/d</u>	<u>c/d</u>
-1.00	-0.90	11.70	-0.60	6.20	-33.13	11.10	-0.26	20.20	-0.02	36.23	1995.7	15.46
-1.00	-0.80	11.10	-0.63	6.20	-30.98	10.50	-0.29	20.20	-0.02	37.69	1866.2	17.73
-1.00	-0.70	10.80	-0.57	6.20	-29.00	10.30	-0.30	20.20	-0.02	34.57	1746.9	18.11
-1.00	-0.60	10.60	-0.51	6.20	-27.14	10.20	-0.30	20.20	-0.02	30.81	1634.7	17.93
-1.00	-0.50	10.40	-0.45	6.20	-25.36	10.20	-0.29	20.20	-0.02	27.25	1527.7	17.57
-1.00	-0.40	10.40	-0.40	6.20	-23.64	10.10	-0.28	20.20	-0.02	24.11	1424.4	17.14
-1.00	-0.30	10.30	-0.36	6.20	-21.98	10.10	-0.28	20.20	-0.02	21.39	1323.9	16.67
-1.00	-0.20	10.20	-0.32	6.20	-20.35	10.10	-0.27	20.20	-0.02	19.01	1225.6	16.17
-1.00	-0.10	10.20	-0.28	6.20	-18.74	10.10	-0.26	20.20	-0.02	16.91	1129.0	15.65
-1.00	0.00	10.10	-0.25	6.20	-17.16	10.10	-0.25	20.20	-0.02	15.09	1033.7	15.09
-0.90	-0.90	10.60	-1.72	6.30	-29.51	10.30	-0.55	19.20	-0.04	43.37	743.41	13.92
-0.90	-0.80	10.30	-1.36	6.30	-27.53	9.90	-0.54	19.20	-0.04	34.30	693.46	13.68
-0.90	-0.70	10.10	-1.13	6.30	-25.73	9.80	-0.53	19.20	-0.04	28.41	647.98	13.27
-0.90	-0.60	10.00	-0.95	6.30	-24.04	9.70	-0.51	19.20	-0.04	23.97	605.61	12.84
-0.90	-0.50	9.90	-0.82	6.30	-22.45	9.70	-0.49	19.20	-0.04	20.53	565.48	12.42
-0.90	-0.40	9.80	-0.71	6.30	-20.92	9.60	-0.48	19.20	-0.04	17.77	527.00	12.04
-0.90	-0.30	9.70	-0.61	6.30	-19.44	9.60	-0.46	19.20	-0.04	15.49	489.76	11.68
-0.90	-0.20	9.70	-0.54	6.30	-18.00	9.60	-0.45	19.20	-0.04	13.60	453.47	11.32
-0.90	-0.10	9.60	-0.48	6.30	-16.59	9.60	-0.44	19.20	-0.04	11.98	417.92	10.97
-0.90	0.00	9.60	-0.42	6.30	-15.20	9.60	-0.42	19.20	-0.04	10.61	382.93	10.61
-0.80	-0.90	9.90	-3.52	6.40	-26.46	9.70	-0.99	18.50	-0.08	46.07	346.36	12.99
-0.80	-0.80	9.70	-2.44	6.40	-24.62	9.40	-0.89	18.50	-0.08	31.99	322.27	11.63
-0.80	-0.70	9.60	-1.91	6.40	-22.96	9.30	-0.83	18.50	-0.08	25.01	300.59	10.91
-0.80	-0.60	9.50	-1.56	6.40	-21.44	9.30	-0.79	18.50	-0.08	20.46	280.56	10.39
-0.80	-0.50	9.40	-1.31	6.40	-20.00	9.20	-0.76	18.50	-0.08	17.16	261.74	9.97
-0.80	-0.40	9.40	-1.12	6.40	-18.63	9.20	-0.74	18.50	-0.08	14.62	243.80	9.62
-0.80	-0.30	9.30	-0.96	6.40	-17.31	9.20	-0.71	18.50	-0.08	12.63	226.53	9.31
-0.80	-0.20	9.30	-0.84	6.40	-16.03	9.20	-0.69	18.50	-0.08	10.99	209.77	9.02
-0.80	-0.10	9.20	-0.74	6.40	-14.78	9.20	-0.67	18.50	-0.08	9.63	193.40	8.75
-0.80	0.00	9.20	-0.65	6.40	-13.55	9.20	-0.65	18.50	-0.08	8.48	177.34	8.48
-0.70	-0.90	9.40	-6.11	6.50	-23.86	9.20	-1.60	18.00	-0.13	47.39	185.07	12.41
-0.70	-0.80	9.20	-3.92	6.50	-22.14	9.10	-1.35	18.00	-0.13	30.43	171.76	10.46
-0.70	-0.70	9.10	-2.96	6.50	-20.61	9.00	-1.24	18.00	-0.13	22.96	159.90	9.58
-0.70	-0.60	9.10	-2.37	6.50	-19.21	8.90	-1.16	18.00	-0.13	18.39	149.05	9.02
-0.70	-0.50	9.00	-1.96	6.50	-17.91	8.90	-1.11	18.00	-0.13	15.21	138.92	8.60
-0.70	-0.40	9.00	-1.66	6.50	-16.67	8.90	-1.07	18.00	-0.13	12.84	129.33	8.27
-0.70	-0.30	8.90	-1.42	6.50	-15.49	8.90	-1.03	18.00	-0.13	10.99	120.14	7.98
-0.70	-0.20	8.90	-1.23	6.50	-14.34	8.90	-1.00	18.00	-0.13	9.52	111.26	7.73
-0.70	-0.10	8.90	-1.07	6.50	-13.23	8.80	-0.97	18.00	-0.13	8.30	102.61	7.50
-0.70	0.00	8.80	-0.94	6.50	-12.14	8.80	-0.94	18.00	-0.13	7.27	94.15	7.27
-0.60	-0.90	9.00	-9.62	6.60	-21.61	8.90	-2.41	17.60	-0.20	48.02	107.81	12.01
-0.60	-0.80	8.90	-5.88	6.60	-20.00	8.70	-1.94	17.60	-0.20	29.32	99.80	9.68
-0.60	-0.70	8.80	-4.32	6.60	-18.58	8.70	-1.75	17.60	-0.20	21.57	92.73	8.71
-0.60	-0.60	8.70	-3.41	6.60	-17.30	8.60	-1.63	17.60	-0.20	17.00	86.31	8.13
-0.60	-0.50	8.70	-2.79	6.60	-16.11	8.60	-1.55	17.60	-0.20	13.93	80.37	7.71
-0.60	-0.40	8.70	-2.34	6.60	-14.99	8.60	-1.48	17.60	-0.20	11.67	74.78	7.39
-0.60	-0.30	8.60	-1.99	6.60	-13.92	8.60	-1.43	17.60	-0.20	9.94	69.44	7.13
-0.60	-0.20	8.60	-1.72	6.60	-12.89	8.60	-1.38	17.60	-0.20	8.56	64.31	6.90
-0.60	-0.10	8.60	-1.49	6.60	-11.89	8.60	-1.34	17.60	-0.20	7.44	59.34	6.69
-0.60	0.00	8.50	-1.30	6.60	-10.92	8.50	-1.30	17.60	-0.20	6.50	54.48	6.50
-0.50	-0.90	8.70	-14.23	6.70	-19.64	8.50	-3.45	17.20	-0.29	48.34	66.74	11.71
-0.50	-0.80	8.60	-8.38	6.70	-18.14	8.40	-2.69	17.20	-0.29	28.47	61.62	9.14
-0.50	-0.70	8.50	-6.05	6.70	-16.82	8.40	-2.39	17.20	-0.29	20.57	57.14	8.11
-0.50	-0.60	8.40	-4.72	6.70	-15.63	8.30	-2.21	17.20	-0.29	16.02	53.12	7.51
-0.50	-0.50	8.40	-3.83	6.70	-14.54	8.30	-2.09	17.20	-0.29	13.02	49.41	7.10
-0.50	-0.40	8.40	-3.19	6.70	-13.52	8.30	-2.00	17.20	-0.29	10.85	45.94	6.79
-0.50	-0.30	8.40	-2.71	6.70	-12.55	8.30	-1.93	17.20	-0.29	9.19	42.65	6.54
-0.50	-0.20	8.30	-2.32	6.70	-11.63	8.30	-1.86	17.20	-0.29	7.90	39.50	6.33
-0.50	-0.10	8.30	-2.01	6.70	-10.73	8.30	-1.81	17.20	-0.29	6.84	36.45	6.14
-0.50	0.00	8.30	-1.76	6.70	-9.86	8.30	-1.76	17.20	-0.29	5.97	33.49	5.97
-0.40	-0.90	8.30	-20.15	6.80	-17.92	8.30	-4.77	16.90	-0.42	48.49	43.12	11.49

λ	χ'	<u>config., a</u>		<u>config., b</u>		<u>config., c</u>		<u>config., d</u>		ratios:		
		r/Å	V*min	r/Å	V*min	r/Å	V*min	r/Å	V*min	a/d	b/d	c/d
-0.40	-0.80	8.30	-11.56	6.80	-16.50	8.20	-3.62	16.90	-0.42	27.82	39.70	8.72
-0.40	-0.70	8.20	-8.23	6.80	-15.27	8.10	-3.18	16.90	-0.42	19.80	36.75	7.66
-0.40	-0.60	8.20	-6.35	6.80	-14.17	8.10	-2.93	16.90	-0.42	15.29	34.11	7.05
-0.40	-0.50	8.10	-5.12	6.80	-13.17	8.10	-2.76	16.90	-0.42	12.33	31.69	6.64
-0.40	-0.40	8.10	-4.25	6.80	-12.24	8.10	-2.63	16.90	-0.42	10.23	29.45	6.33
-0.40	-0.30	8.10	-3.59	6.80	-11.36	8.00	-2.53	16.90	-0.42	8.65	27.33	6.10
-0.40	-0.20	8.10	-3.07	6.80	-10.52	8.00	-2.45	16.90	-0.42	7.40	25.31	5.90
-0.40	-0.10	8.10	-2.66	6.80	-9.71	8.00	-2.38	16.90	-0.42	6.39	23.37	5.72
-0.40	0.00	8.00	-2.31	6.80	-8.92	8.00	-2.31	16.90	-0.42	5.56	21.48	5.56
-0.30	-0.90	8.10	-27.71	6.90	-16.38	8.00	-6.45	16.60	-0.57	48.67	28.78	11.33
-0.30	-0.80	8.00	-15.55	6.90	-15.05	7.90	-4.79	16.60	-0.57	27.31	26.43	8.42
-0.30	-0.70	8.00	-10.92	6.90	-13.90	7.90	-4.16	16.60	-0.57	19.19	24.41	7.31
-0.30	-0.60	7.90	-8.38	6.90	-12.88	7.80	-3.81	16.60	-0.57	14.72	22.62	6.69
-0.30	-0.50	7.90	-6.73	6.90	-11.96	7.80	-3.58	16.60	-0.57	11.82	21.00	6.29
-0.30	-0.40	7.90	-5.56	6.90	-11.10	7.80	-3.41	16.60	-0.57	9.76	19.50	6.00
-0.30	-0.30	7.90	-4.68	6.90	-10.30	7.80	-3.28	16.60	-0.57	8.22	18.09	5.77
-0.30	-0.20	7.80	-3.99	6.90	-9.54	7.80	-3.17	16.60	-0.57	7.01	16.75	5.57
-0.30	-0.10	7.80	-3.45	6.90	-8.81	7.80	-3.08	16.60	-0.57	6.05	15.47	5.41
-0.30	0.00	7.80	-2.99	6.90	-8.10	7.80	-2.99	16.60	-0.57	5.26	14.23	5.26
-0.20	-0.90	7.80	-37.25	7.00	-15.01	7.80	-8.54	16.40	-0.76	48.71	19.63	11.17
-0.20	-0.80	7.80	-20.52	7.00	-13.75	7.70	-6.24	16.40	-0.76	26.83	17.98	8.15
-0.20	-0.70	7.70	-14.29	7.00	-12.68	7.60	-5.37	16.40	-0.76	18.69	16.58	7.02
-0.20	-0.60	7.70	-10.89	7.00	-11.73	7.60	-4.90	16.40	-0.76	14.24	15.34	6.41
-0.20	-0.50	7.70	-8.70	7.00	-10.88	7.60	-4.59	16.40	-0.76	11.38	14.22	6.01
-0.20	-0.40	7.70	-7.16	7.00	-10.09	7.60	-4.37	16.40	-0.76	9.36	13.20	5.71
-0.20	-0.30	7.60	-6.01	7.00	-9.36	7.60	-4.20	16.40	-0.76	7.86	12.24	5.49
-0.20	-0.20	7.60	-5.13	7.00	-8.67	7.60	-4.06	16.40	-0.76	6.70	11.33	5.30
-0.20	-0.10	7.60	-4.41	7.00	-8.00	7.60	-3.94	16.40	-0.76	5.77	10.46	5.15
-0.20	0.00	7.60	-3.83	7.00	-7.36	7.60	-3.83	16.40	-0.76	5.01	9.63	5.01
-0.10	-0.90	7.60	-49.29	7.10	-13.78	7.50	-11.19	16.10	-1.01	48.74	13.63	11.06
-0.10	-0.80	7.50	-26.77	7.10	-12.59	7.50	-8.02	16.10	-1.01	26.47	12.45	7.93
-0.10	-0.70	7.50	-18.49	7.10	-11.58	7.40	-6.87	16.10	-1.01	18.28	11.46	6.79
-0.10	-0.60	7.50	-14.00	7.10	-10.70	7.40	-6.24	16.10	-1.01	13.84	10.58	6.17
-0.10	-0.50	7.50	-11.13	7.10	-9.91	7.40	-5.84	16.10	-1.01	11.01	9.80	5.77
-0.10	-0.40	7.40	-9.14	7.10	-9.19	7.40	-5.54	16.10	-1.01	9.04	9.09	5.48
-0.10	-0.30	7.40	-7.67	7.10	-8.52	7.40	-5.32	16.10	-1.01	7.58	8.42	5.26
-0.10	-0.20	7.40	-6.52	7.10	-7.89	7.40	-5.14	16.10	-1.01	6.45	7.80	5.08
-0.10	-0.10	7.40	-5.60	7.10	-7.28	7.40	-4.99	16.10	-1.01	5.54	7.20	4.93
-0.10	0.00	7.40	-4.85	7.10	-6.70	7.40	-4.85	16.10	-1.01	4.80	6.63	4.80
0.00	-0.90	7.30	-64.56	7.20	-12.67	7.30	-14.52	15.90	-1.33	48.68	9.56	10.95
0.00	-0.80	7.30	-34.64	7.20	-11.55	7.20	-10.26	15.90	-1.33	26.12	8.71	7.74
0.00	-0.70	7.30	-23.72	7.20	-10.60	7.20	-8.73	15.90	-1.33	17.89	7.99	6.59
0.00	-0.60	7.30	-17.87	7.20	-9.78	7.20	-7.90	15.90	-1.33	13.48	7.37	5.96
0.00	-0.50	7.20	-14.18	7.20	-9.04	7.20	-7.37	15.90	-1.33	10.69	6.82	5.56
0.00	-0.40	7.20	-11.61	7.20	-8.38	7.20	-7.00	15.90	-1.33	8.76	6.32	5.28
0.00	-0.30	7.20	-9.71	7.20	-7.76	7.20	-6.71	15.90	-1.33	7.32	5.85	5.06
0.00	-0.20	7.20	-8.24	7.20	-7.19	7.20	-6.48	15.90	-1.33	6.22	5.42	4.88
0.00	-0.10	7.20	-7.07	7.20	-6.64	7.20	-6.28	15.90	-1.33	5.33	5.01	4.74
0.00	0.00	7.20	-6.11	7.20	-6.11	7.20	-6.11	15.90	-1.33	4.61	4.61	4.61
0.10	-0.90	7.10	-84.18	7.20	-11.67	7.10	-18.74	15.70	-1.73	48.72	6.76	10.85
0.10	-0.80	7.10	-44.60	7.30	-10.60	7.00	-13.09	15.70	-1.73	25.81	6.13	7.58
0.10	-0.70	7.10	-30.33	7.30	-9.71	7.00	-11.07	15.70	-1.73	17.55	5.62	6.41
0.10	-0.60	7.00	-22.76	7.30	-8.94	7.00	-9.98	15.70	-1.73	13.17	5.17	5.78
0.10	-0.50	7.00	-18.01	7.30	-8.26	7.00	-9.29	15.70	-1.73	10.42	4.78	5.38
0.10	-0.40	7.00	-14.71	7.30	-7.65	7.00	-8.81	15.70	-1.73	8.51	4.43	5.10
0.10	-0.30	7.00	-12.27	7.30	-7.08	7.00	-8.44	15.70	-1.73	7.10	4.10	4.88
0.10	-0.20	7.00	-10.40	7.30	-6.55	7.00	-8.14	15.70	-1.73	6.02	3.79	4.71
0.10	-0.10	7.00	-8.90	7.30	-6.05	7.00	-7.90	15.70	-1.73	5.15	3.50	4.57
0.10	0.00	7.00	-7.69	7.30	-5.58	7.00	-7.69	15.70	-1.73	4.45	3.23	4.45
0.20	-0.90	6.90	-109.57	7.30	-10.77	6.80	-24.18	15.50	-2.25	48.74	4.79	10.76
0.20	-0.80	6.90	-57.40	7.30	-9.75	6.80	-16.72	15.50	-2.25	25.53	4.34	7.44

λ	χ'	<u>config., a</u>		<u>config., b</u>		<u>config., c</u>		<u>config., d</u>		ratios:		
		r/Å	V*min	r/Å	V*min	r/Å	V*min	r/Å	V*min	a/d	b/d	c/d
0.20	-0.70	6.80	-38.83	7.30	-8.90	6.80	-14.04	15.50	-2.25	17.28	3.96	6.25
0.20	-0.60	6.80	-29.03	7.40	-8.18	6.80	-12.63	15.50	-2.25	12.92	3.64	5.62
0.20	-0.50	6.80	-22.89	7.40	-7.55	6.80	-11.73	15.50	-2.25	10.18	3.36	5.22
0.20	-0.40	6.80	-18.64	7.40	-6.98	6.80	-11.10	15.50	-2.25	8.29	3.11	4.94
0.20	-0.30	6.80	-15.52	7.40	-6.46	6.80	-10.63	15.50	-2.25	6.91	2.88	4.73
0.20	-0.20	6.80	-13.13	7.40	-5.98	6.80	-10.25	15.50	-2.25	5.84	2.66	4.56
0.20	-0.10	6.80	-11.22	7.40	-5.52	6.80	-9.94	15.50	-2.25	4.99	2.46	4.42
0.20	0.00	6.80	-9.68	7.30	-5.09	6.80	-9.68	15.50	-2.25	4.30	2.27	4.30
0.30	-0.90	6.60	-143.02	7.40	-9.95	6.60	-31.42	15.20	-2.95	48.56	3.38	10.67
0.30	-0.80	6.60	-74.35	7.40	-8.98	6.60	-21.44	15.20	-2.95	25.25	3.05	7.28
0.30	-0.70	6.60	-50.00	7.40	-8.18	6.60	-17.90	15.20	-2.95	16.98	2.78	6.08
0.30	-0.60	6.60	-37.22	7.40	-7.50	6.60	-16.04	15.20	-2.95	12.64	2.55	5.45
0.30	-0.50	6.60	-29.24	7.40	-6.91	6.60	-14.87	15.20	-2.95	9.93	2.35	5.05
0.30	-0.40	6.60	-23.76	7.40	-6.38	6.60	-14.06	15.20	-2.95	8.07	2.17	4.77
0.30	-0.30	6.60	-19.74	7.40	-5.90	6.60	-13.45	15.20	-2.95	6.70	2.00	4.57
0.30	-0.20	6.60	-16.66	7.40	-5.46	6.60	-12.97	15.20	-2.95	5.66	1.85	4.40
0.30	-0.10	6.60	-14.22	7.40	-5.05	6.50	-12.58	15.20	-2.95	4.83	1.71	4.27
0.30	0.00	6.50	-12.24	7.40	-4.66	6.50	-12.24	15.20	-2.95	4.16	1.58	4.16
0.40	-0.90	6.40	-189.22	7.50	-9.19	6.40	-41.19	15.00	-3.89	48.59	2.36	10.58
0.40	-0.80	6.40	-97.32	7.50	-8.27	6.40	-27.76	15.00	-3.89	24.99	2.12	7.13
0.40	-0.70	6.40	-65.02	7.50	-7.51	6.40	-23.04	15.00	-3.89	16.70	1.93	5.92
0.40	-0.60	6.40	-48.17	7.50	-6.88	6.30	-20.60	15.00	-3.89	12.37	1.77	5.29
0.40	-0.50	6.40	-37.72	7.50	-6.33	6.30	-19.07	15.00	-3.89	9.69	1.62	4.90
0.40	-0.40	6.40	-30.56	7.50	-5.84	6.30	-18.01	15.00	-3.89	7.85	1.50	4.63
0.40	-0.30	6.30	-25.33	7.50	-5.40	6.30	-17.23	15.00	-3.89	6.50	1.39	4.42
0.40	-0.20	6.30	-21.36	7.50	-4.99	6.30	-16.61	15.00	-3.89	5.49	1.28	4.27
0.40	-0.10	6.30	-18.22	7.50	-4.62	6.30	-16.11	15.00	-3.89	4.68	1.19	4.14
0.40	0.00	6.30	-15.68	7.50	-4.26	6.30	-15.68	15.00	-3.89	4.03	1.09	4.03
0.50	-0.90	6.20	-254.12	7.60	-8.49	6.10	-54.94	14.70	-5.25	48.44	1.62	10.47
0.50	-0.80	6.10	-129.53	7.60	-7.62	6.10	-36.67	14.70	-5.25	24.69	1.45	6.99
0.50	-0.70	6.10	-86.09	7.60	-6.91	6.10	-30.29	14.70	-5.25	16.41	1.32	5.77
0.50	-0.60	6.10	-63.56	7.60	-6.31	6.10	-26.98	14.70	-5.25	12.12	1.20	5.14
0.50	-0.50	6.10	-49.64	7.60	-5.80	6.10	-24.92	14.70	-5.25	9.46	1.10	4.75
0.50	-0.40	6.10	-40.14	7.60	-5.34	6.10	-23.50	14.70	-5.25	7.65	1.02	4.48
0.50	-0.30	6.10	-33.22	7.60	-4.94	6.10	-22.45	14.70	-5.25	6.33	0.94	4.28
0.50	-0.20	6.10	-27.94	7.60	-4.57	6.10	-21.64	14.70	-5.25	5.33	0.87	4.12
0.50	-0.10	6.10	-23.78	7.60	-4.22	6.10	-20.97	14.70	-5.25	4.53	0.80	4.00
0.50	0.00	6.10	-20.41	7.60	-3.90	6.10	-20.41	14.70	-5.25	3.89	0.74	3.89
0.60	-0.90	5.90	-353.48	7.60	-7.85	5.90	-75.64	14.40	-7.29	48.48	1.08	10.37
0.60	-0.80	5.90	-178.22	7.70	-7.02	5.80	-49.80	14.40	-7.29	24.44	0.96	6.83
0.60	-0.70	5.90	-117.60	7.70	-6.35	5.80	-40.90	14.40	-7.29	16.13	0.87	5.61
0.60	-0.60	5.90	-86.37	7.70	-5.79	5.80	-36.31	14.40	-7.29	11.85	0.79	4.98
0.60	-0.50	5.80	-67.19	7.70	-5.31	5.80	-33.47	14.40	-7.29	9.22	0.73	4.59
0.60	-0.40	5.80	-54.19	7.70	-4.89	5.80	-31.53	14.40	-7.29	7.43	0.67	4.32
0.60	-0.30	5.80	-44.75	7.70	-4.51	5.80	-30.10	14.40	-7.29	6.14	0.62	4.13
0.60	-0.20	5.80	-37.57	7.70	-4.17	5.80	-28.99	14.40	-7.29	5.15	0.57	3.98
0.60	-0.10	5.80	-31.92	7.70	-3.86	5.80	-28.10	14.40	-7.29	4.38	0.53	3.85
0.60	0.00	5.80	-27.35	7.70	-3.56	5.80	-27.35	14.40	-7.29	3.75	0.49	3.75
0.70	-0.90	5.50	-518.55	7.70	-7.27	5.50	-109.95	14.10	-10.75	48.22	0.68	10.22
0.70	-0.80	5.50	-258.85	7.80	-6.47	5.50	-71.51	14.10	-10.75	24.07	0.60	6.65
0.70	-0.70	5.50	-169.72	7.80	-5.83	5.50	-58.31	14.10	-10.75	15.78	0.54	5.42
0.70	-0.60	5.50	-124.09	7.80	-5.31	5.50	-51.54	14.10	-10.75	11.54	0.49	4.79
0.70	-0.50	5.50	-96.19	7.80	-4.86	5.50	-47.38	14.10	-10.75	8.94	0.45	4.41
0.70	-0.40	5.50	-77.29	7.80	-4.47	5.50	-44.55	14.10	-10.75	7.19	0.42	4.14
0.70	-0.30	5.50	-63.62	7.80	-4.13	5.50	-42.48	14.10	-10.75	5.92	0.38	3.95
0.70	-0.20	5.50	-53.26	7.80	-3.81	5.50	-40.89	14.10	-10.75	4.95	0.35	3.80
0.70	-0.10	5.50	-45.12	7.80	-3.52	5.50	-39.62	14.10	-10.75	4.20	0.33	3.68
0.70	0.00	5.50	-38.56	7.80	-3.26	5.50	-38.56	14.10	-10.75	3.59	0.30	3.59
0.80	-0.90	5.10	-849.19	7.80	-6.73	5.10	-177.47	13.70	-17.66	48.08	0.38	10.05
0.80	-0.80	5.10	-418.47	7.80	-5.97	5.10	-113.56	13.70	-17.66	23.69	0.34	6.43
0.80	-0.70	5.10	-272.02	7.90	-5.36	5.10	-91.79	13.70	-17.66	15.40	0.30	5.20

λ	χ'	<u>config., a</u>		<u>config., b</u>		<u>config., c</u>		<u>config., d</u>		ratios:		
		r/Å	V*mir	r/Å	V*mir	r/Å	V*mir	r/Å	V*mir	a/d	b/d	c/d
0.80	-0.60	5.10	-197.61	7.90	-4.87	5.10	-80.71	13.70	-17.66	11.19	0.28	4.57
0.80	-0.50	5.10	-152.38	7.90	-4.45	5.10	-73.96	13.70	-17.66	8.63	0.25	4.19
0.80	-0.40	5.10	-121.90	7.90	-4.09	5.10	-69.40	13.70	-17.66	6.90	0.23	3.93
0.80	-0.30	5.10	-99.94	7.90	-3.77	5.10	-66.08	13.70	-17.66	5.66	0.21	3.74
0.80	-0.20	5.10	-83.34	7.90	-3.48	5.10	-63.55	13.70	-17.66	4.72	0.20	3.60
0.80	-0.10	5.10	-70.35	7.90	-3.22	5.10	-61.54	13.70	-17.66	3.98	0.18	3.48
0.80	0.00	5.10	-59.89	7.90	-2.97	5.10	-59.89	13.70	-17.66	3.39	0.17	3.39
0.90	-0.90	4.50	-1829.0	7.90	-6.23	4.60	-373.52	13.10	-38.21	47.86	0.16	9.78
0.90	-0.80	4.50	-886.54	7.90	-5.51	4.60	-234.00	13.10	-38.21	23.20	0.14	6.12
0.90	-0.70	4.50	-569.61	7.90	-4.93	4.60	-186.93	13.10	-38.21	14.91	0.13	4.89
0.90	-0.60	4.60	-410.09	8.00	-4.46	4.60	-163.18	13.10	-38.21	10.73	0.12	4.27
0.90	-0.50	4.60	-313.91	8.00	-4.07	4.60	-148.83	13.10	-38.21	8.22	0.11	3.89
0.90	-0.40	4.60	-249.47	8.00	-3.74	4.60	-139.19	13.10	-38.21	6.53	0.10	3.64
0.90	-0.30	4.60	-203.25	8.00	-3.44	4.60	-132.26	13.10	-38.21	5.32	0.09	3.46
0.90	-0.20	4.60	-168.46	8.00	-3.18	4.60	-127.01	13.10	-38.21	4.41	0.08	3.32
0.90	-0.10	4.60	-141.32	8.00	-2.94	4.60	-122.89	13.10	-38.21	3.70	0.08	3.22
0.90	0.00	4.60	-119.55	8.00	-2.71	4.60	-119.55	13.10	-38.21	3.13	0.07	3.13

λ	χ'	<u>config., a</u>		<u>config., b</u>		<u>config., c</u>		<u>config., d</u>		ratio:		
		r/Å	V*min	r/Å	V*min	r/Å	V*min	r/Å	V*min	<u>a/d</u>	<u>b/d</u>	<u>c/d</u>
-0.20	-0.90	6.90	-33.42	6.20	-12.65	6.90	-7.62	16.20	-0.67	49.80	18.85	11.35
-0.20	-0.89	6.90	-30.68	6.20	-12.55	6.80	-7.22	16.20	-0.67	45.71	18.70	10.76
-0.20	-0.88	6.90	-28.37	6.20	-12.45	6.80	-6.89	16.20	-0.67	42.27	18.55	10.27
-0.20	-0.87	6.90	-26.40	6.20	-12.35	6.80	-6.61	16.20	-0.67	39.33	18.40	9.85
-0.20	-0.86	6.90	-24.69	6.20	-12.25	6.80	-6.36	16.20	-0.67	36.79	18.25	9.48
-0.20	-0.85	6.90	-23.20	6.20	-12.16	6.80	-6.15	16.20	-0.67	34.57	18.11	9.16
-0.20	-0.84	6.90	-21.89	6.20	-12.06	6.80	-5.96	16.20	-0.67	32.61	17.97	8.88
-0.20	-0.83	6.90	-20.72	6.20	-11.97	6.80	-5.79	16.20	-0.67	30.87	17.83	8.63
-0.20	-0.82	6.90	-19.67	6.20	-11.87	6.80	-5.64	16.20	-0.67	29.30	17.69	8.41
-0.20	-0.81	6.90	-18.72	6.20	-11.78	6.80	-5.51	16.20	-0.67	27.89	17.55	8.20
-0.20	-0.80	6.90	-17.86	6.20	-11.69	6.80	-5.38	16.20	-0.67	26.61	17.42	8.02

Table B.2.1

λ	χ'	<u>a</u>		<u>b</u>		<u>c</u>		<u>d</u>		<u>a/d</u>	<u>b/d</u>	<u>c/d</u>
		r/Å	V*min	r/Å	V*min	r/Å	V*min	r/Å	V*min			
-0.10	-0.90	6.90	-45.36	6.50	-11.83	6.90	-10.25	16.20	-0.91	49.60	12.94	11.20
-0.10	-0.89	6.90	-41.59	6.50	-11.73	6.90	-9.69	16.20	-0.91	45.48	12.83	10.60
-0.10	-0.88	6.90	-38.42	6.50	-11.63	6.90	-9.23	16.20	-0.91	42.02	12.72	10.10
-0.10	-0.87	6.90	-35.72	6.50	-11.53	6.80	-8.84	16.20	-0.91	39.07	12.61	9.67
-0.10	-0.86	6.90	-33.39	6.50	-11.43	6.80	-8.51	16.20	-0.91	36.51	12.50	9.30
-0.10	-0.85	6.90	-31.35	6.50	-11.34	6.80	-8.21	16.20	-0.91	34.28	12.40	8.98
-0.10	-0.84	6.90	-29.55	6.50	-11.25	6.80	-7.96	16.20	-0.91	32.31	12.30	8.70
-0.10	-0.83	6.90	-27.95	6.50	-11.15	6.80	-7.73	16.20	-0.91	30.56	12.20	8.45
-0.10	-0.82	6.90	-26.51	6.50	-11.06	6.80	-7.52	16.20	-0.91	29.00	12.10	8.22
-0.10	-0.81	6.90	-25.22	6.50	-10.98	6.80	-7.33	16.20	-0.91	27.58	12.00	8.02
-0.10	-0.80	6.90	-24.05	6.50	-10.89	6.80	-7.17	16.20	-0.91	26.30	11.91	7.84

Table B.2.2

λ	χ'	<u>a</u>		<u>b</u>		<u>c</u>		<u>d</u>		<u>a/d</u>	<u>b/d</u>	<u>c/d</u>
		r/Å	V*min	r/Å	V*min	r/Å	V*min	r/Å	V*min			
0.00	-0.90	6.90	-60.69	6.80	-11.11	6.90	-13.60	16.20	-1.23	49.43	9.05	11.07
0.00	-0.89	6.90	-55.60	6.80	-11.01	6.90	-12.85	16.20	-1.23	45.28	8.97	10.46
0.00	-0.88	6.90	-51.32	6.80	-10.91	6.90	-12.23	16.20	-1.23	41.79	8.89	9.96
0.00	-0.87	6.90	-47.68	6.80	-10.82	6.90	-11.69	16.20	-1.23	38.83	8.81	9.52
0.00	-0.86	6.90	-44.53	6.80	-10.72	6.90	-11.23	16.20	-1.23	36.26	8.73	9.15
0.00	-0.85	6.90	-41.78	6.80	-10.63	6.80	-10.84	16.20	-1.23	34.02	8.66	8.83
0.00	-0.84	6.90	-39.35	6.80	-10.54	6.80	-10.49	16.20	-1.23	32.05	8.58	8.54
0.00	-0.83	6.90	-37.20	6.80	-10.45	6.80	-10.18	16.20	-1.23	30.29	8.51	8.29
0.00	-0.82	6.90	-35.27	6.80	-10.36	6.80	-9.90	16.20	-1.23	28.72	8.44	8.06
0.00	-0.81	6.90	-33.53	6.80	-10.27	6.80	-9.65	16.20	-1.23	27.31	8.37	7.86
0.00	-0.80	6.90	-31.96	6.80	-10.19	6.80	-9.43	16.20	-1.23	26.02	8.30	7.68

Table B.2.3

λ	χ'	<u>a</u>		<u>b</u>		<u>c</u>		<u>d</u>		<u>a/d</u>	<u>b/d</u>	<u>c/d</u>
		r/Å	V*min	r/Å	V*min	r/Å	V*min	r/Å	V*min			
0.10	-0.90	6.90	-80.52	7.10	-10.48	6.90	-17.89	16.20	-1.63	49.26	6.41	10.95
0.10	-0.89	6.90	-73.70	7.10	-10.38	6.90	-16.90	16.20	-1.63	45.09	6.35	10.34
0.10	-0.88	6.90	-67.98	7.10	-10.29	6.90	-16.06	16.20	-1.63	41.58	6.29	9.83
0.10	-0.87	6.90	-63.10	7.10	-10.19	6.90	-15.35	16.20	-1.63	38.60	6.23	9.39
0.10	-0.86	6.90	-58.89	7.10	-10.10	6.90	-14.73	16.20	-1.63	36.03	6.18	9.01
0.10	-0.85	6.90	-55.22	7.10	-10.01	6.80	-14.20	16.20	-1.63	33.78	6.12	8.69
0.10	-0.84	6.90	-51.98	7.10	-9.92	6.80	-13.74	16.20	-1.63	31.80	6.07	8.40
0.10	-0.83	6.90	-49.11	7.10	-9.83	6.80	-13.32	16.20	-1.63	30.04	6.01	8.15
0.10	-0.82	6.90	-46.53	7.10	-9.74	6.80	-12.95	16.20	-1.63	28.47	5.96	7.92
0.10	-0.81	6.90	-44.22	7.10	-9.66	6.80	-12.62	16.20	-1.63	27.05	5.91	7.72
0.10	-0.80	6.90	-42.12	7.10	-9.57	6.80	-12.31	16.20	-1.63	25.76	5.85	7.53

Table B.2.4

λ	χ'	<u>a</u>		<u>b</u>		<u>c</u>		<u>d</u>		<u>a/d</u>	<u>b/d</u>	<u>c/d</u>
		r/Å	V*min	r/Å	V*min	r/Å	V*min	r/Å	V*min			
0.20	-0.90	6.90	-106.4	7.40	-9.93	6.90	-23.47	16.20	-2.17	49.11	4.58	10.83
0.20	-0.89	6.90	-97.33	7.40	-9.83	6.90	-22.14	16.20	-2.17	44.91	4.54	10.21
0.20	-0.88	6.90	-89.70	7.40	-9.73	6.80	-21.03	16.20	-2.17	41.39	4.49	9.70
0.20	-0.87	6.90	-83.20	7.40	-9.64	6.80	-20.09	16.20	-2.17	38.39	4.45	9.27
0.20	-0.86	6.90	-77.59	7.40	-9.54	6.80	-19.28	16.20	-2.17	35.80	4.40	8.90
0.20	-0.85	6.90	-72.70	7.40	-9.45	6.80	-18.57	16.20	-2.17	33.55	4.36	8.57
0.20	-0.84	6.90	-68.40	7.40	-9.36	6.80	-17.95	16.20	-2.17	31.56	4.32	8.28
0.20	-0.83	6.90	-64.58	7.40	-9.28	6.80	-17.40	16.20	-2.17	29.80	4.28	8.03
0.20	-0.82	6.90	-61.16	7.40	-9.19	6.80	-16.90	16.20	-2.17	28.22	4.24	7.80
0.20	-0.81	6.90	-58.08	7.40	-9.11	6.80	-16.46	16.20	-2.17	26.80	4.20	7.59
0.20	-0.80	6.90	-55.30	7.40	-9.02	6.80	-16.05	16.20	-2.17	25.52	4.16	7.41

Table B.2.5

APPENDIX C

Publications

The following publications are reproduced as appendix C.

M. D. De Luca, M. P. Neal, and C. M. Care, 1994, Molecular dynamics simulations of discotic liquid crystals using a hybrid Gay-Berne Luckhurst-Romano potential, *Liquid Crystals*, **16**, 257-266.

M. D. De Luca, M. K. Griffiths, C. M. Care, and M. P. Neal, 1994, Computer modelling of discotic liquid crystals, *International Journal of Electronics*, **6**, 907-917.

M. P. Neal, M. D. De Luca and C. M. Care, 1995, Molecular dynamics simulations of calamitic and discotic liquid crystals using a hybrid Gay-Berne Luckhurst-Romano Potential, *Molecular Simulation*, **14**, 245-258.

Molecular dynamics simulations of discotic liquid crystals using a hybrid Gay–Berne Luckhurst–Romano potential

by M. D. DE LUCA†, M. P. NEAL*†‡ and C. M. CARE§

Sheffield Hallam University, City Campus,
Pond Street, Sheffield S1 1WB, England

(Received 5 April 1993; accepted 12 July 1993)

We report the results of the computer simulation of a collection of particles interacting via an anisotropic potential proposed by Luckhurst and Romano and modified by scaling with part of the anisotropic well depth formalism employed by Gay–Berne. Using the molecular dynamics technique for 256 particles in the NVE ensemble, the system is shown to exhibit a variety of mesophases, as the temperature is lowered, and these are provisionally identified as isotropic, discotic nematic, a highly ordered fluid phase with some columnar features and a crystal.

1. Introduction

Significant progress has been made in recent years in modelling liquid crystal phases using hard non-spherical models, soft non-spherical models and realistic atom–atom potentials. Orientationally ordered mesophases have been simulated using non-spherical rod-like and disc-like hard-core mesogens [1–3], but longer range attractive forces are expected to influence the formation of mesophases, as well as short range repulsive forces. Luckhurst and Romano [4] represented cylindrically symmetric particles by a Lennard–Jones 12–6 potential, V_o together with an additional anisotropic term V_a

$$V = V_o + V_a, \quad (1)$$

where

$$V_o = 4\epsilon \left\{ \left(\frac{\sigma}{r} \right)^{12} - \left(\frac{\sigma}{r} \right)^6 \right\}, \quad (2)$$

$$V_a = -4\lambda\epsilon \left\{ \left(\frac{\sigma}{r} \right)^{12} + \left(\frac{\sigma}{r} \right)^6 \right\} P_2(\cos(\beta_{12})) \quad (3)$$

and β_{12} is the angle between the particle symmetry axes. They demonstrated a weak first order transition from a nematic to an isotropic phase using a value of $\lambda=0.15$ determined by preliminary calculations.

Everitt and Care [5] carried out a Monte Carlo simulation of a siloxane ring system using the Luckhurst and Romano potential given by equation (1) to represent the mesogenic units attached to the ring. The system exhibited a transition from calamitic ordering to discotic ordering as the ring–mesogen bond varied from fully rigid to fully flexible.

* Author for correspondence.

† Division of Applied Physics.

‡ Present address, School of Mathematics and Computing, University of Derby, Derby DE22 1GB.

§ Materials Research Institute.

Berne and Pechukas [6] developed a soft non-spherical single site potential based on the Gaussian overlap model. The original potential had several unrealistic features and was modified [7] by obtaining a function which gave the best fit to the potential described by a linear array of four equidistant Lennard–Jones centres. This potential has been used extensively by Luckhurst and co-workers, for example, [8, 9] and by de Miguel and Rull [10] with rod-like parameterization to simulate nematic, smectic A and smectic B phases, and by Emerson and Luckhurst [11] with disc-like parameterization to simulate discotic nematic and discotic columnar phases. The Gay–Berne potential is a single site potential so that a smooth transition in shape is obtained as the parameterization is varied from the rod-like to the disc-like form. To model the complex spectrum of molecular interactions of rods and discs more realistically, we propose in future work to rigidly join together soft anisotropic potentials in a variety of geometries. Such simulations are computationally very expensive, so in a bid to reduce the time required, we have investigated a modified form of potential (1) [12]. The pair potential is scaled by part of the well depth formalism employed to fit the Gay–Berne potential [7], where

$$\varepsilon'(\hat{\mathbf{u}}_1, \hat{\mathbf{u}}_2, \mathbf{r}) = 1 - \frac{\chi'}{2} \left\{ \frac{(\hat{\mathbf{r}} \cdot \hat{\mathbf{u}}_1 + \hat{\mathbf{r}} \cdot \hat{\mathbf{u}}_2)^2}{1 + \chi'(\hat{\mathbf{u}}_1 \cdot \hat{\mathbf{u}}_2)} + \frac{(\hat{\mathbf{r}} \cdot \hat{\mathbf{u}}_1 - \hat{\mathbf{r}} \cdot \hat{\mathbf{u}}_2)^2}{1 - \chi'(\hat{\mathbf{u}}_1 \cdot \hat{\mathbf{u}}_2)} \right\} \quad (4)$$

so that the potential becomes

$$V = \varepsilon'(\hat{\mathbf{u}}_1, \hat{\mathbf{u}}_2, \mathbf{r}) \{V_o + V_a\}. \quad (5)$$

The orientation of the molecule is specified by the unit vector $\hat{\mathbf{u}}$ and the intermolecular vector by the unit vector $\hat{\mathbf{r}}$. The parameter χ' determines the relative ratio of the end to end and side to side interactions and is given by

$$\chi' = (1 - \varepsilon_e/\varepsilon_s)/(1 + \varepsilon_e/\varepsilon_s), \quad (6)$$

where $\varepsilon_e/\varepsilon_s$ is the ratio of end to end and side to side potential well depths [8]. The original potential (1) is dependent on the relative orientation of the intermolecular axes and so favours end to end (e) and side to side (s) configurations compared to cross (X) and tee (T) configurations, but does not distinguish between side–side and end–end or between X and T. It should be noted however that the modified potential given by equation (5) does distinguish between s and e and between X and T, as shown in table 1. The modified potential (5) requires one tenth the CPU time of the Gay–Berne on an iPSC860 processor. Further it has the advantage that the effect of ε' alone can be investigated by varying $\varepsilon_e/\varepsilon_s$. Extensive studies of the Gay–Berne fluid have used values of 5.0 to represent a disc-like potential and 0.2 or less [11] to represent a rod-like potential as part of the parameterization. Setting the ratio equal to 1 removes the effect of ε' . We present preliminary results for potential (5) with $\lambda = 0.15$ and $\varepsilon_e/\varepsilon_s$ equal to 5.0 so that the end to end interaction is favoured as shown in figure 1.

Table 1. Values of $\varepsilon'(\hat{\mathbf{u}}_1, \hat{\mathbf{u}}_2, \mathbf{r})$ (4), for different configurations.

Configuration	$\varepsilon_e/\varepsilon_s = 0.2$	$\varepsilon_e/\varepsilon_s = 5.0$	β_{12}	$\varepsilon'(\hat{\mathbf{u}}_1, \hat{\mathbf{u}}_2, \mathbf{r})$
end–end	0.2	5.0	0°	$\varepsilon_e/\varepsilon_s$
side–side	1.0	1.0	0°	1
X	1.0	1.0	90°	1
T	1.0/3.0	5.0/3.0	90°	$2/(1 + \varepsilon_e/\varepsilon_s)$

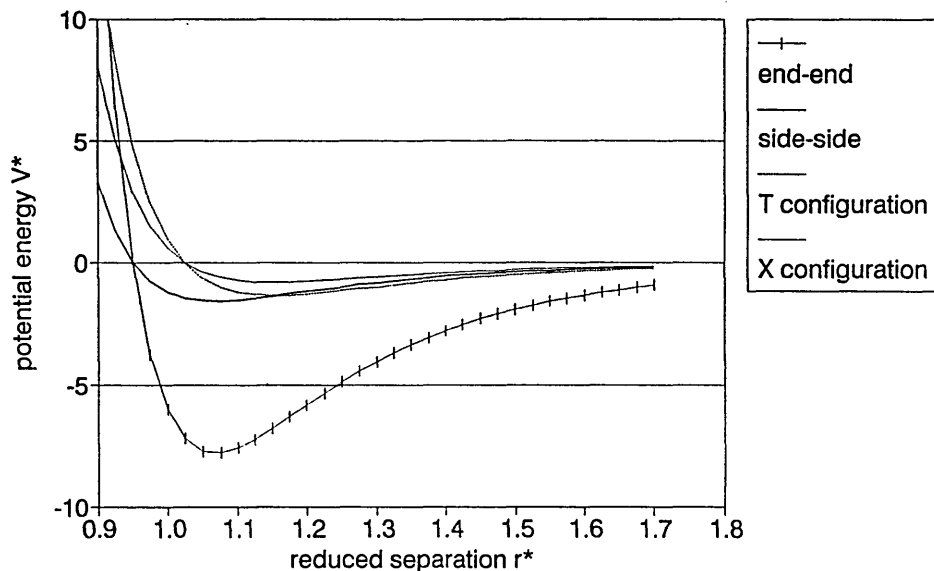


Figure 1. The distance dependence of the potential energy calculated from the modified anisotropic potential for particular orientations of the molecules with respect to one another and to the intermolecular vector. The parameterization of the potential is that used in the molecular dynamics simulation and described in the text.

2. Molecular dynamics simulation

Our primary aim was to see if potential (5) could be used to model discotic liquid crystals, and to compare the phase temperatures with those obtained for the Gay-Berne fluid. We have performed molecular dynamics simulations (MD) for 256 particles in the NVE ensemble in a cubic box, employing periodic boundary conditions. No cut off was used as this did not aid the vectorization, and one time step in the simulation required 0.03 s of CPU time on an Amdahl VP1200 supercomputer. The translational equations of motion were solved numerically using a Verlet half-step leapfrog algorithm [13, 14], and the rotational equations of motion were solved in a similar manner using a constraint method [15]. Preliminary calculations were performed with a variety of number densities and at low temperatures. At values close to that of liquid argon near the triple point, cavities formed in the box. Results are presented for a reduced number density $\rho^* = 1.1$ which enabled equilibration of the system at low temperatures without cavity formation. The particles are axially symmetric about the vector \hat{u} with a spherical repulsive core surrounded by a non-spherical attractive region, equivalent to a disc-like moment of inertia. A reduced moment of inertia of $I^* = 1.00$ ($I^* = I/(m\sigma^2)$) was employed to provide a reasonable rate of equilibration between translational and rotational energy. From the simulation, the following quantities were calculated: the pressure $P^* = P\sigma^3/\epsilon$, temperature $T^* = Tk_B/\epsilon$, the root mean square displacement $\langle |\mathbf{r}^*(t) - \mathbf{r}^*(0)|^2 \rangle^{1/2}$ and its components parallel and perpendicular to the director, the total internal energy per particle $E^* = E/\epsilon$, the potential and the kinetic energy per particle U^* and K^* , the order parameter $\langle P_2 \rangle$ and the director of the phase \hat{n} . The second rank order parameter $\langle P_2 \rangle$ was evaluated using the tensor Q defined by

$$Q_{z\beta} = \frac{1}{N} \sum_{i=1}^N \frac{3u_z^i u_\beta^i - \delta_{z\beta}}{2} \quad (7)$$

where u_i^α is the α -component of the unit vector along the symmetry axis of the molecule i . $\langle P_2 \rangle$ was defined as the ensemble average of the largest eigenvalue of the Q -tensor, and the director as the corresponding eigenvector [16] and these were calculated every 100 steps. Additionally the second rank orientational correlation function G_2 ,

$$G_2 = \langle P_2(\cos \beta_{ij}(r^*)) \rangle \quad (8)$$

the radial distribution function $g(r)$ together with the longitudinal and transverse pair correlation functions $g_{\parallel}(r_{\parallel}^*)$ and $g_{\perp}(r_{\perp}^*)$ were calculated.

The first simulation was started from an α -fcc crystal with kinetic and rotational energy such that the initial lattice melted. The system was allowed to equilibrate over 30 000 steps, equipartition between translational and rotational energy being observed, and production runs of 30 000 step were employed. The temperature was reduced by scaling the linear velocities and allowing the system to equilibrate for 30 000 steps between each production run. The reduced time step $\Delta t^* = (\epsilon/m\sigma^2)^{1/2}\Delta t$ was adjusted to give acceptable energy conservation for each state point; fluctuations of less than 1 part in 1000 of the total energy were observed for all runs except one just before the region identified as the isotropic–nematic transition in which the energy fluctuated by 1 part in 100. A value of $\Delta t^* = 0.005$ was employed in the isotropic region, but this was lowered to 0.0015 in regions where the second rank order parameter $\langle P_2 \rangle$ rose indicating the onset of order.

3. Results

The variation of $\langle P_2 \rangle$ as the system was cooled is shown in figure 2. We see that the system is isotropic at a reduced temperature of $\langle T^* \rangle = 10.0$ and remains orientationally disordered until the temperature is lowered to about $\langle T^* \rangle = 5.5$, although finite size fluctuations in evaluating Q lead to a small non-zero value for $\langle P_2 \rangle$. In the reduced temperature range of $\langle T^* \rangle = 5.5$ to $\langle T^* \rangle = 5.0$, the order parameter rapidly rises to about $\langle P_2 \rangle = 0.64$. It then slowly tends to 1.0 as the system is cooled further. Figure 3

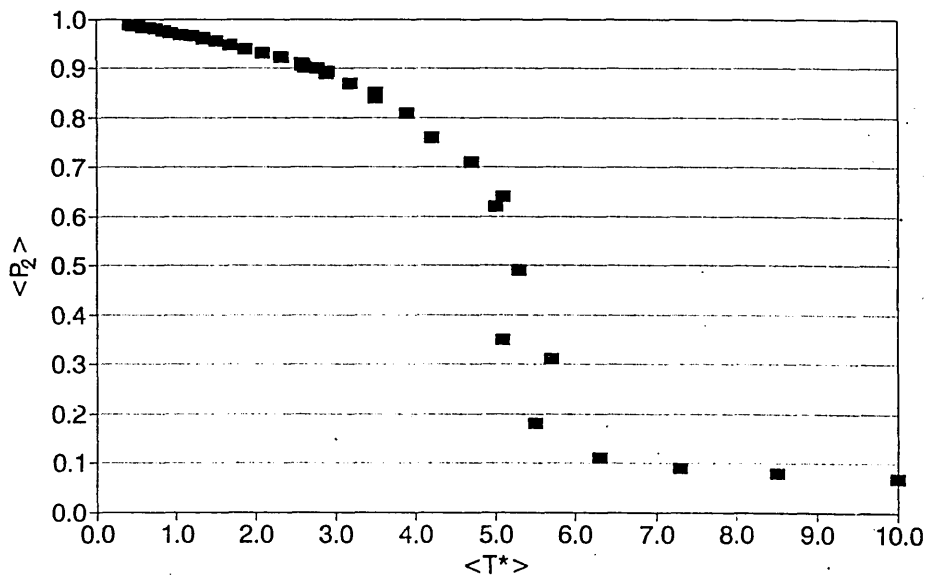


Figure 2. The variation of the second rank orientational order parameter $\langle P_2 \rangle$ as a function of reduced temperature.

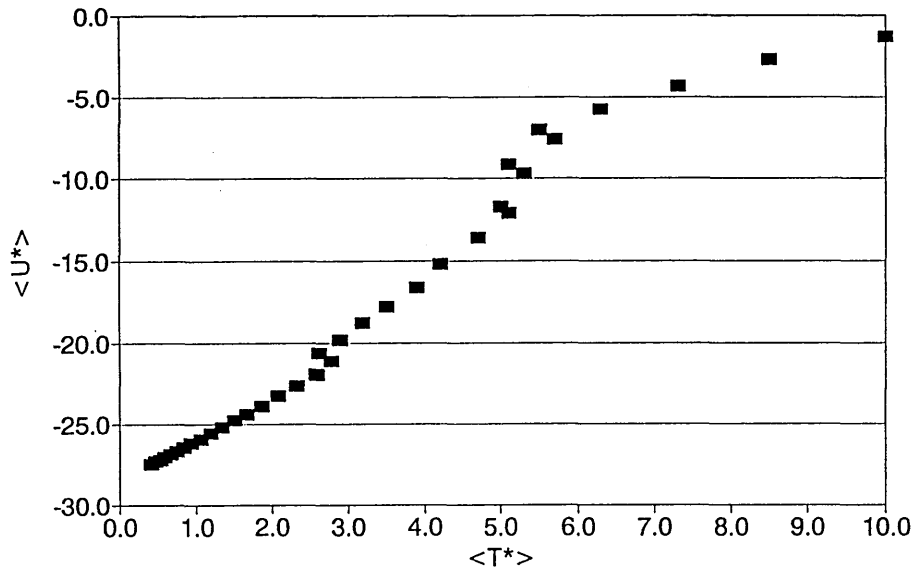


Figure 3. The variation of the potential energy $\langle U^* \rangle$ as a function of reduced temperature.

shows the change of the potential energy with temperature. At reduced temperatures of 5.3 ± 0.2 and 2.7 ± 0.1 , a fall in potential energy is seen while the temperature remains constant, indicating the presence of two phase transitions. The entropy of transition $\Delta \langle U^* \rangle / \langle T^* \rangle$ was estimated to be 0.6 in each case. The mean square displacement was monitored during each production run and the diffusion coefficient calculated from its gradient with respect to time as a check on the fluidity of the phase. Simulation runs near phase transitions were extended a further 150 000 steps and the diffusion coefficients D^* and its components D_{\parallel}^* and D_{\perp}^* parallel and perpendicular to the director obtained from the gradient of these curves which relate to the Einstein relation [17], valid at long times, were calculated by considering the final two-thirds of the simulation only. These results are presented in table 2. In these extended runs it was found that close to the nematic–isotropic transition, the system was subject to large energy fluctuations. This problem was resolved by substituting a full step Verlet algorithm to solve the rotational equations of motion [9].

Figure 4(a) shows that diffusion in a direction parallel and perpendicular to the director is equal at a reduced temperature of $\langle T^* \rangle = 5.0$. This is not observed in simulations of a Gay–Berne discotic nematic fluid [11]. This effect is attributed to the fact that the modified potential has a spherical repulsive core, whereas the repulsive

Table 2. Reduced diffusion coefficients, mean order parameters and mean temperatures.

$\langle T^* \rangle$	D^*	D_{\parallel}^*	D_{\perp}^*	$\langle P_2 \rangle$
5.3 ± 0.2	57.8	19.4	19.2	0.49 ± 0.06
5.0 ± 0.2	51.7	17.9	16.9	0.62 ± 0.02
2.88 ± 0.08	19.3	6.2	6.6	0.889 ± 0.008
2.77 ± 0.09	5.4	1.3	2.0	0.901 ± 0.007
2.58 ± 0.07	0.7	0.1	0.3	0.911 ± 0.007

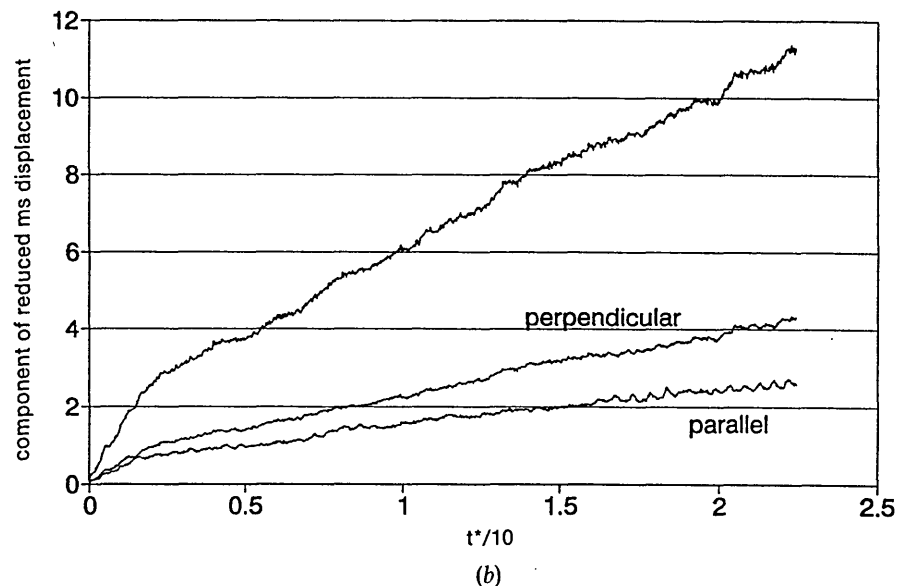
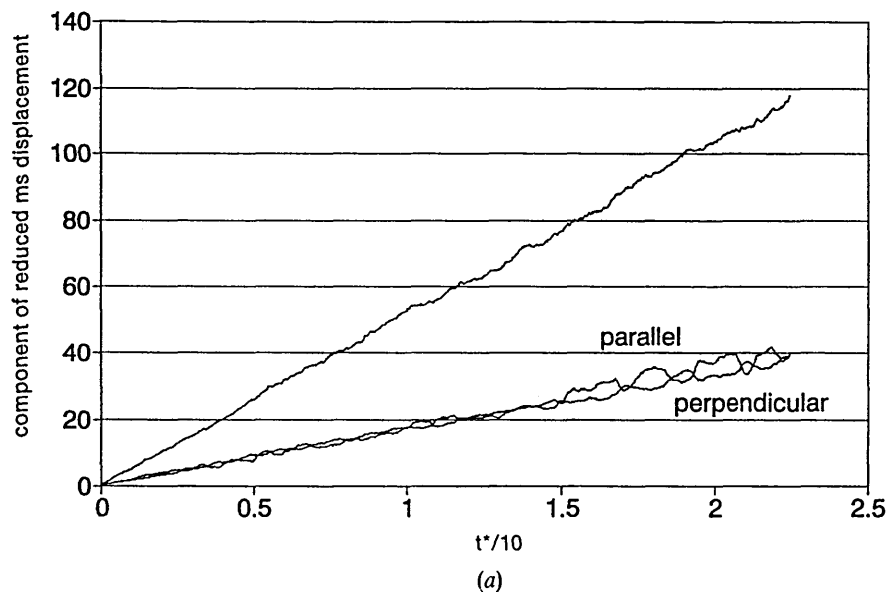


Figure 4. Mean square (MS) displacement versus time resolved with respect to the system director at a reduced temperature of (a) $\langle T^* \rangle = 5.0$ and (b) $\langle T^* \rangle = 2.77$.

core of the Gay-Berne potential possesses ellipsoidal symmetry. By the time the system has cooled to a reduced temperature of $\langle T^* \rangle = 2.77$, initially coincident curves, describing the components of diffusion with respect to the director, diverge at long time, although the total mean square displacement still exhibits liquid like behaviour, see figure 4(b). This reduction in diffusion parallel to the director below $\langle T^* \rangle = 2.8$ is further evidence for a transition to a highly ordered, possibly columnar fluid phase. At reduced temperatures lower than $\langle T^* \rangle \approx 2.6$, diffusion in all directions has virtually ceased, indicating the presence of a solid like phase.

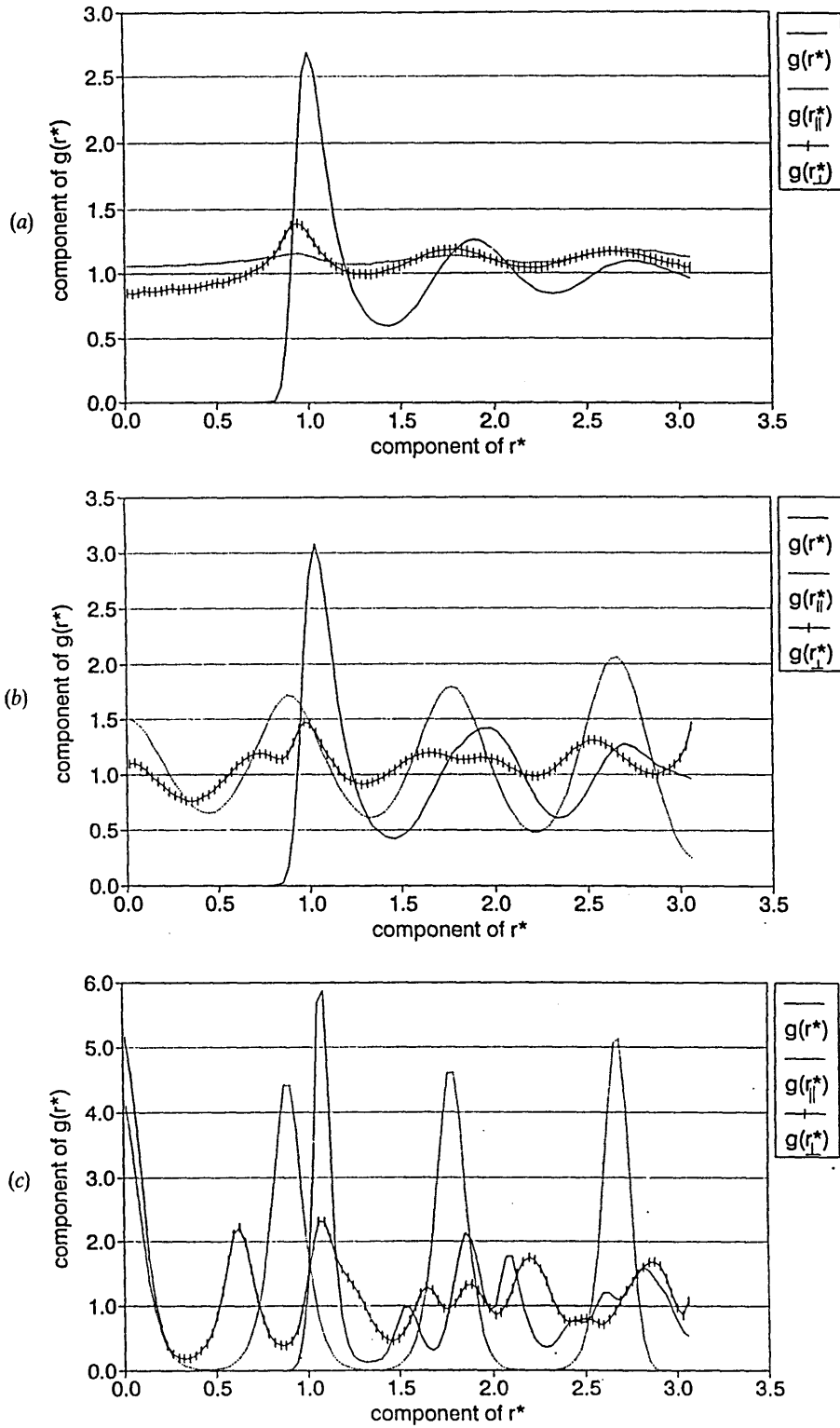


Figure 5. The radial distribution function $g(r^*)$ as a function of the scaled separation r^* and the longitudinal and transverse pair correlation functions $g_{||}(r^*)$ and $g_{\perp}(r^*)$ resolved with respect to the system director as a function of the components of the scaled separations $r_{||}^*$ and r_{\perp}^* respectively, simulated for the modified anisotropic potential at a series of reduced temperatures (a) $\langle T^* \rangle = 5.0$, $\langle P_2 \rangle = 0.62$, (b) $\langle T^* \rangle = 2.77$, $\langle P_2 \rangle = 0.90$, and (c) $\langle T^* \rangle = 0.47$, $\langle P_2 \rangle = 0.99$.

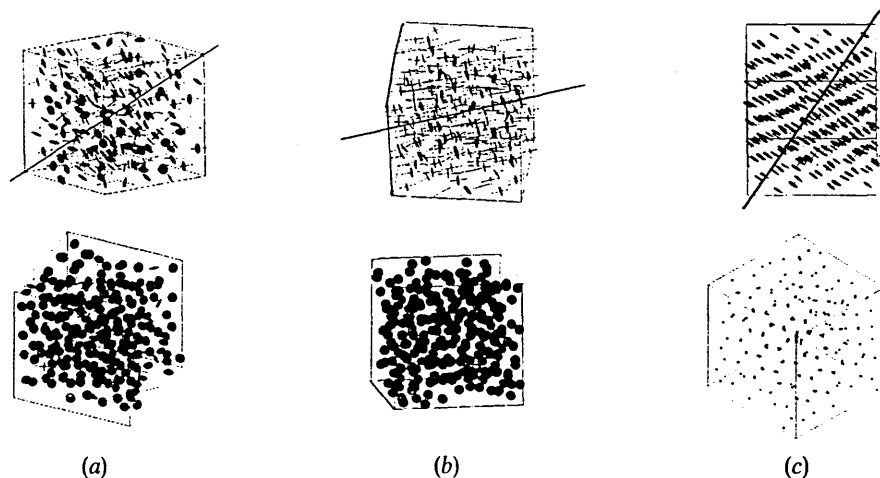


Figure 6. Three pairs of snapshots from typical configurations at instantaneous values of the order parameter $\langle P_2 \rangle$ of (a) 0.67, (b) 0.91 and (c) 0.99. The thick line in the box represents the direction of the director of the phase. The second snapshot is shown looking down the director for (a) and (b). In (c) the second snapshot shows the centres of mass of the molecules orthogonal to the column axes.

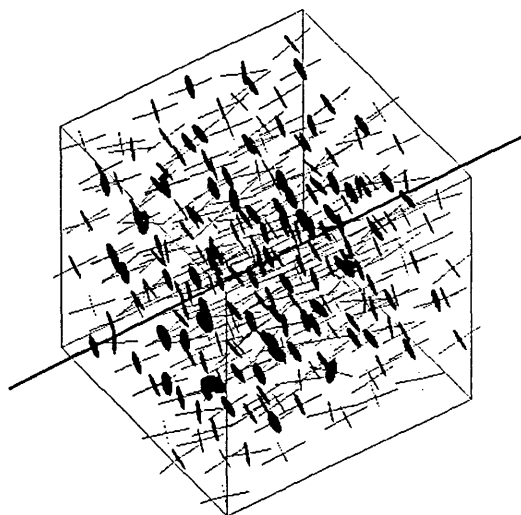


Figure 7. An enlarged snapshot of the configuration in figure 6(b) at an instantaneous value of the order parameter $\langle P_2 \rangle$ of 0.91, exhibiting examples of short stacks of discs.

Figures 5(a) and (b) show the radial distribution function together with transverse and longitudinal correlation functions at temperatures of $\langle T^* \rangle = 5.0$ and $\langle T^* \rangle = 2.77$, respectively. Figure 5(a) demonstrates that there is no discernible change from liquid-like structure as the phase changes from isotropic to discotic nematic, but figure 5(b) exhibits a one-dimensional density oscillation parallel to the director, consistent with the molecules being arranged in columns or layers with a separation $r^* = 0.96$, coincident with the energy minimum in the pair potential. At the same temperatures, the transverse pair correlation function also begins to indicate the presence of structure with peaks occurring that become much more enhanced in the crystal phase as shown in figure 5(c) at a reduced temperature of $\langle T^* \rangle = 0.47$.

The second rank orientational correlation function, $G_2(r^*)$, exhibited a peak close to a reduced separation $r^* = 0.7$ in all cases. In the isotropic phase, $G_2(r^*)$ quickly decayed to a limiting value close to zero, indicating the absence of any long range order. In the nematic and higher order phases, $G_2(r^*)$ attains a limiting value of approximately $\langle P_2 \rangle^2$ indicative of the persistence of orientational order at long range in these phases.

Figure 6 represents 'snapshots' of sample configurations taken during production runs at reduced temperatures of $\langle T^* \rangle = 5.0$, $\langle T^* \rangle = 2.8$ and $\langle T^* \rangle = 0.47$ corresponding to instantaneous values of the order parameter $\langle P_2 \rangle = 0.67$, $\langle P_2 \rangle = 0.91$ and $\langle P_2 \rangle = 0.99$. In each case, two views of the same configuration are presented parallel and perpendicular to the director. Figure 6(a) illustrates the discotic nematic phase. In figure 6(b) we present two views of the higher order phase. Although these snapshots do not appear to exhibit a full discotic columnar phase, there is evidence of short stacks of discs as shown in figure 7. This short range columnar order is supported by the density oscillation in the longitudinal distribution function parallel to the director. Frenkel [1], in simulations of cut spheres, observed highly ordered short range stacks, but in this case the oscillations in the longitudinal distribution function died away within the simulation box. It is interesting to note that in figure 6(c) and to a lesser extent in figure 6(b), the molecules appear tilted within the columns. A similar effect was observed in the liquid crystal phase diagram of the Gay-Berne fluid [10] as a smectic B phase was compressed. Finally figure 6(c) shows a crystal phase. The crystal shows a honeycomb structure with hexagonal symmetry, but not close packing. Other simulations of discotics using the Gay-Berne potential have yielded a final crystal with rectangular symmetry [11].

4. Conclusion

We have used molecular dynamics to simulate a system of discs interacting by a modified Luckhurst-Romano potential scaled by part of the well depth anisotropy term of the Gay-Berne potential. We have identified a phase transition from an isotropic liquid to a discotic nematic at a reduced temperature of $\langle T^* \rangle \approx 5.5$. The discotic nematic phase is stable over a range of about three reduced temperature units, subsequently undergoing a further transition to a higher ordered phase at $\langle T^* \rangle \approx 2.7$. The higher order phase is observed over a small reduced temperature range, with a transition to a crystal phase possessing hexagonal symmetry at $\langle T^* \rangle \approx 2.6$. These results are similar to those of Emerson [11] for the Gay-Berne potential which provisionally identified nematic discotic and columnar discotic phase transitions at reduced temperatures of $\langle T^* \rangle \approx 11.0$ and $\langle T^* \rangle \approx 4.0$ respectively, at a reduced density of $\rho^* = 3.0$, the Gay-Berne crystal showing rectangular symmetry. The reduced CPU time required for the modified potential (5) will allow multi-site versions of the potential with differing geometries to be used to simulate discotic liquid crystals more realistically, allowing investigation of the effect of variable bond lengths, and more direct comparison with the Gay-Berne fluid.

We wish to acknowledge the award of a research studentship to MDD from the Science and Engineering Research Council (RS Quota Award ref. No. 9031742X0), plus a grant of CPU time on the Manchester Computing Centre Amdahl VP1200 vector processor (Award ref. GR/H55994).

References

- [1] VEERMAN, J. A. C., and FRENKEL, D., 1992, *Phys. Rev. A*, **45**, 5632.
- [2] AZZOUZ, H., CAILLO, J. M., LEVESQUE, D., and WEIS, J. J., 1992, *J. chem. Phys.*, **96**, 4551.

- [3] FRENKEL, D., MULDER, B. M., and McTAGUE, J. P., 1985, *Molec. Crystals liq. Crystals*, **123**, 119.
- [4] LUCKHURST, G. R., and ROMANO, S., 1980, *Proc. R. Soc. A*, **373**, 111.
- [5] EVERITT, D. R. R., and CARE, C. M., 1990, *Molec. Simul.*, **5**, 167.
- [6] BERNE, B. J., and PECHUKAS, 1972, *J. chem. Phys.*, **56**, 4213.
- [7] GAY, J. G., and BERNE, B. J., 1981, *J. chem. Phys.*, **74**, 3316.
- [8] ADAMS, D. J., LUCKHURST, G. R., and PHIPPEN, R. W., 1987, *Molec. Phys.*, **61**, 1575.
- [9] LUCKHURST, G. R., STEPHENS, R. A., and PHIPPEN, R. W., 1990, *Liq. Crystals*, **8**, 451.
- [10] DE MIGUEL, E., RULL, L. F., CHALAM, M. K., and GUBBINS, K. E., 1991, *Molec. Phys.*, **74**, 405.
- [11] EMERSON, A. P. J., 1991, Ph.D. thesis, University of Southampton, UK.
- [12] NEAL, M. P., DE LUCA, M. D., and CARE, C. M., 1991, Poster presented at the NATO Advanced Workshop, Il Ciocco, Italy.
- [13] HOCKNEY, R. W., 1970, *Meth. comput. Phys.*, **9**, 136.
- [14] ALLEN, M. P., and TILDESLEY, D. J., 1987, *Computer Simulation of Liquids* (Clarendon Press).
- [15] FINCHAM, D., 1984, *CCPS Quart.*, **12**, 47.
- [16] ZANNONI, C., 1979, *The Molecular Physics of Liquid Crystals*, edited by G. R. Luckhurst and G. W. Gray (Academic Press), Chap. 9, p. 191.
- [17] TILDESLEY, D. J., 1984, *Molecular Liquids, Dynamics and Interactions*, edited by A. J. Barnes, W. J. Orville-Thomas and J. Yarwood (Reidel), (NATO ASI Series, Vol. 135) p. 519.

Computer modelling of discotic liquid crystals †

M. D. DE LUCA†, M. K. GRIFFITHS§, C. M. CARE§
and M. P. NEAL||

The majority of liquid crystals are based on elongated molecules that form so-called calamitic phases. In the late 1970s liquid crystals based on flat disc-shaped molecules were first synthesized. These molecular systems are known as discotics, and most exhibit two kinds of structure: nematic and columnar. An understanding of the molecular structure and interaction potentials of these molecules allows us to gain insight into the alignment of discotic materials. We review here the use of hard and soft potentials to undertake molecular dynamics and Monte Carlo simulations of discotics, with particular reference to the phases obtained from these models. We also discuss the possibility of using realistic models for specific liquid crystal systems.

1. Introduction

The first computer models of liquids were developed in the early 1950s (for reviews see Allen and Tildesley 1987, Ciccotti *et al.* 1987). Since this pioneering work, many advances have been made both in the techniques for carrying out simulations and in the theories of liquid structure. There are also continuous improvements in the associated computer hardware. Simulations of the anisotropic fluids which form liquid crystal (LC) phases are now readily undertaken. These computer simulations give an improved understanding of the way in which intermolecular interactions affect the observed LC phases and the form of the molecular ordering in these phases. This understanding is of use in the development and synthesis of new materials. In this paper we review the progress that has been made in the use of Monte Carlo (MC) and molecular dynamics (MD) techniques to simulate discotic liquid crystals.

The unique properties of liquid crystals lead to a variety of applications. Liquid crystal materials are used in a wide range of low-power display devices (Scheuble 1989) and rapid switching, high-definition, flat television screens are just coming on to the market. The use of liquid crystals for optical data storage devices is being investigated (e.g. Meier *et al.* 1975, Gray 1987). Interest in discotic liquid crystals has been growing since the discovery that derivatives of benzene and derivatives of triphenylene form thermodynamically stable liquid crystalline phases (Chandrasekhar *et al.* 1977, Billard 1978). One possible application of discotic liquid crystals as 'molecular wires' is currently being investigated (Boden *et al.* 1993).

†This paper was presented at the Fourth International Workshop on the Electronic Properties of Metal/Non-metal Microsystems, held at Sheffield Hallam University, U.K., on 31 August to 3 September 1993.

‡Division of Applied Physics, Sheffield Hallam University, Pond Street, Sheffield S1 1WB, U.K.

§Materials Research Institute, Sheffield Hallam University, Pond Street, Sheffield S1 1WB, U.K.

||School of Mathematics and Computing, University of Derby, U.K.

In the following, we describe the computer simulations that have been carried out on discotic systems. It is convenient to break the discussion into three separate parts; hard particle potentials, soft anisotropic potentials and multisite potentials.

2. Hard particle potentials

Much of the early work on simulating fluids has been undertaken on hard particle models because the results can be used to test the quality of analytical approximations within the theory of the liquid state. The work also allows a study of the interactions which are necessary to induce LC behaviour.

Although the first LC simulations were attempted in the early 1970s (Vieillard-Baron 1972, 1974) the first numerical determination of the thermodynamic isotropic-nematic transition in a system of three-dimensional particles was achieved for discotic type particles by Frenkel and Eppenga (1982) and Eppenga and Frenkel (1984) who studied a system of infinitely thin hard circular platelets of diameter σ . Such a system has only one parameter, the reduced (scaled) density $\rho^* = \rho\sigma^3$, making the system similar in this respect to the hard-sphere fluid. Indeed, the motivation for choosing the hard-platelet fluid is that it forms a reference system that may be used to model disc-like nematogens (discogens). The results of these simulations were compared with a five-term virial equation of state, the Onsager (1949) theory and a version of the scaled particle theory (Savithramma and Madhusudana 1981). Frenkel and Eppenga pointed out that comparison of their work with Onsager theory would be particularly interesting because any discrepancy between it and their MC results would be due solely to the higher order virial coefficients. The Onsager theory was consistently found to yield pressures that were too low in the isotropic regime. In conclusion, they found that none of the theories was fully satisfactory in describing the equation of state over the complete isotropic regime.

Hard ellipsoids of revolution have been studied extensively (Frenkel *et al.* 1984, Frenkel and Mulder 1985, Talbot *et al.* 1990). These simulations are characterized by the number density and axial ratio, $e = a/b$ where a is the length of the major symmetry axis and b is the length of the two equal corresponding minor perpendicular axes. Hard ellipsoids with axial ratios $e = 3, 2.75, 2, 1.25$ (prolate) and $e = 1/1.25, 1/2, 1/2.75, 1/3$ (oblate), were studied via MC simulation. Four distinct phases are identified at various reduced densities and axial ratios; isotropic liquid, nematic liquid, ordered solid and plastic solid. The plastic solid (sometimes called a plastic crystal) is a phase where the constituent particles possess long-range translational order but are orientationally disordered at long range. First-order phase transitions are located between solid and fluid, and between isotropic liquid and nematic liquid phases by computing the absolute free energy of the coexisting phases. The nematic phase is found to exist only in the range $1/2.75 \geq e \geq 2.75$. With this information, and existing data on the hard sphere, $e = 1$, system (Hoover and Ree 1968), a phase diagram of the hard ellipsoids of revolution may be constructed with the reduced density (packing fraction) and axial ratio e as independent variables (see Fig. 1). Such a phase diagram shows remarkable symmetry under the $e \leftrightarrow 1/e$ transformation. However, this symmetry cannot be exact because, in the limit that the oblate ellipsoids become infinitely thin, higher order virial coefficients do not vanish. With ellipsoids of axial ratio in the approximate range $1/1.5$ to 1.5 a plastic crystal phase is formed on compressing the orientationally ordered fluid. In this case the order

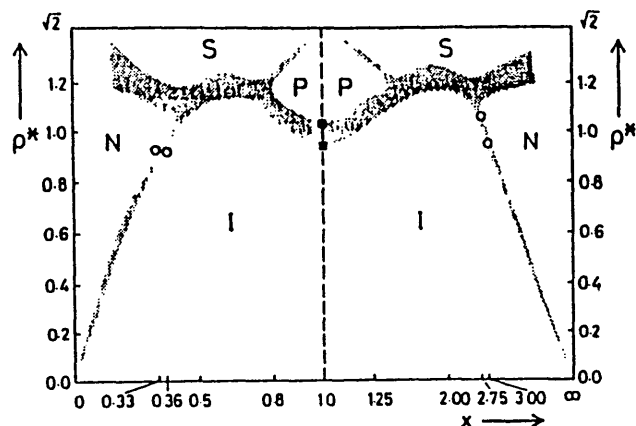


Figure 1. The phase diagram for hard ellipsoids of revolution. Axial ratio a/b is plotted against the scaled density ρ^* . Open circles indicate observed isotropic-to-nematic transitions. Black squares are the values for the coexistence densities of the hard-sphere liquid obtained by Hoover and Ree (1968). Shading denotes coexisting phases. The following phases are identified: I—*isotropic liquid*; N—*nematic liquid crystal*; P—*plastic crystal*; S—*solid*. [Diagram reproduced from Frenkel *et al.* 1984.]

parameter decays to zero continuously, with no discontinuous changes in density indicating a higher order (or possibly weakly first-order) phase transition.

More recently, ellipsoids of more extreme axial ratios have been examined via MD simulations (Allen and Wilson 1989) and there are seen to be systematic differences between the prolate and oblate ellipsoids; the oblate ellipsoids are more aligned at a given density than the respective prolate ellipsoids.

Ellipsoids with non-equal axial ratios, $a \neq b \neq c$, have been used to simulate a biaxial liquid crystalline phase (Allen 1990). The three distinct semi-axes were chosen such that $abc=1$, $c/a=10$ and b/a ranged between 1 and 10. The phase diagram obtained is found to be approximately symmetrical under the transformation $\{a, b, c\} \leftrightarrow \{a^{-1}, b^{-1}, c^{-1}\}$, as for the axially symmetric hard ellipsoids. For axial ratios equivalent to the self-conjugate value ($b = \sqrt{ac}$) the most stable biaxial phase is formed directly on compression from the isotropic phase. Away from these axial ratios, a discotic nematic or calamitic nematic, respectively, is identified.

The hard ellipsoid models only show the nematic and biaxial LC phases and hence work has also been undertaken on cut-sphere, hard particle, models. The cut-sphere is formed by removing two slices from a hard sphere above and below the equator, parallel to the equatorial plane and at an equal distance normal to it. Such a model is specified by the diameter of the sphere D and the perpendicular distance between the cut planes $L (L < D)$. Unlike oblate (or prolate) ellipsoids, perfectly aligned cut-spheres cannot be mapped on to the hard-sphere model by scaling arguments (Frenkel 1989, Veerman and Frenkel 1992) and thus it is possible that they may show additional liquid crystal phases. A further advantage of the cut-sphere model is that, with the ratio $L/D=1$, we once again retrieve the hard sphere reference system, which is always useful as a check on the simulation conditions and for pinning the solid-isotropic liquid transition on any derived phase diagrams.

Cut-sphere systems with ratio $L/D=0.1, 0.2, 0.3$ have been studied extensively by MC techniques (Veerman and Frenkel 1992) and the simulations have shown cut-spheres exhibit a range of interesting phases. For $L/D=0.1$, a total of four thermodynamically stable phases are identified as isotropic liquid, discotic nematic, discotic columnar and a solid phase. Simulations with $L/D=0.2$ turned out to exhibit solid, columnar and isotropic phases but with no apparent stable nematic phase. Instead, a novel phase (cubatic) consisting of short stacks of cut spheres arranged with cubic orientational order between the isotropic and discotic columnar phases was observed. For cut-spheres of ratio $L/D=0.3$ a columnar phase is not observed, and instead a strong first-order phase transition from isotropic liquid direct to a crystalline solid exists. An MC simulation on cut-spheres constrained to be oriented parallel to each other does not exhibit a columnar phase at all for $L/D=0.1$ (Azzouz *et al.* 1992). In this case, the low density nematic undergoes a phase transition to a discotic smectic where the parallel cut-spheres lie in layers parallel to the system director but with no ordering within these layers.

Recently, MC simulations have been performed on a model of cut-spheres, $L/D=0.1$ with an imposed permanent dipole moment μ^* , either parallel to the molecular symmetry axis or perpendicular to it (Weis *et al.* 1992, Zarragoicoechea *et al.* 1991, 1993). Motivation for these simulations comes from experimental evidence that compounds with strong permanent dipoles exhibit unusual properties different from the usual liquid crystal phases (Weber *et al.* 1987; Palfy-Muhoray *et al.* 1988). It was found in this work that, with a dipole moment, the isotropic and nematic phases are not altered qualitatively with respect to non-polar cut spheres. However, increasing the dipole moment of a pre-existing nematic phase to $\mu^*=0.5$, induces a phase transition to a columnar configuration.

3. Single-site soft potentials

A number of soft, single-site potentials have been developed to represent calamitic nematogens (e.g. Gay and Berne 1981, Luckhurst and Romano 1980). The calamitic form of the Gay-Berne potential has been studied extensively (Adams *et al.* 1987, Luckhurst *et al.* 1990, 1993, Chalam *et al.* 1991, de Miguel *et al.* 1990, 1991a, 1991b, 1991c, 1992).

We begin by examining the results of a parametrization of the Gay-Berne potential to represent a discotic liquid crystal, and then describe simulation studies that have been performed by the authors of this paper on a hybrid Gay-Berne, Luckhurst-Romano potential.

Berne and Pechukas (1972) developed a gaussian overlap model to represent calamitic nematogens. Gay and Berne (1981) improved the original model by removing unrealistic features that would not be present in the interaction potential between two real liquid crystal mesogens. Emerson (1991) suggested a parametrization of the Gay-Berne potential to make it represent a discotic mesogen and examined this system in some detail using MD. Four liquid crystal phases were identified; isotropic liquid, discotic nematic, discotic columnar and crystal. The use of MD simulations made it possible to obtain particle self-diffusion in the liquid crystal phases and an investigation of the particle distribution functions showed that the orientationally disordered isotropic phase possesses a liquid-like structure which remains through the discotic nematic phase.

In the discotic nematic phase the Gay-Berne discs possess a higher diffusion coefficient compared with the isotropic regime, despite being at a lower temperature. This may be explained because in the nematic phase the molecules possess a higher degree of translational freedom (due to the reduction in possible reorientation of the discs). Resolving the components of mean square particle displacements shows that molecular translational motion is greater perpendicular to the director than parallel to it. In the columnar phase this remains the case, although the overall magnitude of mean square displacement is much reduced.

Turning our attention to the columnar phase, as the discotic nematic is cooled further, the distribution functions indicate that long-range positional ordering sets in and this is consistent with the molecules being arranged in stacks parallel to the director. Values for the mean square particle displacement, and snapshots from the simulation confirm that this is a fluid phase, in the form of a columnar phase with a rectangular arrangement of columns that are intercalated. As the system is cooled further a solid crystal phase is formed.

The authors of this article have recently carried out a MD study of a single site potential (De Luca *et al.* 1994) which is a hybrid Gay-Berne, Luckhurst-Romano potential (HGBLR). The potential has the form

$$V_{\text{HGBLR}}(\hat{u}_1, \hat{u}_2, \hat{r}, r) = \varepsilon'(\hat{u}_1, \hat{u}_2, \hat{r}) \{V_0(r) + V_A(\hat{u}_1, \hat{u}_2, r)\} \quad (1)$$

where

$$V_0(r) = 4\varepsilon \left\{ \left(\frac{\sigma}{r} \right)^{12} - \left(\frac{\sigma}{r} \right)^6 \right\} \quad (2)$$

$$V_A(\hat{u}_1, \hat{u}_2, r) = -4\varepsilon\lambda \left\{ \left(\frac{\sigma}{r} \right)^{12} + \left(\frac{\sigma}{r} \right)^6 \right\} P_2(\hat{u}_1 \cdot \hat{u}_2) \quad (3)$$

$$\varepsilon'(\hat{u}_1, \hat{u}_2, \hat{r}) = 1 - \frac{\chi'}{2} \left\{ \frac{(\hat{r} \cdot \hat{u}_1 + \hat{r} \cdot \hat{u}_2)^2}{1 + \chi'(\hat{u}_1 \cdot \hat{u}_2)} + \frac{(\hat{r} \cdot \hat{u}_1 - \hat{r} \cdot \hat{u}_2)^2}{1 - \chi'(\hat{u}_1 \cdot \hat{u}_2)} \right\} \quad (4)$$

and

$$\chi' = \frac{1 - \frac{\varepsilon_c}{\varepsilon_s}}{1 + \frac{\varepsilon_c}{\varepsilon_s}} \quad (5)$$

The above variables take the following meanings: \hat{u}_1 and \hat{u}_2 are unit vectors describing the orientation of the principal symmetry axis of molecules 1 and 2 respectively; \hat{r} is the intermolecular unit vector and $r = |\mathbf{r}|$, is the intermolecular separation. The anisotropy parameter, χ' , in the strength of the potential is calculated from the relative potential well depths for side-by-side (ε_s), and end-to-end (ε_c) configurations of molecules. The parameters σ and ε are the usual Lennard-Jones parameters. The scaling factor λ takes the value 0.15 determined from preliminary calculations (Luckhurst and Romano 1980), and P_2 is the second Legendre polynomial.

The potential is characterized by a hard core which is spherically symmetrical for a fixed orientation between the two molecules. This core is surrounded by an anisotropic attractive region. Such a potential allows us to study the effects of anisotropic dispersion forces on the formation of liquid crystal phases.

Performing MD simulations with the HGBLR potential parametrized as a disc, we have obtained four distinct phases: isotropic liquid, discotic nematic, a highly ordered fluid phase with some columnar characteristics and a crystal. As the system is cooled it undergoes a first-order phase transition to a discotic nematic phase at about $T^* = 5.5$. If we examine the components of diffusion resolved with respect to the nematic director, we do not find a separation of the components of the mean square particle displacement parallel and perpendicular to the director, in contrast to that observed by Emerson (1991). This is attributed to the fact that the HGBLR potential has a spherically symmetric hard-core repulsive region.

If the system is cooled further, a second phase transition to a higher ordered fluid phase occurs. This phase is characterized by a strong one-dimensional density wave along the direction of the director. Structure perpendicular to the system director is also present, suggestive of a columnar phase. Instantaneous snapshots of our system are shown in Fig. 2. In the higher ordered fluid phase, the plane of the discs is seen to be tilted with respect to the column axis. Columnar structures consisting of columns of tilted molecules have been observed experimentally (Chandrasekhar 1983), with a rectangular arrangement of columns. In this phase we find that there is much more translation of the discs perpendicular to the director compared with parallel to it. Cooling the system even further yields a crystal that has a honeycomb structure.

The HGBLR will be used as a basis for multi-site simulations, as described in the next sections. Its principal advantage is that it is an order of magnitude faster than the Gay-Berne potential. A multisite version of the HGBLR potential is currently being used in a simulation of triphenylene derivatives.

4. Combined site potentials

Although the hard and soft potential models have made some progress in our understanding of the formation of liquid crystals, these models do not have the ability to describe specific molecular systems. In the case of the hexa-*n*-alkoxybenzoates of triphenylene, the presence of the alkyl chains is essential in order for the system to form a liquid crystal; the temperature for the isotropic-nematic transition is found to increase as the alkyl chain length is reduced (Chandrasekhar 1983). It has also been demonstrated that the methylation of the benzoate groups leads to a reduction in the phase transition temperatures. The phase behaviour is critically dependent on the position of methylation (Philips *et al.* 1993). A challenge to a simulator is to attempt to model the subtleties in a particular molecular system.

A realistic simulation of a complicated system, based on a quantum mechanical approach is not yet feasible. It is still a major feat to undertake a simulation of triphenylene derivatives by representing each atomic site by a simple potential and to include sufficient molecules to obtain thermodynamically significant results. Thus Wilson and Allen (1991, 1992) attempted a detailed simulation of the mesogen *trans*-4-(*trans*-4-*n*-pentylcyclohexyl) cyclohexylcarbonitrile (CCH5). Here, atomic sites are represented by a Lennard-Jones and a coulombic potential and extra potential terms are included to model bond stretching, bending and torsional interactions. Some

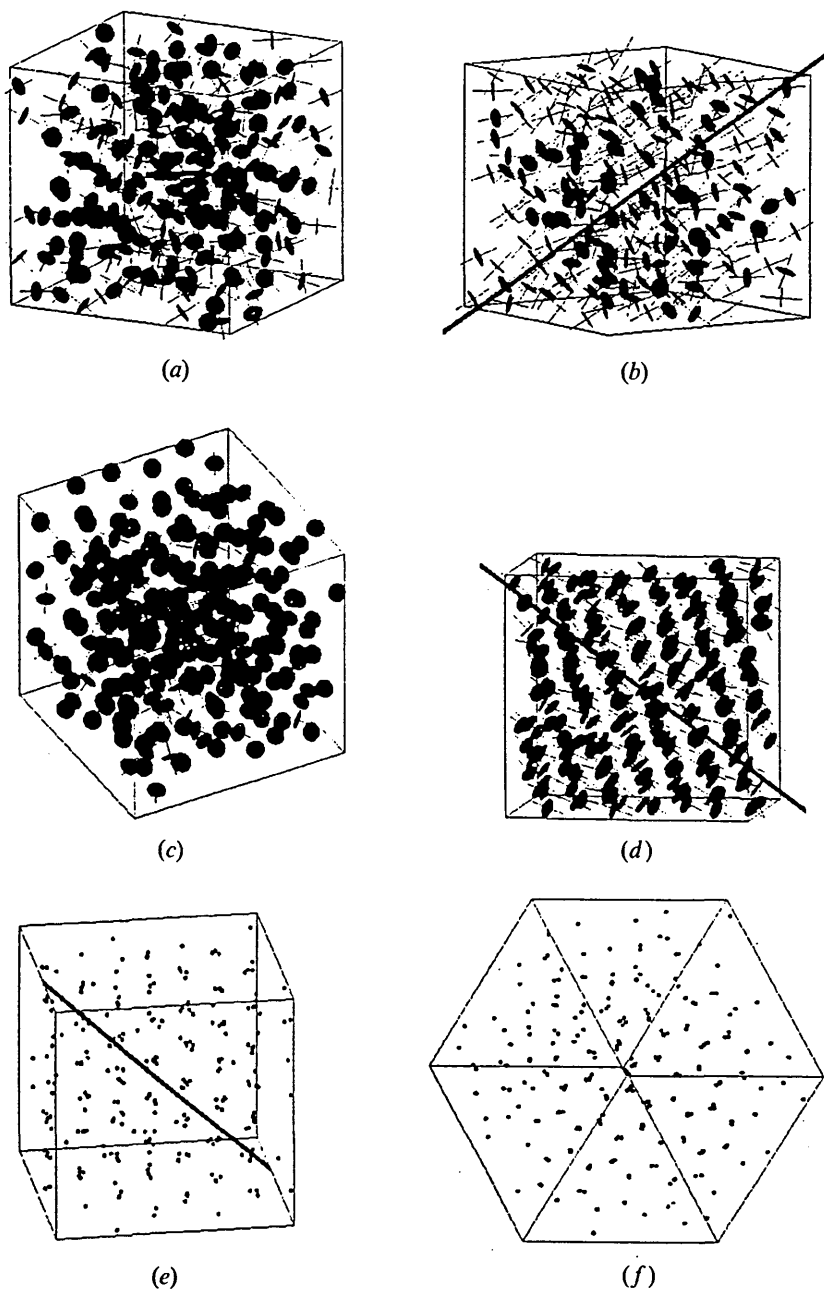


Figure 2. Six snapshots of typical configurations from a simulation of a discotic parametrization of the hybrid Luckhurst-Romano Gay-Berne potential exhibiting various phases: (a) isotropic phase from a simulation with order parameter $\langle P_2 \rangle = 0.08$; (b) a view of a nematic phase taken from a simulation with $\langle P_2 \rangle = 0.64$. The thick line through the simulation box represents the orientation of the system director; (c) as (b) but looking down the director; (d) a view of a highly ordered phase showing molecules stacked in columns with the molecular axis tilted with respect to the columnar axis. For this simulation $\langle P_2 \rangle = 0.91$; (e) as for (d) but showing only the centres of mass of the molecules looking down the columns; (f) a view of the crystal phase looking down the director, exhibiting the honeycomb structure (here $\langle P_2 \rangle = 0.99$).

atomic carbon and non-electronegative hydrogen sites are combined to achieve computational efficiency. For a relatively small system of 128 CCH₅ molecules, in excess of 800 hours was required on an IBM 3090-VF to simulate three state points. This work indicates the possibility of predicting the properties of a given mesogen prior to its synthesis.

Komolkin *et al.* (1989) have attempted a Monte Carlo simulation of 4-ethoxybenzylidene-4-*n*-butylaniline (EBBA). Seventy EBBA molecules are simulated in the isobaric-isothermal ensemble. In common with Allen and Wilson this simulation uses Lennard-Jones atom-atom potentials with an extra term to take account of torsional interactions. The simulation approach here has two stages; the atom-atom potentials are first used to calculate the conformational energy of an isolated molecule. In the second stage the molecular structure and bulk phase structure are modelled simultaneously using the Monte Carlo technique. From this approach it is clear that the liquid crystal environment has a significant effect on the molecular conformation. The main computational difficulty with this approach is the limited number of molecules that may be studied.

The correct simulation of benzene will be an important first step in the modelling of molecular systems that contain aromatic hydrocarbons. The unified atom approach has been employed in the simulation of benzene using both molecular dynamics and Monte Carlo techniques. A Monte Carlo approach was used by Evans and Watts (1976) with a six-site Lennard-Jones potential. This model gives sensible agreement with the structure of liquid benzene and the model can also predict the unit cell structure of solid benzene. Claessens *et al.* (1983), performed a molecular dynamics simulation with a six-site Lennard-Jones model that features a quadrupole term placed at the centre of the ring, which improves the prediction for the lattice parameters of solid benzene. It is also possible to simulate benzene by using a quadrupole potential and single site gaussian overlap model (Berne and Pechukas 1972). When parametrized correctly these models (Gupta *et al.* 1988) give good agreement with the six-site potential models. For large molecules it is clear that a site-site simulation approach becomes computationally expensive. The success of the gaussian overlap potential in modelling the behaviour of benzene suggests the possibility of describing more complex molecules by making use of multisite anisotropic pair potentials. A two-site gaussian overlap potential has been used to model naphthalene (Sediawan *et al.* 1989). Such an approach has also been suggested by Stone and co-workers (Price and Stone 1984, Rodger *et al.* 1988). The agreement of this simulation with the experimental data for liquid naphthalene indicates the important role of molecular shape in modelling a fluid. Everitt and Care (1987) have made a study of siloxane ring polymers with attached side chain mesogens. An MC simulation in the NVT ensemble was performed in which the attached mesogens were represented by anisotropic Luckhurst-Romano (1980) potentials and the sites were flexibly attached to a ring. A phase diagram was obtained which demonstrated the relationship between the discotic and calamitic phases for a given flexibility.

Multisite anisotropic potential models unite the use of isotropic site-site models and explicit orientation dependent potentials. This leads to the possibility of modelling more complex molecular fluids. However, a number of problems remain, such as a systematic method of parametrization and the inclusion of flexibility, bond stretching and charge distributions.

5. Conclusions

Hard-particle models have proved particularly useful in extending our knowledge of the formation of orientationally ordered and, in some cases, one-dimensional translationally ordered discotic phases through excluded volume effects. The importance of hard-particle reference systems in the development of perturbative theories of the formation of liquid crystal phases cannot be underestimated and, indeed, attention has been turned to two-dimensional models in order to investigate further the effects of dimensionality on liquid crystalline transitions (Cuesta and Frenkel 1990).

Anisotropic attractions (dispersive interactions) also influence the formation of real mesophases. With this in mind, soft models based on the Lennard-Jones 12-6 potentials have been devised and shown to exhibit a rich polymorphism.

To date, there are no published results on full site-site potentials of specific discotic mesogens. This is not surprising when we consider the complexity of discotic systems such as the triphenylene derivatives and the difficulties of simulating CCH5 and EBBA. Success with the simulation of benzene and naphthalene introduces the idea of modelling discotics by making use of multisite anisotropic potentials.

In conclusion, it is clear that the use of computer simulations will form an important tool in the future development of materials such as discotic liquid crystals, particularly as the power of computer hardware increases.

ACKNOWLEDGMENTS

We wish to acknowledge a grant of CPU time on the MCC VP1200 (award ref. GR/H55994) and one of us (MDD) would like to acknowledge the award of a research studentship (RS Quota Award ref. No. 9031742X0) from the SERC.

REFERENCES

- ADAMS, D. J., LUCKHURST, G. R., and PHIPPEN, R. W., 1987, Computer simulation studies of anisotropic systems—XVII: The Gay-Berne model mesogen. *Molecular Physics*, **61**, 1575-1580.
- ALLEN, M. P., 1990, Computer simulation of a biaxial liquid crystal. *Liquid Crystals*, **8**, 499-511.
- ALLEN, M. P., and TILDESLEY, D. J., 1987, *Computer Simulation of Liquids* (Oxford, U.K.: Clarendon Press).
- ALLEN, M. P., and WILSON, M. R., 1989, Computer simulation of liquid crystals. *Journal of Computer-Aided Molecular Design*, **3**, 335-353.
- AZZOUZ, H., CAILLOL, J. M., LEVESQUE, D., and WEIS, J. J., 1992, Phase behavior of parallel cut spheres. Monte Carlo and integral equation results. *Journal of Chemical Physics*, **96**, 4551-4558.
- BERNE, B. J., and PECHUKAS, P., 1972, Gaussian model potentials for molecular interactions. *Journal of Chemical Physics*, **56**, 4213-4216.
- BILLARD, J., DUBOIS, J. C., TINH, N. H., and ZANN, A., 1978, Une mesophase discotique. *Nouveau Journal de Chimie*, **2**, 535.
- BODEN, N., BUSHBY, R. J., and CLEMENTS, J., 1993, Mechanism of quasi-one-dimensional electronic conductivity in discotic liquid crystals. *Journal of Chemical Physics*, **98**, 5920-5931.
- CHALAM, M. K., GUBBINS, K. E., DE MIGUEL, E., and RULL, L. F., 1991, A molecular simulation of a liquid crystal model: bulk and confined fluid. *Molecular Simulation*, **7**, 357-385.
- CHADRASEKHAR, S., 1983, Liquid crystals of disc-like molecules. *Philosophical Transactions of The Royal Society, London*, **A309**, 93-103.

- CHANDRASEKHAR, S., SADASHIVA, B. K., and SURESH, K. A., 1977, Liquid crystals of disc-like molecules. *Pramana*, **9**, 471.
- CICCOTTI, G., FRENKEL, D., and McDONALD, I. R., 1987, *Simulations of Liquids and Solids* (Amsterdam: Elsevier Science Publishers B.V.).
- CLAESSENS, M., FERRARIO, M., and RYCKAERT, J. P., 1983, The structure of liquid benzene. *Molecular Physics*, **50**, 217-227.
- CUESTA, J. A., and FRENKEL, D., 1990, Monte Carlo simulation of two-dimensional hard ellipses. *Physical Review*, **A42**, 2126-2136.
- DE LUCA, M. D., NEAL, M. P., and CARE, C. M., 1994, Molecular dynamics simulations of discotic liquid crystals using a hybrid Gay-Berne Luckhurst-Romano potential. *Liquid Crystals*, **16**, 257-266.
- DE MIGUEL, E., RULL, L. F., CHALAM, M. K., and GUBBINS, K. E., 1990, Liquid-vapour coexistence of the Gay-Berne fluid by Gibbs ensemble simulation. *Molecular Physics*, **71**, 1223-1231.
- DE MIGUEL, E., RULL, L. F., and GUBBINS, K. E., 1991a, Effect of molecular elongation on liquid-vapour properties: computer simulation and virial approximation. *Physica*, **A177**, 174-181.
- DE MIGUEL, E., RULL, L. F., and GUBBINS, K. E., 1992, Dynamics of the Gay-Berne fluid. *Physical Review*, **A45**, 3813-3822.
- DE MIGUEL, E., RULL, L. F., CHALAM, M. K., and GUBBINS, K. E., 1991c, Liquid crystal phase diagram of the Gay-Berne fluid. *Molecular Physics*, **74**, 405-424.
- DE MIGUEL, E., RULL, L. F., CHALAM, M. K., GUBBINS, K. E., and VAN SWOL, F., 1991b, Location of the isotropic-nematic transition in the Gay-Berne model. *Molecular Physics*, **72**, 593-605.
- EMERSON, A. P. J., 1991, Ph.D. thesis, Southampton University, U.K., Chapter 8.
- EPPENGA, R., and FRENKEL, D., 1984, Monte Carlo study of the isotropic and nematic phases of infinitely thin hard platelets. *Molecular Physics*, **52**, 1303-1334.
- EVANS, D. J., and WATTS, R. O., 1976, On the structure of liquid benzene. *Molecular Physics*, **32**, 93-100.
- EVERITT, D. R. R., CARE, C. M., and WOOD, R. M., 1987, A Monte Carlo simulation of cyclic polymeric liquid crystals. *Molecular Crystals and Liquid Crystals*, **1987**, 55-62.
- FRENKEL, D., and EPPENGA, R., 1982, Monte Carlo study of the isotropic-nematic transition in a fluid of thin hard disks. *Physical Review Letters*, **49**, 1089-1092.
- FRENKEL, D., 1989, Invited lecture. Columnar ordering as an excluded volume effect. *Liquid Crystals*, **5**, 929-940.
- FRENKEL, D., and MULDER, B. M., 1985, The hard-ellipsoid-of-revolution fluid. I. Monte Carlo simulations. *Molecular Physics*, **55**, 1171-1192.
- FRENKEL, D., MULDER, B. M., and MCTAQUE, J. P., 1984, Phase diagram of a system of hard ellipsoids. *Physical Review Letters*, **52**, 287-290.
- GAY, J. G., and BERNE, B. J., 1981, Modification of the overlap potential to mimic a linear site-site potential. *Journal of Chemical Physics*, **74**, 3316-3319.
- GRAY, G. W., 1987, *Advances in Liquid Crystal Materials* (Poole, U.K.: BDH Chemicals Ltd).
- GUPTA, S., SEDIAWAN, B. W., and MCLAUGHLIN, E., 1988, Computer simulation of benzene using the modified Gaussian overlap and six-site potentials. *Molecular Physics*, **65**, 961-975.
- HOOVER, W. G., and REE, F. H., 1968, Melting transition and communal entropy for hard spheres. *Journal of Chemical Physics*, **49**, 3609-3617.
- KOMOLKIN, A. V., MOLCHANOV, Y. V., and YAKUTSENI, P. P., 1989, Computer simulation of a real liquid crystal. *Liquid Crystals*, **6**, 39-45.
- LUCKHURST, G. R., and ROMANO, S., 1980, Computer simulation studies of anisotropic systems. IV. The effect of translational freedom. *Proceedings of The Royal Society, London*, **A373**, 111-130.
- LUCKHURST, G. R., and SIMMONDS, P. S. J., 1993, Computer simulation studies of anisotropic systems—XXI: Parameterisation of the Gay-Berne potential for model mesogens. *Molecular Physics*, **80**, 233-252.
- LUCKHURST, G. R., STEPHENS, R. A., and PHIPPEN, R. W., 1990, Computer simulation studies of anisotropic systems—XIX: Mesophases formed by the Gay-Berne model mesogen. *Liquid Crystals*, **8**, 451-464.

- MEIER, G., SACKMANN, E., and GRABMEIER, J. G., 1975, *Applications of Liquid Crystals* (Berlin: Springer-Verlag).
- ONSAGER, L., 1949, The effects of shape on the interaction of colloidal particles. *Annals of the New York Academy of Science*, **51**, 627-659.
- PALFFY-MUHORAY, P., LEE, M. A., and PETSCHKE, R. G., 1988, Ferroelectric nematic liquid crystals: realizability and molecular constraints. *Physical Review Letters*, **60**, 2303-2306.
- PHILIPS, T. C., JONES, J. C., and McDONNELL, D. G., 1993, On the influence of short range order on the physical properties of triphenylene nematic discogens. *Liquid Crystals*, **15**, 203.
- PRICE, S. L., and STONE, A. J., 1984, A 6-site intermolecular potential scheme for the azabenzene molecules, derived by crystal-structure analysis. *Molecular Physics*, **51**, 569-583.
- RODGER, M. P., STONE, A. J., and TILDESLEY, D. J., 1988, The intermolecular potential of chlorine. A three phase study. *Molecular Physics*, **63**, 173-188.
- SAVITHRAMMA, K. L., and MADHUSUDANA, N. V., 1981, Scaled particle theory of a system of hard right circular-cylinders. *Molecular Crystals and Liquid Crystals*, **74**, 243-259.
- SCHEUBLE, B. S., 1989, Liquid crystal displays with high information content. *Kontakte*, **1**, 34-48.
- SEDIWAN, B. W., GUPTA, S., and MCLAUGHLIN, E., 1989, Computer modelling of naphthalene. *Journal of Chemical Physics*, **90**, 1888-1900.
- TALBOT, J., KIVELSON, D., ALLEN, M. P., EVANS, G. T., and FRENKEL, D., 1990, Structure of the hard ellipsoid fluid. *Journal of Chemical Physics*, **92**, 3048-3057.
- VEERMAN, J. A. C., and FRENKEL, D., 1992, Phase behavior of disklike hard-core mesogens. *Physical Review*, **A45**, 5632-5648.
- VIELLARD-BARON, J., 1972, Phase transitions of the classical hard ellipse system. *Journal of Chemical Physics*, **56**, 4729-4744; 1974, The equation of state of a system of hard spherocylinders. *Molecular Physics*, **28**, 809-818.
- WEBER, P., GUILLON, D., and SKOULIOS, A., 1987, Antiferroelectric stacking in lead phthalocyanine columnar mesophases. *Journal of Physical Chemistry*, **91**, 2242-2243.
- WEIS, J. J., LEVESQUE, D., and ZARRAGOICOEHEA, G. J., 1992, Orientational order in simple dipolar liquid-crystal models. *Physical Review Letters*, **69**, 913-916.
- WILSON, M. R., and ALLEN, M. P., 1991, Computer simulations of mesogenic molecules using realistic atom-atom potentials. *Molecular Crystals and Liquid Crystals*, **198**, 465-477.
- WILSON, M. R., and ALLEN, M. P., 1992, Structure of CCH5 in the isotropic and nematic phases: a computer simulation study. *Liquid Crystals*, **12**, 157-176.
- ZARRAGOICOEHEA, G. J., LEVESQUE, D., and WEIS, J. J., 1991, Monte Carlo study of dipolar ellipsoids. I. The isotropic phase. *Molecular Physics*, **74**, 629-637; 1993, Monte Carlo simulations of polar discotic molecules. *Molecular Physics*, **78**, 1475-1492.

MOLECULAR DYNAMICS SIMULATIONS OF CALAMITIC AND DISCOTIC LIQUID CRYSTALS USING A HYBRID GAY-BERNE LUCKHURST ROMANO POTENTIAL

M.P. NEAL*†, M.D. De LUCA** and C.M. CARE§

* *School of Mathematics and Computing, University of Derby, UK*

** *Division of Applied Physics, Sheffield Hallam University, UK*

§ *Materials Research Institute, Sheffield Hallam University, UK*

(Received September 1993, accepted January 1995)

We report a molecular dynamics simulation study of a system of particles interacting via an anisotropic potential proposed by Luckhurst and Romano and modified by scaling with part of the well depth formalism employed by Gay-Berne. Parameters are selected to model calamitic mesogens and the system exhibits a variety of mesophases as the temperature is lowered. The phases are provisionally identified as isotropic, nematic, a highly ordered fluid with some smectic features and crystal. Comparison is made with a previous study with the same potential parameterised to model discotic mesogens.

KEY WORDS: Calamitic, discotic, liquid crystal, soft anisotropic potential

1 INTRODUCTION

Computer models of the liquid crystal phases of rod-like and disc-like molecules, calamitics and discotics, employing anisotropic potentials have led to an improved understanding of the way in which the intermolecular interactions between anisotropic molecules affect the observed liquid crystal phases.

Hard non-spherical molecules e.g. [1, 2, 3] have proved successful in simulating a variety of mesophases and are important as hard particle reference systems by comparison with theoretical studies [4]. A simulation [5] of a biaxial hard-ellipsoid fluid with three distinct semi-axes has been undertaken and found to be in semi-quantitative agreement with recent theories. A computer study of a calamitic mesogenic molecule has been undertaken [6] for three state points using realistic atom-atom potentials modelled by a standard empirical force field and building in realistic features such as molecular flexibility, complicated structural anisotropy and electrostatic forces. It provided predictions for phase behaviour and ordering that are in good agreement with experiment but suggested such simulations are currently beyond the range of modern computers.

† Author for correspondence

Single site phenomenological anisotropic potentials describing both short range repulsive and long range attractive contributions to the potential have been developed in an attempt to provide computationally simple potentials for complex liquid crystal molecules and have proved valuable in simulating a variety of mesophases of calamitic and discotic mesogens [7, 8, 9] using adjustable parameters. Berne and Pechukas [10] proposed a gaussian overlap potential model to simulate liquid crystal behaviour. The original model suffered from several unrealistic features which would not be present in the pair potential between two liquid crystal mesogens and Gay and Berne [11] modified the potential by obtaining a function which gave the best fit to a linear array of four equi-distant Lennard-Jones centres. Real mesogenic molecules are biaxial and the Gay-Berne potential which is cylindrically symmetric provides an over-idealised model. Recently [12] a study has been undertaken of the Gay-Berne fluid using realistic molecule-molecule parameter values estimated for p-terphenyl from a total potential constructed from atom-atom terms with the biaxially projected out. The molecule p-terphenyl was chosen because of its rigidity and non-polar character.

Making the simplifying assumption of a rigid model we are in current work modelling p-terphenyl by a more realistic rigid biaxial three-site model in which the central site is twisted through an angle with respect to each to the end sites; each site interacts via an anisotropic potential which is a hybrid Gay-Berne Luckhurst-Romano potential (HGBLR).

Luckhurst and Romano [13] represented cylindrically symmetric particles by a Lennard-Jones 12-6 potential V_0 together with an additional anisotropic term V_a

$$V = V_0 + V_a \quad (1)$$

The Luckhurst Romano pair potential is scaled by part of the well depth formalism employed to fit the Gay-Berne so that the hybrid Gay-Berne Luckhurst-Romano potential becomes:

$$V = \varepsilon'(\hat{\mathbf{u}}_1, \hat{\mathbf{u}}_2, \hat{\mathbf{r}}) \{ V_0 + V_a \} \quad (2)$$

where

$$V_0 = 4\varepsilon \left\{ \left(\frac{\sigma}{r} \right)^{12} - \left(\frac{\sigma}{r} \right)^6 \right\} \quad (3)$$

and

$$V_a = -\lambda 4\varepsilon \left\{ \left(\frac{\sigma}{r} \right)^{12} + \left(\frac{\sigma}{r} \right)^6 \right\} P_2(\hat{\mathbf{u}}_1 \cdot \hat{\mathbf{u}}_2) \quad (4)$$

and

$$\varepsilon'(\hat{\mathbf{u}}_1, \hat{\mathbf{u}}_2, \mathbf{r}) = 1 - \frac{\chi'}{2} \left[\frac{(\hat{\mathbf{r}} \cdot \hat{\mathbf{u}}_1 + \hat{\mathbf{r}} \cdot \hat{\mathbf{u}}_2)^2}{1 + \chi' \hat{\mathbf{u}}_1 \cdot \hat{\mathbf{u}}_2} + \frac{(\hat{\mathbf{r}} \cdot \hat{\mathbf{u}}_1 - \hat{\mathbf{r}} \cdot \hat{\mathbf{u}}_2)^2}{1 - \chi' \hat{\mathbf{u}}_1 \cdot \hat{\mathbf{u}}_2} \right] \quad (5)$$

The orientation of the molecules is specified by the unit vector $\hat{\mathbf{u}}$ and the intermolecular vector by the unit vector $\hat{\mathbf{r}}$. The parameter χ' determines the relative ratio of the end-to-end and side-to-side interactions and is given by

$$\chi' = (1 - \varepsilon_e/\varepsilon_s)/(1 + \varepsilon_e/\varepsilon_s) \quad (6)$$

where ϵ_e/ϵ_s is the ratio of the end-to-end and side-to-side potential well depths. The parameters σ and ϵ are the usual Lennard-Jones parameters. The scaling factor λ takes the value 0.15 determined from preliminary calculations [13] and P_2 is the second Legendre polynomial.

The HGBLR potential is shown Figure 1 and as can be seen from equations (2) to (5) is characterised by a hard core which has spherical symmetry for a fixed orientation. The core is surrounded by an anisotropic attractive region. Such a potential allows us to study the effects of anisotropic dispersive forces upon the formation of liquid crystal phases by investigating the effect of ϵ' alone by varying ϵ_e/ϵ_s . Prior to undertaking a multi-site simulation the authors [14] have recently undertaken a molecular dynamics (MD) study of a single-site HGBLR potential parameterised in a disc-like form following previous work [9] so that ϵ_e/ϵ_s takes the value 5.0 and favours the end-to-end interaction i.e. a discotic mesogen. We present here results for a single site HGBLR potential with ϵ_e/ϵ_s set to 0.2 favouring the side-to-side interaction i.e. a calamitic mesogen.

2 MOLECULAR DYNAMICS SIMULATION

We have performed MD simulations for 256 and 500 particles in a cubic box with the usual periodic boundary conditions. No cut off was used as this did not aid vector-

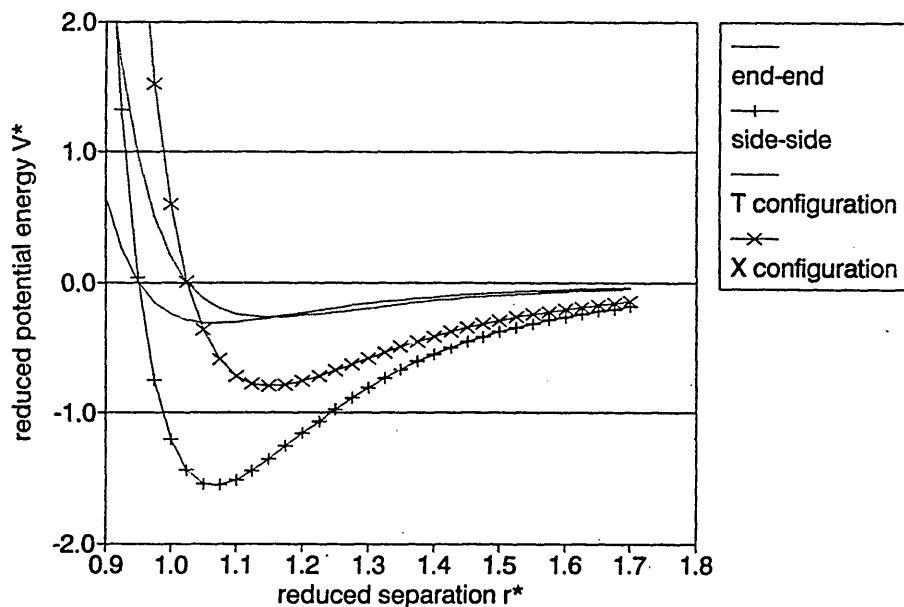


Figure 1 The distance dependence of the potential energy calculated from the hybrid Gay-Berne Luckerst-Romano Potential for particular orientations of the particles with respect to one another and to the intermolecular vector. The parameterisation of the potential is that used in the molecular dynamics simulation, and described in the text.

isation. A more detailed description of the method is given in [14]. The results are presented for a reduced number density of $\rho^* = 1.1$ which enables equilibration of the system at low temperatures without cavity formation. The particles are axially symmetric about $\hat{\mathbf{u}}$ with a spherical repulsive core surrounded by a non-spherical attractive region equivalent to a rod. A reduced moment of inertia of $I^* = 1.00$, ($I^* = I/(m\sigma^2)$) was chosen to ensure a reasonable rate of equilibration between translational and rotational kinetic energy. The first simulation was started from an α -fcc crystal with kinetic energy such that the lattice method. The system was allowed to equilibrate over 15,000 steps, equipartition between translational and rotational energy being observed, and production runs of 15,000 steps were employed. The temperature was reduced by scaling the linear velocities and allowing the system to equilibrate for 15,000 steps between each production run. To provide acceptable energy conservation for each state point a value of reduced time step $\Delta t^* = (\epsilon/m\sigma^2)^{1/2} \Delta t$ of 0.003 was employed and fluctuations of less than 1 part in 1000 of the total energy were observed for all state points except one just before the region identified as the isotropic-nematic transition in which the energy fluctuated by 1 part in 100. The following reduced quantities were calculated from the simulation: the pressure $P^* = P\sigma^3/\epsilon$, temperature $T^* = Tk_B/\epsilon$, the total internal energy per particle $E^* = E/\epsilon$ the potential and kinetic energy per particle, V^* and K^* , the mean square displacement, $\langle |\mathbf{r}^*(t) - \mathbf{r}^*(0)|^2 \rangle$ and its components parallel and perpendicular to the director, the order parameter $\langle P_2 \rangle$ and the director of the phase $\hat{\mathbf{n}}$. The second rank order parameter $\langle P_2 \rangle$ was evaluated using the \mathbf{Q} tensor defined by

$$Q_{\alpha\beta} = \frac{1}{N} \sum_{i=1}^N \frac{3u_\alpha^i u_\beta^i - \delta_{\alpha\beta}}{2}$$

where u_α^i is the α -component of the unit vector along the symmetry axis of the molecule i . $\langle P_2 \rangle$ was defined as the ensemble average of the largest eigenvalue for the \mathbf{Q} tensor, and the director as the corresponding eigenvector [15] and were calculated every 100 steps.

Additionally the second rank orientation correlation function $G_2(r^*) = \langle P_2(\hat{\mathbf{u}}_1, \hat{\mathbf{u}}_2) \rangle$, the radial distribution function $g(r^*)$ together with the longitudinal and transverse pair correlation functions $g_{\parallel}(r_{\parallel}^*)$ and $g_{\perp}(r_{\perp}^*)$ were calculated.

3 RESULTS

The variations with temperatures of the second rank order parameter $\langle P_2 \rangle$ for the cooling runs for systems of 256 and 500 particles are shown in Figure 2. We see that the system is isotropic at reduced temperatures above $\langle T^* \rangle = 1.6$ although finite size fluctuations in evaluating the \mathbf{Q} tensor lead to a small non-zero value for $\langle P_2 \rangle$. Cooling the system below $\langle T^* \rangle = 1.6$ causes the order parameter to rise rapidly to about 0.5. It then tends slowly to 1.0 as the system is cooled further. The internal energy also shows a transition at $\langle T^* \rangle = 1.65 \pm 0.05$ as shown in Figure 3; however there is a further significant decrease in internal energy at $\langle T^* \rangle = 0.88 \pm 0.03$ indicating the presence of a second phase transition between two highly ordered systems. The cooling runs were repeated for a system of 500 particles to investigate the effect of box size upon the phase

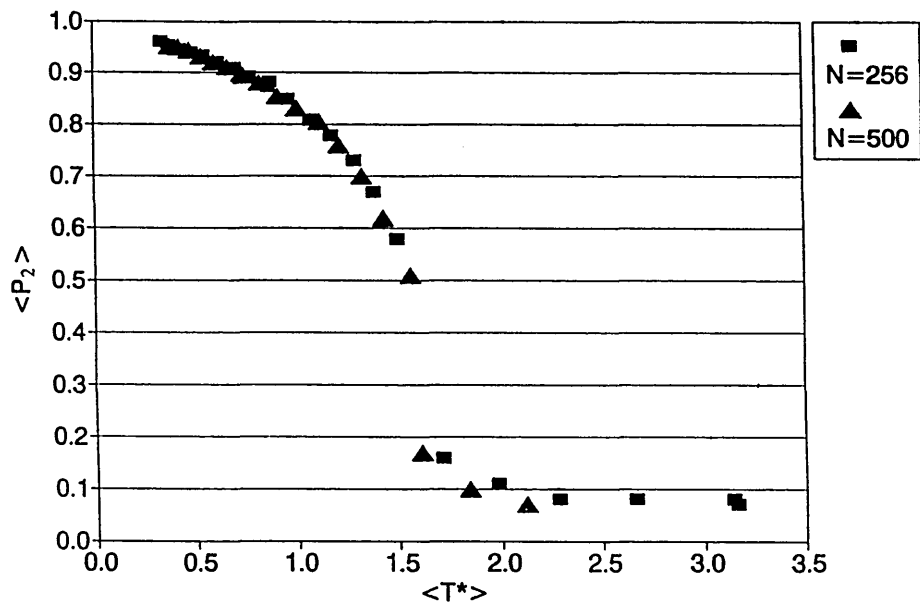


Figure 2 The variation of the second rank orientational order parameter $\langle P_2 \rangle$ as a function of temperature.

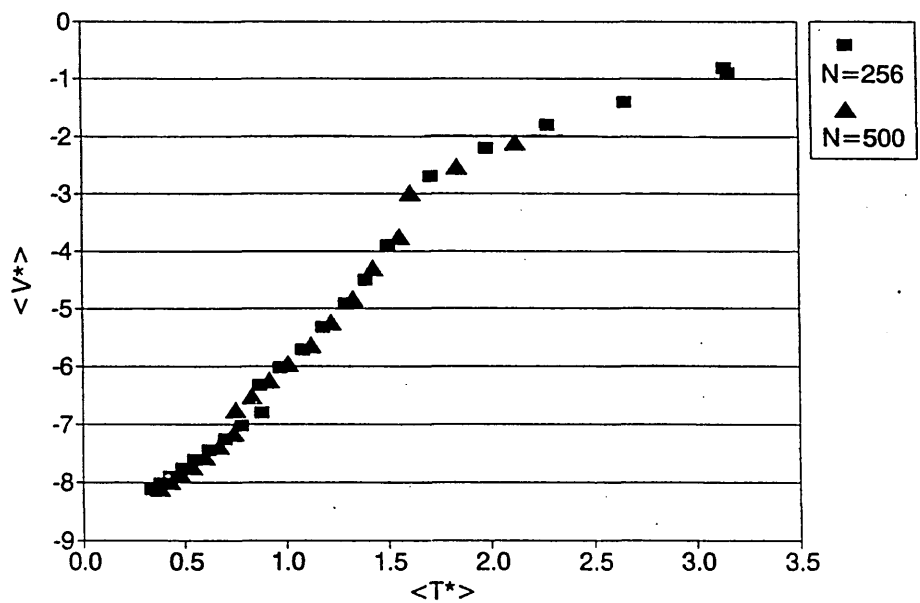


Figure 3 The variation of the potential energy $\langle V^* \rangle$ as a function of temperature.

diagram but no appreciable system size dependence was noted in the nematic region although the nematic isotropic transition region seemed somewhat affected by system size, as can be seen in Figures 2 and 3. The entropy of transition $\Delta\langle V^* \rangle / \langle T^* \rangle$ was estimated to be 0.5 for each transition. The two mesophase transitions that were identified for the disc-like parameterisation [14] were relatively sharper with an estimated entropy of transition of 0.6.

Simulation runs near the transition at $\langle T^* \rangle = 1.6$ were extended to 60,000 steps and near the transition at $\langle T^* \rangle = 0.88$ were extended to 120,000 steps for the system of 256 particles. The diffusion coefficients D^* and its components D_{\parallel}^* and D_{\perp}^* , parallel and perpendicular to the director were calculated from the Einstein relation valid at long times [16] by considering the final 30,000 and 35,000 steps of the simulation respectively as shown in Table 1.

Plots of the mean square displacement with time are shown in Figures 4(a), (b) and (c) for reduced temperatures of $\langle T^* \rangle = 1.57$, 0.93 and 0.84 respectively and are straight

Table 1 Reduced diffusion coefficients, mean order parameter and mean temperature for the system of 256 particles.

$\langle T^* \rangle$	D^*	D_{\parallel}^*	D_{\perp}^*	$\langle P_2 \rangle$
1.98 ± 0.05	0.360	0.108	0.126	0.12 ± 0.05
1.72 ± 0.05	0.340	0.115	0.113	0.18 ± 0.17
1.57 ± 0.07	0.220	0.079	0.071	0.38 ± 0.08
0.93 ± 0.03	0.0156	0.0041	0.0057	0.861 ± 0.009
0.84 ± 0.02	0.0182	0.0067	0.0057	0.878 ± 0.009

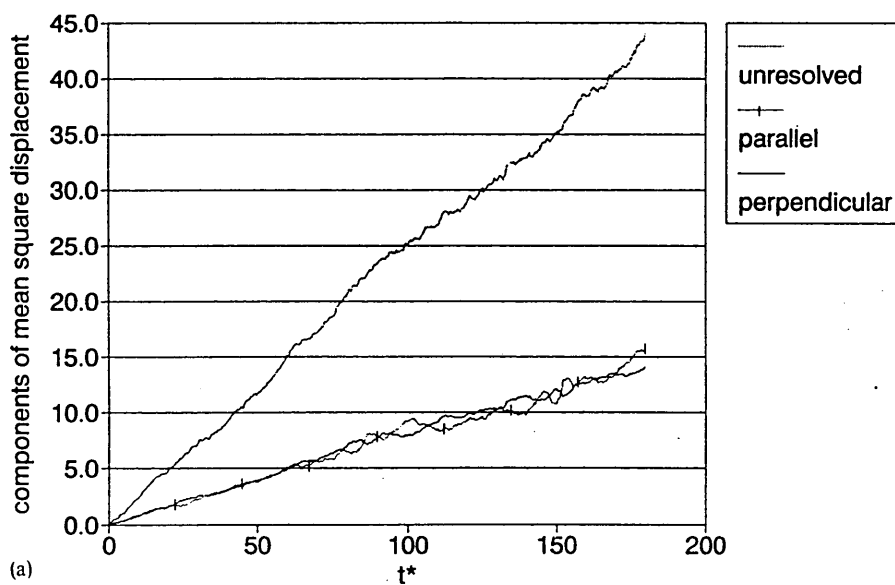


Figure 4 Mean square displacement versus time resolved with respect to the system director at reduced temperatures of (a) $\langle T^* \rangle = 1.57$ (b) $\langle T^* \rangle = 0.93$ and (c) $\langle T^* \rangle = 0.84$.

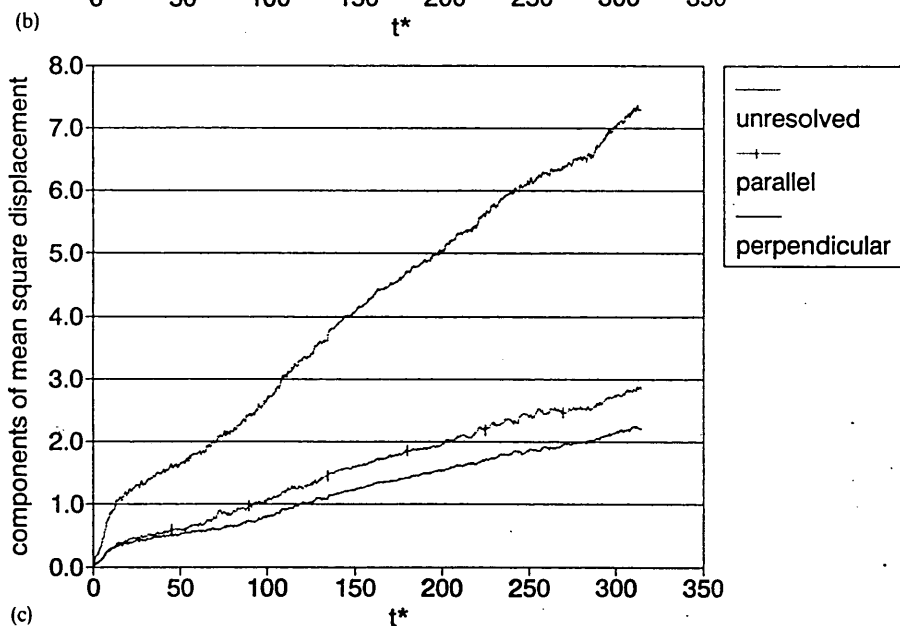
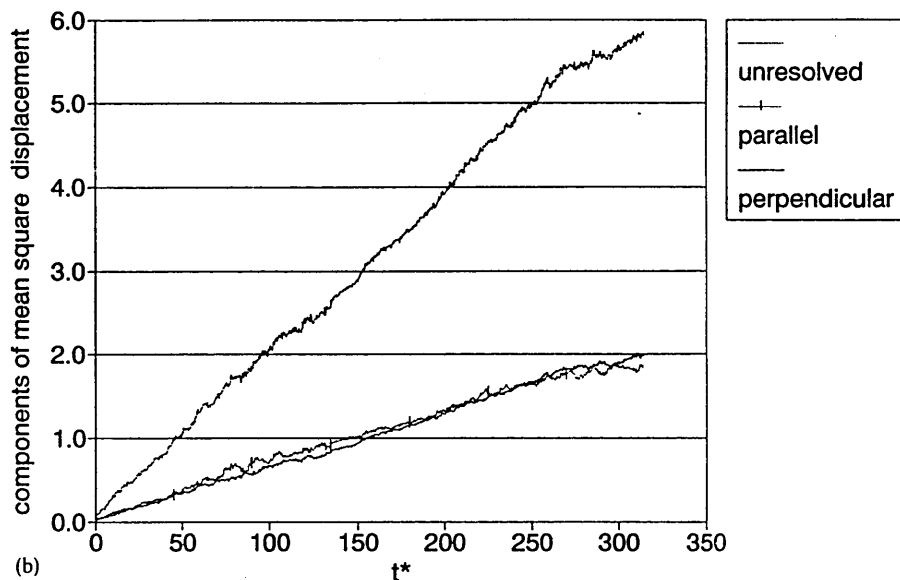


Figure 4 (Continued)

lines exhibiting liquid-like diffusion; below $\langle T^* \rangle \approx 0.8$ the diffusion virtually ceases indicating a solid phase. As Table 1 shows, the diffusion coefficient reduces as the temperature is lowered until $\langle T^* \rangle = 0.93$, and then shows an increase at $\langle T^* \rangle = 0.84$. This increase is due to an increase in diffusion parallel to the director, showing motion is less hindered parallel to the director although both values are very low at this temperature. This increase in diffusion parallel to the director is indicative of the onset

of a smectic phase. We note however that at $\langle T^* \rangle = 0.93$ the diffusion coefficient is greater perpendicular to the director than parallel to it. Figures 5(a), 5(b), 5(c) and 5(d) show the radial distribution function $g(r^*)$ together with the longitudinal and transverse correlation functions $g_{\parallel}(r_{\parallel}^*)$ and $g_{\perp}(r_{\perp}^*)$ at temperatures of $\langle T^* \rangle = 1.57, 0.93, 0.88$

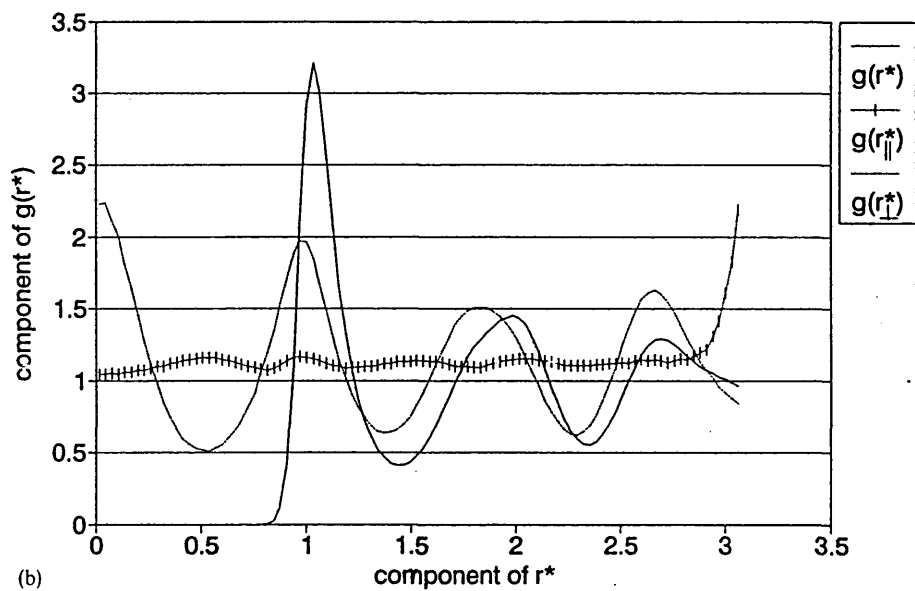
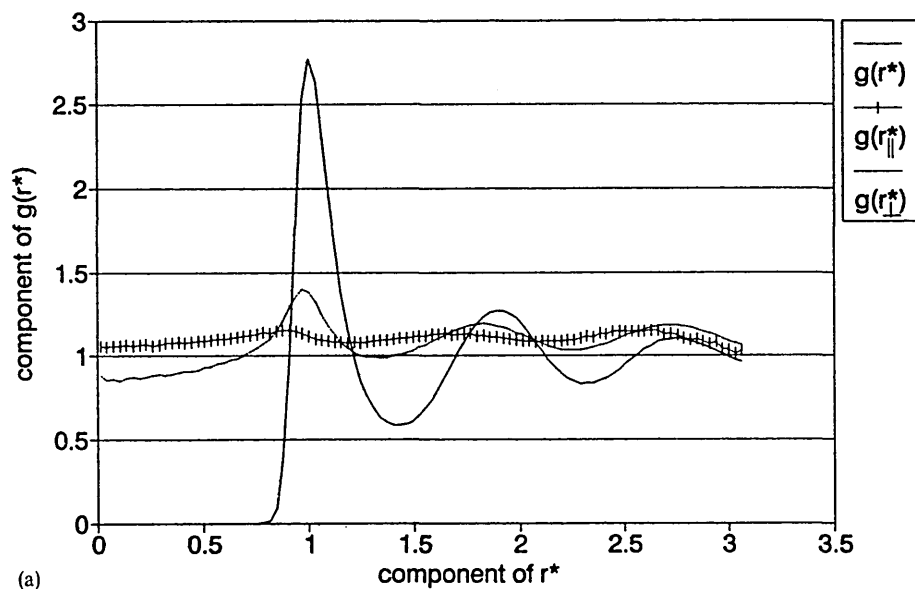


Figure 5 The radial distribution function $g(r^*)$ and the longitudinal and transverse pair correlation functions $g_{\parallel}(r_{\parallel}^*)$ and $g_{\perp}(r_{\perp}^*)$ resolved with respect to the system director as a function of scaled separation r^* simulated for the hybrid Gay-Berne Luckhurst-Romano potential at a series of reduced temperatures (a) $\langle T^* \rangle = 1.57$ (b) $\langle T^* \rangle = 0.93$ (c) $\langle T^* \rangle = 0.84$ and (D) $\langle T^* \rangle = 0.34$.

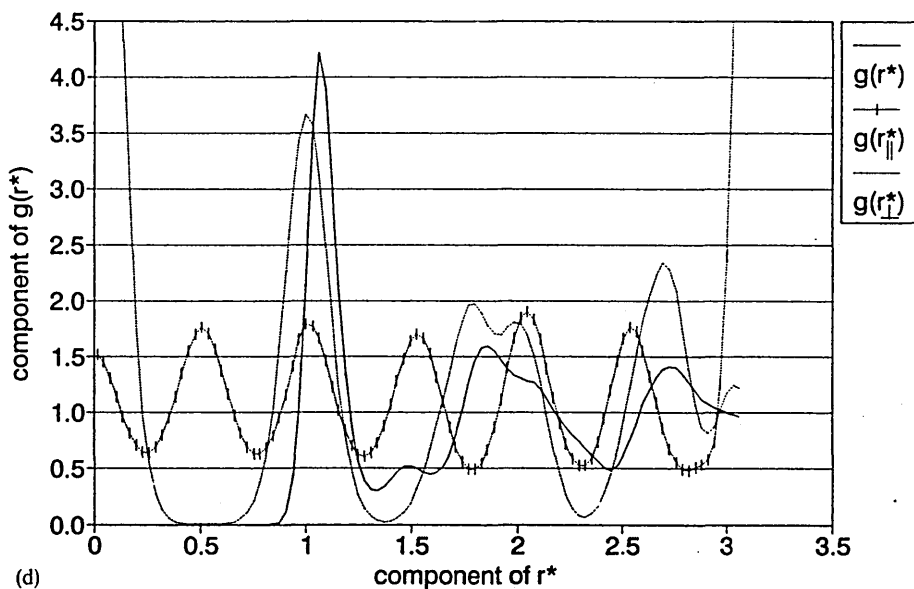
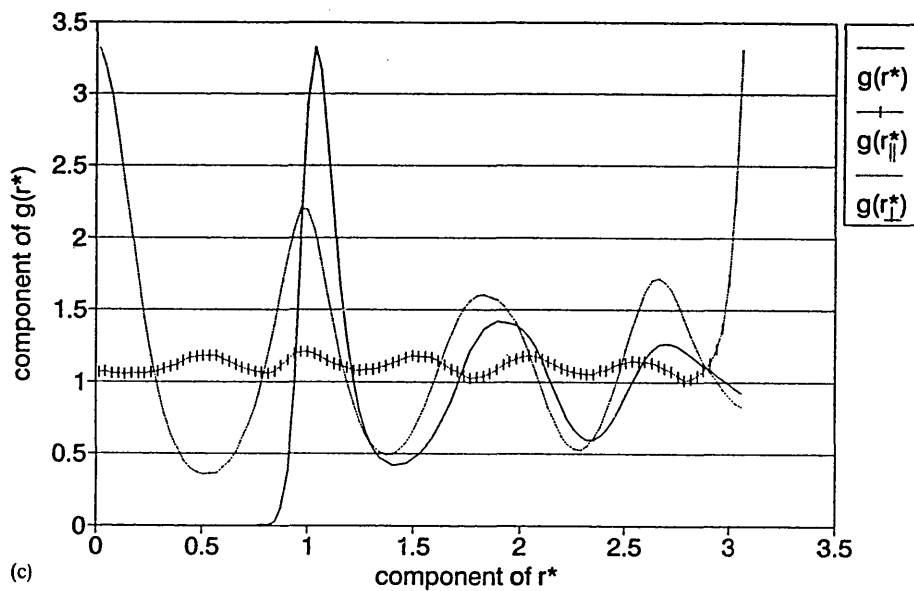


Figure 5 (Continued)

and 0.34 respectively. Figure 5(a) demonstrates that there is no discernible change from liquid-like behaviour at $\langle T^* \rangle = 1.57$ so that this phase is identified as nematic. Figure 5(b) exhibits a strong 1-dimensional oscillation in the pair correlation function perpendicular to the director and a weak oscillation in the pair correlation function parallel to the director. Figure 5(c) and 5(d) demonstrate that both these oscillations

increase in magnitude progressively as the temperature is reduced to $\langle T^* \rangle = 0.84$ and to the solid phase at $\langle T^* \rangle = 0.34$. Figure 6 represents "snapshots" of sample configurations taken during runs at $\langle T^* \rangle = 1.29$, $\langle T^* \rangle = 0.88$ and $\langle T^* \rangle = 0.34$ corresponding to instantaneous values of the order parameter of $\langle P_2 \rangle = 0.71$, 0.90 and 0.96 respectively; the orientation of a particle is represented by a line pointing along the vector \hat{u} and the position of the centre of mass by a dot. In Figure 6(a) illustrating the nematic phase two views of the same configuration are presented perpendicular and parallel to the director. In Figure 6(c) two views are presented parallel to the director,

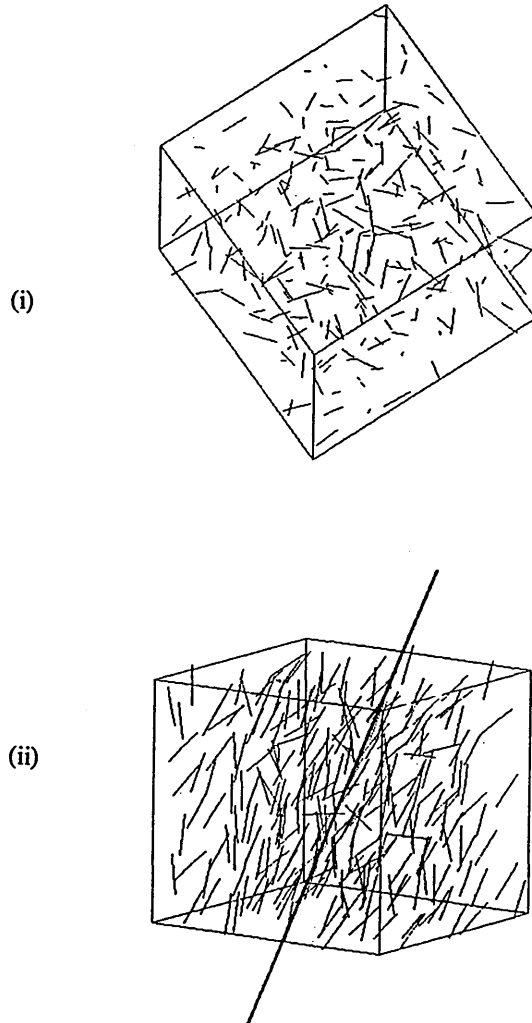


Figure 6a $\langle P_2 \rangle = 0.71$ $\langle T^* \rangle = 1.29$

Figure 6 Three sets of snapshots from typical configurations at instantaneous values of the order parameter $\langle P_2 \rangle$ of (a) 0.71 (b) 0.90 and (c) 0.96.

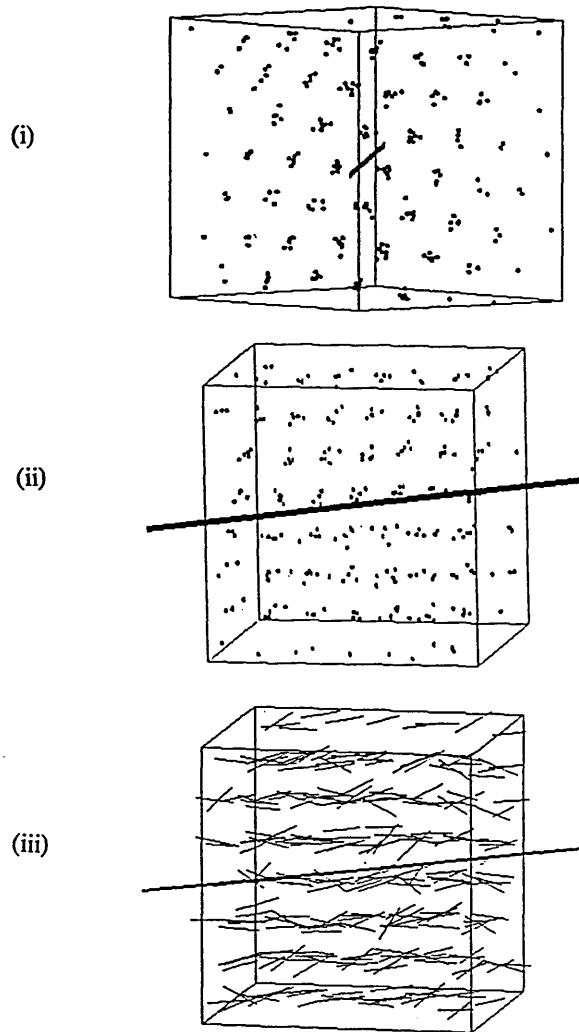


Figure 6b $\langle P_2 \rangle = 0.90$ $\langle T^* \rangle = 0.88$

Figure 6 (Continued)

and one perpendicular to the director; showing a structure with hexagonal symmetry, the intercalation of the rows accounting for the periodicity in of $g_{ij}(r_i^*)$ in Figures 5(c) and (d). Figure 6(b) shows an ordered phase with more clearly delineated columns than rows indicated by the greater order shown in 6(i) than in 6(ii). Together with the larger diffusion coefficient perpendicular to the director at this temperature it appears the particles diffuse first into columns then into rows as temperature is reduced. Stroobants *et al.*

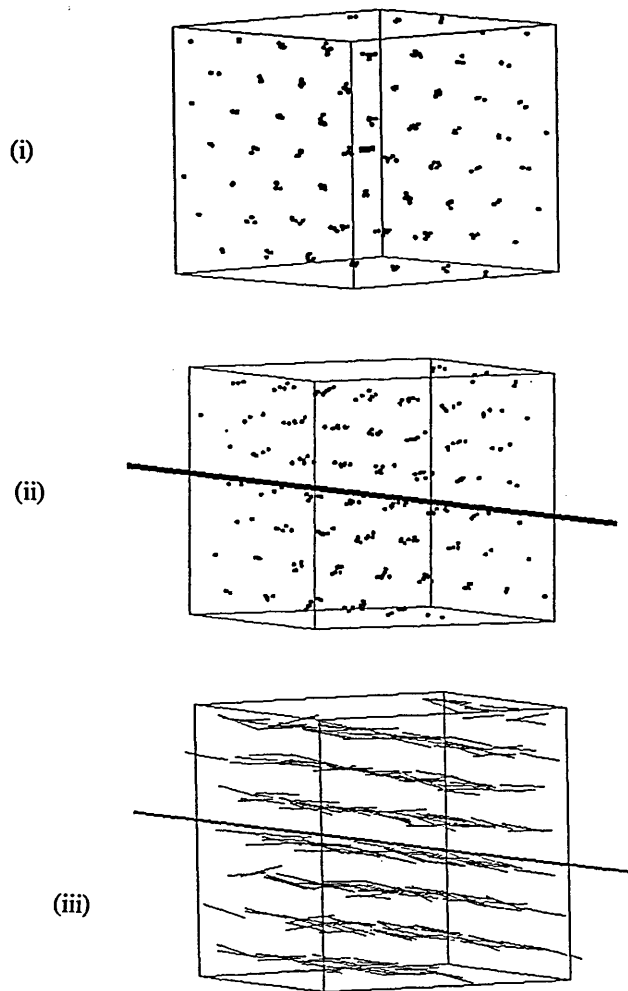


Figure 6c $\langle P_2 \rangle = 0.96$ $\langle T^* \rangle = 0.34$

Figure 6 (Continued)

[17] observed a columnar phase at densities intermediate between the smectic and crystalline phases for a system of hard parallel spherocylinders with length to width ratios of greater than 3.

The second rank orientational correlation function $G_2(r^*)$ exhibited a peak close to a reduced separation of $r^* = 0.7$ in all cases. In the isotropic phase $G_2(r^*)$ quickly decayed to a limiting value close to zero, indicating the absence of any long range order. In the nematic and highly ordered phases $G_2(r^*)$ attains a limiting value of approxi-

mately $\langle P_2 \rangle^2$ indicative of the persistence of long range orientational order in this phases.

Performing MD simulations with the HGBLR potential parameterised as a disc we have obtained four distinct phases; isotropic liquid, discotic nematic, a highly ordered phase with some columnar characteristics and a crystal with honeycomb symmetry. The diffusion in a direction parallel and perpendicular to the director is approximately equal in the nematic phase but the diffusion coefficient perpendicular to the director is significantly greater in the columnar-type phase. In the highly ordered phase the plane of the discs is seen to be tilted with respect to the column axis. Columnar structures consisting of columns of tilted molecules have been observed experimentally [18], with a rectangular arrangement of columns.

4 CONCLUSIONS

We have used molecular dynamics simulations to simulate systems of rod-like particles interacting via an anisotropic potential proposed by Luckhurst and Romano and scaled by part of the well depth formalism employed by Gay-Berne. The potential has proved successful in simulating a wide variety of mesophases. We have identified a phase transition from an isotropic liquid to a nematic at a reduced temperature of $\langle T^* \rangle \approx 1.6$. The calamitic nematic phase is stable until the temperature is lowered to $\langle T^* \rangle \approx 0.88$ and subsequently undergoes a transition through a short-lived columnar phase to a smectic phase, before cooling to a crystal with hexagonal symmetry. The reduced cpu time required for the HGBLR potential will allow simulation studies of biaxial models of liquid crystals to be undertaken.

Acknowledgements

We are grateful to G.R. Luckhurst and P.S. Simmonds for a pre-print of their paper. We wish to acknowledge the award of a research studentship to MDD from the Science and Engineering Council (RS Quota Award ref. no. 9031742XO) plus a grant of CPU time on the Manchester Computer Centre VP1200 vector processor (SERC Award ref. GR/H55994).

References

- [1] J.A.C. Veerman and D. Frenkel. Phase behaviour of disklike hard-core mesogens. *Phys. Rev. A.*, **45**, 5632–5648 (1992).
- [2] H. Azzouz, J.M. Calliol, D. Levesque and J.J. Weiss. Phase behaviour of parallel cut spheres. Monte Carlo and integral equation results. *J. Chem. Phys.*, **96**, 4551–4558 (1992).
- [3] D. Frenkel, B.M. Mulder and J.P. Mctague. Phase diagram of hard ellipsoids of revolution. *Mol. Cryst. Liq. Cryst.*, **123**, 119–128 (1985).
- [4] D. Frenkel and R. Eppenga. Monte Carlo study of the isotropic-nematic transition in a fluid of thin hard discs. *Phys. Rev. Lett.*, **49**, 1089–1092 (1982).
- [5] M.P. Allen. Computer simulation of biaxial liquid crystal. *Liq. Cryst.*, **8**, 499–511 (1990).
- [6] M.R. Wilson and M.P. Allen. Computer simulations of mesogenic molecules using realistic atom-atom potentials. *Mol. Cryst. Liq. Cryst.*, **198**, 465–477 (1991).
- [7] G.R. Luckhurst, R.A. Stephens and R.W. Phippen. Computer simulation of anisotropic systems. XIX Mesophases formed by the Gay-Berne model mesogen. *Liq. Crystal.*, **8**, 451–464 (1990).

- [8] E. de Miguel, L.F. Rull, M.K. Challam and K.E. Gubbins. Liquid crystal phase diagram of the Gay-Berne fluid. *Mol. Phys.*, **74**, 405–424 (1991).
- [9] A.P.J. Emerson. Molecular theories and computer simulations of liquid crystals PhD thesis, University of Southampton, UK (1991).
- [10] B.J. Berne and P. Pechukas. Gaussian model potentials for molecular interactions. *J. Chem. Phys.*, **56**, 4213–4216 (1972).
- [11] J.G. Gay and B.J. Berne. Modification of the overlap potential to mimic a linear site–site potential. *J. Chem. Phys.*, **74**, 3316–3319 (1981).
- [12] G.R. Luckhurst and P.S.J. Simmonds. Computer simulation studies of anisotropic systems. XXI Parameterization of the Gay-Berne potential for model mesogens. *Molecular Physics* **80**, 233–252 (1993).
- [13] G.R. Luckhurst and S. Romano. Computer simulation studies of anisotropic systems IV. The effect of translational freedom. *Proc. R. Soc. Lond. A.*, **373**, 111–130 (1981).
- [14] M.D. De Luca, M.P. Neal and C.M. Care. Molecular dynamics simulations of discotic liquid crystals using a hybrid Gay-Berne Luckhurst-Romano potential. *Liq. Cryst.* **16** (1994), 257–266
- [15] C. Zannoni, in *The Molecular Physics of Liquid Crystals* (ed. Luckhurst G.R. & Gray G.W.), Ch. 9., Academic Press, New York, USA (1979).
- [16] D.J. Tildesley, in *Molecular Liquids, Dynamics and Interactions*, (ed. Barnes A.J., Orville Thomas W.J. and Yarwood J.) NATO ASI series Vol. 135, pp 519–560, Reidel, New York (1984).
- [17] A. Stroobants, H.N.W. Lekkerkerker and D. Frenkel. Evidence for one-, two-, and three-dimensional order in a system of hard parallel spherocylinders. *Phys. Rev. A.*, **36**, 2929–2945 (1987).
- [18] S. Chandrasekhar. Liquid crystals of disc-like molecules. *Phil. Trans. Roy. Soc., London*, **A309**, 93–103 (1983).